

The Pennsylvania State University

The Graduate School

**ELECTRON TRANSFER IN IONIC LIQUIDS:
INTRAMOLECULAR AND TRANSFER-TO-SOLVENT REACTIONS**

A Dissertation in

Chemistry

by

Marissa N. Saladin

© 2020 Marissa Saladin

Submitted in Partial Fulfillment

of the Requirements

for the Degree of

Doctor of Philosophy

December 2020

The dissertation of Marissa Saladin was reviewed and approved by the following:

Mark Maroncelli
Distinguished Professor of Chemistry
Dissertation Advisor
Chair of Committee

John Asbury
Professor of Chemistry

Lasse Jensen
Professor of Chemistry

John H. Golbeck
Professor of Biochemistry and Biophysics, and Chemistry

Phillip Bevilacqua
Distinguished Professor of Chemistry and of Biochemistry and Molecular
Biology
Head of the Department or Chair of the Graduate Program

ABSTRACT

Ionic liquids (ILs) are being tested as potential replacements for electrolytes in energy-related applications. Bimolecular electron transfer (ET) reactions play a central role in many of these applications, making it important to obtain a fundamental understanding of ET in ionic liquids, which may differ from the well-understood case of ET in conventional dipolar solvents. Because reactant diffusion is slow and only partially understood in ionic liquids, diffusion often masks the underlying ‘pure’ ET dynamics. This dissertation explores two approaches to circumventing reactant diffusion in order to learn more about ET reactions in ionic liquid environments: study of a covalently linked electron donor-acceptor dyad and measurements of electron transfer between a solute and an electroactive ionic liquid. Reactions in both cases occur over a range of femtosecond to nanosecond times and is probed via fluorescence quenching measurements using time-correlated single photon counting and Kerr-gated emission spectroscopy.

In the first study, a new intramolecular electron donor-acceptor probe was synthesized by covalently linking the photoacceptor coumarin 152 with the electron donor dimethylaniline to create a C152-DMA dyad for use in probing dynamical solvent effects in ionic liquids. Molecular dynamics simulations of this dyad show considerable conformational flexibility of the linker group, but only over a range of geometries where ET rate-determining parameters are expected to vary minimally. Steady-state and time-resolved fluorescence spectra demonstrate that the C152-DMA dyad is highly responsive to solvent polarity. ET rate constants are shown to vary by a factor of $>10^5$ between nonpolar and high polarity conventional solvents. Results in the few ionic liquids

examined show that C152-DMA is also sensitive to solvent fluidity or solvation times. Unfortunately, sensitivity to hydrolysis in the presence of acidic impurities limits this dyad's use to ionic liquids of high purity.

In the second study, the neat ionic liquid 1-butylpyridinium bis(trifluoromethylsulfonyl) imide ([Py₄][Tf₂N]) was used as the acceptor in ET reactions with 12 coumarin dyes which act as photo-excited electron donors. There have been a number of such studies of reaction between solutes and neat redox active conventional liquids, primarily coumarin dyes in neat aromatic amines; however, the work reported here is the first in a neat reactive ionic liquid. The spectroscopy of the coumarins in [Py₄][Tf₂N] was characterized along with two reference solvents, acetonitrile and a nonreactive imidazolium ionic liquid, all of which have similar polarities. Electronic properties, such as absorption and emission frequencies are found to be nearly the same between the three solvents, allowing data in acetonitrile to be used to estimate the electron transfer driving force for all reactions, which are found to span a range of nearly 0.70 eV. Stern-Volmer analyses of the quenching by 1-butylpyridinium dilute in acetonitrile solution yielded bimolecular rate constants k_q that were found to be positively correlated with the driving force, but close to the diffusion limit in all cases. In the neat quenching ionic liquid, electron transfer times varied by about a factor of ~300, ranging from 0.3 ps to 100 ps. The measured rates are remarkably similar to those found for coumarins in neat quenching aromatic amine solvents despite the difference of >0.5 eV difference in driving force, due to the much higher polarity of [Py₄][Tf₂N]. What dynamical factors ultimately control the rates of these reactions -- modulation of the

energetics by solvation dynamics or modulation of electronic coupling by small-amplitude motions of the reactant pairs, is not clear at this point.

TABLE OF CONTENTS

LIST OF FIGURES	viii
LIST OF TABLES	xvi
ACKNOWLEDGEMENTS	xvii
Chapter 1 Introduction	1
1.1 Basics of Photoinduced Electron Transfer Theory	2
1.2 Electron Transfer Kinetics in Conventional Solvents	6
1.3 Electron Transfer Kinetics in Ionic Liquids	8
1.4 The Research Described in this Dissertation	10
References.....	19
Chapter 2 Experimental and Analysis Methods.....	24
2.1 Experimental Methods.....	24
2.1.1 Materials	24
2.1.2 Steady State Spectroscopic Measurements	25
2.1.3 Time-Correlated Single Photon Counting Measurements	27
2.1.4 Kerr-Gated Emission Spectroscopy	28
2.1.5 Cyclic Voltammetry	29
2.2 Data Analysis Methods.....	30
2.2.1 Deconvolution of TCSPC Decays	30
2.2.2 Deconvolution of KGE Data	31
References.....	37
Chapter 3 Characterization of a New Electron Donor-Acceptor Dyad in Conventional Solvents and Ionic Liquids.....	38
3.1 Introduction.....	38
3.1 Methods	42
3.1.1 Reagents and Materials.....	42
3.2.2 Spectroscopic Methods.....	45
3.2.3 Computational Methods	47
3.3 Results and Discussion	48
3.3.1 Molecular Dynamics Simulations	48
3.3.2 Steady State Characterization.....	51
3.3.3 Time-Resolved Measurements	54
3.4 Summary and Conclusions	60
Acknowledgements.....	62
References.....	78

Chapter 4 Electron Transfer Kinetics Between an Electron Accepting Ionic Liquid and Coumarin Dyes.....	84
4.1 Introduction.....	84
4.2 Methods	88
4.2.1 Chemicals	88
4.2.2 Steady State Spectroscopy.....	89
4.2.3 Time-Resolved Fluorescence Measurements	90
4.2.4 Stern-Volmer Analysis	91
4.2.5 Cyclic Voltammetry	92
4.3 Results and Discussion	93
4.3.1 Characterization of the Coumarin Studied	93
4.3.2 Quenching by Py_4^+ in Dilute Acetonitrile Solution	97
4.3.3 Quenching Dynamics in Neat $[\text{Py}_4][\text{Tf}_2\text{N}]$	101
4.3.4 Quenching in Concentrated $[\text{Py}_4][\text{Tf}_2\text{N}]$ + Acetonitrile Mixtures	109
4.4 Summary & Conclusions.....	110
Acknowledgements.....	113
References.....	130
Chapter 5 Summary and Future Work	136
References.....	140
Appendix A Supporting Information for Chapter 3.....	141
A.1 Acid-Catalyzed Decomposition of the Dyad and Impurity Emission	141
A.2 The TICT Reaction of C152 and its use as a Lifetime Reference	150
A.3 Temperature Dependence in $[\text{N}_{881}][\text{Tf}_2\text{N}]$ and $[\text{P}_{14,666}][\text{Tf}_2\text{N}]$	153
References.....	160
Appendix B Supporting Information for Chapter 4.....	162
B.1 $[\text{Py}_4][\text{Tf}_2\text{N}]$ Impurity Absorption and Emission and its Effect on Coumarin Spectra	165
B.2 Oxidation Potentials from Cyclic Voltammetry and Quantum Chemical Calculations	169
B.3 Photodegradation of Coumarins by Py_4^+ and its Effects.....	177
B.4 Combining of TCSPC and KGE Data Sets	184
B.5 Maximum Entropy Estimation of Lifetime Distributions: ⁹⁻¹²	187
References.....	189

LIST OF FIGURES

- Figure 1.1: Schematic of photoinduced electron transfer kinetics between an excited fluorophore (F^*) that acts as an electron acceptor and a quencher (Q) that acts as an electron donor. k_0 is the rate of normal fluorescence of the fluorophore in the absence of quenching. k_d and k_{-d} are the diffusion rate constants of the quencher and the fluorophore. k_{ET} and k_{-ET} are the rates of electron transfer and the back electron transfer between the complexed pair. 12
- Figure 1.2: Marcus theory diagram of Gibbs free energy vs. electron transfer reaction coordinate..... 13
- Figure 1.3: Free energy diagrams demonstrating reactant and product potential energy surface overlap types as reorganization energy remains constant. (a) the normal region, where $0 \leq -\Delta G_{ET}$ (b) a barrierless reaction where $\Delta G \ddot{=} 0$ and (c) the Marcus inverted region where $\Delta G \ddot{>} 0$ with the barrier on the opposite end of the parabola. 14
- Figure 1.4: Bimolecular fluorescence quenching rates as a function of ΔG_{ET} , taken from the work of Rehm and Weller.¹⁴ 15
- Figure 1.5: Electron transfer rates of intramolecular donor-acceptor dyads in methyltetrahydrofuran by Closs and Miller, which was the first to conclusively prove the existence of the Marcus turnover, taken from their work in 1984.²⁹ Reprinted (adapted) with permission from J. R. Miller, L. T. Calcaterra, and G. L. Closs, "Intramolecular long-distance electron transfer in radical anions. The effects of free energy and solvent on the reaction rates," *J. Am. Chem. Soc.* **106** (1984). Copyright 2020 American Chemical Society. 16
- Figure 1.6: Ionic liquids are comprised of a cation and an anion, some examples of which are shown here. R_1 and R_2 represent alkyl chains of the cations. 17
- Figure 1.7: Calculated reaction rates in solvent from differential encounter theory and the effect of viscosity on the non-stationary and stationary regimes. Reprinted (adapted) with permission from A. Rosspeintner, M. Koch, G. Angulo, and E. Vauthey, "Spurious Observation of the Marcus Inverted Region in Bimolecular Photoinduced Electron Transfer," *J. Am. Chem. Soc.* **134**, 11396-11399 (2012). 10.1021/ja3049095. Copyright 2020 American Chemical Society. 18
- Figure 2.1: Standard labeling scheme of coumarins (top) and two examples: coumarin 152 (bottom left) and coumarin 337 (bottom right). 33
- Figure 2.2: C152-DMA dyad molecule used for studies in Chapter 3. 34

- Figure 2.3: Diagram of the home-build TCSPC instrument used in this work. BS: beam splitter; $\lambda/2$: half-wave plate; L: 50 mm focal length lens; BBO: 0.2 mm BBO crystal; P: polarizer; F: optical filter; MONO: monochromator; MCP-PMT: micro-channel plate photomultiplier tube; TAC: time-to-amplitude converter; MCA: multichannel analyzer. This schematic is simplified to demonstrate the basic theory of the experiment. Full details can be found in previous work.⁶ 35
- Figure 2.4: Diagram of the Kerr-gated emission (KGE) spectrometer used in this work. L: lens; BB: beam blocker; BS: beam splitter; BBO: 0.2 mm BBO crystal; $\lambda/2$: half-wave plate; SC: 0.5 mm sample flow cell; SO: Schwarzschild objective with 1:10 magnification; F: optical filter; PH: 300 μm pinhole; GL: Glan-Laser calcite polarizer; BC: 0.65 mm benzene flow cell/Kerr shutter; GT: Glan-Taylor polarizer; This schematic is simplified and used here only to illustrate the basic operation of the experiment. Full details can be found in previous work.^{7,8}. 36
- Figure 3.1: Scheme of C152-DMA dyad, coumarin 152, and precursor H152 63
- Figure 3.2: Scheme of synthesis of C152-DMA dyad. 64
- Figure 3.3: (a) Dihedral angle definitions. (b) One-dimensional distributions of angles D1-D3 in acetonitrile (solid curves) and in the gas phase (dashed). (c) 2-dimensional distributions in acetonitrile. In both the 1d and 2d distributions the values shown are the numbers of occurrences out of 5×10^5 samples. 65
- Figure 3.4: The most populated regions of conformational space shown as isosurfaces capturing 65% of the population. For clarity, values of $|\text{D1}| > 90^\circ$ here are folded into $-90^\circ \leq \text{D1} \leq 90^\circ$ using the 2-fold rotational symmetry of the DMA group. The conformer regions designated 1-4 are defined by the planes $\text{D2} = 0$ and $\text{D3} = 0$. The molecular structures show representative geometries selected from the most populated areas within these four regions. 66
- Figure 3.5: Distributions of (a) the center-of-mass distance between the donor and acceptor groups R_{DA} and (b) the angle between their aromatic planes, θ_π , observed in acetonitrile. The dashed red curves in these two panels indicate the approximate variation in electron transfer rates expected from these geometric parameters ($\beta = 15 \text{ nm}^{-1}$). (c) and (d) show the autocorrelation functions of R_{DA} and θ_π averaged over the 50 ns trajectories. The τ values indicated are the correlation times of these functions. 67

Figure 3.6: Normalized absorption and emission spectra of the dyad (black) and reference fluorophores C152 (red) and H152 (blue dashed) in (a) cyclohexane and (b) acetonitrile. 68

Figure 3.7: Normalized absorption (a) and emission (b) spectra of the dyad in selected solvents: cyclohexane (CHEX), dibutyl ether (DBE), toluene (TOL), 1,4-dioxane (DIOX), methyl acetate (MEAC) and acetonitrile (ACN)... 69

Figure 3.8: Correlation of the average absorption and emission (b) frequencies of the dyad with those of C152. The regressions shown are: (a) $\langle \nu \rangle_{dyad} = 0.71 \langle \nu \rangle_{C152} + 7.29$ ($N=24$, $R^2=0.92$) and (b) $\langle \nu \rangle_{dyad} = 0.64 \langle \nu \rangle_{C152} + 7.57$ ($N=24$, $R^2=0.95$). 70

Figure 3.9: Lippert-Mataga plots of the Stokes shifts $\Delta \nu = \nu_{abs} - \nu_{em}$ of the three fluorophores vs solvent orientational polarizability, Δf , defined in Eq. 2. All Stokes shifts are relative to the value of each probe in cyclohexane, and values for the dyad and C152 are vertically displaced by 1000 and 2000 cm^{-1} for clarity. Data in the quadrupolar solvents (toluene and dioxane) and ionic liquids are omitted from these correlations. In binary solvent mixtures, Δf is assumed to be the volume-weighted average of the values of Δf of the pure solvents. 71

Figure 3.10: Fluorescence (TCSPC) decays of the dyad in selected solvents. The uppermost curve is an H152 decay, shown for comparison. Solvents abbreviations are defined in Table 2. IRF denotes the instrument response function of the TCSPC instrument. 73

Figure 3.11: A representative KGE data set of the dyad in propylene carbonate. (a) Time-resolved spectra (solid curves) and lognormal fits (dashed). (b) The peak frequency and (c) the normalized peak height and integrated area. Symbols in panels (b) and (c) are the KGE data and the curves are multi-exponential fits..... 75

Figure 3.12: Electron transfer rate constants of the dyad plotted versus emission frequency. Points denote the logarithmic average of $k_{ET}^{(1)}$ and $k_{ET}^{(2)}$, and the ends of the error bars their individual values. Electron transfer in the ionic liquids $[\text{N}_{8881}][\text{Tf}_2\text{N}]$ and $[\text{P}_{14,666}][\text{Tf}_2\text{N}]$ is too slow to be measured, even at 353 K and the points plotted are only upper limits..... 76

Figure 3.13: TCSPC emission decays of the dyad in $[\text{Pr}_{41}][\text{Tf}_2\text{N}]$ as a function of temperature. The inset shows the electron transfer rates derived from these decays in an Arrhenius format. The fit shown is $\ln(k_{ET} / \text{s}^{-1}) = 32.5 - 2.48(10^3 \text{ K} / T)$ 77

- Figure 4.1: Structures and labels of the coumarin dyes used in this study. The bold numbering scheme **C1** – **C12** is ordered by increasing driving force for excited-state electron transfer. The second numbers shown are the Kodak designations except for **C4/545** and **C6/498**, where Exciton labels are used. (See also Table 4.1.) 114
- Figure 4.2: Normalized (a) absorption and (b) emission spectra of coumarins in acetonitrile. 115
- Figure 4.3: Representative absorption (Abs) and emission (Em) spectra of two coumarins in acetonitrile (ACN), [Im₄₁][Tf₂N] (Im₄₁), and [Py₄][Tf₂N] (Py₄). The bottom panel illustrates the emission observed (obs) in one of the dyes one of the three cases where emission from the solvent could not be adequately subtracted from the dye emission. The curve labeled “fit” is an estimate for the corrected emission of **C11** obtained from time-resolved spectra as described in Appendix Section B.1. 117
- Figure 4.4: Comparisons of the first moment frequencies and the derivative quantities ΔG_{01} and λ_{01} (Eqs. 4.1 & 4.2) in the ionic liquids with these same quantities in acetonitrile (plotted on the abscissa). Panels (a) and (b) compare absorption ($\langle \nu_{abs} \rangle$, blue) and emission ($\langle \nu_{em} \rangle$, orange) frequencies in [Im₄₁][Tf₂N] and [Py₄][Tf₂N], respectively, to acetonitrile. Two values of $\langle \nu_{em} \rangle$ are shown in the case C10-C12 in [Py₄][Tf₂N]. The open symbols are the values measured from steady-state spectra and the filled symbols from fits using time-resolved spectra as described in Appendix Section B.1. The dashed lines in panels (a) and (b) indicated equality between frequencies in the two solvents. Panels (c) and (d) plot the free energy change and reorganization energy associated with the $S_0 \leftrightarrow S_1$ transition as defined in Eqs. 4.1 and 4.2. The lines are least-squares fits to the data. 118
- Figure 4.5: Example Stern-Volmer data for quenching of C2/152 by [Py₄][Tf₂N] in acetonitrile. Panels (a) and (b) show absorption and emission spectra and panel (c) emission decays recorded with TCSPC at the quencher concentrations shown. Panel (d) are plots of relative emission intensities and lifetimes (Eqs. 4.4 & 4.5) from which k_q values are determined. 119
- Figure 4.6: (a) Rate constants for quenching of coumarin dyes by [Py₄][Tf₂N] in acetonitrile solution obtained from Stern-Volmer analysis of the steady-state spectra (blue circles) and emission lifetimes (red squares). The dashed line in this panel shows the predicted diffusion limited rate constant, k_d . (b) Average quenching constants obtained here (squares) compared to data on quenching of coumarin dyes by aromatic amines (circles) from Nad and Pal⁶⁶ (squares) and the a fit to the large collection of aromatic fluorophore quencher pairs

reported by Rehm and Weller⁶⁶ (solid curve). The dashed curve is the dependence predicted by the classical Marcus theory (as provided in Ref.⁶⁶). 120

Figure 4.7: (a) Comparison of the emission decays of C7/153 in [Py4][Tf2N] (Py4) and with those in acetonitrile (ACN) and [Im41][Tf2N] (Im41). The black decay (IRF) is the TCSPC instrument response function and the data labeled “Neat Py4” is the emission from impurities in the ionic liquid recorded under the same conditions as C7. (b) Emission decays of a selection of coumarin dyes in [Py4][Tf2N]. 121

Figure 4.8: A representative KGE data set of C7/153 in [Py4][Tf2N]. (a) Time-resolved spectra (solid curves) and lognormal fits (dashed). (b) The peak frequency and (c) the normalized peak height and integrated area determined from the lognormal fits. Symbols in panels (b) and (c) are the KGE data and the curves are multi-exponential fits..... 122

Figure 4.9: (a) Normalized intensity decays resulted from spliced decays from TCSPC and KGE. (b) Lifetime distributions from maximum entropy fits. 123

Figure 4.10: Characteristic rate coefficients obtained from emission decays in [Py4][Tf2N] using Eqs. 6-8. The lines are fits to $k = A \exp(-b\Delta G_{ET})$. Slopes b are 1.6, 8.9, and 7.8 eV⁻¹ for k_0 , k_{le} , and k_{av} , respectively..... 124

Figure 4.11: Comparison of the present results in [Py4][Tf2N] (solid curves and blue symbols) with literature data on quenching of coumarin dyes in aromatic amine solvents^{26,27} (dashed curves and orange symbols). Panel (a) shows pairs of normalized emission decays selected to have approximately the same t_{le} values in the two solvents. DMA = dimethylaniline, DEA = diethylaniline. Panel (b) shows rate coefficients k_{le} (points) and fits of these data to Eq. 9 (curves). 125

Figure 4.12: (a) Comparison of the emission decays, $\ln(t)$, of coumarins C7/153 and C10/6H in [Py4][Tf2N] with solvation response functions, $S(t)$, in [Im41][Tf2N] (Im41, Ref. 72), dimethylaniline (DMA; Ref. 26) and acetonitrile (ACN, Ref. 85). (b) Lifetime distributions obtained from maximum entropy fits to the data in (a). 127

Figure 4.13: Representative (a) intensity decays and (b) lifetime distributions of C10/6H in [Py4][Tf2N] + acetonitrile mixtures. 128

Figure 4.14: Characteristic rate coefficients obtained from emission decays C10/6H in [Py4][Tf2N] + acetonitrile mixtures. Curves are only to guide the eye. 129

- Figure A.1: *Left*: Mechanism of the acid-catalyzed decomposition of C152-DMA: (i) protonation; (ii) cleavage with concomitant formation of the highly fluorescent by product H152; and (iii) carbocation scavenging. *Right*: Vials 1 and 2 show C152-DMA dissolved in ethanol containing one drop of water (vial 1) or one drop of 0.1 N HCl (vial 2). The dye cleavage is essentially instantaneous upon acid addition leading to the fluorescent product H152. Vials 3 and 4 show the aminocoumarin H152 in ethanol, in the absence and presence of a drop of HCl, respectively. Under UV lamp excitation, no visual difference was discernable for these two samples. 143
- Figure A.2: Comparison of the longest lifetime component (τ_4) of the dyad with the lifetime of H152. Dyad decays were fit to 4 exponential components without any constraints on the time constants. Only solvents in which the longest lifetime dyad component accounted for $\leq 6\%$ of the amplitude are included. 144
- Figure A.3: 2d representations of dyad conformational distributions in the gas-phase and in acetonitrile solution. The values indicated here are the numbers of occurrences out of 5×10^5 samples. Angles are measured in degrees. 145
- Figure A.4: Time dependence of the dyad dihedral angles D1-D3 during a 10 ns portion of the acetonitrile simulations. 146
- Figure A.5: Distributions of (a) the angle between the aromatic planes and (b) the center-of-mass distance between the donor and acceptor groups of the dyad in acetonitrile. The distributions are separated into contributions from the four conformational regions defined by the quadrants D2 and D3 = 0 (as shown in Fig. 3.2). 147
- Figure A.6: The frontier molecular orbitals and select properties of the LE and CT states of C152-DMA based on gas-phase TD-DFT calculations at a typical ground state geometry using the CAM-B3LYP/6-311++G(d,p) model chemistry. 149
- Figure A.7: Lifetimes of C152, H152, and the C152-DMA dyad plotted versus average emission frequency of the dyad. For the dyad lifetime $\langle \tau \rangle_{dyad}$ is used, which omits the small decay component attributed to H152 impurity. 151
- Figure A.8: Electron transfer rate constants of the dyad plotted versus the total electric polarizability of the solvent. Symbols denote the logarithmic average of $k_{ET}^{(1)}$ and $k_{ET}^{(2)}$, and the ends of the error bars their individual values. Note that the polarities of the quadrupolar solvents toluene and dioxane and the ionic liquids are not properly represented by $f(\epsilon_r)$ and are therefore shown in parenthesis. 152

Figure A.9: Emission spectra of C152 and the dyad in $[P_{14,666}][Tf_2N]$ between 213-353 K.	156
Figure A.10: (a) Parameterized viscosities of the ionic liquids studied. The solid portions of the curves indicate the temperature range over which experimental data are available. (b, c) Average emission frequencies of C152 (blue) and the dyad (red) in $[N_{8881}][Tf_2N]$ and $[P_{14,666}][Tf_2N]$	157
Figure A.11: Average lifetimes of the dyad and C152 at different temperatures in $[N_{8881}][Tf_2N]$ and $[P_{14,666}][Tf_2N]$	159
Figure B.1: Steady state absorption and emission spectra of coumarins in acetonitrile	162
Figure B.2: Steady state absorption and emission spectra of coumarins in $[Im41][Tf_2N]$	163
Figure B.3: Steady state absorption and emission spectra of coumarins in $[Py4][Tf_2N]$	164
Figure B.4: Comparison of the (a) absorption and (b) emission spectra and (c) emission decays of neat $[Py4][Tf_2N]$ to two coumarin dye solutions. In (b) and (c) the same excitation and emission collection parameters were used for the neat solvent and the dye solutions.	167
Figure B.5: Spectra of C10 (102) in $[Py4][Tf_2N]$ illustrating the method of extracting C10 spectral information from the steady-state spectrum: (a) time-resolved emission at the times indicated; (b) peak-normalized spectra at the same times as panel (a) (solid curves) and the steady-state spectrum ("SS", points); (c) fit of the 5 ps.	168
Figure B.6: Cyclic voltammetry measurements of (a) C3/337 and (b) C11/102 in acetonitrile.	172
Figure B.7: Results of computational estimations of calculated oxidation potential vs. experimental results for coumarins with reversible oxidation peaks using methods by Roth et. al. and Crespo-Hernández et. al. using Gaussian 09 calculations.....	174
Figure B.8: Correlation between the net Hammett σ values of substituents at the 3 and 4 coumarin ring positions and ΔGET , E_{ox} , and ΔG_{01} . Effective values of σ were obtained from the tabulation in Ref. 8 assuming $\sigma_{eff} \cong \sigma_{p3} + \sigma_{m4}$ where para and meta refer to the location relative to the 7-amino ring position. Values of σ_{eff} calculated in this manner for C1-C12 are: 0.43, 0.43, 0.66, n.a., 0.50, 0.72, 0.43, 0.45, -0.069, 0, -0.069, -0.221.....	175

- Figure B.9: Representative data for Stern-Volmer experiment in acetonitrile with [Py4][Tf₂N] as addition quencher to C11/102. (a) Steady state absorption spectra. (b) Steady state emission spectra. (c) TCSPC emission decays. (d) Resulting Stern-Volmer analysis from both steady-state and time-resolved results. 176
- Figure B.10: Set of absorption, emission, and TCSPC measurements of C3/337 in acetonitrile in neat (a-c) [Im₄₁][Tf₂N] and (d-f) [Py₄][Tf₂N] over time. Excitation wavelength for both sets is 400 nm and emission decays were collected at 470 nm for TCSPC measurements. 180
- Figure B.11 TCSPC emission decays in neat [Py₄][Tf₂N], measured over time to demonstrate the photodegradation of the coumarins. 181
- Figure B.12: A representative KGE data set of C10/6H in neat [Py₄][Tf₂N]. (a) Time-resolved spectra (solid curves) and lognormal fits (dashed). (b) The peak frequency and (c) the normalized peak height and integrated area. Symbols in panels (b) and (c) are the KGE data and the curves are multi-exponential fits. 183
- Figure B.13: C7 (coumarin 153) data illustrating the method of combining KGE and TCSPC data. (a) Normalized peak (pk, blue) and integral (int, green) intensities from three KGE data sets. (b) Average (solid green curve) and uncertainties (dotted green) from the data in panel (a) as well as the normalized TCSPC decay collected at the steady-state emission peak. (c) The composite data set (solid red) and its components – the KGE data in lime green and the scaled TCSPC decay (blue). The combined set is an interpolation of the KGE data for $t \leq 50$ ps, the scaled TCSPC data for $t \geq 200$ ps, and a weighted average of the two between $50 < t < 200$ ps, the gray shaded region in panel (b). 186
- Figure B.14: Two example fits to composite $I_n(t)$ decays for C4/153 and C10/6H. Panels (a) show average composite $S(t)$ curves (solid) and the uncertainties used in fitting (dashed limiting curves). Panels (b) reproduce the average $I_n(t)$ data (solid blue curve) and their fits (red dashed curve). Panels (c) are the lifetime distributions that provide the fits shown in panels (b). The points in these distributions show the 40 discrete $\{\tau_j\}$ used to represent them. 188

LIST OF TABLES

Table 3.1: S_1 - S_0 Dipole Difference Estimates from Solvatochromic Analysis and DFT Calculations.....	72
Table 3.2: Multi-Exponential Representations of Dyad Emission Decays and ET Rate Constants	74
Table 4.1: Measured Electronic Properties of Coumarins in Acetonitrile.....	116
Table 4.2: Comparisons of ET Parameters in Redox-Active Liquids and Other Systems	126
Table A.1: Solvent Properties and Characteristics of the Steady-State Spectra of C152, H152, and the C152-DMA Dyad ^(a)	148
Table A.2: Fits to Reported Viscosity Data of the Ionic Liquids ^(a)	158
Table B.1: Compilation of data from calculations estimating oxidation potentials using methods of Crespo-Hernández et. al. and Roth et. al.....	173
Table B.2: Results of Stern-Volmer measurements of coumarins in acetonitrile with Py4 ⁺ added as quencher	182

ACKNOWLEDGEMENTS

I'd first like to thank my advisor, Mark Maroncelli, for his constant support and guidance throughout my time at Penn State. Because of it, I became a better writer, communicator and more confident as a scientist and researcher. I am sincerely grateful for the contributions he has made to this work, which might not be possible without him, and his encouragement in pursuing my love of teaching.

I'd also like to acknowledge all of the members of the Maroncelli lab that I was lucky enough to overlap with: Chris, Brian, Caleb, Sourav, and Kallol. Thank you for keeping me on my toes in group presentations and keeping me sane when things got tough. I'd like to give a special thanks to Chris Rumble, who taught me everything I know about ultrafast spectroscopy, contributed MD simulations to this work, and always had a dog picture ready to cheer me up when I needed it.

Thank you to the friends I met during my time at Penn State. A huge thank you to the members of the Sen lab, who quickly adopted me as one of their own for lunch at the group table and many social outings; To Alicia, my Jeopardy rival, thank you for all of those dinner dates and reminding me to kick back and have fun sometimes; To Kate, my weekly lunch buddy, thank you for always being passionate and teaching me to stand up for myself when I needed to; and of course, I will always be grateful for Ben, who has been a constant source of support.

I'd like to thank my incredibly supportive family, including my extended family. Despite not always understanding, they were always eager to hear about "school". Thank for helping me keep focused on my goal. I look forward to celebrating with you all soon.

Chapter 1

Introduction

Electron transfer is one of the most fundamental reactions in chemistry. Many essential biological processes involve the movement of electrons. Photosynthesis is the most commonly referenced example: plants use sunlight to push an electron through an enzyme transport chain in order to ultimately store energy in the form of adenosine triphosphate.¹ Biological electron transfer reactions occur in the complex environments found within living cells and rely on a sensitive balance of pH, ionicity, and solvent polarity in order to catalyze individual reaction steps and overcome energetic barriers. Many attempts have been made to mimic nature's approach with man-made solar cells in order to capture solar energy and convert it into electricity for immediate use or store it in chemical form. Such devices employ various electrolyte solutions as media through which charges are transported during the capture and conversion of sunlight to these more useful forms.^{2,3} Fine tuning the properties of the electrolytes employed, such as the solvent polarity and fluidity can lead to better charge separation, and transport by shifting energy barriers, changing reactant diffusion rates, or refining intermolecular interactions. Numerous studies since the 1940's have tried to understand what factors are important for optimizing charge separation and transport in conventional solvent electrolytes. In the past decade, ionic liquids have emerged as candidates for replacing conventional solvents in these applications due to favorable properties such as such as their low volatilities, high conductivities and wide electrochemical windows.

The research described in this dissertation aims to determine how electron transfer kinetics differ in an ionic liquid compared to conventional solvents. As background, this Introduction will describe the essentials of electron transfer theory, briefly review the developments in the electron transfer since the 1950's and summarize what is currently known about electron transfer in ionic liquids.

1.1 Basics of Photoinduced Electron Transfer Theory

Bimolecular electron transfer can be studied using a number of methods. One of the most popular is time-resolved fluorescence probing of photoinduced electron transfer (PET) reactions, due to the ease it provides for both triggering the reaction and tracking the ensuing kinetics. PET can be described as a three-step process, as outlined in Figure 1.1.⁴ First, light is used to excite a fluorophore (F), which could be either the electron donor or acceptor. For this discussion, F will be the electron acceptor, Q the donor, and F and Q are both uncharged before reaction. The reactants diffuse following excitation, and if the fluorophore encounters the quencher before it fluoresces, a reactive complex, [QF*], can form. The rate of complex formation is controlled by the rate of diffusion both reactants and their concentrations. Once the reactive complex is formed, the forward electron transfer (charge separation) will proceed at a rate k_{ET} , forming a pair of radical ions. These products then can either diffuse apart and form free ions, or the back reaction (charge recombination, k_{-ET}) can occur to return to neutral molecules. Assuming the reaction occurs within the lifetime of the fluorophore, steady-state analysis can be used to estimate the overall rate of PET. While Figure 1.1 shows the general

scheme, in many cases, one can assume k_{ET} is negligible. This simplification yields Equation 1.1, where $d[Q^+F^-]/dt$ is the experimentally observable rate of the fluorescence quenching.⁴

$$\frac{d[Q^+F^-]}{dt} = \frac{k_d k_{ET}}{k_{-d} + k_{ET}} [F^*][Q]. \quad (1.1)$$

If $k_{-d} \gg k_{ET}$, then diffusion is the rate limiting step. The rate simplifies to Equation 1.2, where the quenching rate constant depends only on the equilibrium constant for the formation of the reactive complex, $K_{eq} = k_d/k_{-d}$ and the electron transfer rate constant k_{ET} .

$$\frac{d[Q^+F^-]}{dt} \approx \frac{k_d}{k_{-d}} k_{ET} [F^*][Q]. \quad (1.2)$$

If the fluorophore and quencher are linked by covalent bonds, creating an intramolecular rather than intermolecular reaction, diffusion becomes irrelevant and the rate of electron transfer is directly determined from the observed quenching rate, as shown by Equation 1.3.

$$\frac{d[Q^+F^-]}{dt} \approx k_{ET} [QF^*] \quad (1.3)$$

The work for this dissertation takes advantage of this simplification to measure the electron transfer rate as different parameters are varied.

In 1992, Rudolph A. Marcus won the Nobel Prize in Chemistry for his work developing the theory for predicting the electron transfer rate constants k_{ET} and k_{-ET} .⁵⁻⁸ Marcus theory assumes a linear response of the nuclear degrees of freedom (both intra and intermolecular) to the electronic state of $[QF^*]$, which implies the reactant and product free energies can be described as equal curvature parabolas along the reaction coordinate, as illustrated in Figure 1.2. The reaction is assumed to only occur when the free energy of reactants (blue curve, $[QF^*]$) is equal to that of products (red curve, $[Q^+F^-]$).

)). This point is called the ‘transition state’. The free energy difference between the lowest energy of the reactant state and the transition state is the free energy of activation, ΔG^\ddagger . When the reactants reach this intersection, the system has some finite probability of jumping from the reactant surface to that of the products and forming the charge separated species $[Q^+F^-]$. Transition state theory predicts the rate of transfer from the reactant to product surfaces depends on this activation energy, as shown in Equation 1.4.

$$k_{ET} = A \exp\left(-\frac{\Delta G^\ddagger}{k_B T}\right). \quad (1.4)$$

One of the key results of Marcus theory was to show that the barrier height can be estimated in terms of the reorganization energy λ and the free energy change, ΔG_{ET} , using Equation 1.5.

$$\Delta G^\ddagger = \frac{(\Delta G_{ET} + \lambda)^2}{4\lambda}. \quad (1.5)$$

The reorganization energy, λ , can be defined as the energy difference on the reactant surface between $q = q_R$ and $q = q_P$, i.e. $\lambda = G_R(q_P) - G_R(q_R)$.⁴ Reorganization energy can be split into two components, inner and outer sphere. The inner sphere component refers to the energy associated with intramolecular relaxation, such as changes in bond length and angles needed to adapt to the new charge state. The outer-sphere reorganization energy refers to the relaxation of the solvent surrounding the reacting pair and directly relates to the dielectric constants of the solvent. For photoinduced electron transfer reactions, the reaction free energy can be estimated using the Rehm-Weller equation⁹

$$\Delta G_{ET} = eE_{D/D^+}^{ox} - eE_{A/A^-}^{red} - \Delta G_{01} - \frac{e^2}{\epsilon d} \quad (1.6)$$

The oxidation and reduction potentials of the donor and acceptor, E_{D/D^+}^{ox} and E_{A/A^-}^{red} respectively, are typically measured by cyclic voltammetry. The free energy difference between the ground and excited states of the fluorophore, ΔG_{01} , is estimated from steady state absorption and emission spectra. The last term estimates the contribution from Coulomb forces between charged products.

One of the remarkable features of Marcus theory is that it predicts the rate of reaction will not always increase with increasing driving force ($-\Delta G_{ET}$). If one can vary this driving force at fixed reorganization energy, Equation 1.5 predicts ΔG^\ddagger first increases at low values of $-\Delta G_{ET}$. When the $[Q^+F^-]$ free energy surface passes through the minimum of the $[QF^*]$ surface, as shown in Figure 1.3, the reaction becomes barrierless and k_{ET} is maximal. As the driving force increases past this point, the transition state moves to the left of the minimum and the barrier begins to increase again. This region is called the Marcus inverted region, where the electron transfer rate slows as $-\Delta G_{ET}$ becomes even larger and the barrier grows higher.

Marcus theory culminates in Equation 1.7, which describes the relationship between the electron transfer rate and the three variables of interest: the reaction free energy, ΔG_{ET} , the electronic coupling, H_{DA} , and the reorganization energy, λ . This equation establishes the turnover in rate with increasing driving force, as well as providing an explicit expression for the prefactor A in Equation 1.4, which can be related to the frequency of attempting to cross from the reactant to the product surfaces once the transition state energy is achieved.

$$k_{ET} = \frac{2\pi}{\hbar} \frac{H_{DA}^2}{\sqrt{4\pi\lambda k_B T}} \exp\left(-\frac{(\Delta G_{ET} + \lambda)^2}{4\lambda k_B T}\right) \quad (1.7)$$

The electronic coupling constant, H_{DA} describes the mixing of wavefunctions of the diabatic reactant and product states before electron transfer.⁴ The larger the mixing, the more frequently the reaction occurs. The coupling can be estimated using computational methods, such as Mulliken-Hush analysis,¹⁰ Boys-localized diabaticization,¹¹ and constrained DFT.^{12,13}

In summary, Marcus theory provides a relatively simple model that experimentalists can use to describe electron transfer kinetics using only three variables: the reorganization energy λ , the electronic coupling, H_{DA} , and the driving force ΔG_{ET} .

1.2 Electron Transfer Kinetics in Conventional Solvents

In order to compare the differences in driving force to rates of ET and test Marcus's theory, bimolecular electron transfer studies became popular in the 1960's. The earliest experiments were done in dilute solutions of donor and acceptor molecules with varying redox potentials chosen to cover wide ranges of driving force.^{14,15} Prominent among these studies is the landmark work of Rehm and Weller,¹⁴ who found that the electron transfer rate did not turn over at higher driving forces as predicted; instead the curve flattened at the rate of diffusional approach (k_d in Fig. 1.1) without decreasing even for very large values of driving force.¹⁴ Their compilation of the rates of over 60 donor–acceptor pairs is shown in Figure 1.4. As described by Equation 1.1, bimolecular reaction rates depend on both the rates of electron transfer rate and diffusion, and when diffusion is the rate-limiting step, the value of k_{ET} cannot be obtained from the bimolecular rate constant k_q , hence the flattening of the curve. However, the fact that k_q did not decrease

as predicted (dashed curve in Figure 1.4) for very large $-\Delta G_{ET}$, seemed to discredit Marcus' theory, and the reality of the so-called inverted region was questioned.

Validation came for the inverted region came with improved ultrafast methods in the 1980's. In order to overcome the limitations of diffusion, the reactants needed to be within electron transfer distance. One popular method for ensuring this proximity was to create a covalent bridge between the donor and acceptor molecules and study intramolecular electron transfer. Ideally, this bridge would be rigid to fix the distance and orientation between the donor and acceptor, and the driving force systematically varied by chemical substitution of the donor and/or acceptor.¹⁶⁻²⁷ The first observations of the Marcus turnover were made by Closs and Miller in 1984, who attached different electron acceptors to a long, rigid spacer whose other end held an electron donating biphenyl moiety.²⁸ The molecules involved and the rates measured using pulsed radiolysis are shown in Figure 1.5. This work was revolutionary in demonstrating the Marcus turnover, and it was quickly followed by several similar studies involving intramolecular dyads with a variety of other donor-acceptor pairings.²⁹⁻³²

In the 1990's, further advances in time-resolution enabled a different approach to defeat the diffusion limit: fluorescence quenching in neat reactive solvents. In most cases, aniline derivatives were used as electron donating solvents with perylene³³⁻³⁶ or coumarins³⁷⁻⁴¹ as dilute photoexcited electron acceptors. This method ensured that the first solvation shell of the acceptor was comprised entirely of the electron donating molecules, with no need for diffusion. All of these studies found fast quenching kinetics, but fluorescence decays were nonexponential, corresponding to distributed kinetics. The distributed character of these reactions was partly attributed to the electronic coupling

(H_{DA} in Eq. 1.7) between donor and nearby acceptor molecules being variable, because of the range of possible orientations, distances, and angles between the electron acceptor and the surrounding electron donating molecules.^{36,37} Nevertheless, use of different pairings of donor and acceptor in order to vary ΔG_{ET} showed electron transfer rates in these reactions do increase with driving force in the manner predicted by Marcus theory in the normal regime. Thus far such measurements have not yet been extended to the Marcus inverted regime.^{33,42}

1.3 Electron Transfer Kinetics in Ionic Liquids

In the 2000's, ionic liquids became a new focus of electron transfer research. The goal in such studies was to understand the effect of a purely ionic system on electron transfer. A number of groups have recently examined electron transfer in ionic liquids, in part because of their promise as an alternative for electrolytes in energy-related applications. Ionic liquids in current use are typically composed of an organic cation, such as a pyridinium, alkylammonium, or imidazolium cation, often with asymmetrical alkyl tails, and an inorganic anion, such as tetrafluoroborate or bis(trifluoromethylsulfonyl)imide.⁴³ If it is difficult for the two ions to crystallize, the system can remain a liquid without the need for any solvent. Ionic liquids are currently being used in industrial separation technologies, for example to make biofuels from seaweed and extract cellulose from trees to make fibers.⁴⁴ One of the key advantages of ionic liquids is the ability to vary the molecular structures of each ion to fine-tune

physical properties such as melting point, viscosity, conductivity, and solubility.^{43,45} Because of this ability, ionic liquids have earned the nickname “designer solvents”.⁴⁶ Ionic liquids are particularly favorable as electrolytes due to their wide electrochemical windows and high conductivities, which lends well to charge transport. Additionally, ionic liquids have low volatilities and are thus nonflammable, providing safer alternatives to most organic solvents. A few commonly used examples of ionic liquid components are shown in Figure 1.6.

For bimolecular electron transfer reactions in conventional solvents, Equation 1.8 is usually sufficient for estimating diffusion-limited bimolecular reactions rates with reasonable accuracy.⁴⁷ This equation predicts reaction rates to be inversely proportional to the bulk viscosity of the solvent, η .

$$k_d = \frac{8k_BT}{3\eta}. \quad (1.8)$$

Bimolecular electron transfer reactions in ionic liquids are hindered by their high viscosities, which dramatically slows molecular diffusion. Studies using differential encounter theory have broken down the measured kinetics into three regimes based on distance between the reacting molecules: static (where the two molecules are already close to one another, revealing the fastest rate constant k_0), nonstationary (the time window during which most evolution of the reactant pair distribution occurs), and stationary (when the equilibrated diffusion limited rate, k_∞), shown in Figure 1.7.^{48,49} In solvents such as ionic liquids, the nonstationary regime is exaggerated because of their high viscosity, which forces the kinetics to become more distributed than in conventional solvents as solvation time slows.⁵⁰⁻⁵² Equation 1.8 is only an estimate for the rate constant

k_{∞} associated with the stationary regime. As illustrated in Figure 1.7, because reaction proceeds faster during the static and nonstationary regimes, Equation 8 underestimates reaction rates in ionic liquids, sometimes by factors of up to 100.^{23,53}

Additionally, the way in which reactants interact with the ionic liquid environment can lead to significant variations in diffusion rates and thus diffusion-limited reaction rates. Neutral solutes, such as dimethylaniline and most coumarins, appeared to react at rates much faster than the predicted by Eq. 1.8.⁵⁴⁻⁵⁶ On the other hand, charged molecules, like ruthenium derivatives with neutral partners, seemed to react much more slowly.⁵⁷⁻⁵⁹ As described by a few computational works, charged solutes are “trapped” by Columbic forces within a solvation shell to a much greater extent than are neutral molecules.⁶⁰⁻⁶² Additionally, neutral compounds more frequently occupy the nonpolar regions of the long alkyl chains, giving a higher likelihood of two neutral reactants being within reaction radius. These two effects cause significant and opposing deviations predictions of Equation 1.8.

1.4 The Research Described in this Dissertation

In order to understand electron transfer in ionic liquids without the influence of diffusion, intramolecular electron donor-acceptor dyads have been studied in ionic liquids as they have been in conventional solvents.¹⁶⁻²⁷ Chapter 3 describes a new dyad molecule constructed by connecting a coumarin dye, which acts as a fluorophore and electron acceptor, with a dimethylaniline moiety, which acts as the electron donor. Results of

experiments characterizing this dyad in over twenty different solvents, which span wide ranges of polarity and viscosity, are used to compare solvent effects in conventional and ionic liquids. Just like the bridged compounds in conventional solvents, intramolecular electron transfer rates in ionic liquids roughly track solvation time. Most dyads in the literature have fairly strong coupling, which allows for more through-bond electron transfer than through space. Weaker coupling with a nonconjugated bridge between the donor and acceptor in a dyad may better compare to a bimolecular reaction. The electron transfer dyad discussed in Chapter 3 was created to help fill this gap. This project demonstrated clear relationships between solvent polarity and viscosity and the electron transfer rate of the dyad.

Chapter 4 describes fluorescence quenching measurements of electron transfer between coumarin dyes and a neat pyridinium ionic liquid. Whereas analogous reactions between fluorophores and neat aniline-based solvents have been studied since the late 1990's, this is the first such study in an ionic liquid. It was found that the electron transfer rates between the coumarins and the reactive ionic liquid was similar to reactive conventional solvents, despite the large difference in driving force due to the higher polarity of the ionic liquid.

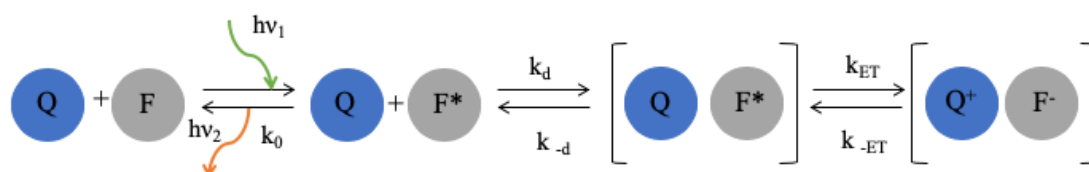


Figure 1.1: Schematic of photoinduced electron transfer kinetics between an excited fluorophore (F^*) that acts as an electron acceptor and a quencher (Q) that acts as an electron donor. k_0 is the rate of normal fluorescence of the fluorophore in the absence of quenching. k_d and k_{-d} are the diffusion rate constants of the quencher and the fluorophore. k_{ET} and k_{-ET} are the rates of electron transfer and the back electron transfer between the complexed pair.

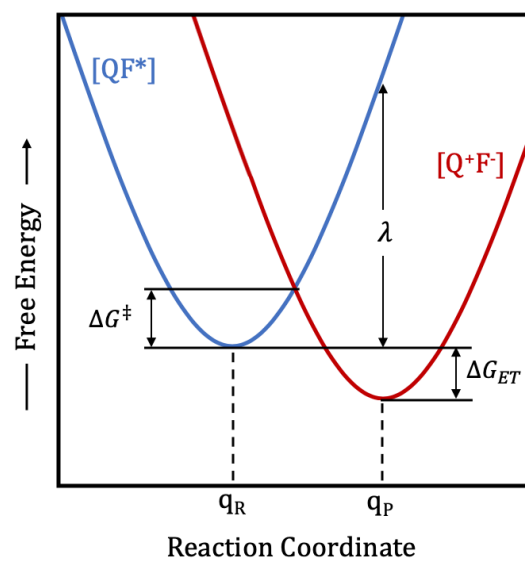


Figure 1.2: Marcus theory diagram of Gibbs free energy vs. electron transfer reaction coordinate.

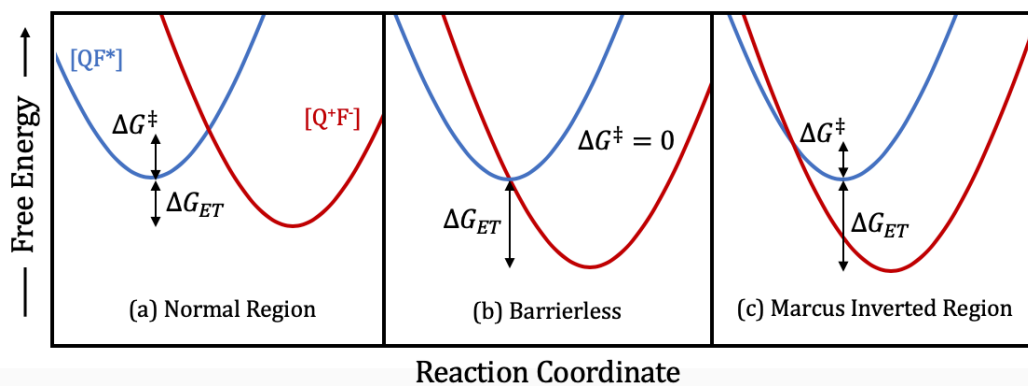


Figure 1.3: Free energy diagrams demonstrating reactant and product potential energy surface overlap types as reorganization energy remains constant. (a) the normal region, where $0 \leq -\Delta G_{ET}$ (b) a barrierless reaction where $\Delta G^\ddagger = 0$ and (c) the Marcus inverted region where $\Delta G^\ddagger > 0$ with the barrier on the opposite end of the parabola.

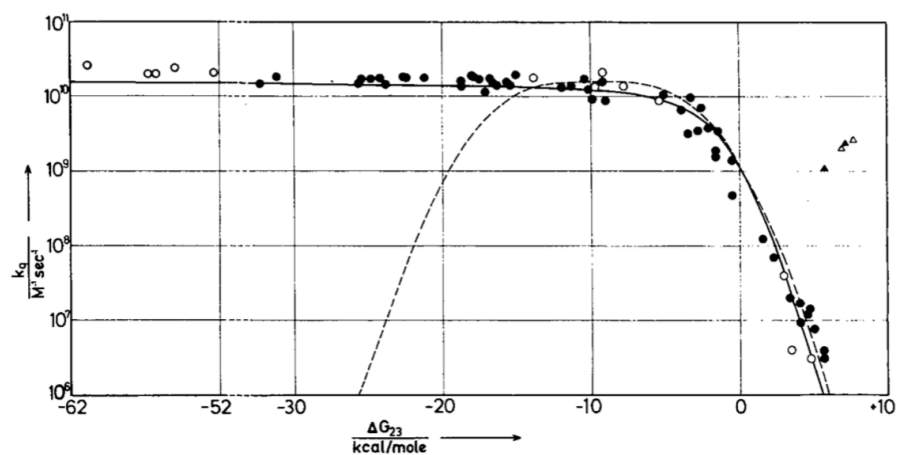


Figure 1.4: Bimolecular fluorescence quenching rates as a function of ΔG_{ET} , taken from the work of Rehm and Weller.¹⁴

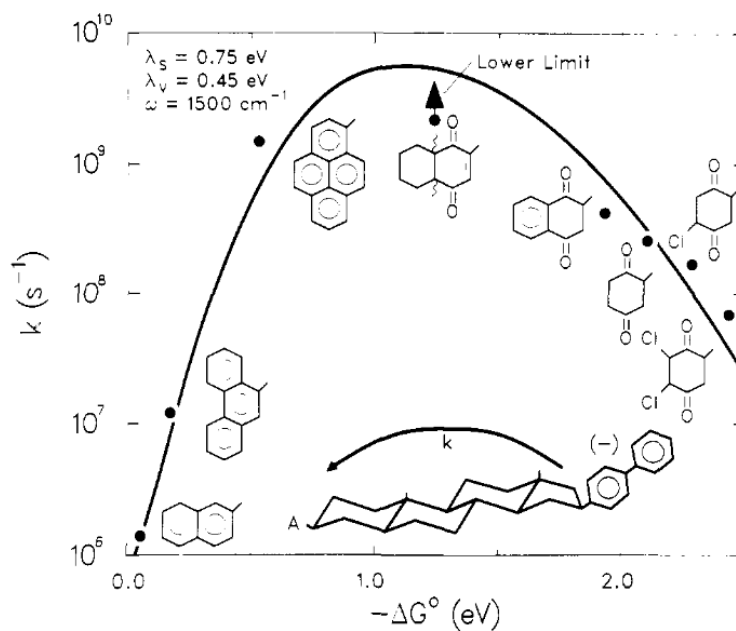


Figure 1.5: Electron transfer rates of intramolecular donor-acceptor dyads in methyltetrahydrofuran by Closs and Miller, which was the first to conclusively prove the existence of the Marcus turnover, taken from their work in 1984.²⁹ Reprinted (adapted) with permission from J. R. Miller, L. T. Calcaterra, and G. L. Closs, "Intramolecular long-distance electron transfer in radical anions. The effects of free energy and solvent on the reaction rates," *J. Am. Chem. Soc.* **106** (1984). Copyright 2020 American Chemical Society.

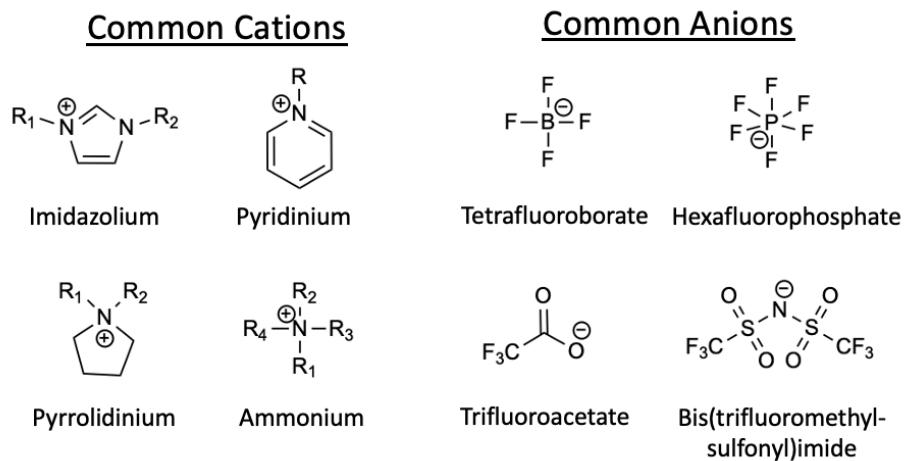


Figure 1.6: Ionic liquids are comprised of a cation and an anion, some examples of which are shown here. R_1 and R_2 represent alkyl chains of the cations.

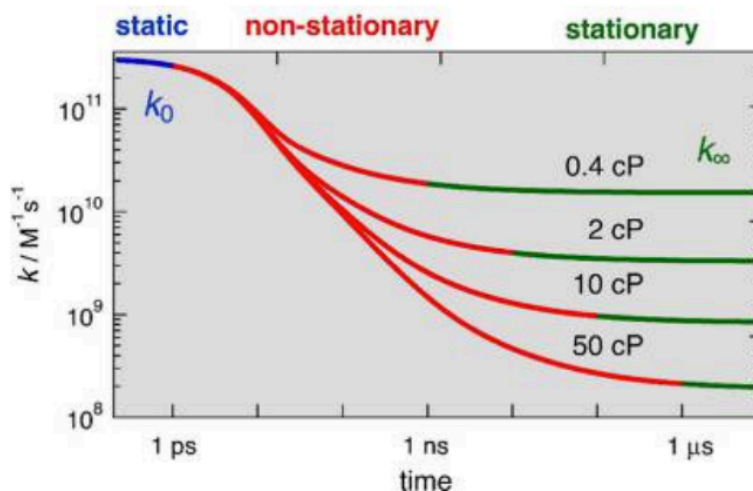


Figure 1.7: Calculated reaction rates in solvent from differential encounter theory and the effect of viscosity on the non-stationary and stationary regimes. Reprinted (adapted) with permission from A. Rosspeintner, M. Koch, G. Angulo, and E. Vauthey, "Spurious Observation of the Marcus Inverted Region in Bimolecular Photoinduced Electron Transfer," *J. Am. Chem. Soc.* **134**, 11396-11399 (2012). 10.1021/ja3049095. Copyright 2020 American Chemical Society.

References

1. V. Krishnan, "Electron Transfer in Chemistry and Biology: The Primary Events in Photosynthesis," *Resonance* **2**, 77-86 (1997).
2. D. R. MacFarlane, N. Tachikawa, M. Forsyth, J. M. Pringle, P. C. Howlett, G. D. Elliott, J. H. Davis, M. Wantanabe, P. Simon, and C. A. Angell, "Energy Applications of Ionic Liquids," *Energy Environ. Sci.* **7** (2014).
3. H. Makita and G. Hastings, "Inverted-region electron transfer as a mechanism for enhancing photosynthetic solar energy conversion efficiency," *Proc Natl Acad Sci U S A* **114**, 9267-9272 (2017). 10.1073/pnas.1704855114
4. J. R. Bolton and M. D. Archer, "Basic Electron-Transfer Theory," in *Electron Transfer in Inorganic, Organic, and Biological Systems*, edited by J. R. Bolton (American Chemical Society, Washington, D. C., 1991).
5. R. A. Marcus, "On the Theory of Oxidation-Reduction Reactions Involving Electron Transfer," *J. Chem. Phys.* **24**, 966-978 (1956).
6. R. A. Marcus, "On the Theory of Oxidation-Reduction Reactions Involving Electron Transfer III: Applications to Data on the Rates of Organic Redox Reactions," *J Chem Phys* **26**, 872-877 (1957).
7. R. A. Marcus, "Chemical and Electrochemical Electron-Transfer Theory," *Annu. Rev. Phys. Chem.* **15**, 155-196 (1964).
8. R. A. Marcus and N. Sutin, "Electron Transfers in Chemistry and Biology," *Biochim. Biophys. Acta.* **811**, 265 (1985).
9. J. R. Lakowicz, *Principles of Fluorescence Spectroscopy*, 3rd ed. (Springer, New York, 2006).
10. N. S. Hush, "Intervalence-Transfer Absorption. Part 2. Theoretical Considerations and Spectroscopic Data.," in *Progress in Inorganic Chemistry* (Wiley, 2007).
11. J. E. Subotnik, S. Yeganeh, R. J. Cave, and M. A. Ratner, "Constructing diabatic states from adiabatic states: extending generalized Mulliken-Hush to multiple charge centers with boys localization," *J Chem Phys* **129**, 244101 (2008). 10.1063/1.3042233
12. T. Van Voorhis, T. Kowalczyk, B. Kaduk, L. P. Wang, C. L. Cheng, and Q. Wu, "The diabatic picture of electron transfer, reaction barriers, and molecular dynamics," *Annu Rev Phys Chem* **61**, 149-170 (2010). 10.1146/annurev.physchem.012809.103324
13. B. Kaduk, T. Kowalczyk, and T. Van Voorhis, "Constrained density functional theory," *Chem Rev* **112**, 321-370 (2012). 10.1021/cr200148b
14. D. Rehm and A. Weller, "Kinetics of Fluorescence Quenching by Electron and H-atom Transfer," *Isr. J. Chem.* **8**, 259-271 (1970).
15. G. Jones, S. F. Griffin, C. Y. Choi, and W. R. Bergmark, "Electron Donor-Acceptor Quenching and Photoinduced Electron-Transfer for Coumarin Dyes," *J Org Chem* **49**, 2705-2708 (1984). DOI 10.1021/jo00189a010
16. S. Farid, J. P. Dinnocenzo, P. B. Merkel, R. H. Young, D. Shukla, and G. Guirado, "Reexamination of the Rehm-Weller data set reveals electron transfer quenching that follows a Sandros-Boltzmann dependence on free energy," *J Am Chem Soc* **133**, 11580-11587 (2011). 10.1021/ja2024367
17. Y. Nagasawa and H. Miyasaka, "Ultrafast solvation dynamics and charge transfer reactions in room temperature ionic liquids," *Phys. Chem. Chem. Phys.* **16**, 13008-13026 (2014). 10.1039/c3cp55465a

18. J. V. Lockard and M. R. Wasielewski, "Intramolecular Electron Transfer within a Covalent, Fixed-Distance Donor-Acceptor Molecule in an Ionic Liquid," *Journal of Physical Chemistry B* **111**, 11638-11641 (2007).
19. N. Banerji, G. Angulo, I. Barabanov, and E. Vauthey, "Intramolecular Charge-Transfer Dynamics in Covalently Linked Perylene-Dimethylaniline and Cyanoperylene-Dimethylaniline," *The Journal of Physical Chemistry A* **112**, 9665-9674 (2008).
20. D. C. Khara, A. Paul, K. Santhosh, and A. Samanta, "Excited state dynamics of 9,9'-bianthryl in room temperature ionic liquids as revealed by picosecond time-resolved fluorescence study," *J. Chem. Sci. (Bangalore)* **121**, 309-315 (2009).
21. Y. Nagasawa, A. Oishi, T. Itoh, M. Yasuda, M. Muramatsu, Y. Ishibashi, S. Ito, and H. Miyasaka, "Dynamic Stokes Shift of 9,9'-Bianthryl in Ionic Liquids: A Temperature Dependence Study," *Journal of Physical Chemistry C* **113**, 11868-11876 (2009).
22. K. Santhosh, S. Banerjee, N. Rangaraj, and A. Samanta, "Fluorescence response of 4-(N,N'-Dimethylamino)benzonitrile in room temperature ionic liquids: observation of photobleaching under mild excitation condition and multiphoton confocal microscopic study of the fluorescence recovery dynamics," *Journal of Physical Chemistry B* **114**, 1967-1974 (2010).
23. K. Santhosh and A. Samanta, "Modulation of the Excited State Intramolecular Electron Transfer Reaction and Dual Fluorescence of Crystal Violet Lactone in Room Temperature Ionic Liquids," *Journal of Physical Chemistry B* **114**, 9195-9200 (2010).
24. H. Wu, H. Wang, L. Xue, Y. Shi, and X. Li, "Hindered Intramolecular Electron Transfer in Room-Temperature Ionic Liquid," *The Journal of Physical Chemistry B* **114**, 14420-14425 (2010). 10.1021/jp101240a
25. X. Li, M. Liang, A. Chakraborty, M. Kondo, and M. Maroncelli, "Solvent-Controlled Intramolecular Electron Transfer in Ionic Liquids," *Journal of Physical Chemistry B* **115**, 6592-6607 (2011). 10.1021/jp200339e
26. H. Y. Lee, J. B. Issa, S. S. Isied, E. W. Castner, Jr., Y. Pan, C. L. Hussey, K. S. Lee, and J. F. Wishart, "A Comparison of Electron-Transfer Dynamics in Ionic Liquids and Neutral Solvents," *J. Phys. Chem. C* **116**, 5197-5208 (2012). 10.1021/jp208852r
27. J. A. DeVine, M. Labib, M. E. Harries, R. A. M. Rached, J. Issa, J. F. Wishart, and E. W. Castner, "Electron-Transfer Dynamics for a Donor-Bridge-Acceptor Complex in Ionic Liquids," *J. Phys. Chem. B* **119**, 11336-11345 (2015). 10.1021/acs.jpcc.5b03320
28. C. A. Rumble and M. Maroncelli, "Solvent controlled intramolecular electron transfer in mixtures of 1-butyl-3-methylimidazolium tetrafluoroborate and acetonitrile," *J. Chem. Phys.* **148**, 193801/193801-193801/193807 (2018). 10.1063/1.5000727
29. J. R. Miller, L. T. Calcaterra, and G. L. Closs, "Intramolecular long-distance electron transfer in radical anions. The effects of free energy and solvent on the reaction rates," *J. Am. Chem. Soc.* **106** (1984).
30. M. R. Wasielewski, M. P. Neimeczyk, W. A. Svec, and E. B. Pewitt, "Dependence of rate constants for photoinduced charge separation and dark charge recombination on the free energy of reaction in restricted-distance porphyrin-quinone molecules," *J Am Chem Soc* **107**, 1080-1082 (1985).
31. I. R. Gould, D. Ege, S. L. Mattes, and S. Farid, "Return electron transfer within geminate radical ion pairs. Observation of the Marcus inverted region," *J Am Chem Soc* **109**, 3794-3796 (1987).
32. N. Mataga, T. Asahi, Y. Kanda, T. Okada, and T. Kakitani, "The bell-shaped energy gap dependence of the charge recombination reaction of geminate radical ion pairs produced by fluorescence quenching reaction in acetonitrile solution," *Chem. Phys.* **127**, 249-261 (1988).

33. E. Vauthey, P. Suppan, and E. Haselbach, "Free-energy dependence of the ion yield of photo-induced electron-transfer reactions in solution," *Helv. Chim. Acta* **71**, 93-99 (1988).
34. A. Morandeira, A. Fürstenberg, and E. Vauthey, "Fluorescence Quenching in Electron-Donating Solvents. 2. Solvent Dependence and Product Dynamics," *J. Phys. Chem. C* **108**, 8190-8200 (2004).
35. M. G. Kuzmin and I. V. Soboleva, "Analysis of transformations of the ultrafast electron transfer photoreaction mechanism in liquid solutions by the rate distribution approach," *Photochem Photobiol Sci* **13**, 770-780 (2014).
36. G. Angulo, A. Cuetos, A. Rosspeintner, and E. Vauthey, "Experimental Evidence of the Relevance of Orientational Correlations in Photoinduced Bimolecular Reactions in Solution," *J. Phys. Chem. A* **117**, 8814-8825 (2013).
37. A. Rosspeintner, G. Angulo, and E. Vauthey, "Driving Force Dependence of Charge Recombination in Reactive and Nonreactive Solvents," *J Phys Chem A* **116**, 9473-9483 (2012).
38. E. W. J. Castner, D. Kennedy, and R. J. Cave, "Solvent as Electron Donor: Donor/Acceptor Electronic Coupling Is a Dynamical Variable," *The Journal of Physical Chemistry A* **104**, 2869-2885 (2000).
39. H. Shirota, H. Pal, K. Tominaga, and K. Yoshihara, "Substituent Effect and Deuterium Isotope Effect of Ultrafast Intermolecular Electron Transfer: Coumarin in Electron-Donating Solvent," *J. Phys. Chem. A* **102**, 3089-3102 (1998).
40. H. Pal, Y. Nagasawa, K. Tominaga, and K. Yoshihara, "Deuterium Isotope Effect on Ultrafast Intermolecular Electron Transfer," *J. Phys. Chem.* **100**, 11964-11974 (1996).
41. Y. Nagasawa, A. P. Yartsev, K. Tominaga, P. B. Bisht, A. E. Johnson, and K. Yoshihara, "Dynamical Aspects of Ultrafast Intermolecular Electron Transfer Faster Than Solvation Process: Substituent Effects and Energy Gap Dependence," *J. Phys. Chem.* **99**, 653-662 (1995).
42. H. N. Ghosh, S. Verma, and E. T. J. Nibbering, "Ultrafast Forward and Backward Electron Transfer Dynamics of Coumarin 337 in Hydrogen-Bonded Anilines As Studied with Femtosecond UV-Pump/IR-Probe Spectroscopy," *J. Phys. Chem. A* **115**, 664-670 (2011).
43. N. Barman and K. Sahu, "Anomalous modulation of photoinduced electron transfer of coumarin 102 in aniline-dimethylaniline mixture: dominant role of hydrogen bonding," *Phys Chem Chem Phys* **16**, 27096-27103 (2014). 10.1039/c4cp04441j
44. N. V. Plechkova and K. R. Seddon, "Applications of ionic liquids in the chemical industry," *Chem Soc Rev* **37**, 123-150 (2008). 10.1039/b006677j
45. R. S. Kalb, *Commercial Applications of Ionic Liquids* (Springer, 2020).
46. Z. Fei, V. M. Manzanares, and P. J. Dyson, "Ionic Liquids: From Synthesis to Applications in Solar Cells," *Chimia (Aarau)* **71**, 762-767 (2017). 10.2533/chimia.2017.762
47. J. F. Wishart, "Energy applications of ionic liquids.," *Energy Environ. Sci.* **2**, 956-961 (2009).
48. M. J. Earle, S. P. Katdare, and K. R. Seddon, "Paradigm confirmed: the first use of ionic liquids to dramatically influence the outcome of chemical reactions," *Org Lett* **6**, 707-710 (2004). 10.1021/ol036310e
49. R. Ozawa and H. Hamaguchi, "Does photoisomerization proceed in an ionic liquid?," *Chem. Lett.* **30**, 736-737 (2001).
50. D. Chakrabarty, A. Chakraborty, P. Hazra, D. Seth, and N. Sarkar, "Dynamics of photoisomerization and rotational relaxation of 3,3'-diethyloxadiazocyanine iodide in

- room temperature ionic liquid and binary mixture of ionic liquid and water.," *Chem. Phys. Lett.* **397** (2004).
51. M. Liang, A. Kaintz, G. A. Baker, and M. Maroncelli, "Bimolecular Electron Transfer in Ionic Liquids: Are Reaction Rates Anomalously High?," *J. Phys. Chem. B* **116**, 1370-1384 (2012). 10.1021/jp210892c
 52. B. Wu, M. Maroncelli, and E. W. Castner, Jr., "Photoinduced Bimolecular Electron Transfer in Ionic Liquids," *J Am Chem Soc* **139**, 14568-14585 (2017). 10.1021/jacs.7b07611
 53. A. Rosspeintner, D. R. Kattnig, G. Angulo, S. Landgraf, and G. Grampp, "The Rehm-Weller experiment in view of distant electron transfer," *Chemistry* **14**, 6213-6221 (2008). 10.1002/chem.200701841
 54. A. Rosspeintner, M. Koch, G. Angulo, and E. Vauthey, "Spurious observation of the Marcus inverted region in bimolecular photoinduced electron transfer," *J Am Chem Soc* **134**, 11396-11399 (2012). 10.1021/ja3049095
 55. X.-X. Zhang, M. Liang, N. P. Ernsting, and M. Maroncelli, "Complete Solvation Response of Coumarin 153 in Ionic Liquids," *The Journal of Physical Chemistry B* **117**, 4291-4304 (2013). 10.1021/jp305430a
 56. A. Samanta, "Solvation dynamics in ionic liquids: What we have learned from the dynamic fluorescence Stokes shift studies," *J. Phys. Chem. Lett.* **1**, 1557-1562 (2010).
 57. E. W. Castner, Jr., C. J. Margulis, M. Maroncelli, and F. Wishart James, "Ionic Liquids: Structure and Photochemical Reactivity," *Annual Reviews of Physical Chemistry* **62**, 85-105 (2011). 10.1146/annurev-physchem-032210-103421
 58. A. Rosspeintner, M. Koch, G. Angulo, and E. Vauthey, "Spurious Observation of the Marcus Inverted Region in Bimolecular Photoinduced Electron Transfer," *J. Am. Chem. Soc.* **134**, 11396-11399 (2012). 10.1021/ja3049095
 59. A. Skrzypczak and P. Neta, "Diffusion-controlled electron-transfer reactions in ionic liquids.," *J. Phys. Chem. A* **107**, 7800-7803 (2003).
 60. A. J. McLean, M. J. Muldoon, C. M. Gordon, and I. R. Dunkin, "Bimolecular rate constants for diffusion in ionic liquids," *Chem. Commun.*, 1880-1881 (2002).
 61. A. Paul and A. Samanta, "Photoinduced Electron Transfer Reaction in Room Temperature Ionic Liquids: A Combined Laser Flash Photolysis and Fluorescence Study," *J. Phys. Chem. B* **111**, 1957-1962 (2007).
 62. C. M. Gordon and A. J. McLean, "Photoelectron transfer from excited-state ruthenium (II) tris(bipyridyl) to methylviologen in an ionic liquid," *Chem. Commun.*, 1395-1396 (2000).
 63. R. C. Vieira and D. E. Falvey, "Photoinduced Electron-Transfer Reactions in Two Room-Temperature Ionic Liquids: 1-Butyl-3-methylimidazolium Hexafluorophosphate and 1-Octyl-3-methylimidazolium Hexafluorophosphate," *J. Phys. Chem. C* **111**, 5023-5029 (2007).
 64. K. Takahashi, S. Sakai, H. Tezuka, Y. Hiejima, Y. Katsumura, and M. Watanabe, "Reaction between diiodide anion radiacals in ionic liquids," *J. Phys. Chem. B* **111** (2007).
 65. C. A. Rumble, C. Uitvlugt, B. Conway, and M. Maroncelli, "Solute Rotation in Ionic Liquids: Size, Shape, and Electrostatic Effects," *J Phys Chem B* **121**, 5094-5109 (2017). 10.1021/acs.jpcc.7b01704
 66. J. C. Araque, S. K. Yadav, M. Shadeck, M. Maroncelli, and C. J. Margulis, "How Is Diffusion of Neutral and Charged Tracers Related to the Structure and Dynamics of a Room-Temperature Ionic Liquid? Large Deviations from Stokes-Einstein Behavior Explained," *J Phys Chem B* **119**, 7015-7029 (2015). 10.1021/acs.jpcc.5b01093

67. C. A. Rumble, A. Kaintz, S. K. Yadav, B. Conway, J. C. Araque, G. A. Baker, C. Margulis, and M. Maroncelli, "Rotational Dynamics in Ionic Liquids from NMR Relaxation Experiments and Simulations: Benzene and 1-Ethyl-3-Methylimidazolium," *J Phys Chem B* **120**, 9450-9467 (2016). 10.1021/acs.jpcc.6b06715
68. S. Li, A. Yu, and R. Lu, "Fluorescence quenching of coumarin 153 by hydroxyl-functionalized room temperature ionic liquids," *Spectrochim. Acta A* **165**, 161-166 (2016).
69. A. Yadav, S. Trivedi, V. Haridas, J. B. Essner, G. A. Baker, and S. Pandey, "Effect of ionic liquid on the fluorescence of an intramolecular exciplex forming probe," *Photochem Photobiol Sci* **19**, 251-260 (2020). 10.1039/c9pp00458k

Chapter 2

Experimental and Analysis Methods

2.1 Experimental Methods

2.1.1 Materials

A majority of the fluorescent molecular probes used in this dissertation were coumarin dyes. The standard labeling scheme and a few representatives are shown in Figure 2.1. Coumarins are frequently used in fluorescence spectroscopy due to their high quantum yields and their long fluorescence lifetimes (nanosecond scale) in most conventional solvents, making them excellent molecular probes for monitoring reactions or other processes that occur on sub-nanosecond time scales. Additionally, their energetic properties can be easily tuned by varying the substituents at the 3, 4, or 7-positions.^{1,2} All coumarins were used as purchased from Exciton or Kodak with a stated 99% purity. For the project discussed in Chapter 3, an electron transfer dyad molecule comprised of coumarin 152 as the photoexcited electron acceptor, dimethylaniline as the electron donor, and a methylene spacer was synthesized by collaborators Gary Baker and Durgesh Wagle from the University of Missouri. The structure is shown in Figure 2.2; full details of the synthesis and purification can be found in Chapter 3.

Conventional solvents were purchased from OmniSolv, Sigma-Aldrich, or Fluka in HPLC or spectroscopic grades. All ionic liquids were purchased from IoLiTec with a

stated purity of 98% and were selected based for high optical quality. Ionic liquids were further purified to minimize emission from impurities that often overlap with the S_0 - S_1 absorption bands of the molecular probes studied. This was done by dissolving the ionic liquid in a mixture of dichloromethane and activated charcoal and heating to 60°C under vacuum for 36 hours. Once the dichloromethane was evaporated, the resulting solution was filtered using a silica column to remove the activated charcoal and remaining impurities.³

Solvents used in these studies were tested for water content using a Mettler Toledo DL38 Coulometric Karl-Fischer titrator. All solvents were tested in triplicate and any solvent with a water content over 100 ppm was dried. Conventional solvents such as acetonitrile or dimethylsulfoxide were dried over molecular sieves. Ionic liquids were dried overnight on a Schlenk line at a pressure of approximately 30 mtorr with stirring and slight heating. Before use in fluorescence experiments, all samples were also purged with nitrogen in order to remove oxygen impurities, which are known to quench fluorescence.

2.1.2 Steady State Spectroscopic Measurements

UV-Vis absorption spectra give information on the electronic ground state. Spectra were measured using a Hitachi U-3000 UV-Vis spectrophotometer with 1 nm resolution and 60 nm/s scan rate. Most samples were measured in 1 cm quartz cuvettes, but in a few cases cuvettes with 1 mm path lengths were used in order to conserve sample or solvent. Solvent blanks were measured for each solvent and subtracted from the

sample spectra. Solvent spectra are measured separately rather than being ratioed to the sample during data collection in order to observe whether any visibly absorbing impurities were present in the solvent. Sample concentrations were chosen to have an optical density of approximately 1.0 in order to provide good S/N and accuracy after background subtraction.

Steady-state fluorescence was measured with a SPEX Fluorolog 212 fluorimeter. All emission spectra were recorded with slit widths set to 2 nm with a 1 second integration time, resulting in a 2 nm resolution. (Smaller slit widths yield greater spectral resolution, but also cut down the signal level considerably.⁴) In order to adjust for the wavelength-dependent response of the fluorimeter, the spectra were corrected using the emission spectra of six reference dyes spanning the range of 310-840 nm, according to a published procedure.⁵ The correction file is remade for the instrument once per year or after a new lamp is installed.

Before measuring a sample's fluorescence, an absorption spectrum was first measured to determine the excitation wavelength to be used and to estimate the optical density of the sample. For fluorescence spectra, the optical density should be between 0.1-0.2 in order to prevent self-quenching due to the filter effect.⁴ Fluorescence intensity can be collected either in right-angle or front-face geometries. Right-angle detection is preferred to reduce the amount of reflected excitation light and was used for all samples in 1 cm cuvettes. The front-face method was used for samples made in 1 mm cuvettes. Background solvent emission spectra were also measured and subtracted from the sample spectra before processing. This was especially important for ionic liquid samples, as they frequently contain some solvent fluorescence.

2.1.3 Time-Correlated Single Photon Counting Measurements

Time resolved measurements in the ps – ns range used the home-built time-correlated single photon counting (TCSPC) setup, shown schematically in Figure 2.3. The light source for this system is a cavity-dumped Ti:Sapphire laser with a fundamental wavelength that can be tuned between 700-1000 nm. For most experiments, the wavelength was set to approximately 800 nm, which was frequency doubled to ~400 nm using a β -barium borate (BBO) crystal. The output of the PulseSwitch cavity dumper is split into two beams using a beam splitter (BS), which directs about 5% of the beam to a photodiode. The photodiode uses this pulse as a stop signal for the time-to-amplitude converter.⁴ A 20 ns delay cable is used to delay this stop signal relative to the start signal coming from a fluorescent photon. The transmitted portion of the beam continues to travel through a half-wave plate ($\lambda/2$) to rotate the polarization to vertical and is then focused onto the BBO crystal to be frequency-doubled. The doubled light is directed through either the front-face excitation path or the right-angle excitation path to the sample. As in steady-state fluorescence measurements, right-angle excitation is used for samples in 1 cm cuvettes and front-face excitation is used for samples in 1 mm cuvettes. Independent of the path, the beam is passed through another half-wave plate ($\lambda/2$) and a polarizer P1 to control the light intensity used to excite the sample. The fluorescence of the sample is collected at the magic angle (54.7°) relative to the excitation (to eliminate the effects of solute rotation) and passed through an optical filter (F) to prevent reflected excitation light from entering the monochromator. The filtered light wavelength selected by a monochromator (HFAC-26, Becker & Hickl GmbH) usually with 4 nm resolution

and detected by a multi-channel plate photomultiplier tube (MCP-PMT). For each sample, a collection wavelength is specified using the computer, which is often the peak of the steady state emission spectrum. For every photon that enters the MCP-PMT, an electrical pulse is generated and amplified until it reaches a constant fraction discriminator.⁴ This step records this as the signal to start the MCA and records the difference between the fluorescent photon arrival and the photodiode stop signal. A histogram of these data is collected over time to produce an emission decay. Data collection is continued until at least ten thousand counts have been accumulated at the peak channel. For highly fluorescent samples and MCA bin width of ____, this might take only a few minutes, but for less fluorescent samples, it may take up to 30 minutes.

For the purpose of fitting and analysis, an instrument response function (IRF) is usually deconvoluted from the emission decays measured by TCSPC, in order to partially remove instrumental broadening of fast emission components. To record an IRF, a scattering sample, most frequently a suspension of powdered coffee creamer in water, was used. The full-width half-maximum (FWHM) of the IRF was usually measured to be 25 ps. The deconvolution of the IRF from the emission decay was performed using a convolute-and-compare algorithm written by Dr. Christopher Rumble, which is further detailed in section 2.2.1.

2.1.4 Kerr-Gated Emission Spectroscopy

Kerr-gated emission (KGE) spectroscopy is an ultrafast method that collects emission spectra from 400 – 700 nm using a charge-coupled device (CCD) camera. Our

instrument has an IRF of approximately 400 fs. This technique was used to measure samples with lifetimes faster than the 25 ps IRF of TCSPC. A schematic is shown in Figure 2.4. An amplified pulse at 388 nm from a regeneratively amplified Ti:Sapphire laser is split (BS) into gate and pump beams. The pump beam is doubled using a BBO crystal and used to excite the sample, which is contained in a 0.5 mm flow cell (SC). Fluorescence is collected and focused using a Schwarzschild objective (SO) and passed through an optical filter (F1) to remove the excitation light. The remaining light is passed through a vertical polarizer (GL) and directed through the benzene flow cell (BC). The gate pulse, after transiting a delay stage is overlapped with the fluorescence inside the benzene cell. When the gate pulse reaches the benzene cell, a transient birefringence (an elliptical polarization) is induced, which rotates the vertically polarized fluorescence by a few degrees, enabling a few percent of the fluorescence to pass through the second polarizer (GT), which is horizontally oriented. By changing the distance travelled on the delay stage, the fluorescence spectrum can be measured at different times. Time points measured using this technique range from -5 ps to 300 ps and measures the entire spectral decay within the range specified at the start of the experiment for each time step. Each sample is run in triplicate to average the kinetic parameters measured.

2.1.5 Cyclic Voltammetry

Cyclic voltammetry (CV) was used to determine the oxidation potentials of the coumarin molecules studied in Chapter 4. All CV experiments were done together with Dr. Christopher Gray of the Mallouk lab, whose knowledge was indispensable for

completing this work. As the name suggests, cyclic voltammetry measures the current of electrons as the potential is swept in a cyclical manner, showing positive peaks as oxidation reactions occur. Samples for CV were made as 10 mL, ~1 mM solutions of the coumarins in acetonitrile (dried overnight with molecular sieves). Measurements were conducted in a three-neck flask (dried overnight in an oven). A Ag/AgCl reference electrode was used with a platinum wire as the counter electrode. An Autolab potentiostat (PGSTAT128N) was used to sweep the potential linearly between the reference and working electrodes and a zero-resistance ammeter was used to measure the current between the counter electrode and the working electrode. The experiments swept from 0 to 1 V with a sweep rate of 100 mV/second for at least three cycles. Most coumarins showed the characteristic duck-shaped curve, indicating the reversibility of the oxidation reaction.⁹

2.2 Data Analysis Methods

2.2.1 Deconvolution of TCSPC Decays

TCSPC emission decays were fit to multi-exponential functions of time and the IRF was deconvoluted using a convolute-and-compare algorithm written in MATLAB. First, the measured IRF function is convoluted with a model decay consisting of 1-4 exponential components, $\sum_i a_i \exp(-t/\tau_i)$, where $\sum_i a_i = 1$, with user supplied guesses for the amplitudes (a_i) and decay times (τ_i). This convoluted model decay is compared to the measured decay and a normalized goodness of fit parameter, χ^2 , is calculated. The

value of χ^2 is then minimized using a non-linear least squares solver, and the fit is considered to be good when $\chi^2 \cong 1$. Fitting was typically accomplished by incrementing the number of exponentials in the model, beginning with a fit to a single exponential model. The best representation of a given decay was chosen as the model providing $\chi^2 \approx 1$ with a minimal number of components.

2.2.2 Deconvolution of KGE Data

Deconvolution of the KGE data is similar to the TCSPC data in that it uses an instrument response function convoluted with model multi-exponential decays to compare with experimental data, however the IRF is complicated by the intricacy of the experimental set up. KGE data spans a range of emission wavelengths, which travel through the optics at different rates causing a systematic variation in “time zero”. This temporal dispersion was measured using a white light continuum generated in a 3 mm sapphire plate at the sample position, which traveled the same path as the emission. This continuum covered approximately half of the wavelength range needed, so C153 in cyclohexane and POPOP in benzene were used to measure the blue edge (400-500 nm). Both methods were found to be in good agreement with each other and provided the correction required for further analysis.⁸

After correcting for temporal dispersion, the IRF used for convolution is assumed to be wavelength independent and created using a measurement of the Raman signal of a scattering sample, which is fit using three Gaussian functions. The overall FWHM was typically found to be approximately 400 fs. This model IRF is convoluted with a

specified number of exponential decays, just like TCSPC, and minimized using a nonlinear least-squares data fitting routine. As a result, we obtain an idealized data matrix of the fluorescence over time with the effects of the IRF and temporal dispersion are removed. From this data, we can determine information about the spectra, such as peak frequency, area, and height over time, which are used to estimate the spectral shift and global emission decay of the samples. These decays are often fit with two or three exponential decay functions.

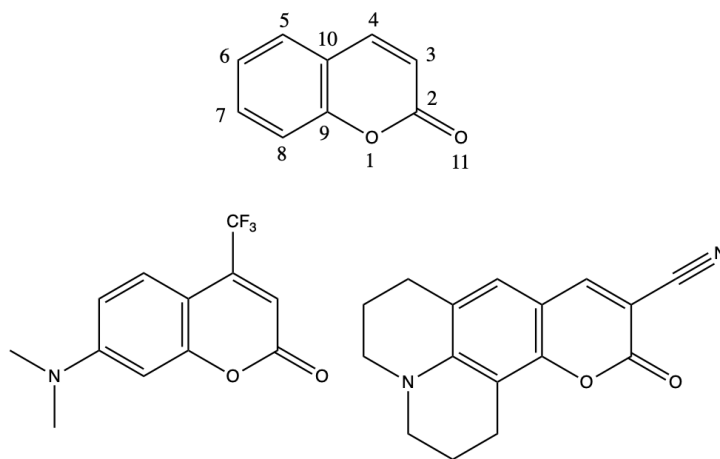


Figure 2.1: Standard labeling scheme of coumarins (top) and two examples: coumarin 152 (bottom left) and coumarin 337 (bottom right).

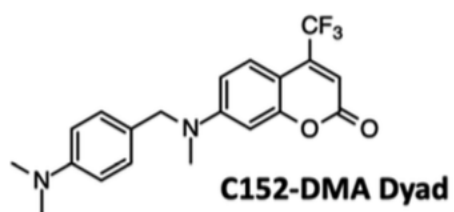


Figure 2.2: C152-DMA dyad molecule used for studies in Chapter 3.

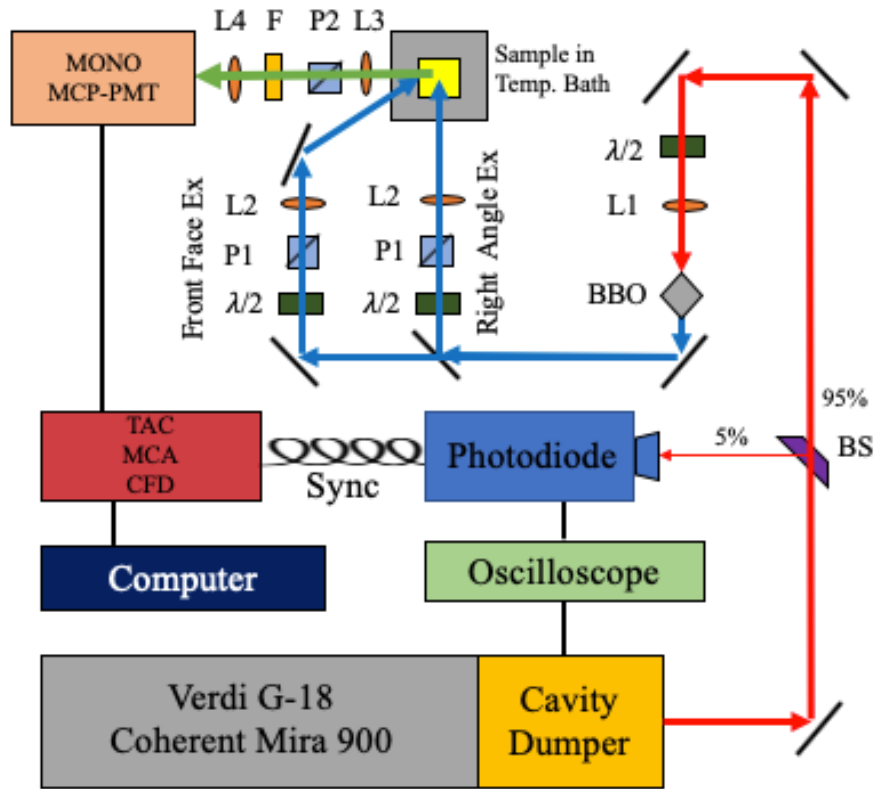


Figure 2.3: Diagram of the home-built TCSPC instrument used in this work. BS: beam splitter; $\lambda/2$: half-wave plate; L: 50 mm focal length lens; BBO: 0.2 mm BBO crystal; P: polarizer; F: optical filter; MONO: monochromator; MCP-PMT: micro-channel plate photomultiplier tube; TAC: time-to-amplitude converter; MCA: multichannel analyzer. This schematic is simplified to demonstrate the basic theory of the experiment. Full details can be found in previous work.⁶

References

1. K. Hara, T. Sato, R. Katoh, A. Furube, Y. Ohga, A. Shinpo, S. Suga, K. Sayama, H. Sugihara, and H. Arakawa, "Molecular Design of Coumarin Dyes for Efficient Dye-Sensitized Solar Cells," *J. Phys. Chem. B* **107**, 597-606 (2003).
2. X. Liu, J. M. Cole, P. G. Waddell, T. C. Lin, J. Radia, and A. Zeidler, "Molecular origins of optoelectronic properties in coumarin dyes: toward designer solar cell and laser applications," *J Phys Chem A* **116**, 727-737 (2012). 10.1021/jp209925y
3. H. Jin, B. O'Hare, J. Dong, S. Arzhantsev, G. A. Baker, J. F. Wishart, A. Benesi, and M. Maroncelli, "Physical Properties of Ionic Liquids Consisting of the 1-Butyl-3-Methylimidazolium Cation with Various Anions and the Bis(trifluoromethylsulfonyl)imide Anion with Various Cations," *Journal of Physical Chemistry B* **112**, 81-92 (2008).
4. J. R. Lakowicz, *Principles of Fluorescence Spectroscopy*, 3rd ed. (Springer, Baltimore, MD, USA, 2006).
5. J. A. Gardecki and M. Maroncelli, "A Set of Secondary Emission Standards for Calibration of Spectral Responsivity in Emission Spectroscopy," *Applied Spectroscopy* **52**, 1179-1189 (1998).
6. J. Breffke, B. W. Williams, and M. Maroncelli, "The Photophysics of Three Naphthylmethylene Malononitriles," *J. Phys. Chem. B* **119**, 9254-9267 (2015). 10.1021/jp509882q
7. C. A. Rumble, J. Breffke, and M. Maroncelli, "Solvation Dynamics and Proton Transfer in Diethylaminohydroxyflavone," *J. Phys. Chem. B* **121**, 630-637 (2017). 10.1021/acs.jpcc.6b12146
8. S. Arzhantsev and M. Maroncelli, "Design and characterization of a femtosecond fluorescence spectrometer based on optical Kerr gating," *Appl. Spectrosc.* **59**, 206-220 (2005). 10.1366/0003702053085007
9. N. Elgrishi, K. J. Rountree, B. D. McCarthy, E. S. Rountree, T. T. Eisnenhart, and J. L. Dempsey, "A practical beginner's guide to cyclic voltammetry," *J. Chem. Ed.* **95**, 197-206 (2017).

Chapter 3

Characterization of a New Electron Donor-Acceptor Dyad in Conventional Solvents and Ionic Liquids

Reproduced with permission from Saladin, M; Rumble, C.A.; Wagle, D. V.; Baker, G. A.; Maroncelli, M.; *J. Phys. Chem. B* **2019**, *123*, 9395-9407. Copyright 2019 American Chemical Society.

Co-author contributions: Synthesis and purification of the electron donor-acceptor dyad was performed by Durgesh Wagle and Gary Baker. Molecular dynamics simulations were performed by Christopher Rumble and analyzed by Mark Maroncelli.

3.1 Introduction

Ionic liquids possess a number of qualities that make them attractive as potential replacements for conventional electrolytes in fuel cells, batteries, and solar cells.^{1,2} In addition to being intrinsic electrical conductors, many ionic liquids possess wide electrochemical windows and high thermal stabilities.^{3,4} Being purely ionic, aprotic ionic liquids also have negligible volatility and thus negligible flammability, an important benefit in many applications. However, the same strong electrostatic interactions that render ionic liquids nonvolatile also make them more viscous than most conventional solvents, which negatively impacts chemical transport and electrical conductivity. High

viscosity also renders solvation in ionic liquids a slow and distributed process, which often results in reaction kinetics involving charge transfer more complex than in conventional solvents.⁵⁻⁷ Both because of their promise for energy applications and the new arena they provide for achieving a fundamental understanding of reactant-solvent coupling, many previous studies have sought to understand the effects of this complex dynamics on both bimolecular and intramolecular electron transfer kinetics.

Studies of bimolecular electron transfer in ionic liquids uncovered a number of distinctive effects. The earliest studies compared reaction rates in ionic liquids and conventional solvents against simple predictions for diffusion-controlled rates.⁸⁻¹² As anticipated, the high viscosities of ionic liquids lead to slower rates compared to conventional solvents. However, in many cases reactions were found to be 10-100 times faster than expected based on viscosity alone.¹³ This apparent rate acceleration was shown to be the result of two effects: enhanced rates of diffusion of neutral solutes in ionic liquids¹⁴ combined with the fact that stationary reaction conditions are often not achieved in the fluorescence quenching experiments typically used to measure rates.^{13,15} In more recent work, a number of groups have measured the rates of electron transfer quenching of coumarin dyes by aromatic amines in ionic liquids and observed an apparent Marcus turnover in rate at smaller than expected values of the driving force.¹⁶⁻¹⁹ Similar results were also reported in micelles and other slowly relaxing media,²⁰⁻²⁴ and attributed to reduction of the effective reorganization energy due to the slow environmental response in these media. The validity of this interpretation has been questioned^{25,26} and is currently still being debated.^{19,27,28} In very recent work, Wu et al.^{29,30} employed a detailed model of the reaction-diffusion problem to analyze data a

range of fluorophore/quencher pairs and concluded that some new feature was leveling reaction rates in ionic liquids in a way that is not apparent in conventional solvents. They proposed the slow reorientation of contact pairs gates reaction in ionic liquids in a manner that is unimportant in highly fluid solvents. Much has been learned from these studies of bimolecular electron transfer reaction. Nevertheless, disentangling the diffusional portion of reaction from the “intrinsic” electron transfer process in contact pairs remains subject to considerable uncertainty.

To focus on the solvent influence over the electron transfer event itself, a number of groups have therefore measured electron transfer rates between chemically bonded donor/acceptor (D/A) dyads in ionic liquids.^{6,31-45} Most studies employed D/A pairs linked by a single bond, and thereby having significant through-bond coupling. In such systems, electron transfer, or at least the achievement of the equilibrium extent of reaction, is often observed to be much slower than in conventional solvents and to closely track solvation times.^{31,40,44,45} Surprisingly few studies have so far employed dyads with the weaker coupling produced by a more extended bridge between the donor and acceptor.^{38,42,43} Of most relevance to the present work are the studies of Castner, Wishart and coworkers.^{42,43} They synthesized two dyads in which a coumarin dye was connected by one or two proline groups to the donor N,N-dimethyl-p-phenylenediamine, and compared the kinetics observed in acetonitrile to that in several ionic liquids. In the compound having a single proline bridge (“P1”),⁵⁷ electron transfer in acetonitrile was found to be dominated by a single component with a time constant near 0.5 ns. In contrast, reactions in the ionic liquids were markedly nonexponential, exhibiting a distribution of time constants ranging between 0.1-10 ns. These researchers attributed the

distributed character of the kinetics to the fact that solvation spans many time scales in ionic liquids.⁷ Because much of the solvation response occurs on time scales comparable to or slower than reaction, substantial heterogeneity in electron transfer rates is produced.^{46,47} Curiously, rather different behavior was observed in the case of the P2 dyad, linked by two proline units.⁵⁸ The P2 dyad showed decays having three well separated components in both acetonitrile and in the ionic liquid solvents, which the authors attributed to the presence of multiple conformations adopted by the diproline linker. Average rate constants of the P2 dyad were also not markedly different from those of the P1 dyad, presumably due to the ability of some P2 conformers to achieve close D/A separations.

The present paper reports the synthesis and characterization of a similar donor acceptor dyad intended for studies of ionic liquids. The dyad, “C152-DMA”, shown in Figure 3.1, is comprised of a coumarin 152 (C152) fluorophore, which acts as the photo-excited electron acceptor, linked to a dimethylaniline (DMA) donor. This combination was chosen because it is one of the most commonly used pairings in studies of bimolecular electron transfer, and it has therefore already been thoroughly characterized in simple solvents,^{25,48} ionic liquids,^{12,18,19,49} micelles and other complex environments,^{18,20,21} and in neat liquid DMA.⁵⁰⁻⁵² During the course of the present work it was found that the C152-DMA dyad has one serious flaw for use in ionic liquids. The linkage between the 7-amino group of the coumarin ring and the DMA readily dissociates in the presence of trace amounts of acidic impurities, which are difficult to completely remove from many ionic liquids. It is suitable for use in a wide range of conventional solvents and some ionic liquids and should still be of value for comparing solvation in

these classes of solvent, if not for wide-ranging studies of ionic liquids. For this reason, the synthesis and photophysics of C152-DMA, hereafter referred to as simply “the dyad”, as well as the two reference compounds C152 and H152 (Figure 3.1), were characterized using molecular dynamics simulations and steady-state and time-resolved fluorescence spectroscopy in a variety of solvents, as described below.

3.1 Methods

3.1.1 Reagents and Materials

The C152-DMA dyad, 7-((4-(dimethylamino)benzyl)(methylamino)-4-(trifluoromethyl)-2H-chromen-2-one, was synthesized using the route outlined in Figure 3.2. The reagents 4-dimethylaminobenzaldehyde (cat. no. 1030580100), 3-aminophenol (98%, 100242), ethyl 4,4,4-trifluoroacetoacetate (99%, E50205), iodomethane (ReagentPlus®, 99.5%, 289566), ethanol (200 proof, E7023), hexane (anhydrous, 95%, 296090), *N,N*-dimethylformamide (ReagentPlus®, ≥99%, D158550), ethyl acetate (anhydrous, 99.8%, 270989), sodium borohydride (≥96% gas-volumetric, 71320), potassium carbonate (anhydrous, free-flowing, Redi-Dri™, ACS reagent, ≥99%, 791776), sodium sulfate (ACS reagent, ≥99.0%, anhydrous, granular, 239313), zinc chloride (99.999% trace metals basis, 229997), and hydrogen bromide (ReagentPlus®, ≥99%, 295418) were used as received from MilliporeSigma (St. Louis, MO).

Preparation of 4-dimethylaminobenzyl alcohol (2): 1.0 g of 4-dimethylaminobenzaldehyde (**1**) was dissolved in 10 mL of ethanol, followed by the slow

addition of 0.279 g (1.1 equiv) of NaBH₄ over the course of 10 minutes. The reaction mixture was stirred for 2 h at room temperature and monitored by TLC. The solvent was evaporated under reduced pressure followed by addition of water and extraction with ethyl acetate. The organic phase was treated with brine and dried over NaSO₄. The ethyl acetate was removed on a rotary evaporator to afford 4-dimethylaminobenzyl alcohol, which was subsequently used for the next step without any further purification.

Preparation of 4-dimethylaminobenzylbromide hydrobromide (3): 3.5 mL of 48% HBr was added to a pressure tube containing 0.5 g of 4-dimethylaminobenzyl alcohol (**2**). The tube was tightly sealed, and the reaction stirred while heating for 2 h at 120 °C. The reaction was allowed to cool to room temperature and water then removed via rotary evaporation under reduced pressure to afford crude product (brown oil) which was used without additional purification.

3-Methylaminophenol (5) was synthesized from 3-aminophenol (**4**) following a literature procedure (yield: 68%).⁵³

Preparation of H152 (6): To generate the coumarin fluorophore by reaction of a phenol with a β -keto ester (i.e., Pechmann condensation), 1.34 g of 3-methylaminophenol (**5**) was dissolved in 20 mL of ethanol, followed by the addition of 2.20 g (1.1 equiv) of ethyl 4,4,4-trifluoroacetoacetate plus 1.78 g (1.2 equiv) of ZnCl₂. This mixture was refluxed for 12 h. The reaction mixture was cooled to room temperature and poured into 104 mL of 0.1 N HCl solution. The crude product was filtered, washed with water, and dried overnight. The crude product was further purified using a silica gel column eluted with a 3:1 (v/v) hexane–ethyl acetate solvent system under gravity (yield: 47%).

^1H NMR (500 MHz, DMSO) of **6**: δ 7.832 (1H, d), 7.099 (1H, q), 6.678 (1H, dd), 6.483 (1H, d), 6.450 (1H, s), 2.775 (3H, d). ^{13}C NMR (125 MHz) of **6**: δ 159.42, 156.91, 154.07, 140.61, 140.36, 140.11, 139.11, 125.28, 123.08, 120.89, 118.70, 111.38, 107.28, 107.24, 101.59, 96.33, 29.11.

Synthesis of the C152-DMA Dyad (7): In a round bottom flask, 0.243 g of **3** was dissolved in 5 mL of acetone, neutralized with 0.125 g of K_2CO_3 (1.1 equiv), and stirred for 5 min. This reaction mixture was added to a 25 mL round bottomed flask equipped with a magnetic stirring bar, followed by the addition of 0.200 g of **6** (1.0 equiv) plus another 0.125 g of K_2CO_3 in 10 mL of DMF. The reaction was stirred for 2 days at room temperature. The reaction was filtered, and the solvent removed via rotary evaporation (1 mmHg, 70 °C) over 8 h. The crude solid was purified using flash column chromatography by eluting with trimethylamine–hexane–ethyl acetate in a 2:29:69 (v/v/v) ratio (yield: 53%). The dyad was found to be highly susceptible to cleavage of the amine linkage in the presence of trace acid.

^1H NMR (500 MHz, DMSO) of **7**: δ 7.426 (d, 2H), 7.046 (d, 2H), 6.886 (d, 1H), 6.707 (d, 1H), 6.685 (d, 1H), 6.501 (s, 1H), 4.603 (s, 2H), 3.314 (s, 3H), 2.844 (s, 6H). ^{13}C NMR (125 MHz) of **7**: 159.33, 156.25, 152.55, 149.64, 139.92, 127.54, 125.31, 124.52, 123.02, 120.83, 112.55, 110.27, 101.73, 98.14, 54.33.⁵³

Coumarin 152 (7-dimethylamino)-4-(trifluoromethyl)coumarin, CAS# 53518-14-2) was purchased from Exciton and used as received.

Solvents used for spectroscopic measurements were HPLC grade acetonitrile and methanol (OmniSolv), spectroscopic grade ethylene glycol, dimethyl sulfoxide,

propylene carbonate, tetrahydrofuran, 1,4-dioxane, toluene, and cyclohexane (Sigma-Aldrich), and methyl acetate (Fluka). Solvent mixture series, cyclohexane and tetrahydrofuran (CHEX/THF) and cyclohexane and dibutyl ether (CHEX/DBE) were made by volumetrically and compositions reported as volume fraction, assuming incompressibility. All conventional solvents were tested for water content using a Karl Fischer titrator. If the water content was less than 100 ppm, the solvent was used as received. Otherwise, solvents were dried with molecular sieves overnight. Samples were purged with nitrogen for three minutes before any experiments to prevent quenching by dissolved O₂. Absorption and emission spectra were recorded for each solvent to confirm lack absorbing impurities and minimal fluorescence in the visible region. Ionic liquid solvents 1-butyl-1-methyl-pyrrolidinium bis(trifluoromethylsulfonyl)imide ([Pr₄₁][Tf₂N]), methyltrioctylammonium bis(trifluoromethylsulfonyl)imide ([N₈₈₈₁][Tf₂N]), and trihexyltetradecylphosphonium bis(trifluoromethylsulfonyl)imide ([P_{14,666}][Tf₂N]) were purchased from IoLiTec having stated purities above 98% but selected for high optical quality. These ionic liquids were purified using the methods described in previous work⁵⁴ in order to minimize impurity emission overlapping with the S₀-S₁ absorption band of the solutes.

3.2.2 Spectroscopic Methods

Steady State Absorption and Emission: All steady state absorption measurements were made in Parafilm-sealed 1-cm path length quartz cuvettes on a Hitachi UV-3010 UV-Vis spectrophotometer. Solvent spectra were measured and subtracted from all sample

spectra. Fluorescence spectra were collected at right angle with 2 nm resolution using a SPEX Fluorolog 212 fluorimeter, calibrated with a set of emission standards from 300 to 800 nm using previously described methods.⁵⁵ Emission spectra were excited at 400 nm and collected over the range 410 - 700 nm. Fluorescence samples were also made in sealed 1 cm quartz cuvettes. Solute concentrations were chosen to provide optical densities of ~ 1.0 for absorption and ~ 0.15 for emission measurements at 395 nm.

Time Correlated Single Photon Counting (TCSPC): Time-correlated single photon counting (TCSPC) was used to measure the lifetimes in the ns-ps range. Instrumental details can be found in previous work.⁵⁶ For the present experiments, excitation pulses were provided by the doubled output of a cavity-dumped Ti:Sapphire oscillator (Coherent Mira 900+PulseSwitch) tuned to 800 nm. All TCSPC samples were measured in sealed 1 cm quartz cuvettes. Emission decays at selected wavelengths (4 nm resolution) were collected in a 90° geometry at magic angle polarization. Stray excitation light was suppressed using a Kopp 3-73 filter. Use of a scattering sample showed the instrument response function (IRF) to be approximately 25 ps FWHM for all experiments.

Kerr-Gated Emission (KGE) Spectroscopy: For samples with decay times faster than 50 ps, time-resolved fluorescence spectra were collected using a Kerr-gated emission instrument, described in earlier work.^{57,58} Each sample was flowed through a 0.2 mm sample cell where it was excited with 388 nm pulses from the frequency doubled output of an amplified Ti:Sapphire system (Coherent Verdi G18/Mira 900/RegA 9050). The entire emission spectrum between 408 to 699 nm was collected at each time step (-5 to 5 ps in steps of 100 fs, from 5 to 50 ps in steps of 200 fs, and from 50 ps to 300 ps in 2 ps

steps) using an Acton SpectraPro-300i grating spectrograph and a liquid-nitrogen cooled CCD (1340 pixels, Princeton instruments). The FWHM of the fitted instrument response was approximately 400 fs. These experiments were performed in triplicate and the kinetic parameters averaged in producing the reported results. Deconvolution of the instrument response function from the spectra was accomplished using a global convolute-and-compare algorithm.^{57,58} Fits to log-normal functions were made after deconvolution to quantify the spectral dynamics.

Temperature Control: Most of the experiments were performed at room temperature, 293 ± 1 K. Steady state fluorescence and TCSPC measurements in ionic liquids were also performed over a range of temperatures between 213 K to 353 K. For temperatures above 273 K, water flowed from a recirculating water bath through a brass cuvette holder and for lower temperatures, an Oxford variable temperature liquid nitrogen cryostat (model DN1754) was used. All samples were equilibrated at each temperature for at least thirty minutes before measurements were made.

3.2.3 Computational Methods

Molecular dynamics simulations of the dyad in vacuum and acetonitrile (ACN) solution were performed using the GROMACS 2018.1 package⁵⁹ and the GAFF force field.⁶⁰ Atomic charges were obtained from a CHELP⁶¹ fit of the electrostatic potential generated from a previously optimized structure at the B3LYP/6-311G++ level using the Gaussian09 package.⁶² Charges on equivalent atoms were symmetrized following the

CHELP fit. Topology files were generated using AmberTools17⁶³ and the *acpype* program.⁶⁴ Simulations in ACN consisted of one dyad molecule and 2450 ACN molecules in a ~6 nm cubic box with cubic periodic boundary conditions. Integration was carried out using the Verlet leapfrog algorithm with a step size of 2 fs. The particle-mesh Ewald method⁶⁵ was used to handle the long-range electrostatics and non-bonded interactions were calculated using a Verlet neighbor list with a 1.4 nm cutoff. The P-LINCS algorithm was used to constrain all hydrogen containing bonds.⁶⁶ The same methods were applied to simulate behavior in the gas phase simply by omitting the ACN molecules.

Following a short energy minimization procedure, the simulation box was equilibrated using three consecutive 500 ps simulations in NVT, NPT, and NVT ensembles. The pressure of the NPT simulation was set to 1 bar and regulated using a Berendsen barostat with a relaxation time of 5 ps, whereas the temperature was 293.15 K and regulated using a modified Berendsen thermostat with a relaxation time of 0.5 ps.⁶⁷ Production NVT simulations were then carried out for 50 ns with dyad coordinates saved every 0.1 ps, giving a total of 5×10^5 structures.

3.3 Results and Discussion

3.3.1 Molecular Dynamics Simulations

The methylene linkage chosen to connect the donor and acceptor groups was expected to lead to significant intramolecular flexibility in the C152-DMA dyad. To

assess conformations present in the ground state, two approaches were used. First, attempts were made to use the conformational search algorithms available in MacroModel 11,⁶⁸ followed by DFT calculations of selected conformers. However, it became clear from such calculations that the dyad structure is not adequately described by a small number of well-defined conformers at room temperature. For this reason, MD simulations using a classical force field were performed both in acetonitrile and the gas phase to provide more appropriate sampling of conformational space.

Three dihedral angles, defined in Figure 3.3a, were used to coarsely specify the geometries of the dyad observed in these simulations. Several representations of the distributions observed for these three angles are shown in Figures 3.3b, Figure 3.3c and Figure 3.4. There are eight heavily populated regions of this conformational space, defined by population minima approximately located by planes at $D1 = \pm 90^\circ$, $D2 = 0$, and $D3 = 0$. For simplicity, if one uses the 2-fold rotational symmetry about $D1$ to fold populations into the range $-90^\circ \leq D1 \leq 90^\circ$, the four occupied regions of conformational space depicted in Figure 3.4 result. As shown by the representative structures in Figure 3.4, all four heavily populated regions involve structures in which the donor and acceptor aromatic planes are nearly orthogonal to one another. Comparison of the structures observed in the gas- and solution-phase simulations (Figure 3.3b and Appendix Figure A.3) show them to be quite similar. The primary difference is that conformer distributions are slightly more localized in solution, particularly with respect to the $D2$ angle.

The time evolution of the three dihedral angles (Appendix Figure A.4) shows that

the dyad samples the conformational space within one of these four regions on a picosecond time scale, with transitions among regions occurring on a much longer time scale. Specifically, in acetonitrile solution, fast fluctuations within each region are such that D1-D3 vary by $\pm 10\text{-}15^\circ$ (1σ) when viewed in 10 ps windows. Transitions among conformer regions take place via $\sim 180^\circ$ jumps, which occur on average once every 0.7 ns. (Interconversion among conformers is faster in the gas-phase, as might be expected given the absence of intermolecular friction.) The remainder of this discussion will consider only the more relevant solution-phase results.

The presence of a distribution of conformers implies electron transfer will be initiated from a distribution of ground-state geometries. This geometric variability should result in distributions over the key parameters controlling electron transfer rates, namely the driving force, reorganization energy, and most importantly, the electronic coupling. Rather than attempt detailed quantum mechanical calculation of these quantities, two simple surrogates, the donor-acceptor (center-of-mass) distance R_{DA} , and the angle θ_π between the aromatic planes of the donor and acceptor were monitored. In Figure 3.5(a, b) the distributions of these quantities are plotted (blue curves). Average values are $R_{DA} = 0.80 \pm .08$ nm and $\theta_\pi = 90 \pm 23^\circ$ (1σ). These averages and the way that R_{DA} and θ_π are distributed are remarkably similar in all four of the conformer regions, as shown in Appendix Figure A.5. Thus, it seems reasonable to conclude that the existence of these four slowly interconverting populations of conformers will have little effect on the electron transfer kinetics observed. However, the variations of R_{DA} and θ_π within

each region are not small and may be expected to give rise to distributed electron transfer kinetics.

To examine this possibility further, the main effect on electron transfer kinetics is assumed to result from geometric variations modulating the electronic coupling, modeled as functions of θ_π and R_{DA} by $k_{ET} \propto \cos^2 \theta_\pi \cdot \exp(-\beta R_{DA})$. The electron coupling decay constant β is assumed to have a value of 15 nm^{-1} , typical of condensed media.^{13,69} The dashed red curves in Figure 3.5 show how these model dependences samples the distributions of conformer geometries. In both cases, the largest values of k_{ET} come from regions well removed from the most probable conformations. Taking the R_{DA} and θ_π variations separately and correlating fluctuations in $\exp\{-\beta R_{DA}(t)\}$ and $\cos^2 \theta_\pi(t)$ over the course of the simulation leads to the normalized time correlation functions shown in panels (c) and (d). These functions both decay rapidly, with correlation times of ~ 5 ps. These times suggest that the distribution of conformers present in C152-DMA should not lead to distributed kinetics for reactions taking place on time scales of 100 ps or more. For such reactions homogeneous kinetics of the geometrically averaged structures is expected. For faster reactions, some distributed character of the reaction rates and perhaps gating of reaction by conformational fluctuations is anticipated.

3.3.2 Steady State Characterization

Steady-state absorption and emission spectra of the dyad and the reference chromophores C152 and H152 were measured in a variety of solvents and solvent

mixtures to characterize their polarity dependence. Relevant data are summarized in Table A.1. We note that several solvatochromic studies of C152 have already been reported,⁷⁰⁻⁷² but no information has previously been published on H152.

Figure 3.6 compares absorption and emission spectra of these three solutes in the nonpolar solvent cyclohexane and the highly polar solvent acetonitrile. In cyclohexane, the spectra of all three molecules exhibit similar vibronic structure, and their absorption and emission spectra are offset by comparable Stokes shifts. In acetonitrile, all spectra are broadened, and the Stokes shifts are increased by solvation, but the similarities in spectral shape among the three are maintained. These similarities suggest that the coumarin aromatic system is the absorbing chromophore in all three cases, and that excitation of the dyad leads to a locally excited (LE) state similar to those of other 7-amino substituted coumarins.⁷³ Because the frequencies of the and chromophore redox properties of the dyad are expected to be closer to those of C152, we will use C152 as a reference for the photophysics expected in the absence of electron transfer.

Absorption and emission spectra of the dyad in solvents having in a range of polarities are shown in Figure 3.7. As solvent polarity increases, both the absorption and emission spectra red shift and broaden. The emission shifts are considerably larger, due to the well-known increase in dipole moment in S_1 compared to S_0 , which is characteristic of this type of coumarin. Similar solvent dependence is found for the C152 and H152 (Table A.1). One feature of the dyad emission of note is the increased noise observed in the higher polarity solvents (MeAC and ACN in Figure 3.7). This noise reflects a roughly ~ 500 -fold reduction in the dyad's fluorescence quantum yield with increasing solvent polarity. Such strong quenching is absent in C152 and H152 and is the

first indication that the anticipated electron transfer is occurring in the dyad.

In Figure 3.8, absorption and emission frequencies of the dyad are compared to those of C152. The excellent correlations shown here underscore the similarity of the dyad LE state to the S_1 state of C152. However, whereas the transition energies of C152 and the dyad are linearly related, the slopes in Figure 6 (0.71 and 0.64) are not close to unity. These slopes indicate the dyad has only 2/3 of the solvent sensitivity of C152, which might suggest a significantly reduced charge separation in the LE state compared to C152.

To examine this possibility, estimates of the dipole differences between the absorbing (S_0) and emitting (S_1 or LE) states, $\Delta\mu = |\vec{\mu}(S_1) - \vec{\mu}(S_0)|$, were made using a Lippert-Mataga type analysis of the Stokes shifts of all three solutes. Modeling the system as a solute consisting of a polarizable point dipole centered in a spherical cavity of radius a and the solvent as a dielectric continuum, such a model predicts

$$\nu_{\text{abs}} - \nu_{\text{em}} = (\nu_{\text{abs}} - \nu_{\text{em}})_{\text{gas}} + \frac{2}{(4\pi\epsilon_0)h} \frac{(\Delta\mu)^2}{a^3} \Delta f. \quad (3.1)$$

where Δf is the solvent orientational polarizability,

$$\Delta f = \frac{\epsilon_r - 1}{\epsilon_r + 2} - \frac{n_D^2 - 1}{n_D^2 + 2}. \quad (3.2)$$

with ϵ_r the relative permittivity and n_D the refractive index of the solvent. Because the solutes examined here are not spherical in shape, there is no unambiguous way to assign an appropriate value of the cavity radius a . Previous work on the similar chromophore coumarin 153⁷⁴ showed that an effective cavity radius based on the van der Waals volume of the solute extended by 50%, to account for the average size of solvent layer, provided estimates of $\Delta\mu$ in line with electronic structure calculations and more definitive

experiments. Adopting this approach, the slopes of the solvatochromic plots in Figure 3.9 yield the dipole difference estimates in Table 3.1. Insofar as this choice of a_{eff} is reasonable, these estimates show the solvatochromic data are consistent with the charge shift between S_0 and the LE state of the dyad being similar to the S_1 - S_0 difference in C152. The value of $\Delta\mu$ estimated for H152 is slightly smaller, as would be expected upon replacing an electron donating alkyl group on the amine with a hydrogen atom.

For comparison, Table 3.1 also lists dipole moments calculated at the CAM-B3LYP/6-311++G(d,p) level in the gas phase. Calculations of the dyad were performed on a number of representative conformers, and the range of values for these conformers are tabulated. All values are for the optimized S_0 geometries. These calculations confirm minimal mixing between the DMA and coumarin portions of the molecule in either the S_0 or (vertical) S_1 /LE states and the similarity of the charge shift in the $S_0 \rightarrow S_1$ transitions of the dyad and C152. They also confirm the presence of a charge-transfer state of the dyad, as indicated by the large dipole moments of the vertical S_2 states of all conformers studied. The frontier molecular orbitals and some additional characteristics of the LE and CT states are provided in Appendix Figure A.6.

3.3.3 Time-Resolved Measurements

Representative fluorescence decays of the dyad are shown in Figure 3.10 and selected multi-exponential fits are provided in Table 3.2. The decays in Figure 3.10 were all recorded using TCSPC, which has an instrumental response time of ~ 25 ps. Five of the highest polarity solvents, represented by acetonitrile (ACN) and methanol (MeOH) in

Figure 3.10, have lifetimes shorter than 25 ps, and these solvents were also measured using Kerr Gated Emission (KGE) spectroscopy. Fits of the KGE data are compiled in Table 3.2b. Finally, emission decays of the reference chromophores C152 and H152 were measured in all solvents, and their lifetimes are also provided in Table 3.2.

With few exceptions⁷⁵ the decays of C152 and H152 are well described by single exponential functions. In contrast, in the case of the dyad, exponential or nearly exponential decays are only observed in some of the least polar solvents, for example cyclohexane (CHEX) and dibutyl ether (DBE) shown in Figure 3.10. In the majority of solvents, dyad emission is significantly non-exponential, requiring 3-4 components for accurate representation. In many solvents, the longest component has an amplitude of a few percent and a lifetime of several nanoseconds, close to that of H152 in the same solvent. In the highest polarity solvents, such as acetonitrile and methanol in Figure 3.10, this long component is readily distinguished, because it decays on a much longer time constant than all other components. These nanosecond components are attributed to the presence of residual H152 impurity in the dyad samples. As discussed in the Supporting Information, H152 is both a precursor in the dyad synthesis and produced by acid-catalyzed heterolysis of the dyad. In most solvents, the amplitude of this longest component is <5 %. When such a small and well-separated component was required in unconstrained fits, we refit the TCSPC data after constraining the lifetime of this component to be equal to the H152 lifetime. These constrained fits are what are reported in Table 3.2, and when calculating average dyad lifetimes and rates, these putative impurity components are omitted, as described below.

Representative KGE data for the dyad in propylene carbonate are shown in Figure

3.11. With the better time resolution (~ 400 fs IRF) of the KGE technique, one observes the dyad emission spectrum to undergo a dynamic Stokes shift. The peak frequencies of these spectra could be fit with bi-exponential functions having times constants in the few picoseconds range. The average times for these shifts of the dyad emission are reasonably correlated ($R^2=0.74$, $N=5$) to the average times measured for the nonreactive solute coumarin 153.⁷⁴ As illustrated by the data in Figure 3.11(c), the time dependence of the peak height and integrated intensity of the emission are quite similar. In all cases, the intensity data could be represented by two main components together with a slower component in the tens of picoseconds range having an amplitude of $\leq 6\%$ (Table 3.2b). Due to the lower signal-to-noise and time range, the small ($<3\%$) nanosecond components found in the TCSPC data of these solvents are not observed in the KGE data.

The non-exponential emission decays observed for the dyad complicate description of the rate of electron transfer and its solvent dependence. Rather than attempt any detailed characterization of the distributed kinetics here, two limiting rate constants from the multi-exponential fits to the decay data are calculated. Using the lifetime of C152 (τ_{C152}) to estimate the dyad lifetime in the absence of electron transfer, the rate constants

$$k_{ET}^{(1)} = 1/\langle\tau\rangle_{\text{dyad}} - 1/\tau_{C152} \quad \langle\tau\rangle_{\text{dyad}} = \sum a_i \tau_i / \sum a_i \quad (3.3)$$

and

$$k_{ET}^{(2)} = \langle k \rangle_{\text{dyad}} - 1/\tau_{C152} \quad \langle k \rangle_{\text{dyad}} = \sum' (a_i / \tau_i) / \sum a_i \quad (3.4)$$

were calculated. The Σ' in these equations indicates omission of small-amplitude ($<6\%$) impurity components in these calculations. One can view $k_{ET}^{(1)}$ and $k_{ET}^{(2)}$ as providing approximate lower and upper bounds to the distribution of rates present.

Before discussing these rates, it should be mentioned that C152 undergoes a twisted intramolecular charge-transfer (TICT) process in high polarity solvents.^{70-73,76} It might be thought that this process might render C152 unsuitable as a lifetime reference for the dyad. This issue is discussed in detail in the Supporting Information (Appendix Section A2) where it is shown that the effect of the TICT process on use of C152 the ET rates determined here should be negligible.

Figure 3.12 plots the observed rate constants versus the steady-state emission frequency of the dyad, $\langle\nu\rangle_{em}$, which is used here as a measure of effective solvent polarity. A similar correlation is found when these rates are plotted versus the dielectric measure of total solvent polarizability $(\epsilon_r - 1)/(\epsilon_r + 2)$, as shown in Appendix Figure A.8. The filled symbols in Figure 3.12 are the logarithmic averages of $k_{ET}^{(1)}$ and $k_{ET}^{(2)}$, and the limits of the error bars serve to denote their individual values. Although there is considerable scatter and, in some cases a large difference between $k_{ET}^{(1)}$ and $k_{ET}^{(2)}$, a clear correlation exists between k_{ET} and $\langle\nu\rangle_{em}$, at least in most solvents. A substantial dependence of the electron transfer rate on solvent polarity of this sort is expected given the large difference in charge separation and thus dipole moments of the LE and CT states of the dyad (~ 20 D based on the calculations in Table 3.1). It seems reasonable to attribute the increasing rate with increasing solvent polarity as being primarily due changes in the driving force for reaction, assuming that the electron transfer lies within the normal regime.

In a number of solvents, explicitly labeled in Figure 3.12, values of k_{ET} appear to be smaller than expected based on the relationship established by the majority of solvents.

With the exception of toluene, these solvents all have much higher viscosities than do the remaining solvents. (See Appendix Table A.1.) The two ionic liquids near the bottom of the figure, [P_{14,666}][Tf₂N] and [N₈₈₈₁][Tf₂N], have viscosities >500 mPa s⁻¹ near room temperature, and in these solvents electron transfer is too slow to measure, and this situation persists even up to 350 K. (See Appendix A Section A.3.) These observations suggest that, in addition to polarity, some other factor such as solvent friction plays a role in determining the rate of electron transfer.

Support for friction being relevant can be found in temperature-dependent TCSPC measurements of the dyad in the ionic liquid [Pr₄₁][Tf₂N], which are shown in Figure 3.13. Over the 25 K temperature range (278-303 K) the ionic liquid's polarity (as judged by $\langle \nu \rangle_{em}$) varies negligibly, the viscosity decreases by nearly a factor of four, and k_{ET} doubles. An Arrhenius analysis of the data, shown in the inset to Figure 3.13, yields an activation energy of 21 kJ/mol and a prefactor of $1.3 \times 10^{14} \text{ s}^{-1}$. This prefactor is too high to be interpreted in terms of a reactive frequency in such a reaction. A more realistic description is a nearly activationless reaction with a frictional prefactor proportional to viscosity, η^p , with $p \sim 0.6$. This dependence on solvent viscosity could either reflect some large-amplitude solute motion required for reaction, or a dependence on solvation time, which approximately tracks viscosity.

It is interesting to compare the electron transfer rates measured for C152-DMA dyad to the intramolecular dyads studied by Castner, Wishart and coworkers,^{42,43} which were constructed from an aromatic amine donor and a coumarin 343 photoacceptor linked by one (P1) or two (P2) proline groups. Electron transfer in both the P1 and P2

molecules is considerably slower than that observed for the C152-DMA dyad. Focusing on the simpler P1 dyad,^{42,43} average rate constants calculated using Equations 3.3 and 3.4 provide values $(k_{ET}^{(1)} | k_{ET}^{(2)}) / 10^9 \text{ s}^{-1}$ of (1.6 | 2.8) in acetonitrile, (1.6 | 3.5) in methanol, and (0.73 | 1.4) in [Pr₄₁][Tf₂N] at 293 K. Comparison to Table 3.2 shows electron transfer in the C152-DMA dyad to be 100-1000 times faster in the two conventional solvents and 10-40 times faster in the ionic liquid [Pr₄₁][Tf₂N]. Differences in both the electronic coupling and the redox properties of the donor and acceptor are likely responsible for the different kinetics in these two dyads. For example, the free energy change of the C152+DMA bimolecular reaction in acetonitrile is estimated to be about -0.43 eV,⁴⁸ and estimates for the C152-DMA dyad are not expected to differ appreciably from this estimate. The reaction free energies of the P1 and P2 dyads in acetonitrile were estimated to be -1.6 eV,^{42,43} much more negative and the driving force much greater than in the C152-DMA dyad.

Comparison can also be made between the present results and rates measured for the equivalent bimolecular reaction between C152 and DMA. Most desirable for such a comparison are effective unimolecular reaction rates between C152 and a single proximal DMA molecule. The rate of this idealized process can be estimated from previously reported data by making some significant assumptions. The fewest assumptions are required for interpreting the quenching dynamics of C152 in neat liquid DMA, which has been reported by two groups.^{51,52} Both reported bi-exponential fluorescence decays with initial rates ($k_{ET}^{(2)}$, Eq. 4) of $(2.0 \pm 0.2) \times 10^{12} \text{ s}^{-1}$. Assuming reaction occurs between C152 and only one of the approximately 10 DMA molecules within its first solvation shell^{29,52}

acting independently, the rate constant for comparison to the dyad data is $k_{ET}^{(2)} \sim 2 \times 10^{11} \text{ s}^{-1}$. Measurements of concentrated DMA solutions, where most reaction is expected to occur between preformed ground-state C152/DMA pairs, also provide similar estimates. In solutions of $>0.5 \text{ M}$ DMA mixed with toluene,⁵² chlorobenzene,⁵² cyclohexane,⁷⁷ and two ionic liquids⁷⁸), one finds values of $k_{ET}^{(2)}$ in the range $(1-5) \times 10^{11} \text{ s}^{-1}$. In both the neat and mixed solvent cases, these effective unimolecular rate constants provide estimates of rates associated with reaction between a single C152 + DMA contact pair averaged over relative positions and orientations of first solvation shell neighbors. The polarities of neat DMA ($\epsilon_r = 5.0$ ⁵²) and these concentrated DMA mixtures are expected to fall roughly in the middle of the range studied, where dyad rates are closer to 10^{10} s^{-1} . Thus, the C152-DMA dyad appears to provide an example of an intramolecular electron transfer only slightly slower than average rates of contact pairs in the intermolecular process it was intended to mimic.

3.4 Summary and Conclusions

This work documented the synthesis and photophysical properties of a new electron donor-acceptor dyad, C152-DMA, made by covalently linking the photo-acceptor C152 and the DMA donor with a single methylene unit. Although the simple linker employed here confers significant conformational flexibility to the dyad, molecular dynamics simulations suggest that this flexibility only causes electron transfer rates to be distributed over a modest range.

Apart from the rapid fluorescence quenching caused by electron transfer, the absorption and emission characteristics of the C152-DMA dyad were shown to be very similar to that of the reference compounds C152 and H152, demonstrating the lack of mixing between the donor and acceptor states in the locally excited electronic state. The coumarin chromophore of the dyad and its references are all strongly solvatochromic, as are most 7-aminocoumarins.

Time-resolved emission of the dyad was found to be multi-exponential/distributed in most solvents. Average rate constants in conventional solvents are strongly dependent on solvent polarity, with rates near 10^8 s^{-1} in nonpolar solvents and increasing to $\sim 10^{12} \text{ s}^{-1}$ in the most polar solvents. This variation is most likely a result of the increasing driving force for charge separation with increasing solvent polarity. Absence of observable quenching in two high-viscosity ionic liquids together with the temperature dependence observed in a low-viscosity ionic liquid suggest that solvent friction also plays an important role in determining dyad electron transfer rates. Further study is needed to determine whether this frictional effect is due to a dependence on solvation times, as found in several other intramolecular cases^{31,40,44,45} or perhaps due to slowdown of conformational sampling with increasing viscosity.

The rates of electron transfer observed in the C152-DMA dyad are considerably faster than rates previously reported for the related coumarin - aromatic amine dyads by Castner, Wishart and coworkers.^{42,43} C152-DMA reaction rates appear to be closer to those between contact DMA + C152 pairs estimated from intermolecular quenching experiments, which suggests that the C152-DMA dyad is an apt intramolecular analog of

the bimolecular process. Although its sensitivity to acid-catalyzed hydrolysis limits its use to only highly purified ionic liquids, the C152-DMA dyad should nevertheless provide a useful new probe for comparisons between electron transfer in ionic liquids and conventional solvents.

Acknowledgements

The authors thank Danny Sykes for help with attempts to quantify impurities in dyad samples using HPLC. This work was supported by grants from the U.S. Department of Energy, Office of Basic Sciences, Division of Chemical Sciences, Geosciences, and Biosciences under contract nos. DE-SC0008640 and DE-SC0019200 (Penn State: MS and CAR), and by the Research Corporation for Science Advancement (GAB).

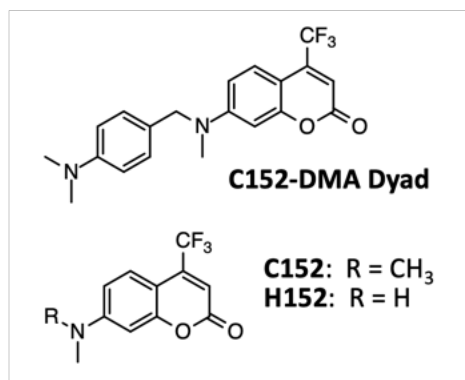


Figure 3.1: Scheme of C152-DMA dyad, coumarin 152, and precursor H152

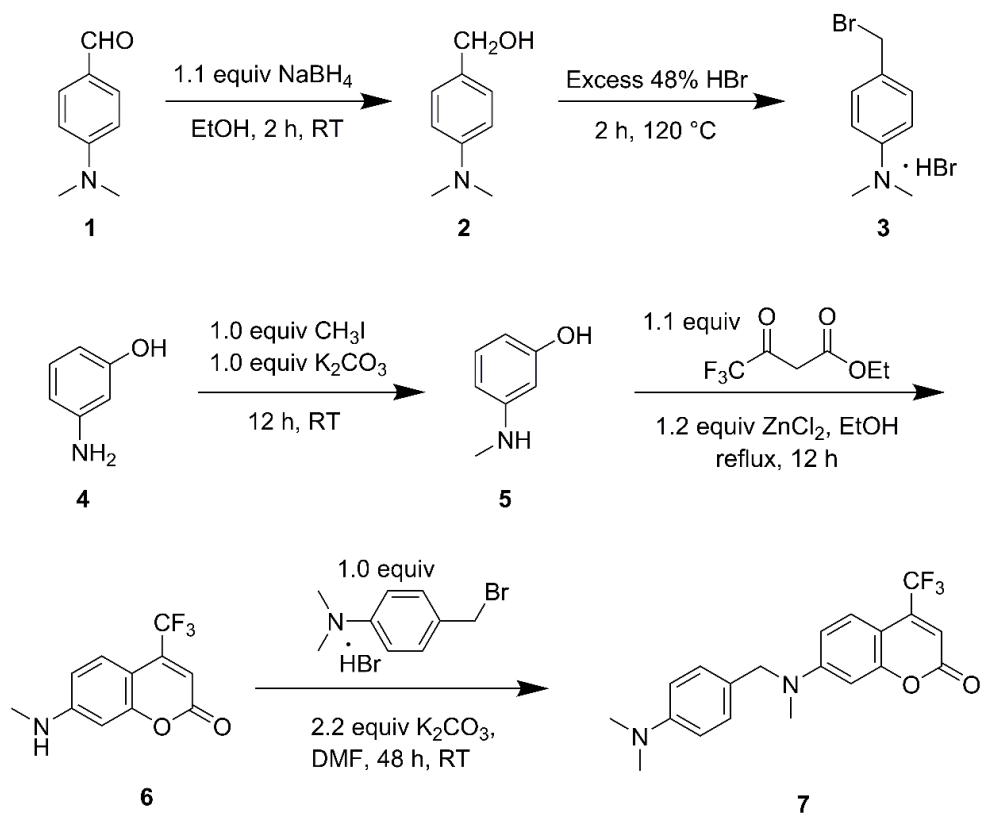


Figure 3.2: Scheme of synthesis of C152-DMA dyad.

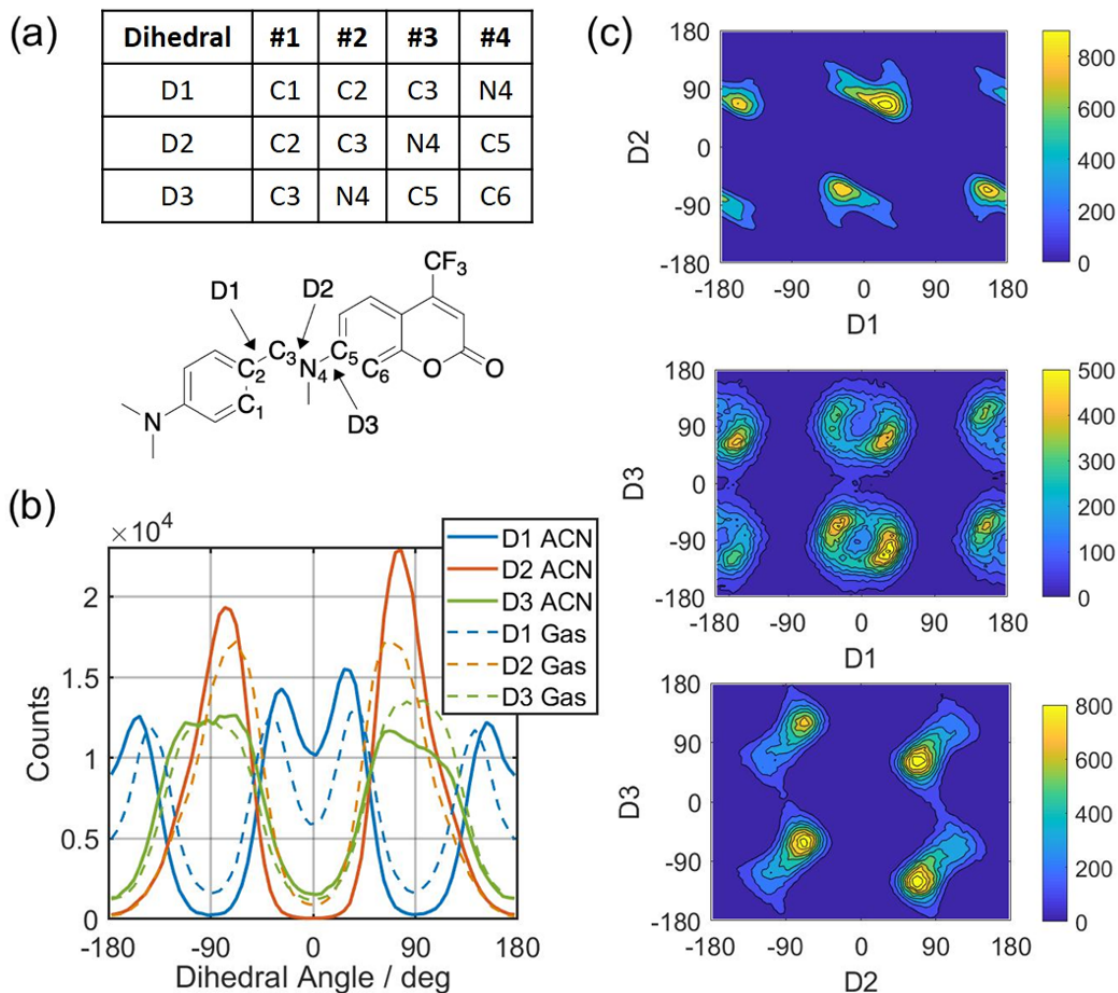


Figure 3.3: (a) Dihedral angle definitions. (b) One-dimensional distributions of angles D1-D3 in acetonitrile (solid curves) and in the gas phase (dashed). (c) 2-dimensional distributions in acetonitrile. In both the 1d and 2d distributions the values shown are the numbers of occurrences out of 5×10^5 samples.

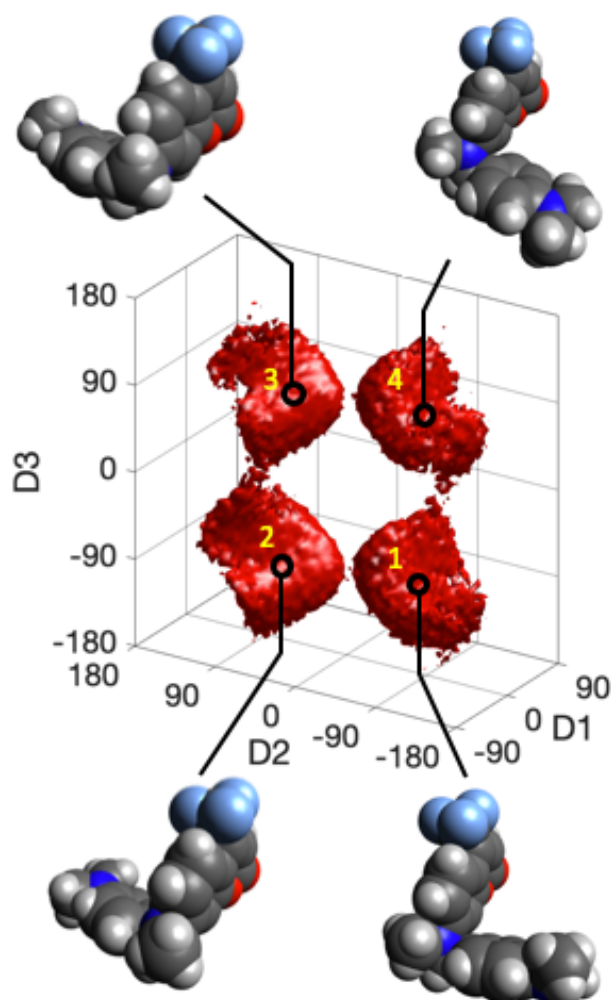


Figure 3.4: The most populated regions of conformational space shown as isosurfaces capturing 65% of the population. For clarity, values of $|D1| > 90^\circ$ here are folded into $-90^\circ \leq D1 \leq 90^\circ$ using the 2-fold rotational symmetry of the DMA group. The conformer regions designated 1-4 are defined by the planes $D2 = 0$ and $D3 = 0$. The molecular structures show representative geometries selected from the most populated areas within these four regions.

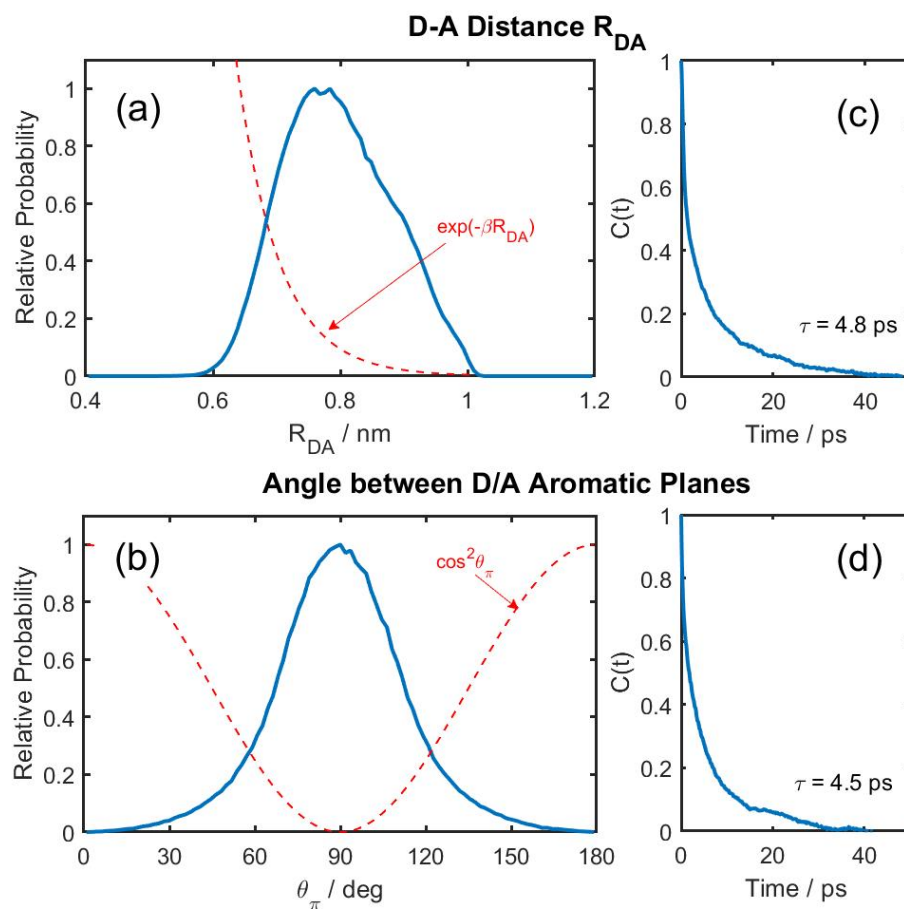


Figure 3.5: Distributions of (a) the center-of-mass distance between the donor and acceptor groups R_{DA} and (b) the angle between their aromatic planes, θ_π , observed in acetonitrile. The dashed red curves in these two panels indicate the approximate variation in electron transfer rates expected from these geometric parameters ($\beta = 15 \text{ nm}^{-1}$). (c) and (d) show the autocorrelation functions of R_{DA} and θ_π averaged over the 50 ns trajectories. The τ values indicated are the correlation times of these functions.

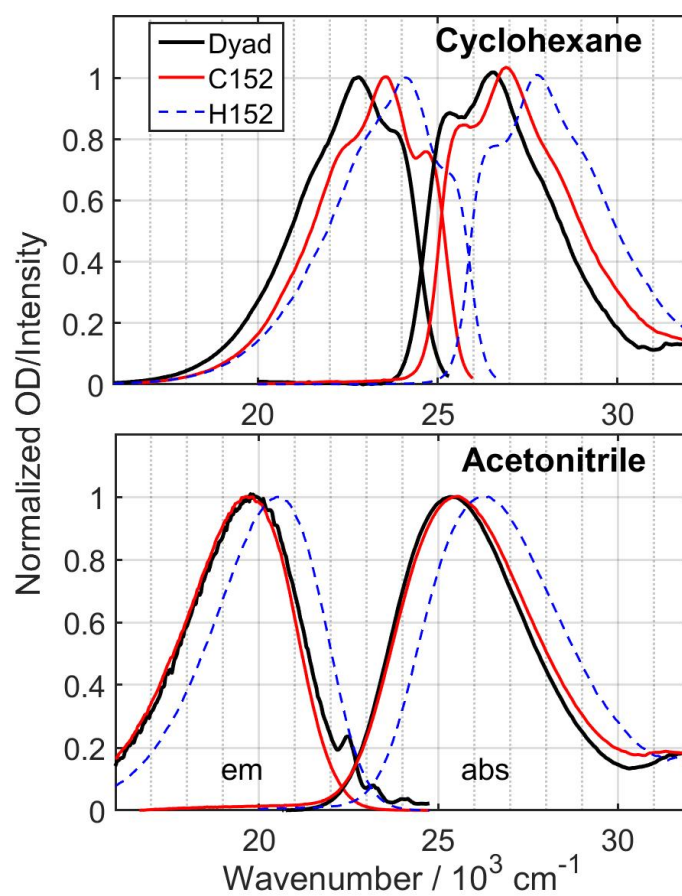


Figure 3.6: Normalized absorption and emission spectra of the dyad (black) and reference fluorophores C152 (red) and H152 (blue dashed) in (a) cyclohexane and (b) acetonitrile.

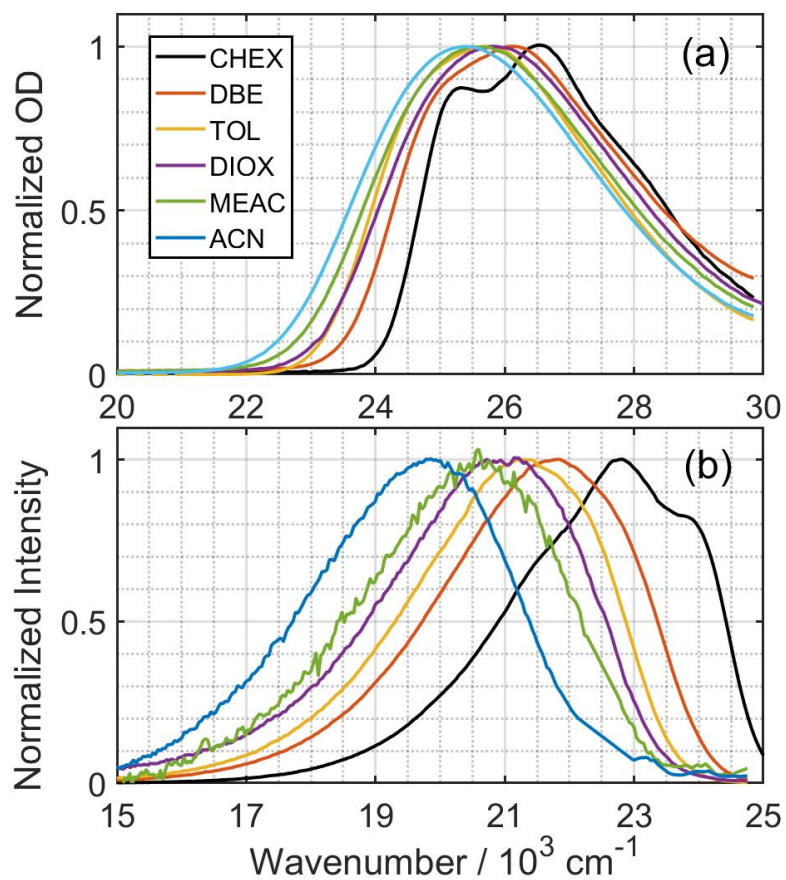


Figure 3.7: Normalized absorption (a) and emission (b) spectra of the dyad in selected solvents: cyclohexane (CHEX), dibutyl ether (DBE), toluene (TOL), 1,4-dioxane (DIOX), methyl acetate (MEAC) and acetonitrile (ACN).

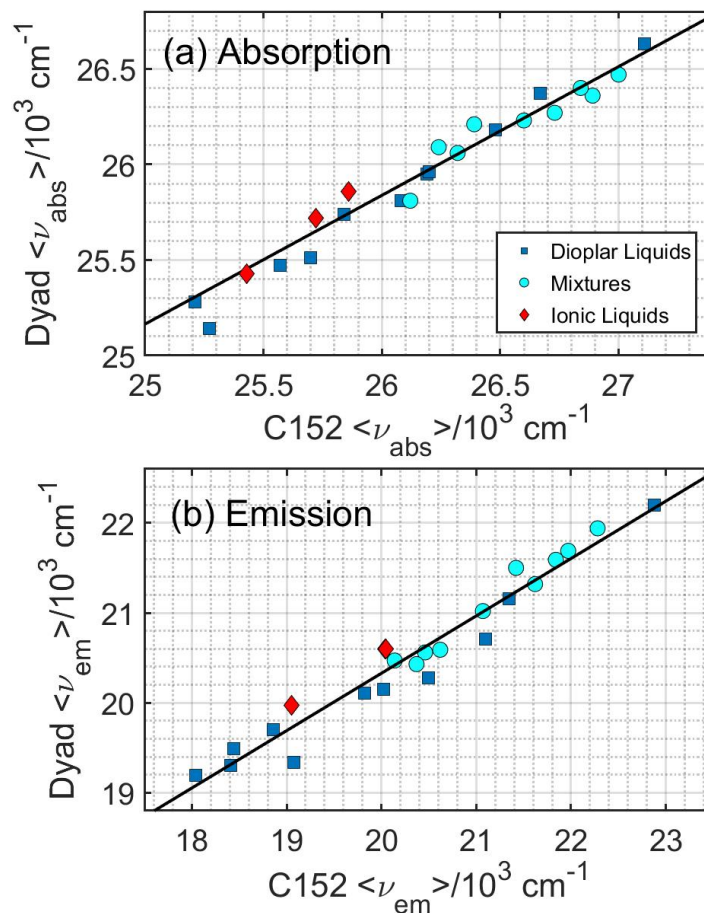


Figure 3.8: Correlation of the average absorption and emission (b) frequencies of the dyad with those of C152. The regressions shown are: (a) $\langle \nu \rangle_{\text{dyad}} = 0.71 \langle \nu \rangle_{\text{C152}} + 7.29$ ($N=24$, $R^2=0.92$) and (b) $\langle \nu \rangle_{\text{dyad}} = 0.64 \langle \nu \rangle_{\text{C152}} + 7.57$ ($N=24$, $R^2=0.95$).

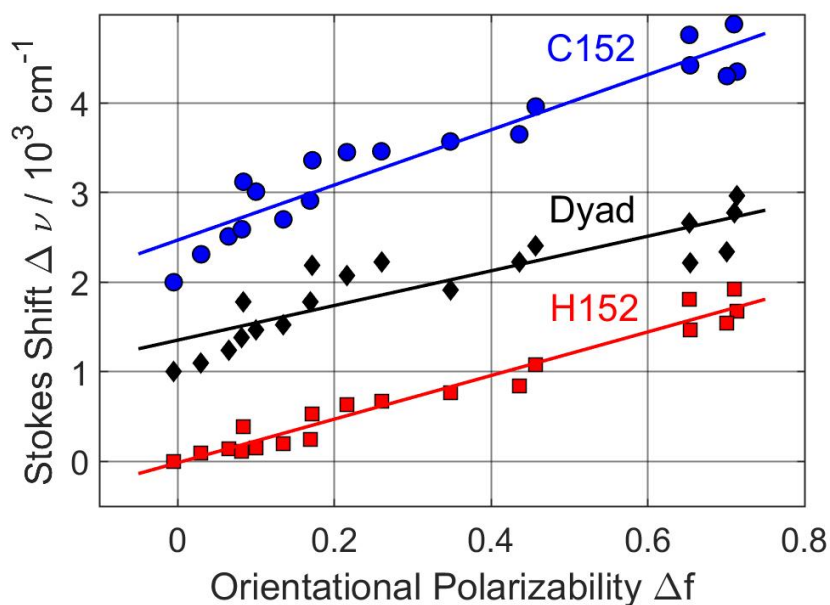


Figure 3.9: Lippert-Mataga plots of the Stokes shifts $\Delta \nu = \nu_{abs} - \nu_{em}$ of the three fluorophores vs solvent orientational polarizability, Δf , defined in Eq. 2. All Stokes shifts are relative to the value of each probe in cyclohexane, and values for the dyad and C152 are vertically displaced by 1000 and 2000 cm^{-1} for clarity. Data in the quadrupolar solvents (toluene and dioxane) and ionic liquids are omitted from these correlations. In binary solvent mixtures, Δf is assumed to be the volume-weighted average of the values of Δf of the pure solvents.

Table 3.1: S_1 - S_0 Dipole Difference Estimates from Solvatochromic Analysis and DFT Calculations

Solute	A. Solvatochromic Analysis			B. DFT Calculations			
	$\Delta\nu / \Delta f$ / 10^3 cm^{-1}	a_{eff} / \AA	$\Delta\mu$ / D	$\mu(S_0)$ / D	$\mu(S_1)$ / D	$\mu(S_2)$ / D	$ \Delta\vec{\mu}_{10} $ / D
C152	3.08	5.43	7.0 ± 0.5	7.79	13.23	11.21	5.53
H152	2.43	5.28	6.0 ± 0.5	7.45	12.48	10.93	5.10
dyad	1.94	6.35	7.0 ± 0.9	8.6- 11	13-17	30-39	5.6-6.6

A. $\Delta\nu / \Delta f$ is the slope of the fit to Eq. 1.

B. Calculated values are from gas-phase CAM-B3LYP/6-311++G(d,p) calculations. Geometries were optimized for the ground state and excited-state values derived from TDDFT calculations at these S_0 geometries. For the dyad, a number of representative conformations were selected, and the range of values obtained from these conformers is tabulated.

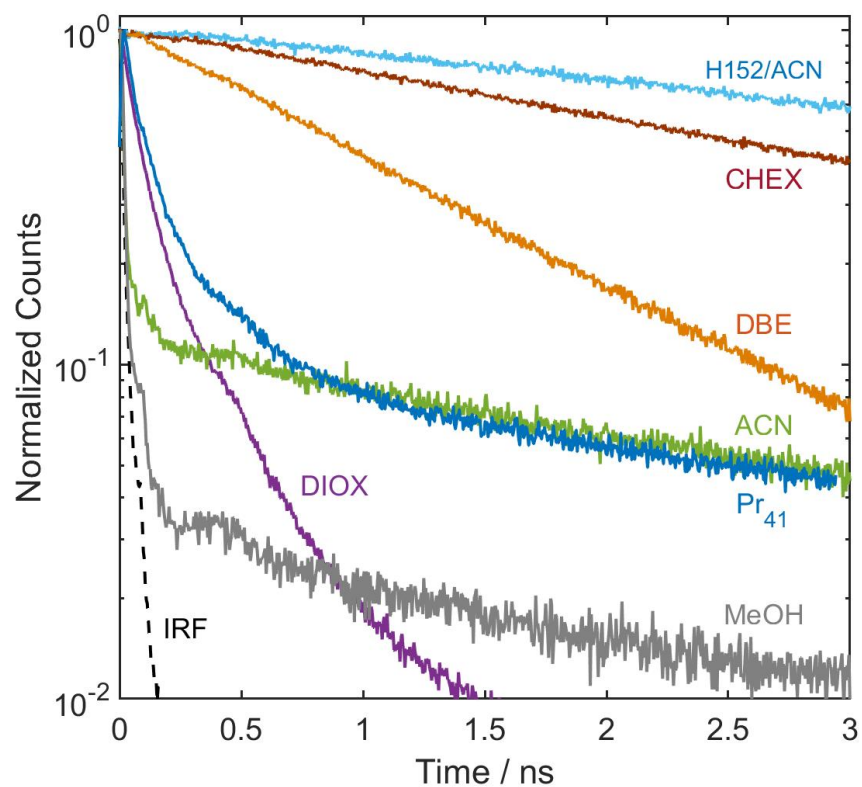


Figure 3.10: Fluorescence (TCSPC) decays of the dyad in selected solvents. The uppermost curve is an H152 decay, shown for comparison. Solvents abbreviations are defined in Table 2. IRF denotes the instrument response function of the TCSPC instrument.

Table 3.2: Multi-Exponential Representations of Dyad Emission Decays and ET Rate Constants

A. TCSPC Measurements

Solvent	a ₁	a ₂	a ₃	a ₄	τ_1 / ps	τ_2 / ps	τ_3 / ps	τ_4 / ns	τ_{H152} / ns	τ_{C152} / ns	$\langle \tau \rangle_{dyad}$ / ps	$k_{ET}^{(1)}$ / s ⁻¹	$k_{ET}^{(2)}$ / s ⁻¹
Cyclohexane (CHEX)	1.00	-	-		3183		-		3.7	4.1	3183	6.9×10^7	6.9×10^7
50/50 vol% CHEX+DBE	0.22	0.77	-	0.02	21	1956	-	(3.9)	3.9	3.8	1531	3.9×10^8	1.1×10^{10}
Dibutyl Ether (DBE)	0.21	0.78	-	0.01	529	1148	-	(4.1)	4.1	4.8	1014	7.8×10^8	8.8×10^8
Toluene (TOL)	0.26	0.69	-	0.05	216	1091	-	(3.9)	3.9	4.4	855	9.4×10^8	1.7×10^9
50/50 vol% CHEX+THF	0.83	0.16	-	0.01	63	170	-	(4.5)	4.5	4.7	81	1.2×10^{10}	1.4×10^{10}
1,4-Dioxane (DIOX)	0.59	0.36	0.05	0.004	32	135	477	(4.7)	4.7	4.9	92	1.1×10^{10}	2.1×10^{10}
Tetrahydrofuran (THF)	0.97	0.02	-	0.004	8	104	-	(4.8)	4.8	5.4	10	1.0×10^{11}	1.3×10^{11}
Ethylene Glycol (EG)	0.97	0.02	-	0.02	18	980	-	(4.4)	4.4	1.1	34	2.8×10^{10}	5.5×10^{10}
[N ₈₈₈₁][Tf ₂ N] (N ₈₈₈₁)	0.093	0.91	-	-	1123	5001	-	-	5.1	4.8	-	$<10^7$	
[P _{14,666}][Tf ₂ N] (P _{14,666})	0.10	0.90	-	-	1201	4921	-	-	4.8	4.5	-	$<10^7$	
[Pr ₄₁][Tf ₂ N] (Pr ₄₁)	0.64	0.30	0.02	0.04	12	105	2138	(5.2)	5.2	3.4	88	1.1×10^{10}	5.8×10^{10}

B. KGE Measurements

Solvent	a ₁	a ₂	a ₃	τ_1 / ps	τ_2 / ps	τ_3 / ps	$\langle \tau \rangle_{dyad}$ / ps	τ_{H152} / ns	τ_{C152} / ns	$k_{ET}^{(1)}$ / s ⁻¹	$k_{ET}^{(2)}$ / s ⁻¹
Methyl Acetate (MEAC)	0.47	0.49	0.04	0.3	1.9	42	2.2	5.0	4.8	1.5×10^{11}	2.2×10^{11}
Propylene Carbonate (PC)	0.56	0.40	0.05	0.4	2.3	39	3.0	5.5	2.0	3.4×10^{11}	1.9×10^{12}
Dimethylsulfoxide (DMSO)	0.56	0.40	0.04	0.1	0.9	64	2.8	5.0	0.97	3.4×10^{11}	1.6×10^{12}
Acetonitrile (ACN)	0.39	0.55	0.06	2.0	10	50	3.6	5.4	2.1	3.5×10^{11}	4.2×10^{12}
Methanol (MeOH)	0.23	0.73	0.04	3.8	10	43	5.0	4.9	0.96	2.3×10^{11}	6.4×10^{11}

Fits are to the function $\sum_i a_i \exp(-t/\tau_i)$ with $\sum_i a_i = 1$. TCSPC decays were measured at the steady-state emission whereas the KGE fits show the average time dependence of the peak height and integrated intensity of the emission band. $\langle \tau \rangle_{dyad}$ is the average decay time of the dyad $\sum_i' a_i \exp(-t/\tau_i) / \sum_i' a_i$ where the prime denotes exclusion of component 4, which is assumed to be due to emission from H152 impurity. $k_{ET}^{(1)}$ and $k_{ET}^{(2)}$ are estimated rates of electron transfer calculated according to Eqs. 3.3-3.4.

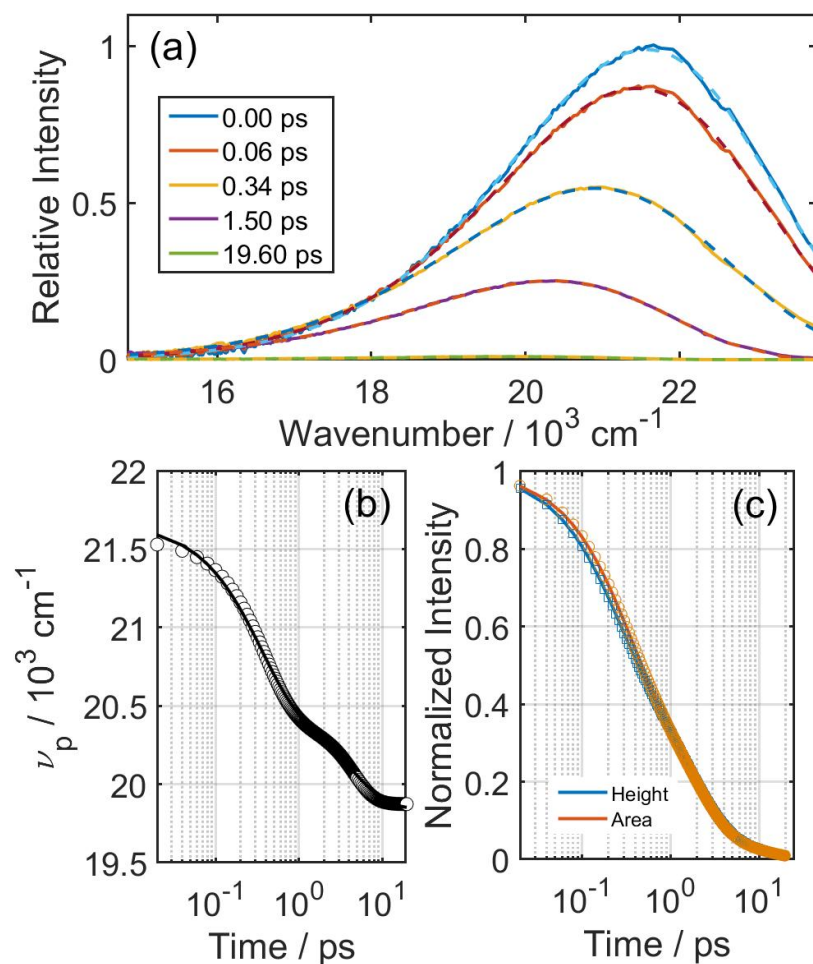


Figure 3.11: A representative KGE data set of the dyad in propylene carbonate. (a) Time-resolved spectra (solid curves) and lognormal fits (dashed). (b) The peak frequency and (c) the normalized peak height and integrated area. Symbols in panels (b) and (c) are the KGE data and the curves are multi-exponential fits.

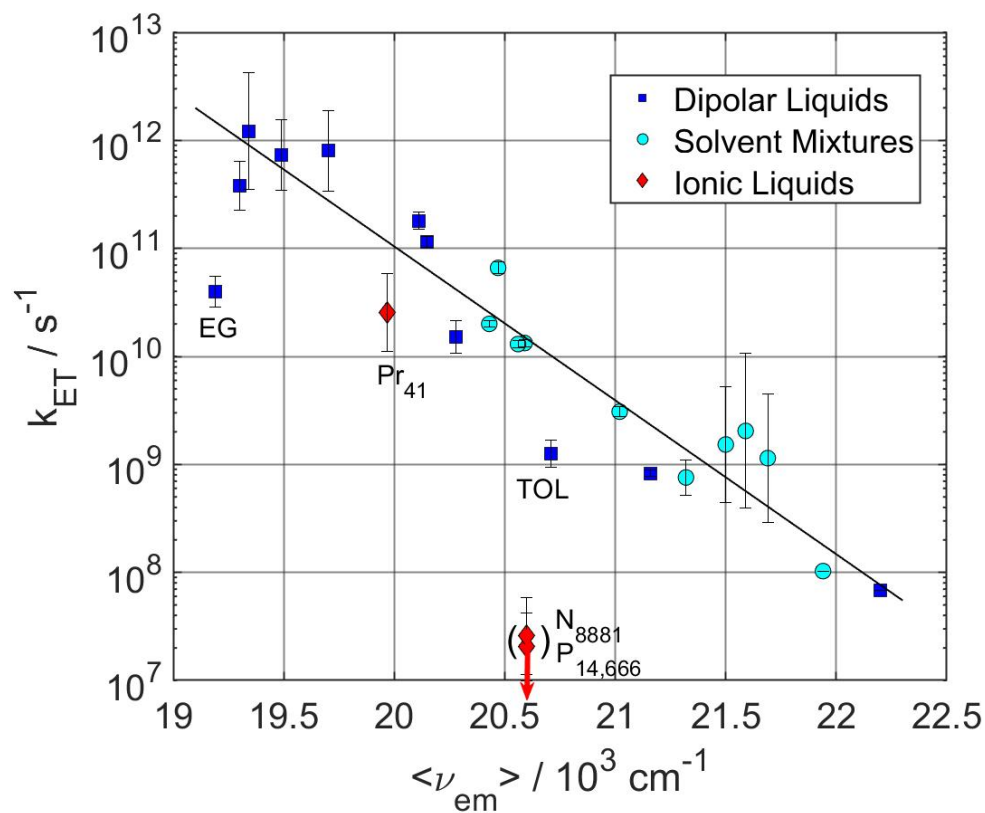


Figure 3.12: Electron transfer rate constants of the dyad plotted versus emission frequency.

Points denote the logarithmic average of $k_{ET}^{(1)}$ and $k_{ET}^{(2)}$, and the ends of the error bars their individual values. Electron transfer in the ionic liquids $[N_{8881}][Tf_2N]$ and $[P_{14,666}][Tf_2N]$ is too slow to be measured, even at 353 K and the points plotted are only upper limits.

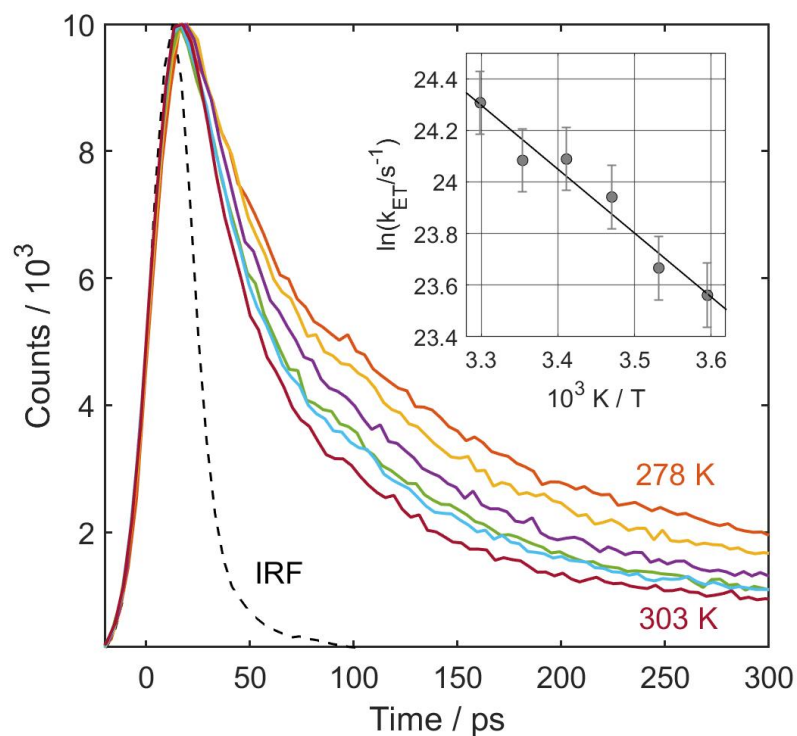


Figure 3.13: TCSPC emission decays of the dyad in [Pr₄₁][Tf₂N] as a function of temperature. The inset shows the electron transfer rates derived from these decays in an Arrhenius format. The fit shown is $\ln(k_{ET} / \text{s}^{-1}) = 32.5 - 2.48(10^3 \text{ K} / T)$.

References

1. D. R. MacFarlane, N. Tachikawa, M. Forsyth, J. M. Pringle, P. C. Howlett, G. D. Elliott, J. H. Davis, M. Watanabe, P. Simon, and C. A. Angell, "Energy applications of ionic liquids," *Energy Environ. Sci.* **7**, 232-250 (2014). 10.1039/c3ee42099j
2. M. Watanabe, M. L. Thomas, S. Zhang, K. Ueno, T. Yasuda, and K. Dokko, "Application of Ionic Liquids to Energy Storage and Conversion Materials and Devices," *Chemical Reviews (Washington, DC, United States)* **117**, 7190-7239 (2017). 10.1021/acs.chemrev.6b00504
3. J. P. Hallett and T. Welton, "Room-Temperature Ionic Liquids: Solvents for Synthesis and Catalysis. 2," *Chem. Rev.* **111**, 3508-3576 (2011). 10.1021/cr1003248
4. T. Welton, "Ionic liquids: a brief history," *Biophys. Rev.* **10**, 691-706 (2018). 10.1007/s12551-018-0419-2
5. A. Samanta, "Solvation Dynamics in Ionic Liquids: What We Have Learned from the Dynamic Fluorescence Stokes Shift Studies," *J. Phys. Chem. Lett.* **1**, 1557-1562 (2010). 10.1021/jz100273b
6. E. W. Castner, Jr., C. J. Margulis, M. Maroncelli, and F. Wishart James, "Ionic Liquids: Structure and Photochemical Reactivity," *Annual Reviews of Physical Chemistry* **62**, 85-105 (2011). 10.1146/annurev-physchem-032210-103421
7. X.-X. Zhang, M. Liang, N. P. Ernstring, and M. Maroncelli, "Complete Solvation Response of Coumarin 153 in Ionic Liquids," *J. Phys. Chem. B* **117**, 4291-4304 (2013). 10.1021/jp305430a
8. C. M. Gordon and A. J. McLean, "Photoelectron transfer from excited-state ruthenium(II) tris(bipyridyl) to methylviologen in an ionic liquid," *Chemical Communications*, 1395-1396 (2000).
9. A. J. McLean, M. J. Muldoon, C. M. Gordon, and I. R. Dunkin, "Bimolecular rate constants for diffusion in ionic liquids," *Chem. Comm.*, 1880-1881 (2002).
10. A. Skrzypczak and P. Neta, "Diffusion-Controlled Electron-Transfer Reactions in Ionic Liquids," *J. Phys. Chem. A* **107**, 7800-7803 (2003).
11. R. C. Vieira and D. E. Falvey, "Photoinduced Electron-Transfer Reactions in Two Room-Temperature Ionic Liquids: 1-Butyl-3-methylimidazolium Hexafluorophosphate and 1-Octyl-3-methylimidazolium Hexafluorophosphate," *J. Phys. Chem. B* **111**, 5023-5029 (2007).
12. S. Sarkar, R. Pramanik, D. Seth, P. Setua, and N. Sarkar, "Photoinduced electron transfer (PET) from N,N-dimethylaniline to 7-amino Coumarin dyes in a room temperature ionic liquid (RTIL): Slowing down of electron transfer rate compared to conventional solvent," *Chem. Phys. Lett.* **477**, 102-108 (2009). 10.1016/j.cplett.2009.06.077
13. M. Liang, A. Kaintz, G. A. Baker, and M. Maroncelli, "Bimolecular Electron Transfer in Ionic Liquids: Are Reaction Rates Anomalously High?," *J. Phys. Chem. B* **116**, 1370-1384 (2012). 10.1021/jp210892c
14. A. Kaintz, "Translational and Rotational Diffusion in Ionic Liquids," PhD, The Pennsylvania State University, 2013.

15. M. Koch, A. Rosspeintner, G. Angulo, and E. Vauthey, "Bimolecular Photoinduced Electron Transfer in Imidazolium-Based Room-Temperature Ionic Liquids Is Not Faster than in Conventional Solvents," *J. Am. Chem. Soc.* **134**, 3729-3736 (2012). 10.1021/ja208265x
16. S. Sarkar, S. Mandal, R. Pramanik, C. Ghatak, V. G. Rao, and N. Sarkar, "Photoinduced Electron Transfer in a Room Temperature Ionic Liquid 1-Butyl-3-methylimidazolium Octyl Sulfate Micelle: A Temperature Dependent Study," *J. Chem. Phys. B* **115**, 6100-6110 (2011).
17. S. Sarkar, S. Mandal, C. Ghatak, V. G. Rao, S. Ghosh, and N. Sarkar, "Photoinduced Electron Transfer in an Imidazolium Ionic Liquid and in Its Binary Mixtures with Water, Methanol, and 2-Propanol: Appearance of Marcus-Type of Inversion," *J. Phys. Chem. B* **116**, 1335-1344 (2012). 10.1021/jp2075995
18. A. K. Das, T. Mondal, M. S. Sen, and K. Bhattacharyya, "Marcus-like Inversion in Electron Transfer in Neat Ionic Liquid and Ionic Liquid-Mixed Micelles," *J. Phys. Chem. B* **115**, 4680-4688 (2011). 10.1021/jp200941c
19. M. Kumbhakar, A. Manna, M. Sayed, A. Kumar, and H. Pal, "Observation of the Marcus inverted region for bimolecular photoinduced electron-transfer reactions in viscous media," *J. Phys. Chem. B* **118**, 10704-10715 (2014). 10.1021/jp506885r
20. A. Chakraborty, D. Chakrabarty, P. Hazra, D. Seth, and N. Sarkar, "Photoinduced intermolecular electron transfer between Coumarin dyes and electron donating solvents in cetyltrimethylammonium bromide (CTAB) micelles: evidence for Marcus inverted region," *Chem. Phys. Lett.* **382**, 508-517 (2003). 10.1016/j.cplett.2003.10.105
21. A. Chakraborty, D. Chakrabarty, D. Seth, P. Hazra, and N. Sarkar, "Photoinduced intermolecular electron-transfer from electron donating solvents to Coumarin dyes in bile salt aggregates: Role of diffusion in electron transfer reaction," *Spectrochim. Acta, Part A* **63A**, 594-602 (2006). 10.1016/j.saa.2005.06.006
22. M. Kumbhakar, S. Nath, T. Mukherjee, and H. Pal, "Intermolecular electron transfer between coumarin dyes and aromatic amines in Triton-X-100 micellar solutions: Evidence for Marcus inverted region," *J. Chem. Phys.* **120**, 2824-2834 (2004). 10.1063/1.1638739
23. S. Dutta Choudhury, M. Kumbhakar, S. Nath, S. K. Sarkar, T. Mukherjee, and H. Pal, "Compartmentalization of reactants in different regions of sodium 1,4-bis(2-ethylhexyl)sulfosuccinate/heptane/water reverse micelles and its influence on bimolecular electron-transfer kinetics," *J. Phys. Chem. B* **111**, 8842-8853 (2007). 10.1021/jp0722004
24. P. Samanta, S. Rane, P. Bahadur, S. Dutta Choudhury, and H. Pal, "Tetronic Star Block Copolymer Micelles: Photophysical Characterization of Microenvironments and Applicability for Tuning Electron Transfer Reactions," *J. Phys. Chem. B* **122**, 6079-6093 (2018). 10.1021/acs.jpcc.8b01778
25. A. Rosspeintner, M. Koch, G. Angulo, and E. Vauthey, "Spurious Observation of the Marcus Inverted Region in Bimolecular Photoinduced Electron Transfer," *J. Am. Chem. Soc.* **134**, 11396-11399 (2012). 10.1021/ja3049095
26. G. Angulo, A. Rosspeintner, M. Koch, and E. Vauthey, "Comment on "Observation of the Marcus Inverted Region for Bimolecular Photoinduced Electron-Transfer Reactions in Viscous Media"," *J. Phys. Chem. B* **120**, 9800-9803 (2016). 10.1021/acs.jpcc.6b06610

27. M. Kumbhakar and H. Pal, "Reply to 'Comment on 'Observation of the Marcus Inverted Region for Bimolecular Photoinduced Electron-Transfer Reactions in Viscous Media'", " *J. Phys. Chem. B* **120**, 9804-9809 (2016). 10.1021/acs.jpcc.6b07633
28. P. Mukherjee, A. Das, A. Sengupta, and P. Sen, "Bimolecular Photoinduced Electron Transfer in Static Quenching Regime: Illustration of Marcus Inversion in Micelle," *J. Phys. Chem. B* **121**, 1610-1622 (2017). 10.1021/acs.jpcc.6b11206
29. B. Wu, M. Maroncelli, and E. W. Castner, "Photoinduced Bimolecular Electron Transfer in Ionic Liquids," *J. Am. Chem. Soc.* **139**, 14568-14585 (2017). 10.1021/jacs.7b07611
30. B. Wu, M. Liang, N. Zmich, J. Hatcher, S. I. Lall-Ramnarine, J. F. Wishart, M. Maroncelli, and E. W. Castner, Jr., "Photoinduced Bimolecular Electron Transfer in Ionic Liquids: Cationic Electron Donors," *J. Phys. Chem. B* **122**, 2379-2388 (2018). 10.1021/acs.jpcc.7b12542
31. Y. Nagasawa and H. Miyasaka, "Ultrafast solvation dynamics and charge transfer reactions in room temperature ionic liquids," *Phys. Chem. Chem. Phys.* **16**, 13008-13026 (2014). 10.1039/c3cp55465a
32. J. V. Lockard and M. R. Wasielewski, "Intramolecular Electron Transfer within a Covalent, Fixed-Distance Donor-Acceptor Molecule in an Ionic Liquid," *J. Phys. Chem. B* **111**, 11638-11641 (2007).
33. N. Banerji, G. Angulo, I. Barabanov, and E. Vauthey, "Intramolecular Charge-Transfer Dynamics in Covalently Linked Perylene-Dimethylaniline and Cyanoperylene-Dimethylaniline," *J. Phys. Chem. A* **112**, 9665-9674 (2008).
34. D. C. Khara, A. Paul, K. Santhosh, and A. Samanta, "Excited state dynamics of 9,9'-bianthryl in room temperature ionic liquids as revealed by picosecond time-resolved fluorescence study," *J. Chem. Sci. (Bangalore)* **121**, 309-315 (2009).
35. Y. Nagasawa, A. Oishi, T. Itoh, M. Yasuda, M. Muramatsu, Y. Ishibashi, S. Ito, and H. Miyasaka, "Dynamic Stokes Shift of 9,9'-Bianthryl in Ionic Liquids: A Temperature Dependence Study," *Journal of Physical Chemistry C* **113**, 11868-11876 (2009).
36. K. Santhosh, S. Banerjee, N. Rangaraj, and A. Samanta, "Fluorescence response of 4-(N,N'-Dimethylamino)benzonitrile in room temperature ionic liquids: observation of photobleaching under mild excitation condition and multiphoton confocal microscopic study of the fluorescence recovery dynamics," *J. Phys. Chem. B* **114**, 1967-1974 (2010).
37. K. Santhosh and A. Samanta, "Modulation of the Excited State Intramolecular Electron Transfer Reaction and Dual Fluorescence of Crystal Violet Lactone in Room Temperature Ionic Liquids," *J. Phys. Chem. B* **114**, 9195-9200 (2010).
38. H. Wu, H. Wang, L. Xue, Y. Shi, and X. Li, "Hindered Intramolecular Electron Transfer in Room-Temperature Ionic Liquid," *J. Phys. Chem. B* **114**, 14420-14425 (2010). 10.1021/jp101240a
39. C. Khurmi and M. A. Berg, "Dispersed Kinetics without Rate Heterogeneity in an Ionic Liquid Measured with Multiple Population-Period Transient Spectroscopy," *J. Phys. Chem. Lett.* **1**, 161-164 (2010). 10.1021/jz900141a
40. X. Li, M. Liang, A. Chakraborty, M. Kondo, and M. Maroncelli, "Solvent-Controlled Intramolecular Electron Transfer in Ionic Liquids," *J. Phys. Chem. B* **115**, 6592-6607 (2011). 10.1021/jp200339e

41. M. Muramatsu, T. Katayama, S. Ito, Y. Nagasawa, D. Matsuo, Y. Suzuma, L. Peng, A. Orita, J. Otera, and H. Miyasaka, "Photoinduced charge-transfer dynamics of sequentially aligned donor-acceptor systems in an ionic liquid," *Photochem. Photobiol. Sci.* **12**, 1885-1894 (2013). 10.1039/c3pp50198a
42. H. Y. Lee, J. B. Issa, S. S. Isied, E. W. Castner, Jr., Y. Pan, C. L. Hussey, K. S. Lee, and J. F. Wishart, "A Comparison of Electron-Transfer Dynamics in Ionic Liquids and Neutral Solvents," *J. Phys. Chem. C* **116**, 5197-5208 (2012). 10.1021/jp208852r
43. J. A. DeVine, M. Labib, M. E. Harries, R. A. M. Rached, J. Issa, J. F. Wishart, and E. W. Castner, "Electron-Transfer Dynamics for a Donor-Bridge-Acceptor Complex in Ionic Liquids," *J. Phys. Chem. B* **119**, 11336-11345 (2015). 10.1021/acs.jpcc.5b03320
44. E. Takeuchi, M. Muramatsu, T. Katayama, Y. Yoneda, S. Ito, Y. Nagasawa, and H. Miyasaka, "Sub-100 fs Charge Separation and Subsequent Diffusive Solvation Observed for Asymmetric Bianthryl Derivative in Ionic Liquid," *J. Phys. Chem. C* **120**, 14502-14512 (2016). 10.1021/acs.jpcc.6b03593
45. C. A. Rumble and M. Maroncelli, "Solvent controlled intramolecular electron transfer in mixtures of 1-butyl-3-methylimidazolium tetrafluoroborate and acetonitrile," *J. Chem. Phys.* **148**, 193801/193801-193801/193807 (2018). 10.1063/1.5000727
46. H. Jin, X. Li, and M. Maroncelli, "Heterogeneous Solute Dynamics in Room-Temperature Ionic Liquids," *J. Phys. Chem. B* **111**, 13473-13478 (2007).
47. K. Sahu, S. J. Kern, and M. A. Berg, "Heterogeneous reaction rates in an ionic liquid: quantitative results from two-dimensional multiple population-period transient spectroscopy," *J. Phys. Chem. A* **115**, 7984-7993 (2011).
48. S. Nad and H. Pal, "Electron Transfer from Aromatic Amines to Excited Coumarin Dyes: Fluorescence Quenching and Picosecond Transient Absorption Studies," *J. Phys. Chem. A* **104**, 673-680 (2000). 10.1021/jp993206z
49. S. Yuan, Y. Zhang, R. Lu, and A. Yu, "Photoinduced electron transfer between coumarin dyes and N,N-dimethylaniline in imidazolium based room temperature ionic liquids: Effect of the cation's alkyl chain length on the bimolecular photoinduced electron transfer process," *J. Photochem. Photobiol., A* **260**, 39-49 (2013). 10.1016/j.jphotochem.2013.03.013
50. K. Yoshihara, K. Tominaga, and Y. Nagasawa, "Effects of the solvent dynamics and vibrational motions in electron transfer," *Bull. Chem. Soc. Jpn.* **68**, 696-712 (1995). 10.1246/bcsj.68.696
51. H. Shirota, H. Pal, K. Tominaga, and K. Yoshihara, "Substituent Effect and Deuterium Isotope Effect of Ultrafast Intermolecular Electron Transfer: Coumarin in Electron-Donating Solvent," *Journal of Physical Chemistry A* **102**, 3089-3102 (1998).
52. E. W. J. Castner, D. Kennedy, and R. J. Cave, "Solvent as Electron Donor: Donor/Acceptor Electronic Coupling Is a Dynamical Variable," *J. Phys. Chem. A* **104**, 2869-2885 (2000).
53. C.-S. Tsai, P.-Y. Liu, H.-Y. Yen, T.-L. Hsu, and C.-H. Wong, "Development of trifunctional probes for glycoproteomic analysis," *Chem. Comm.* **46**, 5575-5577 (2010). 10.1039/c0cc00345j
54. H. Jin, B. O'Hare, J. Dong, S. Arzhantsev, G. A. Baker, J. F. Wishart, A. Benesi, and M. Maroncelli, "Physical Properties of Ionic Liquids Consisting of the 1-Butyl-3-

- Methylimidazolium Cation with Various Anions and the Bis(trifluoromethylsulfonyl)imide Anion with Various Cations," *J. Phys. Chem. B* **112**, 81-92 (2008).
55. J. A. Gardecki and M. Maroncelli, "A Set of Secondary Emission Standards for Calibration of Spectral Responsivity in Emission Spectroscopy," *Appl. Spectrosc.* **52**, 1179-1189 (1998).
 56. J. Breffke, B. W. Williams, and M. Maroncelli, "The Photophysics of Three Naphthylmethylene Malononitriles," *J. Phys. Chem. B* **119**, 9254-9267 (2015). 10.1021/jp509882q
 57. S. Arzhantsev and M. Maroncelli, "Design and characterization of a femtosecond fluorescence spectrometer based on optical Kerr gating," *Appl. Spectrosc.* **59**, 206-220 (2005). 10.1366/0003702053085007
 58. C. A. Rumble, J. Breffke, and M. Maroncelli, "Solvation Dynamics and Proton Transfer in Diethylaminohydroxyflavone," *J. Phys. Chem. B* **121**, 630-637 (2017). 10.1021/acs.jpcc.6b12146
 59. M. J. Abraham, R. Schultz, S. Páll, J. C. Smith, B. Hess, and E. Lindahl, "GROMACS: High Performance Molecular Simulations through Multi-Level Parallelism from Laptops to Supercomputers," *Software X* **1**, 19-25 (2015).
 60. J. Wang, R. M. Wolf, J. W. Caldwell, P. A. Kollman, and D. A. Case, "Development and testing of a general Amber force field," *J. Comput. Chem.* **25**, 1157-1174 (2004). 10.1002/jcc.20035
 61. L. E. Chirlian and M. M. Francl, "Atomic charges derived from electrostatic potentials: a detailed study," *J. Comput. Chem.* **8**, 894-905 (1987). 10.1002/jcc.540080616
 62. Gaussian09, M. J. Frisch, G. W. Trucks, H. B. Schlegel, G. E. Scuseria, M. A. Robb, J. R. Cheeseman, G. Scalmani, V. Barone, G. A. Petersson, H. Nakatsuji, X. Li, M. Caricato, A. Marenich, J. Bloino, B. G. Janesko, R. Gomperts, B. Mennucci, H. P. Hratchian, J. V. Ortiz, A. F. Izmaylov, J. L. Sonnenberg, D. Williams-Young, F. Ding, F. Lipparini, F. Egidi, J. Goings, B. Peng, A. Petrone, T. Henderson, D. Ranasinghe, V. G. Zakrzewski, J. Gao, N. Rega, G. Zheng, W. Liang, M. Hada, M. Ehara, K. Toyota, R. Fukuda, J. Hasegawa, M. Ishida, T. Nakajima, Y. Honda, O. Kitao, H. Nakai, T. Vreven, K. Throssell, J. J. A. Montgomery, J. E. Peralta, F. Ogliaro, M. Bearpark, J. J. Heyd, E. Brothers, K. N. Kudin, V. N. Staroverov, T. Keith, R. Kobayashi, J. Normand, K. Raghavachari, A. Rendell, J. C. Burant, S. S. Iyengar, J. Tomasi, M. Cossi, J. M. Millam, M. Klene, C. Adamo, R. Cammi, J. W. Ochterski, R. L. Martin, K. Morokuma, O. Farkas, J. B. Foresman, and D. J. Fox, (Gaussian, Inc., Wallingford, CT, 2013).
 63. AMBER, D. A. Case, D. S. Cerutti, I. Cheatham, T. E., T. A. Darden, R. E. Duke, T. J. Giese, H. Gohlke, A. W. Goetz, D. Green, N. Homeyer, S. Izadi, A. Kovalenko, T. S. Lee, S. LeGrand, P. Li, C. Lin, J. Liu, T. Lunchko, R. Luo, D. Mermelstein, K. M. Merz, G. Monard, H. Nguyen, I. Omelyan, A. Onufriev, F. Pan, R. Qi, D. R. Roe, A. Roitberg, C. Sagui, C. L. Simmerling, W. M. Botello-Smith, J. Swails, R. C. Walker, J. Wang, R. M. Wolf, X. Wu, L. Xiao, D. M. York, and P. A. Kollman, (University of California, San Francisco, 2017).
 64. A. W. Sousa de Silva and W. F. Vranken, "ACPYPE - AnteChamber PYthon Parser InterfacE.," *BMC Res. Notse* **5** (2012).
 65. U. Essmann, L. Perera, M. L. Berkowitz, T. Darden, H. Lee, and L. G. Pedersen, "A smooth particle mesh Ewald method," *J. Chem. Phys.* **103**, 8577-8593 (1995). 10.1063/1.470117

66. B. Hess, "P-LINCS: A Parallel Linear Constraint Solver for Molecular Simulation," *J. Chem. Theory Comput.* **4**, 116-122 (2008). 10.1021/ct700200b
67. G. Bussi, D. Donadio, and M. Parrinello, "Canonical sampling through velocity rescaling," *J. Chem. Phys.* **126**, 014101/014101-014101/014107 (2007). 10.1063/1.2408420
68. MacroModel 11, Schrödinger Release 2019-2: MacroModel, Schrödinger, LLC, New York, NY, 2019.
69. O. S. Wenger, "How Donor-Bridge-Acceptor Energetics Influence Electron Tunneling Dynamics and Their Distance Dependences," *Acc. Chem. Res.* **44**, 25-35 (2011). 10.1021/ar100092v
70. C. Guo and Y. Feng, "Solvent and substituent effects on intramolecular charge transfer of selected derivatives of 4-trifluoromethyl-7-aminocoumarin," *J. Chem. Soc., Faraday Trans. I* **83**, 2533-2539 (1987).
71. K. Rechthaler and G. Koehler, "Excited state properties and deactivation pathways of 7-aminocoumarins," *Chem. Phys.* **189**, 99-116 (1994). 10.1016/0301-0104(94)80010-3
72. S. Nad, M. Kumbhakar, and H. Pal, "Photophysical properties of Coumarin-152 and Coumarin-481 dyes: unusual behavior in nonpolar and in higher polarity solvents," *J. Phys. Chem. A* **107**, 4808-4816 (2003). 10.1021/jp021543t
73. G. Jones, II, W. R. Jackson, C. Y. Choi, and W. R. Bergmark, "Solvent effects on emission yield and lifetime for coumarin laser dyes. Requirements for a rotatory decay mechanism," *J. Phys. Chem.* **89**, 294-300 (1985). 10.1021/j100248a024
74. M. L. Horng, J. A. Gardecki, A. Papazyan, and M. Maroncelli, "Subpicosecond Measurements of Polar Solvation Dynamics: Coumarin 153 Revisited," *J. Phys. Chem.* **99**, 17311-17337 (1995). 10.1021/j100048a004
75. In some mixtures and ionic liquids these fluorophores are show slightly non-exponential decays, presumably due to some effect of solvation dynamics.
76. P. Dahiya, M. Kumbhakar, T. Mukherjee, and H. Pal, "Effect of protic solvents on twisted intramolecular charge transfer state formation in coumarin-152 and coumarin-481 dyes," *Chem. Phys. Lett.* **414**, 148-154 (2005). 10.1016/j.cplett.2005.08.051
77. R. Letrun and E. Vauthey, "Excitation Wavelength Dependence of the Dynamics of Bimolecular Photoinduced Electron Transfer Reactions," *J. Phys. Chem. Lett.* **5**, 1685-1690 (2014). 10.1021/jz500569r
78. M. Kumbhakar, A. Manna, M. Sayed, A. Kumar, and H. Pal, "Observation of the Marcus Inverted Region for Bimolecular Photoinduced Electron-Transfer Reactions in Viscous Media," *I18* **36** (2014).

Chapter 4

Electron Transfer Kinetics Between an Electron Accepting Ionic Liquid and Coumarin Dyes

Co-author contributions: Cyclic voltammetry measurements were performed by Christopher Gray.

4.1 Introduction

Ionic liquids are emerging as possible replacements for conventional liquids in variety of applications,^{1,2} for example, as electrolytes in energy-related technologies such as fuel cells, batteries, and solar cells.^{3,4} Advantageous characteristics of ionic liquids in the latter context are their intrinsic conductivities, low volatilities, and wide electrochemical windows, all of which can potentially be tuned through proper choice of cation and anion pairings. Partially in support of these applications, there has been a considerable amount of study of electron transfer reactions in ionic liquids, particularly the kinetics of photoinduced electron transfer (PET), with a focus on how PET differs in a purely ionic environment compared to conventional dipolar liquids.

As in conventional solvents, most initial studies of PET in ionic liquids focused on bimolecular reactions. If electron transfer is sufficiently rapid upon reactant contact, the rate of diffusion limits the overall rate of such bimolecular reactions to roughly $10^{10} \text{ M}^{-1} \text{ s}^{-1}$ in conventional solvents like acetonitrile. Because diffusion rates are inversely

proportional to solution viscosity, and the viscosities of ionic liquids are ~100-fold greater than most conventional solvents, it was expected that electron transfer reactions diffusion-limited in conventional solvents would be ~100-fold slower ($\sim 10^8 \text{ M}^{-1} \text{ s}^{-1}$) in ionic liquids. It was therefore initially puzzling when fluorescence quenching and other experiments registered rates apparently exceeding this value by large factors.⁵ The discrepancy was found to be traced both to the unexpectedly rapid diffusion of small neutral solutes in ionic liquids,⁶ and to the fact that the slow diffusion in ionic liquids greatly extends the reach of the transient portion of reaction, which enhances the net reaction rate over its value in the stationary regime.^{5,7} While much has been learned about PET reactions from these studies, the complexity of properly modeling the diffusional portion of the reaction in ionic liquids makes conclusions about the actual electron transfer event subject to uncertainty. For example, there has been some debate in the literature over the question of whether the Marcus turnover is observed in ionic liquids.⁸⁻¹⁰

When the electron transfer event is of primary interest, electron donor–acceptor dyads covalently linked by some type of bridge allow for simpler interpretation, albeit at the cost of sometimes considerable synthetic effort. Such molecules played a central role in early efforts to test electron transfer theories in conventional solvents.^{11,12} A number of groups have adopted this approach for studies of ionic liquids.¹³⁻²¹ With few exceptions, the dyads examined in ionic liquids involved cases of strong electronic coupling and adiabatic electron transfer. In most of these cases, electron transfer rates were found to be markedly slower in ionic liquids than in conventional solvents, and in some cases rates

were found to be proportional to solvation times in both conventional and ionic liquid solvents.^{19,20}

Another technique to eliminate the need for diffusion, and the one adopted here, is to use a neat solvent as the electron donor or acceptor, ensuring that the first solvation shell consists entirely of potential reactants. This approach has been employed by a number of groups beginning in the 1990s.²²⁻³⁵ With only a single exception²⁶ aromatic amines were used neat electron donating solvents and various fluorophores as excited-state electron acceptors. A range of ultrafast methods^{29,31,32,35} have been used to probe electron transfer and other processes and a variety of excited state dyes, resulting in reports of initial electron transfer times as fast as ~ 50 fs³¹ and as slow ~ 2 ns²² reported in different systems. There is little to unify the behavior observed among the various dyes studied to date, apart from the nearly ubiquitous occurrence of non-exponential electron transfer kinetics. However, by concentrating on a series of closely related coumarin dyes, Yoshihara and coworkers²²⁻²⁶ were able to interpret the non-exponential kinetics and the range of reaction times observed, using a theory originally developed to model electron transfer in some intramolecular dyads where electron transfer was observed to be much faster than solvation.³⁶ This model explains the nonexponentiality as resulting from both solvation dynamics dynamically shifting the emission spectra of the initially excited chromophore and from the presence of different vibronic channels each with different rates available for reaction.²²⁻²⁶ Neglected in this model is the fact that in contrast to reactions in dilute solution or covalently bound pairs, each fluorophore is surrounded by multiple donors in the neat solvent, each of which provides a potential reacting partner.

Subsequent computational work^{27,37-39} has stressed the fact that the electronic coupling between a fluorophore and these different partners may vary by orders of magnitude, providing an alternative explanation for the complex fluorescence profiles observed. Additionally, even small relative motions of a fluorophore - quencher pair can effect large changes in this coupling,^{27,37,40} making it an important dynamical variable in the problem. Thus far, there are no theories or simple models that adequately address these different aspects of the problem. Recent studies of dilute bimolecular quenching in ionic liquids hint at the possibility that optimization of electronic coupling between reacting pairs may be as important to determining electron transfer rates as solvation energy relaxation.⁴⁰

The present reports the first to measurements of diffusionless electron transfer using an ionic liquid as a neat quenching solvent. Pyridinium ionic liquids were chosen for this purpose based on the fact that several groups had previously ability of N-alkylpyridinium cations to oxidatively⁴¹ quench the fluorescence of polyaromatic hydrocarbons^{42,43} and coumarin 153.⁴¹ In particular, 1-Butylpyridinium bis(trifluoromethanesulfonyl)imide ([Py₄][Tf₂N]) is studied here, primarily because commercial samples of high optical purity were available. To achieve a wide range of electron transfer driving force, the twelve coumarin laser dyes shown in Figure 4.1 were selected to act as photo-excited electron donors. The results of this work are described in three parts. The first part involves characterization of the coumarins in acetonitrile and a nonreactive imidazolium ionic liquid, [Im₄][Tf₂N] (Im₄⁺ = 1-butyl-4-methylimidazolium), using steady state spectroscopy and time-correlated single photon

counting (TCSPC). This preliminary work was done in order to check for any differences unrelated to electron transfer that might exist between the photophysics of these molecules in a high-polarity conventional solvent and an ionic liquid. The data show solvation energies to be nearly the same in all three solvents, which enables use of measurements in acetonitrile to confidently estimate reaction free energies in neat $[\text{Py}_4][\text{Tf}_2\text{N}]$. Next, measurements of coumarin quenching by Py_4^+ in dilute acetonitrile solution are described. They reveal nearly diffusion-limited electron transfer in these systems, very similar to that found for coumarins reductively quenched by aromatic amines.^{44,45} Finally, results of TCSPC and Kerr-gated emission (KGE) measurements of quenching in neat $[\text{Py}_4][\text{Tf}_2\text{N}]$ are discussed. Emission decays in the neat ionic liquid are found to be highly nonexponential, with overall reaction times ranging from less than 1 ps to over 200 ps. Similarities and differences between these results and prior work on coumarin quenching in aromatic amine solvents are discussed in relation to what they might reveal about the role of solvation dynamics in such reactions.

4.2 Methods

4.2.1 Chemicals

Ionic liquids 1-butylpyridinium bis(trifluoromethane)sulfonimide ($[\text{Py}_4][\text{Tf}_2\text{N}]$) and 1-butyl-1-methylimidazolium bis(trifluoromethane)sulfonimide ($[\text{Im}_{41}][\text{Tf}_2\text{N}]$) were purchased from IoLiTec with a stated purity of 98%. These ionic liquids were selected by the manufacturer for their optical purity in the 300 - 700 nm range. HPLC grade

acetonitrile was purchased from OmniSolv and spectroscopic grade dimethylsulfoxide from Sigma-Aldrich. Solvents were tested for water content using Karl-Fischer titration. If water content was less than 100 ppm, the solvent was used as received. Conventional solvents not meeting this limit were dried over molecular sieves. Ionic liquids with higher water content were dried under vacuum overnight with gentle heating. All solvent mixtures were made volumetrically, assuming ideal mixing. Samples were purged with nitrogen for three minutes to prevent fluorescence quenching by dissolved oxygen. Absorption and emission spectra of each solvent were measured to confirm minimal optical impurities in the visible region. All coumarin compounds, shown in Figure 4.1, were purchased from Exciton Chemical Company, Eastman Kodak Company, and TCI Chemical Company and used as purchased.

4.2.2 Steady State Spectroscopy

Absorption spectra and solvent blanks were measured for all samples using a Hitachi UV-3010 UV-Vis spectrophotometer. Fluorophore samples having optical densities between 1-1.5 at the S_1 absorption maximum in 1 cm quartz cuvettes were collected and solvent subtracted prior to further analysis. Fluorescence spectra were measured using a SPEX Fluorolog 212 with right-angle collection and 2 nm resolution. The spectral response of the fluorimeter was calibrated from 300 nm to 800 nm using emission standards as described in previous work.⁴⁶ Emission samples (~ 2 mL) were prepared with optical densities between 0.10 and 0.20 at the excitation wavelength to prevent self-filtering effects. Spectra were collected of samples in sealed 1 cm quartz

cuvettes after being purged with nitrogen gas for two minutes to remove oxygen.

Excitation was at ~ 400 nm, close to the maximum of the S_0 - S_1 absorption peak of most of the coumarins and emission was collected close to the emission maximum of each coumarin (450-520 nm). After background subtraction and converting to a frequency representation, average (first moment) frequencies of both absorption and emission were estimated by fitting the spectra to log-normal functions.

4.2.3 Time-Resolved Fluorescence Measurements

A home-build time-correlated single photon counting (TCSPC) instrument⁴⁷ was used to measure lifetimes in the range of 25 ps to 15 ns. For the experiments described in this paper, excitation pulses were provided by the frequency-doubled output of a cavity-dumped Ti:Sapphire oscillator (Coherent Mira 900+PulseSwitch) tuned to ~ 800 nm. All samples were purged and sealed in 1 cm quartz cuvettes and all experiments were completed at room temperature, 20 ± 1 °C. Right-angle emission decays were collected at near the peak of the steady-state emission maximum (440 – 520 nm) with 4 nm resolution at magic angle polarization. A Kopp 3-73 filter was also used to prevent stray 400 nm excitation light from entering the detector. Instrument response functions (IRF) were measured using a scatter sample and found to have widths (FWHM) of approximately 25 ps for all experiments.

Kerr-gated emission spectroscopy (KGE) was used to measure lifetimes faster than 50 ps. This method is also well-described in previous work.^{48,49} Samples were flowed through a 0.2 mm quartz sample cell at room temperature (20 ± 1 °C) and excited

at 388 nm by frequency-doubled pulses from an amplified Ti:Sapphire system (Coherent Verdi G18/Mira 900/RegA 9050). Using an Acton, Spectra Pro-300i grating spectrograph and a liquid nitrogen cooled CCD (1340 pixels, Princeton Instruments), the entire emission spectrum was collected for each time step (-5 to 5 ps in steps of 100 fs, 5 to 50 ps in steps of 200 fs, and from 50 ps to 300 ps in 2 ps steps) from 408 to 699 nm. The FWHM of the instrument response function was found to be approximately 400 fs for all experiments. A global convolute-and-compare algorithm written in Matlab was used in the deconvolution of the IRF from the spectra. Fits to log-normal functions were made after deconvolution to quantify spectral dynamics. All experiments were performed in triplicate and the kinetic parameters were averaged to produce the reported results.

4.2.4 Stern-Volmer Analysis

Rates of electron transfer quenching by Py_4^+ in acetonitrile were analyzed using both steady-state and time-resolved Stern-Volmer experiments. Acetonitrile solutions of each coumarin were made to have optical densities of ~ 0.1 - 0.2 at the wavelength of the S_0 - S_1 transition peak. 2 mL of these solutions were transferred to quartz cuvettes via a micropipette to ensure a known starting volume. $[\text{Py}_4][\text{Tf}_2\text{N}]$ was then added dropwise and weighted in order to estimate quencher concentrations. The maximum concentrations of $[\text{Py}_4][\text{Tf}_2\text{N}]$ used were between 0.2-0.25 M. Steady state absorption and emission spectra and TCSPC decays were measured sequentially for each addition of the quencher. The optical density at the S_0 - S_1 absorption peak was used to estimate the

relative coumarin concentration in order to account for both dilution and loss of coumarin due to degradation. Two independent measurements were made for each coumarin and the uncertainty in the quenching rates estimated as the larger of $\pm 10\%$ or twice the difference in the two measurements.

All of the spectroscopic measurements described above were performed at room temperature, 20 ± 1 °C.

4.2.5 Cyclic Voltammetry

Cyclic voltammetry was performed on ten of the twelve coumarins in order to determine their oxidation potentials in acetonitrile. A three-electrode electrochemical cell, consisting of a BASi MF-2079 Ag/AgCl (3 M NaCl) reference electrode, and Pt wire counter and working electrodes. The Pt working electrode was cleaned in 0.5 M H₂SO₄ solution between each experiment by first holding the electrode at +2 V for 2 min to oxidize surface impurities, and then cycling repeatedly between the onset potentials of hydrogen and oxygen evolution. The final scan was stopped at the anodic limit, and the electrode was rinsed with DI water and then air dried. Approximately 1 mM solutions of each coumarin were made in 25 mL of sieve-dried acetonitrile, with 0.1 M tetrabutylammonium hexafluorophosphate added as the electrolyte. Samples were scanned from 0 - 1.0 V at 100 mV/s over three cycles to check for reproducibility and reversibility. Oxidation potentials ($E_{1/2}$) were calculated as the average between the

oxidation and recovery peaks and converted to the saturated calomel scale using the conversion $E(\text{SCE}) = E(\text{Ag}/\text{AgCl}) + 0.042 \text{ V}$.⁵⁰

4.3 Results and Discussion

4.3.1 Characterization of the Coumarin Studied

The steady-state photophysics of the coumarins used here were characterized in three solvents expected to be of similar polarity: $[\text{Py}_4][\text{Tf}_2\text{N}]$, acetonitrile, and the non-reactive ionic reference solvent $[\text{Im}_{41}][\text{Tf}_2\text{N}]$. Representative absorption and emission spectra in acetonitrile are shown in Figure 4.2 and absorption and emission frequencies are listed in Table 4.1. Although there are some variations in vibronic structure, peak width, and Stokes shifts among the spectra in acetonitrile, the main difference among these dyes lies in their frequencies, which span much of the visible and near UV frequency range. Additionally, apart from the much lower emission quantum yields in $[\text{Py}_4][\text{Tf}_2\text{N}]$, the spectra are quite similar in all three of these solvents. Figure 4.3 illustrates this similarity for two cases, **C7**(153) and **C11**(102). (Compilations of all spectra are provided in Appendix Figures B.1-B.3.) The usual situation is represented by the **C7** spectra in Figure 4.3. As shown there, the only differences among either the absorption or emission bands in the three solvents are modest shifts of $<450 \text{ cm}^{-1}$. **C11**, shown in Figure 4.3(b) is one of three dyes (**C10-C12**) whose lifetimes are sufficiently short ($< 1 \text{ ps}$) in $[\text{Py}_4][\text{Tf}_2\text{N}]$ that reliable steady-state emission could not be obtained. The observed emission of **C11** in $[\text{Py}_4][\text{Tf}_2\text{N}]$ is much broader than other emission

spectra, because it is comprised of emission from both **C11** and impurities in the [Py₄][Tf₂N] that could not be adequately removed by solvent subtraction. The curve labeled “fit” in Figure 4.3(b) is an estimate of the C11 emission obtained by fitting two emission bands, using information from early-time spectra, as described in Appendix Section B.1.

Figure 4.4 compares several features of the absorption and emission spectra of all of the coumarins in these three solvents. Panels (a) and (b) compare first moment frequencies, $\langle \nu \rangle$, in the two ionic liquids with those in acetonitrile. Frequencies in [Im₄₁][Tf₂N] are redshifted from those in acetonitrile by an average of $330 \pm 40 \text{ cm}^{-1}$ in absorption and $370 \pm 40 \text{ cm}^{-1}$ in emission. The same is true of absorption frequencies in [Py₄][Tf₂N], where the shifts average $380 \pm 60 \text{ cm}^{-1}$. These comparable absorption and emission shifts can be ascribed to the greater electronic polarizability in the ionic liquids, as represented by their refractive indices: 1.341 in acetonitrile⁵¹ versus 1.423 in [Im₄₁][Tf₂N]⁵² and 1.443 in [Py₄][Tf₂N].⁵³ In contrast to [Im₄₁][Tf₂N], emission frequencies in [Py₄][Tf₂N] are on average equal to those in acetonitrile. This difference probably reflects the fact that the shorter emission lifetimes in [Py₄][Tf₂N] do not allow sufficient time for solvent equilibration in S₁ prior to emission.

The free energy difference between the S₀ and S₁ electronic states, which is needed for calculating the driving force for excited-state electron transfer, can be obtained from the absorption and emission frequencies via

$$\Delta G_{01} = \frac{1}{2} hc (\langle \nu_{abs} \rangle + \langle \nu_{em} \rangle) \quad (4.1)$$

where h is Planck's constant and c the velocity of light. Figure 4.4(c) shows that in these two solvents are well represented by $\Delta G_{01}(\text{Im}_{41}) \cong 0.98\Delta G_{01}(\text{ACN})$. Reorganization energies associated with the $S_0 \leftrightarrow S_1$ change,

$$\lambda_{01} = \frac{1}{2}hc(\langle \nu_{abs} \rangle - \langle \nu_{em} \rangle) \quad (4.2)$$

are likewise highly correlated in these two solvents, $\lambda_{01}(\text{Im}_{41}) \cong 1.01\lambda_{01}(\text{ACN})$. It is not possible to obtain reliable estimates of ΔG_{01} or λ_{01} from the $[\text{Py}_4][\text{Tf}_2\text{N}]$ spectra due to lack of equilibrated emission in this solvent. Nevertheless, based on the similarity in the absorption frequencies, it seems safe to conclude that the energetic aspects of the electron transfer reaction in should be similar in all three solvents.

Reaction free energies of photo-induced electron transfer between the coumarins and the 1-butylpyridinium cation can be estimated from the Rehm-Weller equation,

$$\Delta G_{ET} = -e[E_{red}(\text{Py}^+ / \text{Py}^0) - E_{ox}(C^0 / C^+)] - \Delta G_{01} + \Delta w_{es} \quad (4.3)$$

where $E_{ox}(C^0/C^+)$ and $E_{red}(\text{Py}^+/\text{Py}^0)$ denote the oxidation and reduction potentials of the coumarin donor and 1-butylpyridinium acceptor, respectively, and Δw_{es} accounts for the difference in electrostatic energies of the reactant and product states. For the charge shift processes examined here, this Δw_{es} term is assumed to be zero.

The oxidation potentials of ten of the coumarin donors were measured using cyclic voltammetry. Most the coumarins exhibited reversible oxidation peaks with oxidation potentials ranging from 0.4 to 1.0 V vs. SCE in acetonitrile. Values of E_{ox} are listed in Table 1 and representative voltammograms provided in Appendix Section B.2. As discussed in the Supporting Information, a systematic difference is found between the

present values and the few points of comparison available in the literature.⁵⁴⁻⁵⁶ The only direct comparisons are with early data of Jones et al.,⁵⁴ who measured the oxidation potentials of three of the coumarins studied here in acetonitrile. In these three cases the present values are an average of 0.26 V smaller than theirs. Several other measurements, mostly in water,⁵⁶ also suggest that the present values might be low. Unfortunately, the instruments used for CV measurements became unavailable before the source of these differences could be investigated. For this reason, as well as to estimate values for two additional coumarins, oxidation potentials were also estimated from electronic structure calculations. As described in Appendix Section B.2, the computational approach recently described by Roth⁵⁷ predicts oxidation potentials linearly related to the experimental values with a correlation coefficient of 0.98 and a standard error of ± 0.03 V. This excellent correlation lends confidence to the measured values. For purposes of calculating ΔG_{ET} we therefore use the 10 measured values together with two calculated values (C1/151 and C4/545). The reduction potential of 1-butylpyridinium was not measured in the present work; however, E_{red} of the homologs 1-methyl- and 1-ethylpyridinium were previously reported to be -1.32 and -1.33 V (vs. SCE in acetonitrile).⁵⁸ The value estimated by the method Roth is -1.37 V. For consistency, the latter value is used here for calculating ΔG_{ET} .

Free energies of excited-state electron transfer between these coumarins and the 1-butylpyridinium cation estimated using Eq. 4.3 are also listed in Table 4.1. These values pertain to reaction in acetonitrile, but as already discussed, the energies in $[\text{Py}_4][\text{Tf}_2\text{N}]$ and $[\text{Im}_{41}][\text{Tf}_2\text{N}]$ are expected to differ little from the acetonitrile values.

Note that the numbering of the coumarin dyes here is chosen to coincide with increasing driving force, $-\Delta G_{ET}$. As will soon become evident from their ET kinetics, the coumarins divide into two groups according to ΔG_{ET} . This grouping can be understood in terms of the presence of electron donating or accepting groups at the 3 and 4 positions of the coumarin ring, as quantified by their Hammett σ values.⁵⁹ Coumarins **C1** - **C8** have electron accepting groups ($\sigma > 0$) at these positions, and their $-\Delta G_{ET}$ values span the range $0.53 \leq -\Delta G_{ET} \leq 0.70$ eV, whereas coumarins **C9** - **C12** have electron donating groups ($\sigma \leq 0$) and $1.0 \leq -\Delta G_{ET} \leq 1.2$ eV. As shown in Appendix Figure B.8, electron accepting groups both reduce the $S_0 \leftrightarrow S_1$ transition energy and simultaneously increase the oxidation potential of these molecules, thereby increasing the driving force for excited state electron transfer. No commercially available 7-aminocoumarin dyes were identified having weak electron accepting substituents ($0 < \sigma < 0.4$) that would be expected to fill the 0.3 eV gap in ΔG_{ET} between the two groups of molecules.

4.3.2 Quenching by Py_4^+ in Dilute Acetonitrile Solution

An initial characterization of the electron transfer process was carried out using Stern-Volmer analysis of steady-state and TCSPC measurements of quenching by dilute $[\text{Py}_4][\text{Tf}_2\text{N}]$ in acetonitrile. The fluorescence lifetimes of the coumarins in acetonitrile in the absence of quencher are compiled in Table 4.1. All TCSPC emission decays in acetonitrile were observed to be single exponential, with lifetimes ranging between 2-6 ns. For comparison, decays were also measured in $[\text{Im}_{41}][\text{Tf}_2\text{N}]$. In contrast to acetonitrile, these decays were slightly non-exponential, consisting of a dominant

nanosecond component plus a minor component of a few hundred picoseconds. The latter component is attributed to the slow dynamic Stokes shift in this high-viscosity solvent (63 mPa s at 293 K^{52,60}). The dominant, nanosecond components in [Im₂₁][Tf₂N] were all close to, but an average of 12% larger than the lifetimes in acetonitrile. (The exception is **C2**/152, whose lifetime which was >60% greater, presumably due to the high viscosity inhibiting the well-known twisted intermolecular charge transfer reaction of this molecule.⁶¹⁻⁶⁵)

Representative data sets illustrating the quenching of coumarin emission by Py₄⁺ in acetonitrile solution are shown in Figures 4.5 (**C2**/152) and B.9 (**C11**/102). Panel (a) of Figure 4.5 (a) shows changes to the absorption spectra upon sequential addition of [Py₄][Tf₂N] to a **C2**/acetonitrile solution. The large decrease in peak absorbance here reveals an important general feature of excited-state quenching of 7-aminocoumarins by Py₄⁺: these dyes photodegrade in the presence of Py₄⁺. In the example shown in Figure 4.5, during the time required to make measurements on successive additions of [Py₄][Tf₂N] up to 0.2 M, a 7% dilution, the peak absorbance of **C2** decreases by roughly 40%. Thus, approximately 30% of the dye is degraded over the course of this 2-hour experiment. The increasing absorbance above 31,000 cm⁻¹ in Figure 4.5(a) indicates that a UV-absorbing product is being formed during this process. The constant shape of the emission spectra in panel (b) shows that the photoproduct has little effect on the steady-state emission; however, as can be seen in panel (c), it is emissive enough to add a small-amplitude nanosecond component to the time-resolved emission decays (panel c). Significant degradation is observed only during exposure to the laser excitation used for

TCSPC measurements, and its extent varies considerably among the dyes studied, as can be seen by comparing Figures 4.5 and Appendix Figure B.9. More discussion of this photodegradation and its potential effect on the data reported here can be found in Appendix Section B.3. With suitable precautions, such as limiting exposure times and accounting for any depletion in probe concentration during sequential measurements, reliable kinetic data can be obtained.

Bimolecular rate constants, k_q , were determined by fitting the concentration dependence of the integrated emission intensities I and lifetimes τ to the Stern-Volmer type equations:

$$I_0 / I = 1 + k_q^{(I)} \tau_0 [Q] \quad (4.4)$$

$$\tau_0 / \tau = 1 + k_q^{(\tau)} \tau_0 [Q] \quad (4.5)$$

Where I_0 and τ_0 are the intensity and lifetime in the absence of quencher and $[Q]$ is the quencher concentration. Figure 4.5(d) and B.9(d) provide examples of such fits.

Whereas most of the data conformed to the linear concentration dependence implied by Eqs. 4.4 and 4.5, the steady-state intensities of dyes **C8** – **C12** were better fit by quadratic functions of $[Q]$. (See Figure B.9 for an example.) In these cases, the linear coefficient of the quadratic fit, which corresponds to $[Q] \rightarrow 0$ limiting behavior, was used to estimate $k_q^{(I)}$. When determining lifetimes for this analysis, we ignored the nanosecond components of the decays resulting from photodegradation. However, it should be noted that even if these nanosecond components were included, only produce a few percent difference in the value of $k_q^{(\tau)}$ would be obtained.

Rate constants for dilute quenching in acetonitrile are plotted versus the electron transfer driving force in Figure 4.6. Panel (a) shows that $k_q^{(I)}$ and $k_q^{(\tau)}$ are the same to within uncertainties in nearly all cases. k_q varies by a factor of 5 over the 0.69 V range of ΔG_{ET} accessed by these data. This modest dependence of k_q on ΔG_{ET} presumably reflects the fact that diffusion is limiting the rates at higher driving force. The estimated diffusion-limited rate, $k_D = 8k_B T / 3\eta$, in acetonitrile at 293 K is $17 \text{ ns}^{-1} \text{ M}^{-1}$, indicated by the horizontal dashed line in Figure 4.6(a).

The present results are similar to what has been found in numerous other dilute fluorophore/quencher systems previously studied.^{44,45,66-71} For comparison, Figure 4.6(b) shows these results together with data reported by Nad and Pal⁴⁴ on the quenching of six excited 7-aminocoumarin dyes by six aromatic amine donors in acetonitrile (blue circles). The average quenching rate constants $(k_q^{(I)} + k_q^{(\tau)})/2$ reported here for *oxidative* quenching of excited-state coumarins by Py_4^+ are on average ~24% smaller than those reported by Nad and Pal for *reductive* quenching of coumarins over the same range of ΔG_{ET} . Also shown by the solid black curve in Figure 4.6(b) is the empirical fit of over 70 aromatic fluorophore – quencher pairs in acetonitrile, taken from the seminal work of Rehm and Weller.^{13,66} The Rehm-Weller data covered over a 2 eV range of driving force and clearly demonstrated the limiting action of diffusion as well as the lack of the turnover predicted by Marcus theory (dashed curve). Rates for the most exergonic cases measured here slightly exceed the diffusion limit, which is not unusual when $-\Delta G_{ET} > 1 \text{ eV}$.⁴⁰

4.3.3 Quenching Dynamics in Neat [Py₄][Tf₂N]

Quenching kinetics in liquid [Py₄][Tf₂N] were measured using both TCSPC (25 ps IRF) and KGE (400 fs IRF), in order to capture the full range of quenching times. Figure 4.7 illustrates the type of data observed in TCSPC experiments. Figure 4.7(a) compares the decay of **C7**/153 in neat [Py₄][Tf₂N] with decays in acetonitrile and [Im₄₁][Tf₂N]. In contrast to the exponential fluorescence of **C7** ($\tau = 5.7$ ns) and most other coumarins in acetonitrile, and the nearly exponential fluorescence in [Im₄₁][Tf₂N] ($\tau = 5.9$ ns), in neat [Py₄][Tf₂N], **C7** decays much more rapidly and its decay is clearly nonexponential. [Py₄][Tf₂N] itself, shown for comparison, also has a weak but noticeable and nonexponential emission. The amplitude of the nanosecond tail of the decay of **C7** in [Py₄][Tf₂N] is comparable to that of [Py₄][Tf₂N] alone, as are the nanosecond times associated with this tail. As discussed in Appendix Section B.3, this nanosecond component is attributed to a combination of emission from impurities in [Py₄][Tf₂N] plus contributions from coumarin photoproducts caused by laser irradiation.

Figure 4.7(b) shows TCSPC data of six coumarins in [Py₄][Tf₂N] in order to illustrate the range of dynamics observed. All of the decays are nonexponential, requiring 2-3 exponentials for accurate fits. As in the **C7** data in panel (b), a minority component, comprising <3% of the amplitude, with a time constant in the nanosecond range is often observed. Over the limited time window of Figure 4.7(b) this slow component is only noticeable in the most rapidly decaying dyes, **C8** and **C10**. We attribute any components with time constants greater than 1 ns to impurity emission and

neglect them in analyzing these data. However, such components, are sufficiently small in amplitude and well separated from other components their exclusion has minimal effect on the characteristic times reported here.

Kerr-gated emission spectroscopy was used to capture components of the quenching process faster than 25 ps. KGE data of **C7**/153 in [Py₄][Tf₂N], which are representative of coumarins having broadly distributed kinetics, are shown in Figure 4.8. An example of a case (**C10**/6H) in which quenching is largely complete in a few picoseconds is provided in Appendix Figure B.12. In the top panel of Figure 4.8 are time-resolved spectra. In addition to the overall decay of intensity, the spectrum of **C7** undergoes a red shift with time. This dynamic Stokes shift reflects the dynamics of solvent reorganization, a phenomenon already well-studied in the case of **C7**/C153.⁷² Such dynamic shifts are expected to occur for all of these solvatochromic 7-aminocoumarin dyes. The dashed curves Figure 4.8(a) show fits of the spectra to lognormal functions. The bottom panels of the figure are the peak frequencies and normalized peak and integral intensities obtained from the lognormal fits. Such functions could be reasonably represented as 2- or 3-exponential functions (black curves). The peak shift ($\nu_p(t)$) data are what one would expect for solvation of these molecules except that the short lifetimes in [Py₄][Tf₂N] mean that roughly half of the Stokes shift is unobserved, occurring after most of the S₁ population has decayed. (For example, compare Fig. 4.8(b) to Figure 4 of Ref.⁷²)

To more completely define the complete quenching dynamics in neat [Py₄][Tf₂N], fits to the TCSPC and KGE decays were spliced together using the method described in

Appendix Section B.4. The composite, normalized emission decays, $I_n(t) = I(t)/I(0)$, so produced are shown in Figure 4.9(a). The grouping of dyes into slow (C1 - C8) and fast (C9 - C12) sets is much more evident here than in the TCSPC data alone. All decays are broadly distributed in time, especially those in the slow grouping, as emphasized by the single exponential decay shown for comparison (dashed curve). Figure 4.9(b) provides an alternative representation of these same data in the form of lifetime distributions, $A(\tau)$ defined by $I_n(t) = \int_0^\infty A(\tau) \exp(-t/\tau) d\tau$. Laplace inversion of the emission decays was accomplished using a maximum entropy approach as detailed in Appendix. Section B.5. These lifetime distributions should be viewed as providing only semi-quantitative representations of the decay data because the shapes and widths of peaks in $A(\tau)$ depend upon the uncertainties assigned to the $I_n(t)$, and these uncertainties are only estimates. The main use of the such distributions is to point out the fact that the slower coumarins still contain lifetime components in the 0.1-10 ps range, in addition to primary components in the 10-1000 ps range, highlighting again the remarkable breadth of their quenching dynamics. In contrast, the fast set of dyes (C9 - C12) are dominated by lifetime components below 10 ps. These faster decays are also clearly nonexponential. Finally, it should be noted that three dyes (C1, C4, and C5) are not included in Figure 4.9 because only TCSPC data were collected for these cases.

Three rate coefficients are used to characterize these lifetime data:

$$k_0 \equiv \langle \tau^{-1} \rangle = \int_0^\infty A(\tau) \tau^{-1} d\tau, \quad (4.6)$$

$$k_{1e} \equiv t_{1e}^{-1} \text{ where } t_{1e} : I_n(t_{1e}) = e^{-1}, \quad (4.7)$$

$$\text{and } k_{av} \equiv \langle \tau \rangle^{-1} = \left\{ \int_0^\infty I_n(t) dt \right\}^{-1} \quad (4.8)$$

The coefficients k_0 and k_{av} emphasize the fastest and slowest portions of the decay, and k_{1e} provides an effective overall rate coefficient. In **Figure 4.10** these coefficients are plotted versus the driving force for electron transfer, $-\Delta G_{ET}$. As illustrated here, all three characteristic rates increase approximately exponentially with $-\Delta G_{ET}$, placing the reactions within the “normal” electron transfer regime. In contrast to the strong dependence of k_{1e} , and k_{av} on driving force, the fastest components of the reaction measured by k_0 increase to a much lesser extent; the slopes in Figure 4.10 are 1.6, 8.9, and 7.8 for k_0 , k_{1e} , and k_{av} , respectively.

Of central interest in the present work is to determine how electron transfer quenching in a neat ionic liquid like $[\text{Py}_4][\text{Tf}_2\text{N}]$ differs from the analogous reaction in a neat conventional solvent. Toward this end, the data in Figures 4.9 and 4.10 are compared to the closest reactions previously studied in conventional solvents, coumarin quenching in neat substituted aniline solvents. (Note that one superficial difference between these systems is that quenching of excited coumarin dyes in $[\text{Py}_4][\text{Tf}_2\text{N}]$ entails electron donation to the solvent, whereas in anilines the solvent is the electron donor.) Yoshihara and coworkers²²⁻²⁶ with additional work by Castner *et al.*²⁷ compiled a large database on coumarin + neat aniline reactions including data on 12 different coumarin dyes and 14 aniline derivatives and deuterated variants. The data used here are mainly from the compilation in Ref.²⁵

Figure 4.11(a) compares two pairs of decays observed in [Py₄][Tf₂N] with corresponding decays in aniline solvents. The particular pairs (C10/6H + [Py₄][Tf₂N] and C152 + dimethylaniline) and (C7/153 + Py₄⁺, C153 + diethylaniline) are selected to have close to the same values of t_{1e} (~0.5 ps and ~40 ps) in the two solvent types. The decays are similar in the fast-reacting pair. In aniline solvents, nearly all coumarins have all been characterized as having biexponential emission decays.^{25,27} The fastest decays in [Py₄][Tf₂N] are also close to biexponential, but often have an additional longer time component. In contrast, in the slower reactions studied here, the decays are much more dispersive than in aniline solvents. In the ionic liquid, lifetime components in the 10²-10³ ps range are found, whereas components of more than 100 ps are almost nonexistent in aniline solvents.^{25,27}

Figure 4.11(b) compares values of k_{1e} in [Py₄][Tf₂N] and aniline solvents. The latter times include 40 data on different coumarin / substituted aniline solvents. (The variety of both solvents and solutes is part of the reason for their greater scatter. The filled symbols show data in a single solvent, dimethylaniline.) Two points of comparison with the present data are noteworthy. First, the maximum observed rates observed in the two systems do not differ significantly: $5 \times 10^{13} \text{ s}^{-1}$ in aniline solvents versus $3 \times 10^{13} \text{ s}^{-1}$ in [Py₄][Tf₂N]. Second, the two sets of data span rather different ranges of ΔG_{ET} , with the driving force in [Py₄][Tf₂N] being ~0.5 eV greater than in the aniline solvents. In order to facilitate additional comparisons between these two systems and others, fits to the classical Marcus equation,

$$k_{ET} = \frac{2\pi}{\hbar} H_{DA}^2 \left(\frac{1}{4\pi\lambda k_B T} \right)^{1/2} \exp \left[\frac{-(\Delta G_{ET} + \lambda)}{4\lambda k_B T} \right] \quad (4.9)$$

are plotted in Figure 4.11(b). Equation 4.9 is based on the transition state approximation and assumes the nonadiabatic limit, wherein the electronic coupling between diabatic states, H_{DA} , is much smaller than thermal energies, $k_B T$. λ is the reorganization energy, comprised of intramolecular and solvent contributions, $\lambda = \lambda_{in} + \lambda_{sol}$. Regardless of the appropriateness of this description for modeling neat quenching reactions, fits to Eq. 4.9 provide estimates of two metrics that can be compared among systems: the total reorganization energy λ and the maximum rate coefficient k_{max} , the pre-exponential factor in Eq. 4.9.

Values of λ and k_{max} obtained from the fits in Figure 4.11(b) are compared to literature results on several systems of photo-induced electron transfers between donor-acceptor pairs in Table 4.2. One sees from these comparisons that the reorganization energy of 1.6 ± 0.2 eV estimated from the rate data in $[\text{Py}_4][\text{Tf}_2\text{N}]$ are comparable to those deduced for other systems in the equally polar solvent acetonitrile. Based on electronic structure calculations and continuum estimates similar to those detailed in Ref.⁴⁰, values of $\lambda_{in} = 0.31$ eV and $\lambda_{sol} = 1.09$ eV are obtained, for $\lambda = 1.4$ eV in reasonable agreement with the kinetic value. In the case of the coumarin + substituted aniline reactions, the value fit to Eq. 4.9 is only 0.5 eV, which is smaller than reported in other weakly polar solvents. The maximum rates of electron transfer in both quenching solvents, $10^{12.5} \text{ s}^{-1}$, are comparable to those observed in the porphyrin-based donor-

acceptor dyads^{73,74} in Table 4.2 and roughly 10^1 - 10^2 times more rapid than charge recombination between photogenerated geminate radical pairs.⁷⁵⁻⁷⁷

Prior work on electron transfer quenching in neat redox active solvents has tended to highlight two different aspects of the process. Yoshihara and coworkers²²⁻²⁵ focused on the nonexponentiality of the fluorescence decays observed, as well as the fact that quenching was often faster than solvation. They applied a sophisticated model originally developed by Barbara and coworkers³⁶ for treating intramolecular electron transfer. This approach combined the semiclassical extension of Eq. 4.9⁷⁸ with the 2-dimensional classical diffusion model of Sumi and Marcus.⁷⁹ Using approximate bi-exponential solvation response functions of the various aniline solvents, the Yoshihara group achieved some success in explaining both the nonexponential emission observed and the driving force dependence of the overall rates shown in Figure 4.11(b). As already noted, the nonexponentiality of the emission in the ionic liquid is substantially greater compared to the liquids studied by Yoshihara's group. Figure 4.12 compares the solvation response, $S(t)$, expected for $[\text{Py}_4][\text{Tf}_2\text{N}]$ (blue curve) to the fluorescence decays, $I_n(t)$, observed in this solvent (dashed curves) as well as to the solvation response in dimethylaniline (DMA) and acetonitrile (ACN). Note that the solvation response of $[\text{Py}_4][\text{Tf}_2\text{N}]$ has not been directly measured; however, both $[\text{Im}_{41}][\text{Tf}_2\text{N}]$ (shown here) and the 1-butyl-1-methylpyrrolidinium liquid $[\text{Pr}_{41}][\text{Tf}_2\text{N}]$ exhibit very similar $S(t)$ functions,⁷² and $[\text{Py}_4][\text{Tf}_2\text{N}]$ should not differ significantly. The vastly different character of solvation in these ionic liquids compare to the conventional dipolar solvents DMA and ACN is clear from Figure 4.12. Compared to the largely unimodal lifetime

distributions in these dipolar liquids, solvation in the ionic liquids is well separated into two components, a subpicosecond inertial component and a broadly distributed structural component.⁷² Whereas there is little overlap between the solvation response in DMA (and other aniline-based solvents) with the fastest quenching reaction observed,²⁵ in the case of the ionic liquid reactions, even for the fastest reactions (**C9** – **C12**) there is substantial overlap with the inertial component of solvation. In the slower reactions **C1** – **C8** the broadly distributed quenching profiles $I_n(t)$ resemble the solvation response, although the latter extend out to longer times. Thus, it is not obvious that the approach used by Yoshihara and coworkers is necessary or even appropriate to these liquids.

Later studies^{10,27,37-39,80-82} in of quenching in neat conventional liquids have pointed to fundamental differences compared to the other systems listed in Table 4.2. First, instead of a single nearby partner, in neat redox-active liquids the fluorophore is surrounded by multiple partners. For example, early molecular dynamics simulations of chromophores in dimethylaniline (DMA)^{27,37} indicate between 10-20 quencher molecules in the first solvation shell are close enough to contribute significantly to reaction. Recent simulations of **C7**/153⁸³ and cyanoanthracene fluorophores⁴⁰ in ionic liquids suggest between 8-9 Py_4^+ cations populate the first solvation shell of typical fluorophores. Assuming these reactants act independently and with equal efficiency, the times and rate coefficients discussed above should be divided by these coordination numbers (n_1) and the before comparing them to theories like that behind Eq. 4.9, which apply to a single reacting pair. Doing so would lead to much greater overlap with solvation times, both in DMA and in $[\text{Py}_4][\text{Tf}_2\text{N}]$.

More importantly, simulations indicate that relative product-reactant energies (ΔG_{ET}) and especially their coupling (H_{DA}) vary markedly among the n_1 neighbors of a chromophore.^{27,37,38,40} The electronic coupling is exquisitely sensitive to the relative orientation and position of chromophore-quencher pairs.⁴⁰ For example, in DMA solvent, small relative displacements of solute and a DMA partner are predicted to give rise to 100-fold variations in H_{DA}^2 and thus k_{ET} (Eq. 4.9) on subpicosecond time scales.^{27,37,38} In ionic liquids, much the same behavior is expected, perhaps on much the same time scale, given that only small amplitude motions (1 Å or 20°) are required.⁴⁰ Changes in H_{DA} of this magnitude should change the nonadiabatic/adiabatic character of the reaction and thus substantially alter the nature of the energy surface. Given these observations, consideration of solvation dynamics alone seems unlikely to provide an adequate description of these reactions. Apart from the heuristic kinetic model of Vauthey and coworkers^{80,81} no tractable models for this type of situation are available. Further simulation and theoretical work are needed in order to create realistic approaches to modeling these dynamics.

4.3.4 Quenching in Concentrated [Py₄][Tf₂N] + Acetonitrile Mixtures

To investigate the effects of dilution on the quenching process, the fluorescence decays of **C10**/6H in [Py₄][Tf₂N] + acetonitrile mixtures were measured. Because these decays were rapid in all but the most dilute solutions, only KGE data were collected. Figure 4.13 shows representative decays and lifetime distributions. Characteristic times

obtained from these decays are plotted versus composition in Figure 4.14. To measure composition, volume fractions of the ionic component,

$\varphi_{IL} = (x_{IL} / \bar{V}_{IL}) / [x_{IL} / \bar{V}_{IL} + x_{ACN} \bar{V}_{ACN}]$ are used here, where x_i and \bar{V}_i are the mole fractions and molar volumes of the two components i . ($\bar{V}_{IL} = 286 \text{ cm}^3/\text{mol}$ ⁵³ and $\bar{V}_{ACN} = 41, \text{ cm}^3/\text{mol}$.⁵¹) Surprisingly, dilution down to $\varphi_{IL} = 0.6$ ($x_{IL} = 0.22$ or 2.1 M) has only a modest effect on the decay times -- k_{1e} and k_{av} decrease by $\sim 20\%$ and k_0 increases by about twice this amount. In contrast, the solution viscosity decreases by a factor of ~ 30 at this dilution⁸⁴ and a comparable decrease in solvation times is expected.⁸⁵ However, this dilution is also expected remove $\sim 80\%$ of the Py_4^+ acceptor ions within the first solvation shell.⁸³ These two effects as a function of φ_{IL} , speeding solvent dynamics and diluting reactive partners, have opposing effects on the overall reaction rate and apparently are compensatory over a large range of compositions. At IL concentrations below $\varphi_{IL} = 0.6$, k_0 continues increase slightly, whereas k_{1e} and k_{av} decrease rapidly and the lifetime distribution shifts to longer times as diffusion into the first solvation shell becomes necessary for complete reaction.

4.4 Summary & Conclusions

This study reports the first measurements of the kinetics of electron transfer quenching by an ionic liquid. Its main purpose was to provide a comparison to similar experiments in conventional dipolar solvents, and to explore whether the slower and more distributed solvent/solvation dynamics of ionic liquid solvents gives rise to any

distinctive behavior. It was hoped that such measurements would provide a new window on ionic liquid dynamics.

It was shown that a range of 7-aminocoumarin dyes are rapidly quenched in the ionic liquid 1-butylpyridinium *bis*(trifluoromethylsulfonyl)imide, [Py₄][Tf₂N]. The quenching mechanism entails electron transfer from an excited coumarin to the Py₄⁺ cation, as confirmed by its strong dependence on ΔG_{ET} . The direction of electron transfer is opposite to the well-studied case of electron transfer quenching of coumarin dyes in neat aniline and amine solvents.²²⁻²⁷ Nevertheless, the range of quenching rates observed ($0.01 \leq k_{1e} \leq 3$) $\times 10^{12}$ s⁻¹ is quite similar to the range previously reported for coumarins in substituted anilines.²⁵ The reorganization energy required for the ionic liquid reaction is, however, considerably larger (~ 1 eV) in part due to the greater polarity of the ionic liquid compared to weakly polar aniline solvents. Solvatochromic analyses indicate that solvation energies of coumarins in [Py₄][Tf₂N] are very close to those in acetonitrile solution, as expected from prior work.⁷² Bimolecular rate constants for oxidative quenching of coumarins by Py₄⁺ in dilute acetonitrile solution are also close to ($\sim 24\%$ smaller than) those for reductive quenching by anilines⁴⁴ at the same driving force. Thus, at least superficially, the present system shares much in common with the coumarin dye + substitute aniline system. Preliminary experiments on the related ionic liquid [Py₄][BF₄] suggest that corresponding measurements should be possible in a range of pyridinium ionic liquids, potentially enabling both the driving force and solvent/solvation dynamics to be systematically varied. Dilution with a non-reactive ionic liquid such as

[Im₄₁][Tf₂N] would also enable study of the dilution effect without changing the dynamics.

In the case of the most rapidly quenched coumarins, there is little to distinguish between the aniline and ionic liquid reactions. In both cases reaction is faster than most of the solvation response and occurs over time scales similar to the fastest solvation components. In contrast, quenching of slowly reacting coumarins spans a much larger range of times than in the cases available in the aniline systems. It seems reasonable to associate the more dispersive response with the slow and broadly distributed solvation characteristic of ionic liquids. Whether this association results from solvation dynamics controlling electron transfer, as in a number of intramolecular electron transfer reactions,^{19,20,86} or whether the generally slower motion in ionic liquids affects the small-amplitude motions that modulate the electronic coupling needed to achieve reaction is unclear at this point. More computational and theoretical work will be required in order to help clarify this distinction.

Acknowledgements

The authors thank Chris Rumble for his help in performing the KGE measurements reported here and Chris Gray and Tom Mallouk for assistance collecting and interpreting the cyclic voltammetry data. MS was funded for most of this work by the U.S. Department of Energy, Office of Basic Sciences, Division of Chemical Sciences, Geosciences, and Biosciences under award no. DE-SC0008640. Additional funding during the final stages of the work were provided by the U.S. National Science Foundation, award no. CHE-1665452. Any opinions, findings, and conclusions or recommendations expressed here are those of the authors and do not necessarily reflect the views of either of these funding agencies.

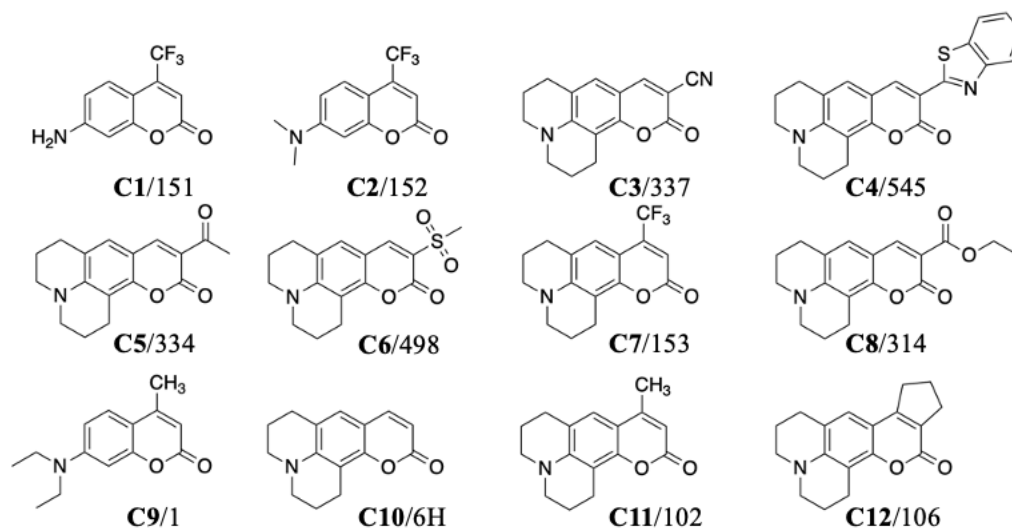


Figure 4.1: Structures and labels of the coumarin dyes used in this study. The bold numbering scheme **C1** – **C12** is ordered by increasing driving force for excited-state electron transfer. The second numbers shown are the Kodak designations except for **C4/545** and **C6/498**, where Exciton labels are used. (See also Table 4.1.)

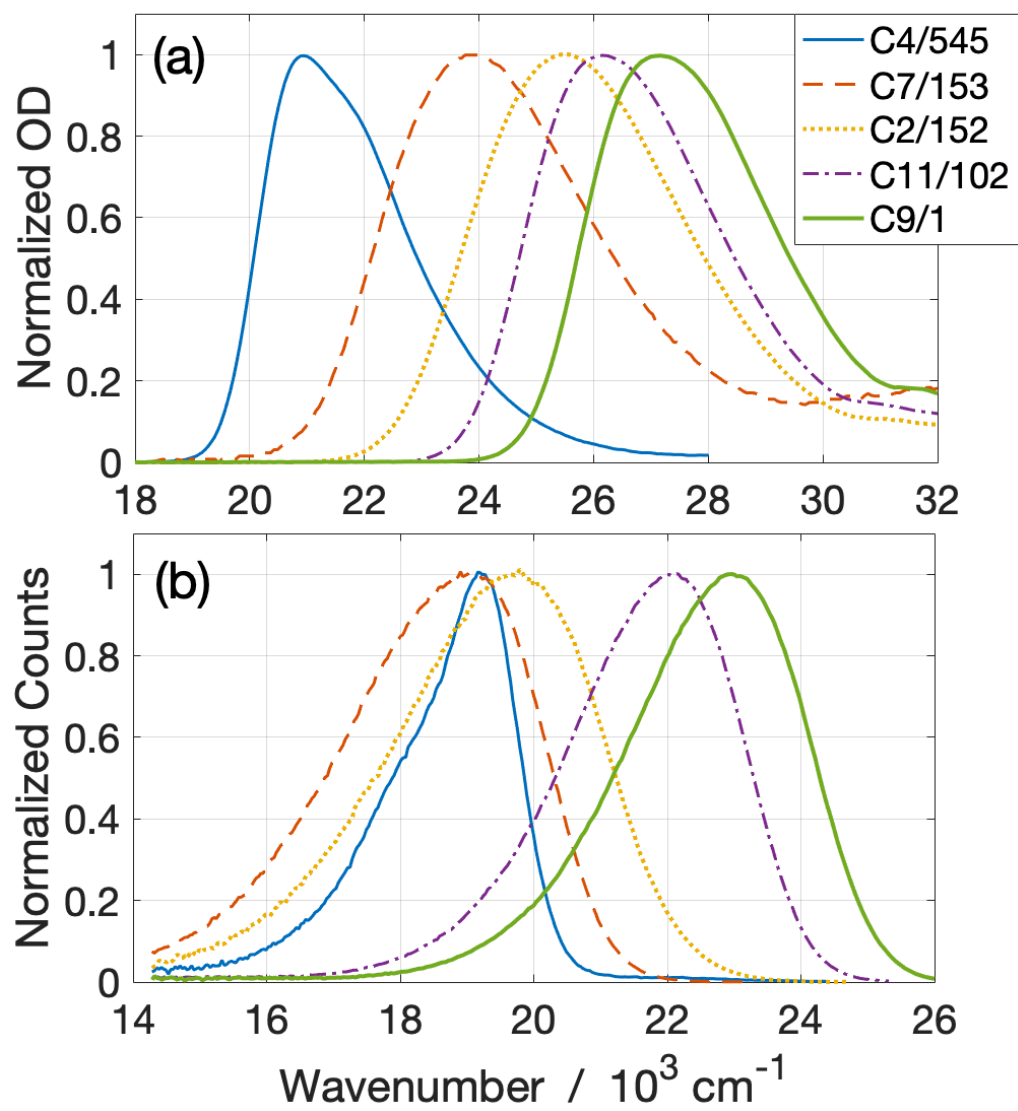


Figure 4.2: Normalized (a) absorption and (b) emission spectra of coumarins in acetonitrile.

Table 4.1: Measured Electronic Properties of Coumarins in Acetonitrile

Label	Kodak Label	CAS Registry Number	$\langle\nu\rangle_{\text{abs}}$ / 10^3 cm^{-1}	$\langle\nu\rangle_{\text{em}}$ / 10^3 cm^{-1}	ΔG_{00} / eV	Oxidation Potential (vs. SCE) / eV	$-\Delta G_{\text{ET}}$ / eV	τ_0 / ns
C1	151	53518-15-3	28.146	20.834	3.036(3)	(1.14(4))	0.53(4)	5.15
C2	152	53518-14-2	26.217	19.12	2.81(1)	0.91(2)	0.53(2)	2.08
C3	337	55804-68-7	22.104	18.488	2.67(1)	0.73(4)	0.58(2)	3.76
C4	545	85642-11-1	24.683	18.232	2.52(2)	(0.55(4))	0.60(4)	2.77
C5	334	55804-67-6	23.089	19.729	2.654(9)	0.67(2)	0.61(2)	3.4
C6	498	87331-48-4	24.011	20.039	2.73(1)	0.75(2)	0.61(2)	3.89
C7	153	53518-18-6	23.431	19.696	2.660(6)	0.67(2)	0.62(2)	5.68
C8	314	55804-66-5	23.921	20.22	2.736(7)	0.67(2)	0.70(2)	3.32
C9	1	91-44-1	28.079	22.473	3.134(5)	(0.73(3))	1.03(3)	3.35
C10	6H	58336-35-9	26.658	21.057	2.958(4)	0.45(2)	1.14(2)	3.96
C11	102	41267-76-9	27.079	21.532	3.013(4)	0.50(2)	1.14(2)	3.75
C12	106	41175-45-5	27.318	21.651	3.036(5)	0.45(2)	1.22(2)	3.53

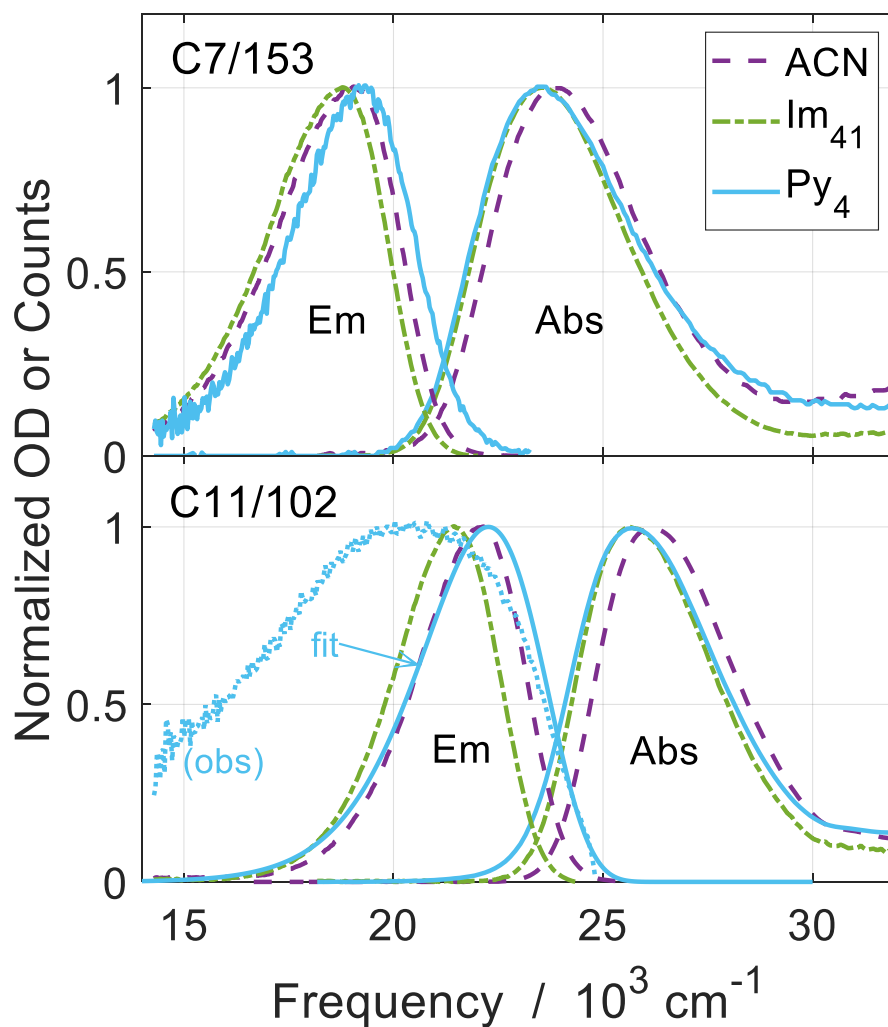


Figure 4.3: Representative absorption (Abs) and emission (Em) spectra of two coumarins in acetonitrile (ACN), $[\text{Im}_{41}][\text{Tf}_2\text{N}]$ (Im_{41}), and $[\text{Py}_4][\text{Tf}_2\text{N}]$ (Py_4). The bottom panel illustrates the emission observed (obs) in one of the dyes one of the three cases where emission from the solvent could not be adequately subtracted from the dye emission. The curve labeled “fit” is an estimate for the corrected emission of **C11** obtained from time-resolved spectra as described in Appendix Section B.1.

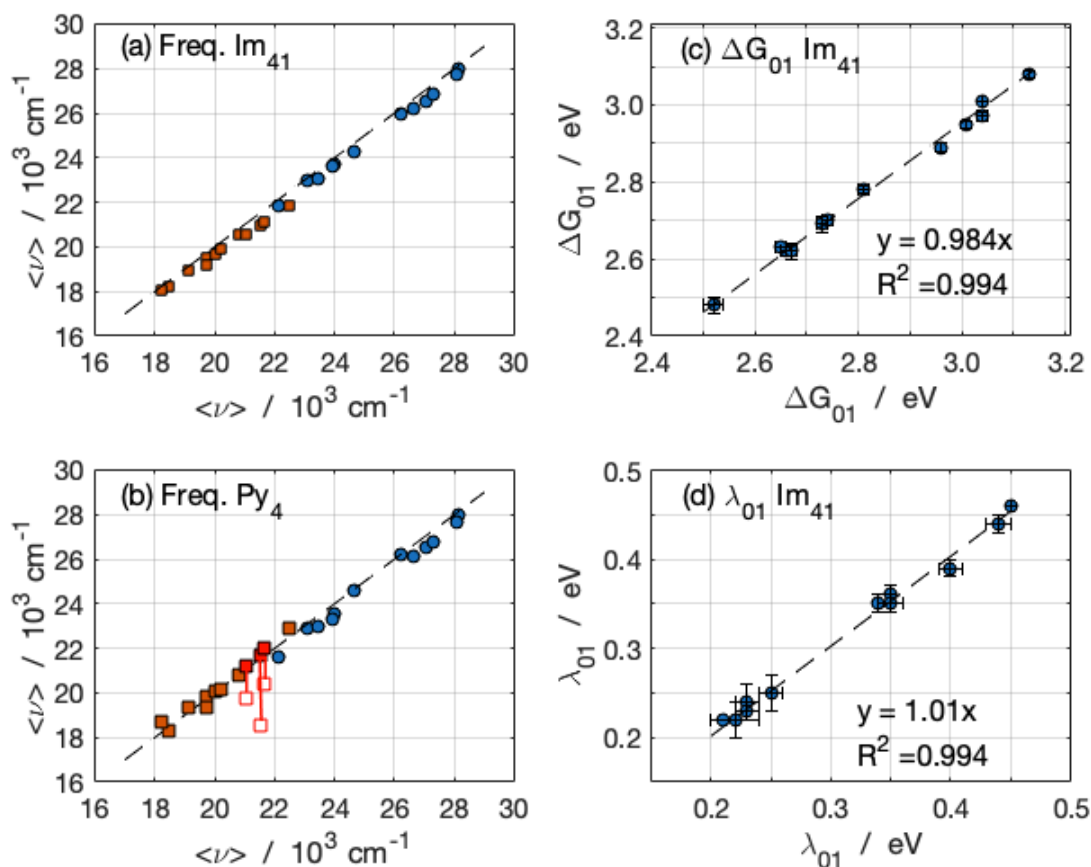


Figure 4.4: Comparisons of the first moment frequencies and the derivative quantities ΔG_{01} and λ_{01} (Eqs. 4.1 & 4.2) in the ionic liquids with these same quantities in acetonitrile (plotted on the abscissa). Panels (a) and (b) compare absorption ($\langle \nu_{abs} \rangle$, blue) and emission ($\langle \nu_{em} \rangle$, orange) frequencies in [Im₄₁][Tf₂N] and [Py₄][Tf₂N], respectively, to acetonitrile. Two values of $\langle \nu_{em} \rangle$ are shown in the case C10-C12 in [Py₄][Tf₂N]. The open symbols are the values measured from steady-state spectra and the filled symbols from fits using time-resolved spectra as described in Appendix Section B.1. The dashed lines in panels (a) and (b) indicated equality between frequencies in the two solvents. Panels (c) and (d) plot the free energy change and reorganization energy associated with the $S_0 \leftrightarrow S_1$ transition as defined in Eqs. 4.1 and 4.2. The lines are least-squares fits to the data.

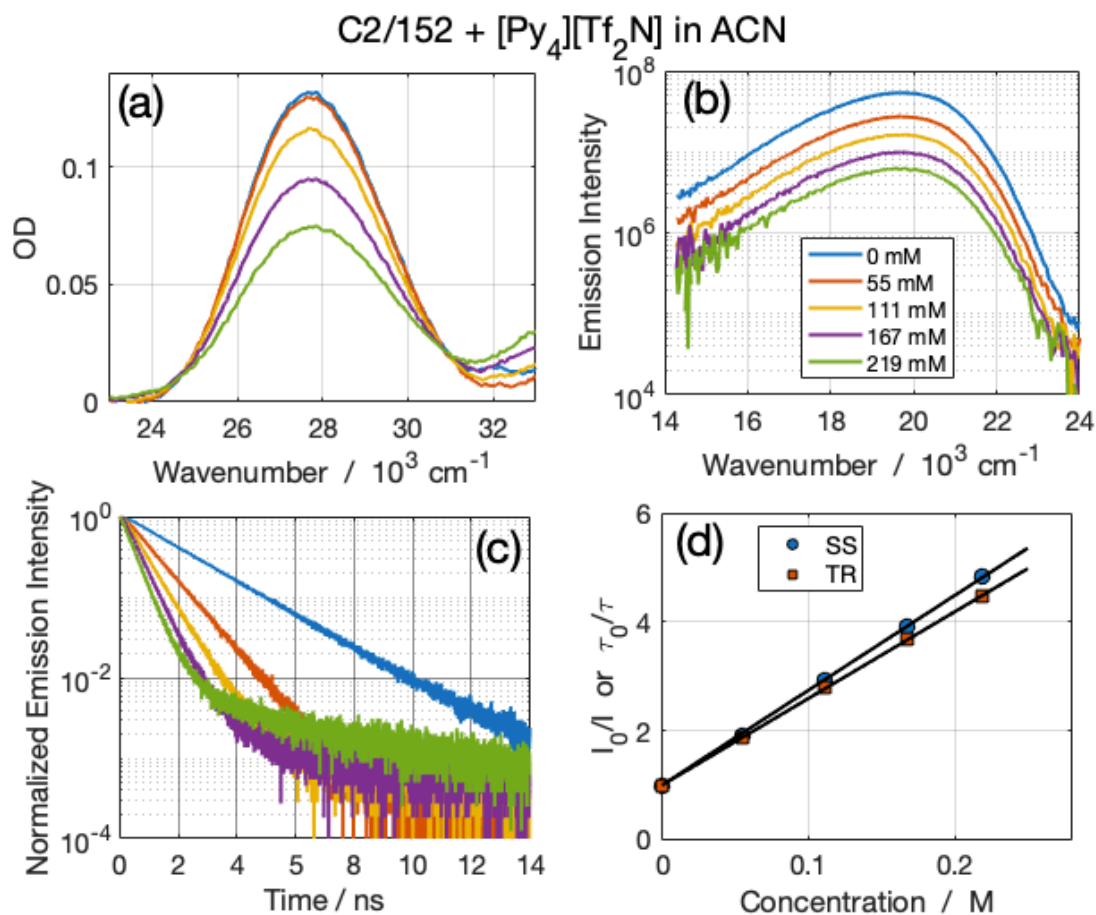


Figure 4.5: Example Stern-Volmer data for quenching of C2/152 by [Py₄][Tf₂N] in acetonitrile. Panels (a) and (b) show absorption and emission spectra and panel (c) emission decays recorded with TCSPC at the quencher concentrations shown. Panel (d) are plots of relative emission intensities and lifetimes (Eqs. 4.4 & 4.5) from which k_q values are determined.

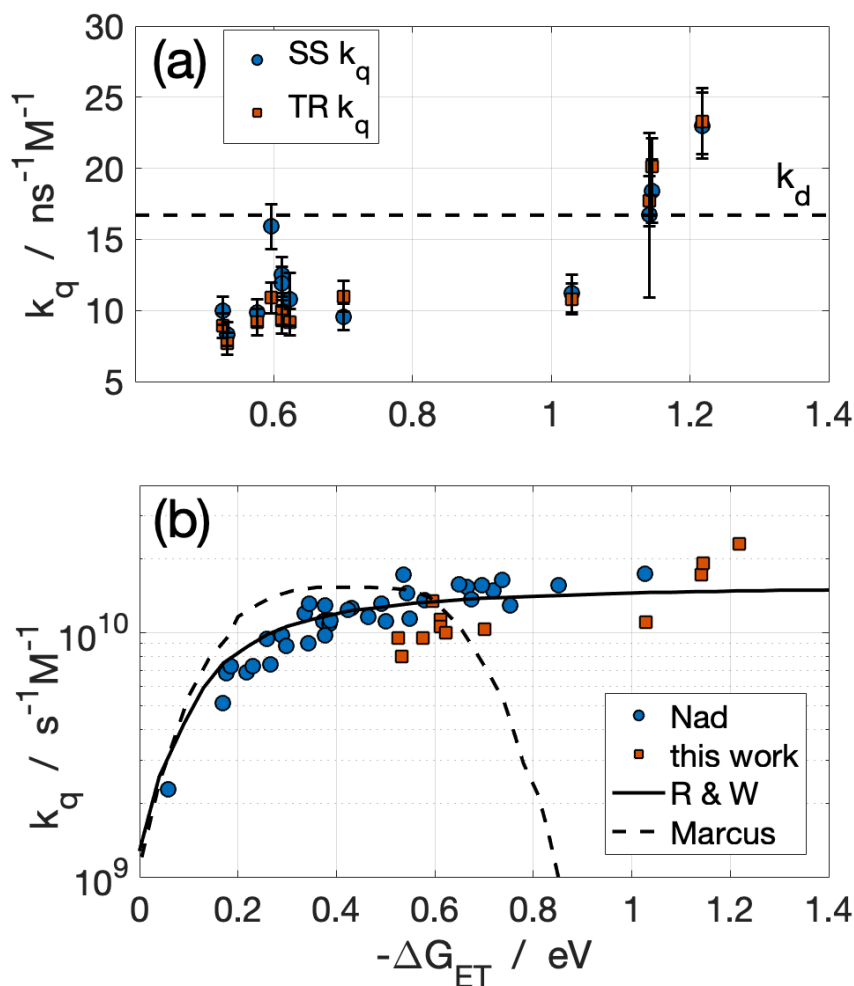


Figure 4.6: (a) Rate constants for quenching of coumarin dyes by $[\text{Py}_4][\text{Tf}_2\text{N}]$ in acetonitrile solution obtained from Stern-Volmer analysis of the steady-state spectra (blue circles) and emission lifetimes (red squares). The dashed line in this panel shows the predicted diffusion limited rate constant, k_d . (b) Average quenching constants obtained here (squares) compared to data on quenching of coumarin dyes by aromatic amines (circles) from Nad and Pal⁶⁶ (squares) and the a fit to the large collection of aromatic fluorophore quencher pairs reported by Rehm and Weller⁶⁶ (solid curve). The dashed curve is the dependence predicted by the classical Marcus theory (as provided in Ref.⁶⁶).

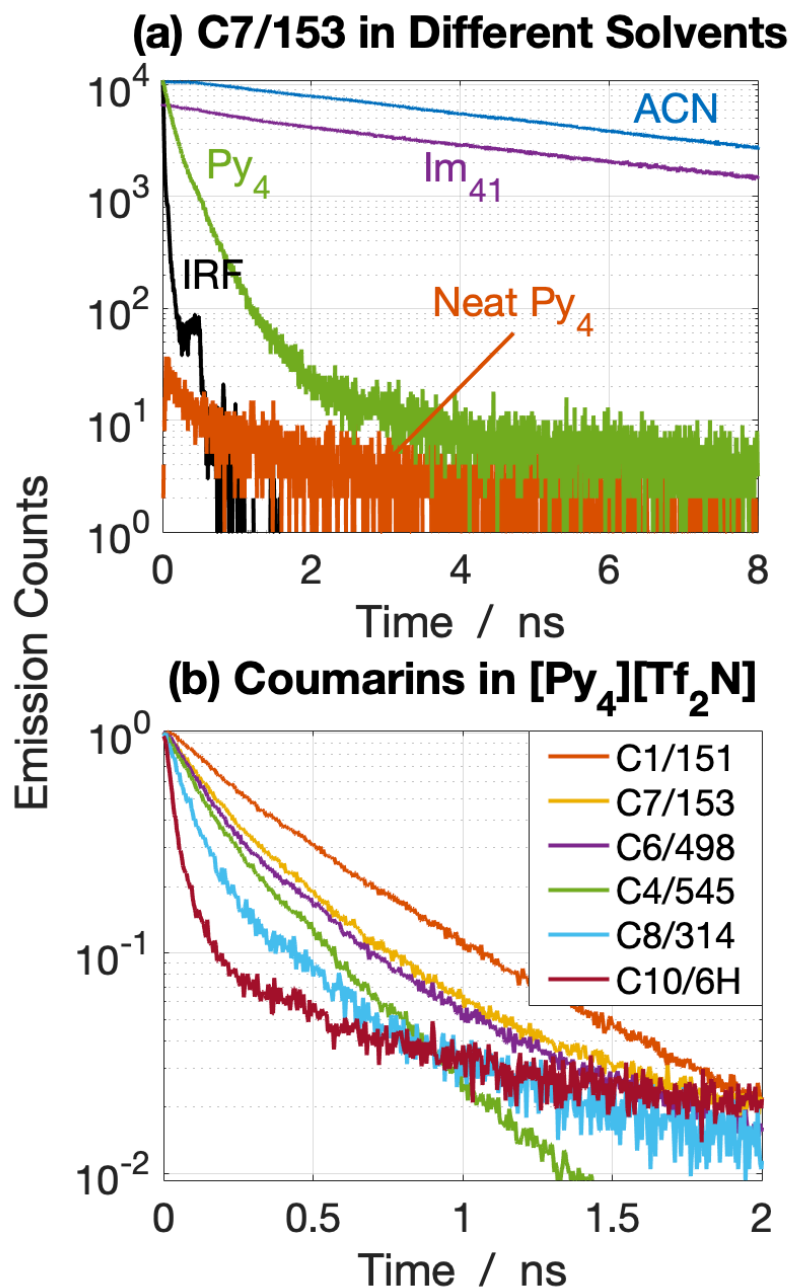


Figure 4.7: (a) Comparison of the emission decays of C7/153 in $[\text{Py}_4][\text{Tf}_2\text{N}]$ (Py_4) and with those in acetonitrile (ACN) and $[\text{Im}_{41}][\text{Tf}_2\text{N}]$ (Im_{41}). The black decay (IRF) is the TCSPC instrument response function and the data labeled “Neat Py_4 ” is the emission from impurities in the ionic liquid recorded under the same conditions as C7. (b) Emission decays of a selection of coumarin dyes in $[\text{Py}_4][\text{Tf}_2\text{N}]$.

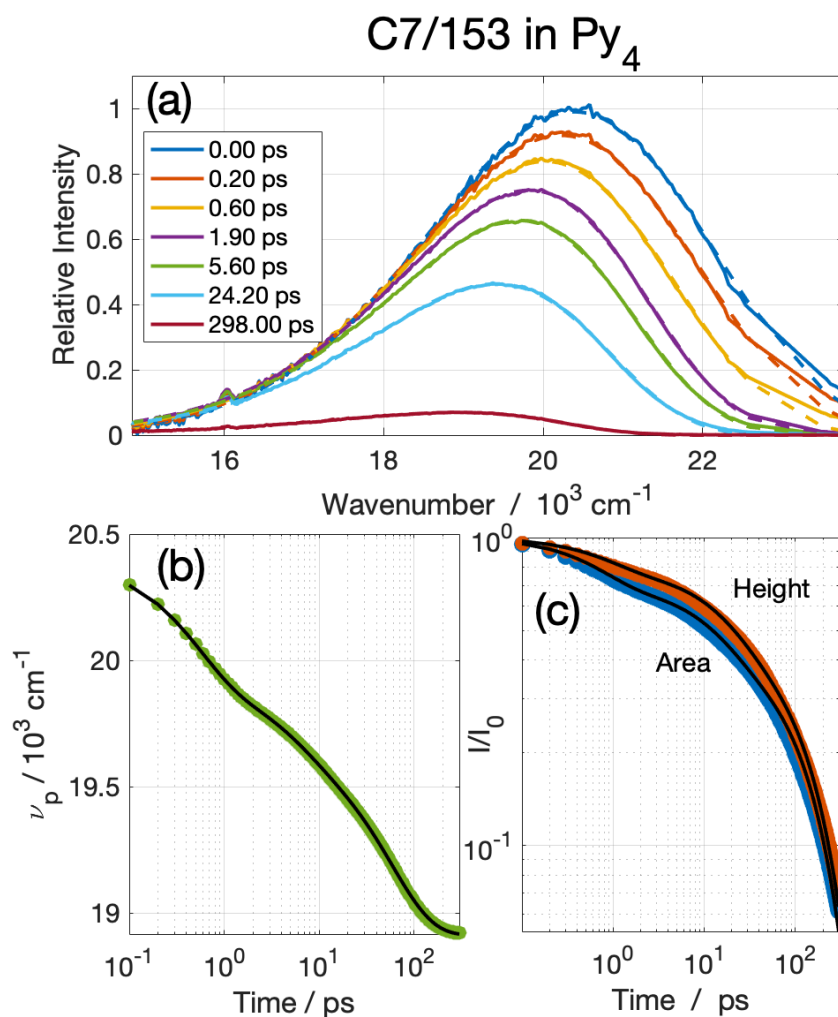


Figure 4.8: A representative KGE data set of C7/153 in [Py₄][Tf₂N]. (a) Time-resolved spectra (solid curves) and lognormal fits (dashed). (b) The peak frequency and (c) the normalized peak height and integrated area determined from the lognormal fits. Symbols in panels (b) and (c) are the KGE data and the curves are multi-exponential fits.

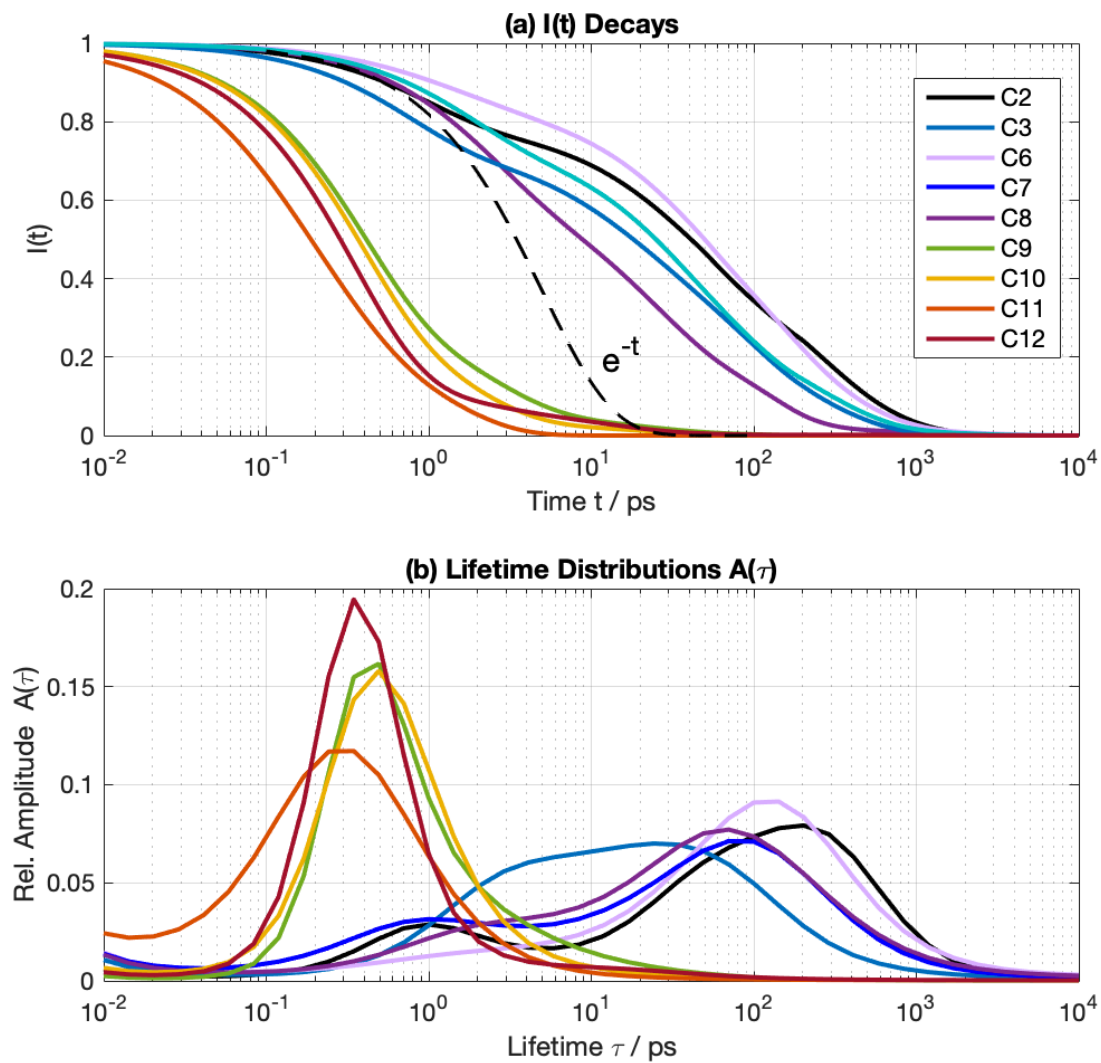


Figure 4.9: (a) Normalized intensity decays resulted from spliced decays from TCSPC and KGE. (b) Lifetime distributions from maximum entropy fits.

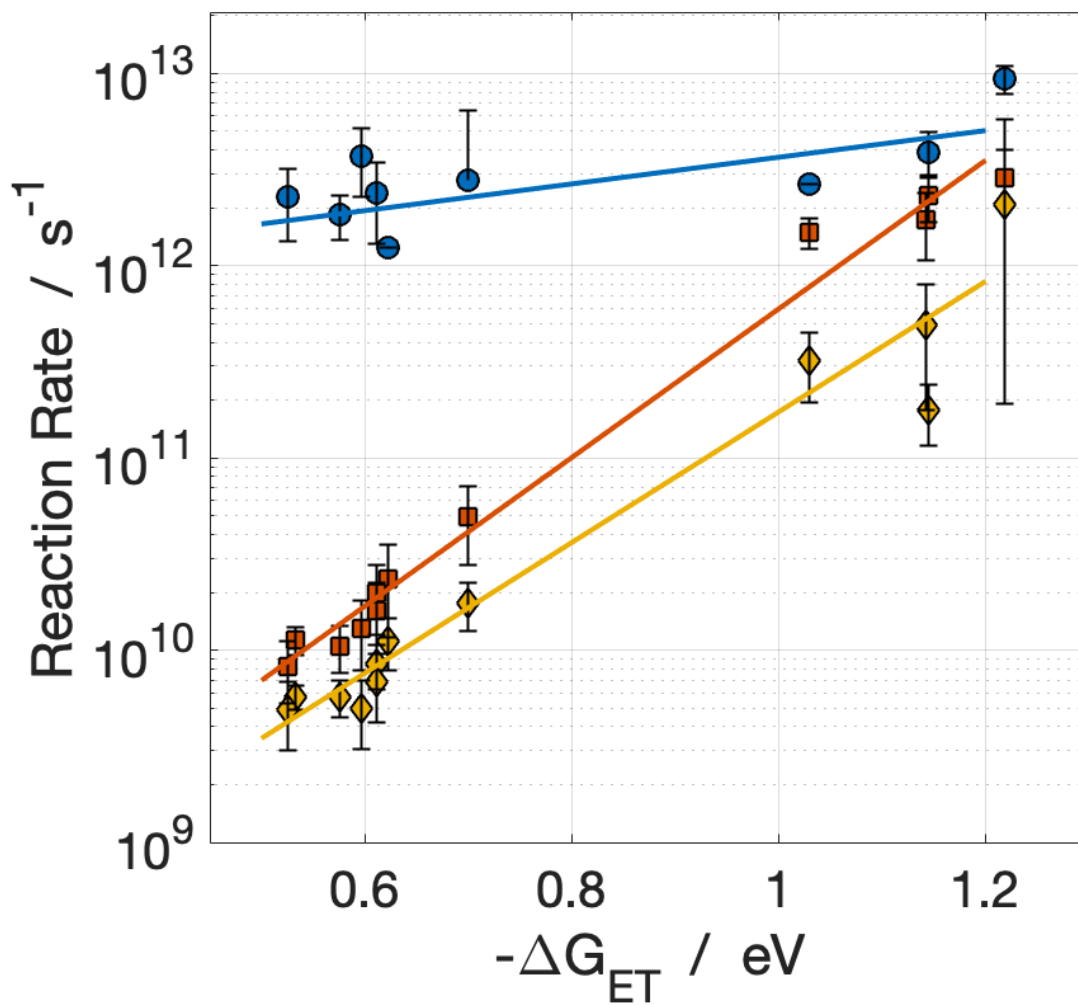


Figure 4.10: Characteristic rate coefficients obtained from emission decays in $[\text{Py}_4][\text{Tf}_2\text{N}]$ using Eqs. 4.6-4.8. The lines are fits to $k = A \exp(-b\Delta G_{ET})$. Slopes b are 1.6, 8.9, and 7.8 eV⁻¹ for k_0 , k_{le} , and k_{av} , respectively.

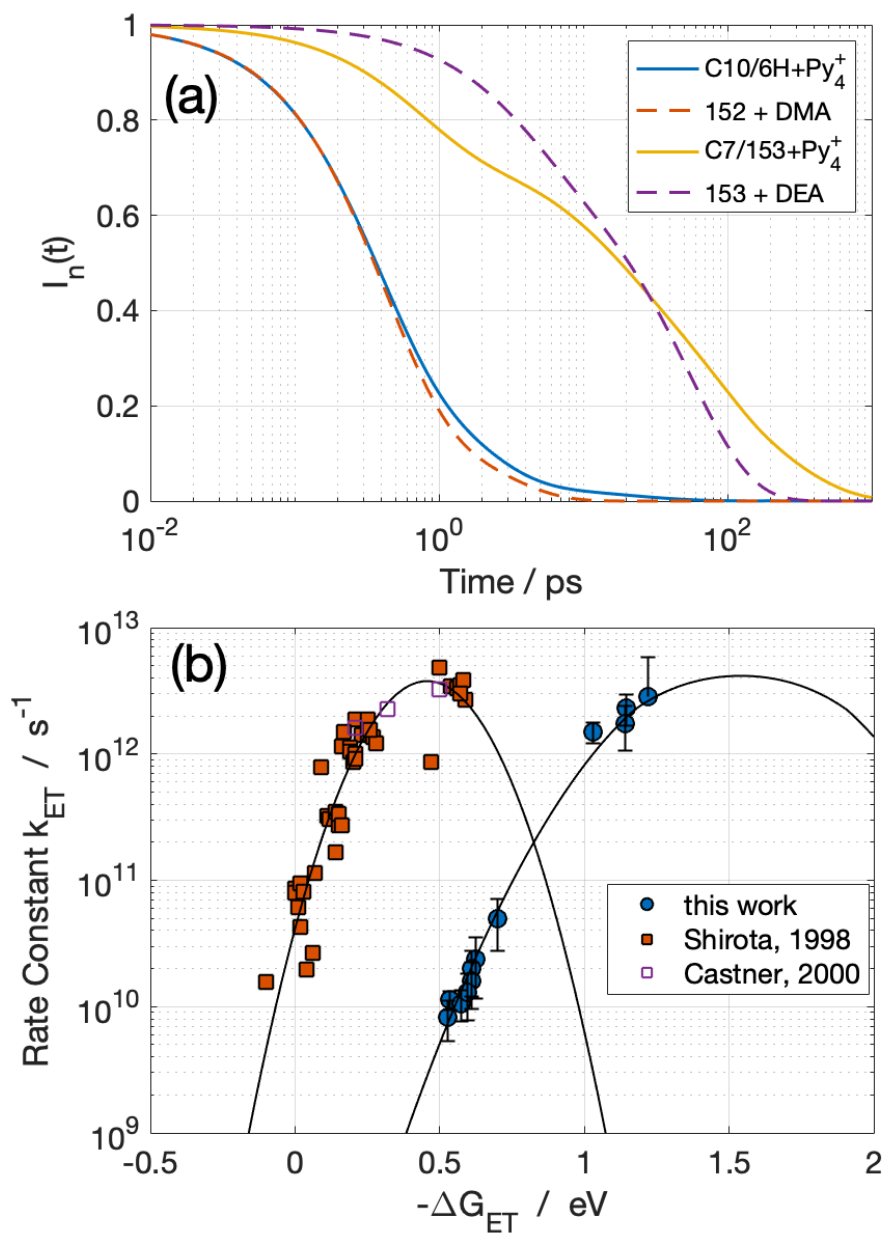


Figure 4.11: Comparison of the present results in [Py₄][Tf₂N] (solid curves and blue symbols) with literature data on quenching of coumarin dyes in aromatic amine solvents^{26,27} (dashed curves and orange symbols). Panel (a) shows pairs of normalized emission decays selected to have approximately the same t_{1e} values in the two solvents. DMA = dimethylaniline, DEA = diethylaniline. Panel (b) shows rate coefficients k_{1e} (points) and fits of these data to Eq. 9 (curves).

Table 4.2: Comparisons of ET Parameters in Redox-Active Liquids and Other Systems

Chromophores/Quenchers	Reference	Solvent	Dielectric	Reorganization Energy / eV	$\log(k_{\max}) / \text{s}^{-1}$
Redox-Active Liquids					
CSh of 12 coumarins in [Py ₄][Tf ₂ N]	this work	[Py ₄][Tf ₂ N]	~38	1.6	12.5
CS of 5 coumarins in 8 aniline solvents	Shirota 1998 ²⁹	anilines	~6	0.5	12.6
Charge Recombination in Contact Pairs					
DCA, TCA + 5 aromatic hydrocarbon donors	Gould 1987 ⁶⁹	acetonitrile	37.5	1.5	10.5
DCA + 21 assorted donors	Vauthey 1988 ⁷¹	acetonitrile	37.5	1.6	11.0
16 assorted donor-acceptor pairs	Mataga 1988 ⁷⁰	acetonitrile	37.5	1.5	11.0
Intramolecular D-A Dyads					
CS & CR in 3 porphyrin-quinone dyads	Wasielowski, 1985 ⁶⁷	butyronitrile	24.8	1.0	11.5
CS in porphyrin-imide dyads	Mataga 2001 ⁶⁸	acetonitrile	37.5	1.1	12.8
		triglyme	7.0	1.0	12.8
		THF	7.6	0.8	12.8

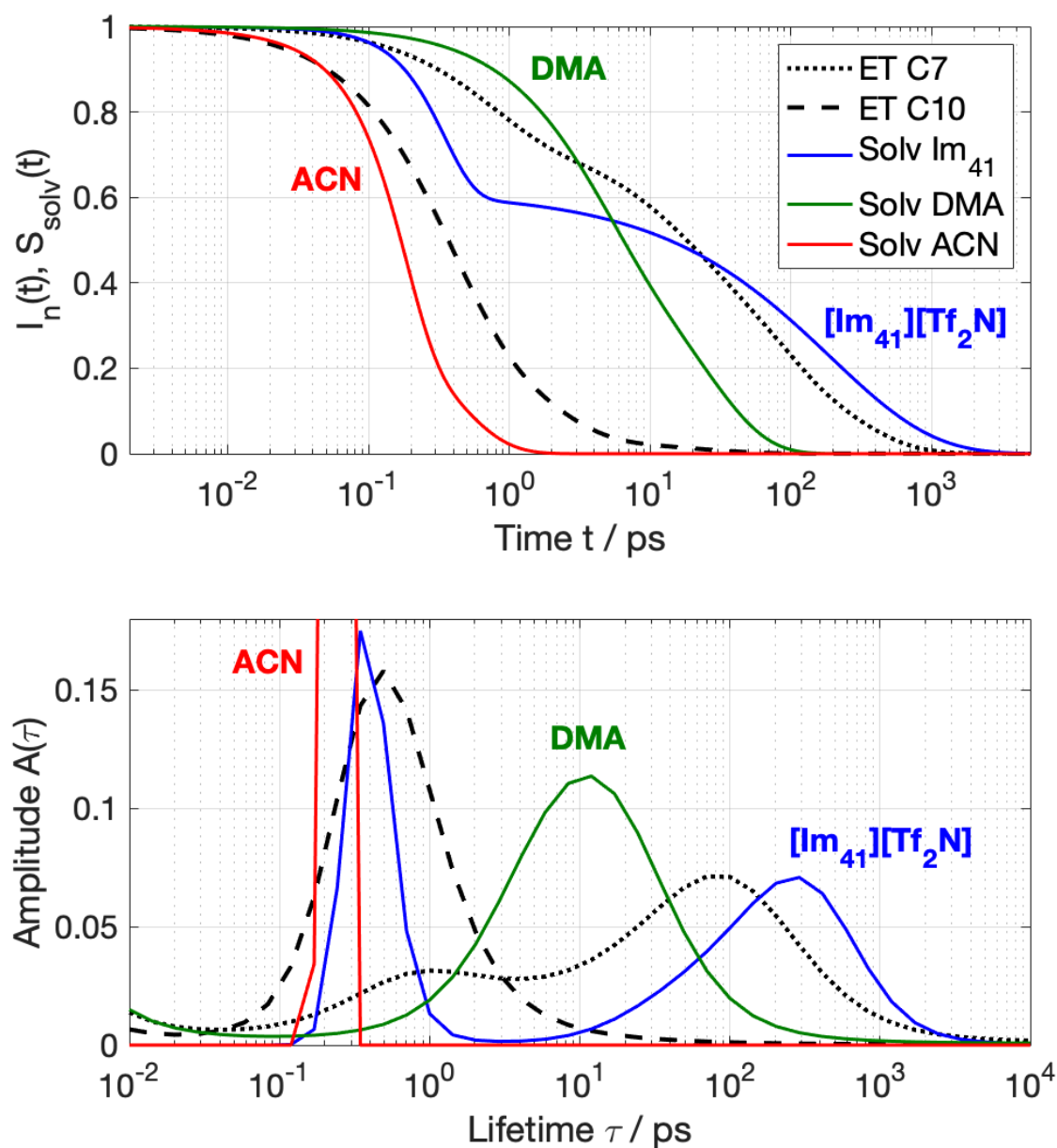


Figure 4.12: (a) Comparison of the emission decays, $I(t)$, of coumarins C7/153 and C10/6H in [Py₄][Tf₂N] with solvation response functions, $S(t)$, in [Im₄₁][Tf₂N] (Im₄₁, Ref. 72), dimethylaniline (DMA; Ref. 26) and acetonitrile (ACN, Ref. 85). (b) Lifetime distributions obtained from maximum entropy fits to the data in (a).

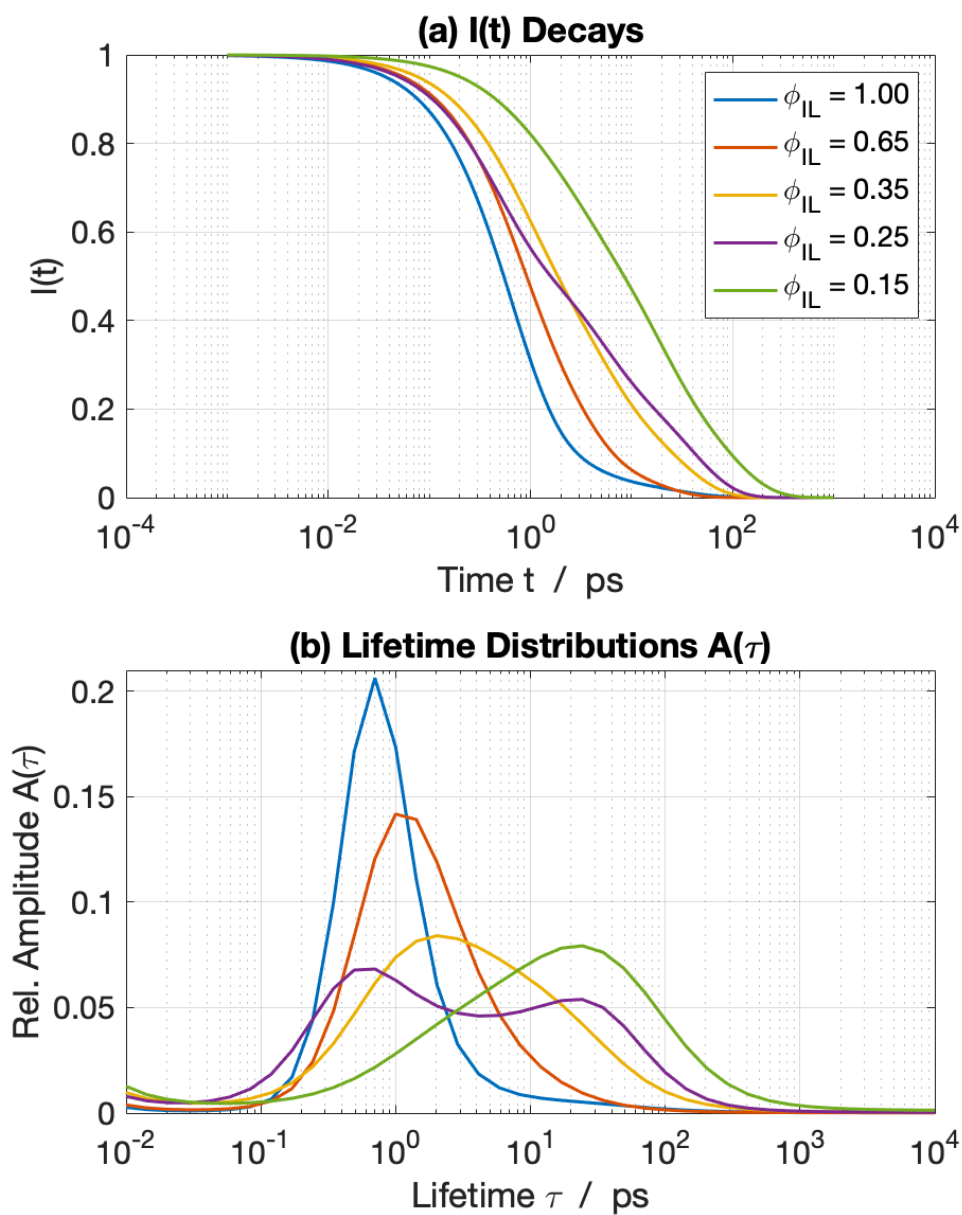


Figure 4.13: Representative (a) intensity decays and (b) lifetime distributions of C10/6H in [Py₄][Tf₂N] + acetonitrile mixtures.

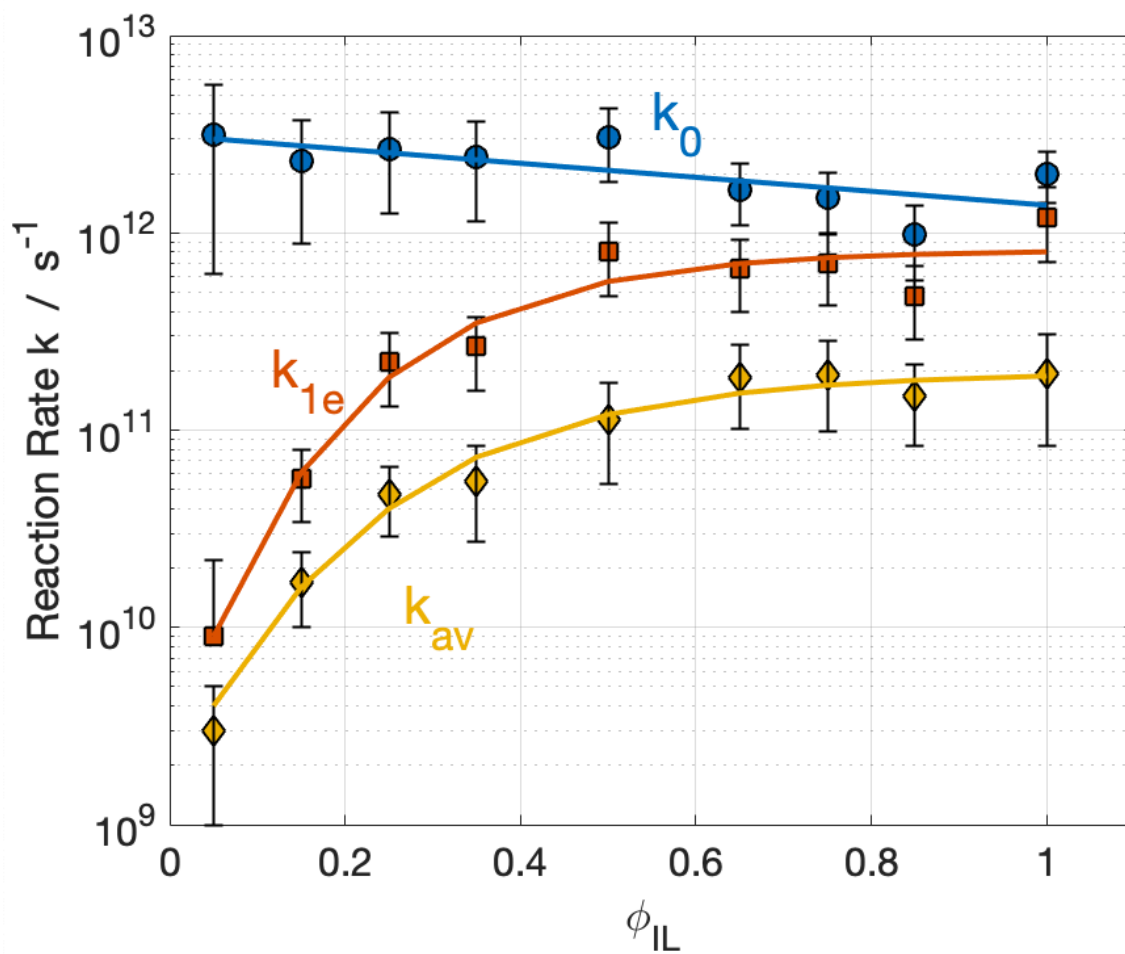


Figure 4.14: Characteristic rate coefficients obtained from emission decays **C10/6H** in $[\text{Py}_4][\text{Tf}_2\text{N}] + \text{acetonitrile}$ mixtures. Curves are only to guide the eye.

References

1. N. V. Plechkova and K. R. Seddon, "Applications of ionic liquids in the chemical industry," *Chem Soc Rev* **37**, 123-150 (2008). 10.1039/b006677j
2. R. S. Kalb, *Commercial Applications of Ionic Liquids* (Springer, 2020).
3. D. R. MacFarlane, N. Tachikawa, M. Forsyth, J. M. Pringle, P. C. Howlett, G. D. Elliott, J. H. Davis, M. Watanabe, P. Simon, and C. A. Angell, "Energy applications of ionic liquids," *Energy Environ. Sci.* **7**, 232-250 (2014). 10.1039/c3ee42099j
4. M. Watanabe, M. L. Thomas, S. Zhang, K. Ueno, T. Yasuda, and K. Dokko, "Application of Ionic Liquids to Energy Storage and Conversion Materials and Devices," *Chem. Rev. (Washington, DC, U. S.)* **117**, 7190-7239 (2017). 10.1021/acs.chemrev.6b00504
5. M. Liang, A. Kaintz, G. A. Baker, and M. Maroncelli, "Bimolecular Electron Transfer in Ionic Liquids: Are Reaction Rates Anomalously High?," *J. Phys. Chem. B* **116**, 1370-1384 (2012). 10.1021/jp210892c
6. A. Kaintz, G. Baker, A. Benesi, and M. Maroncelli, "Solute Diffusion in Ionic Liquids, NMR Measurements and Comparisons to Conventional Solvents," *The Journal of Physical Chemistry B* **117**, 11697-11708 (2013). 10.1021/jp405393d
7. M. Koch, A. Rosspeintner, G. Angulo, and E. Vauthey, "Bimolecular photoinduced electron transfer in imidazolium-based room-temperature ionic liquids is not faster than in conventional solvents," *J Am Chem Soc* **134**, 3729-3736 (2012). 10.1021/ja208265x
8. G. Angulo, A. Rosspeintner, M. Koch, and E. Vauthey, "Comment on 'Observation of the Marcus Inverted Region for Bimolecular Photoinduced Electron-Transfer Reactions in Viscous Media'," *J Phys Chem B* **120**, 9800-9803 (2016). 10.1021/acs.jpcc.6b06610
9. M. Kumbhakar and H. Pal, "Reply to 'Comment on 'Observation of the Marcus Inverted Region for Bimolecular Photoinduced Electron-Transfer Reactions in Viscous Media'," *J Phys Chem B* **120**, 9804-9809 (2016). 10.1021/acs.jpcc.6b07633
10. M. G. Kuzmin and I. V. Soboleva, "Analysis of transformations of the ultrafast electron transfer photoreaction mechanism in liquid solutions by the rate distribution approach," *Photochem. Photobiol. Sci.* **13**, 770-780 (2014). 10.1039/c3pp50388g
11. G. L. Closs and J. R. Miller, "Intramolecular long-distance electron transfer in organic molecules," *Science* **240**, 440-447 (1988). 10.1126/science.240.4851.440
12. *Electron Transfer- From Isolated Molecules to Biomolecules, Parts 1-2. [In: Adv. Chem. Phys., 1999; 106]*, Vol., edited by J. Jortner and M. Bixon (John Wiley & Sons, 1999).
13. J. V. Lockard and M. R. Wasielewski, "Intramolecular Electron Transfer within a Covalent, Fixed-Distance Donor-Acceptor Molecule in an Ionic Liquid," *Journal of Physical Chemistry B* **111**, 11638-11641 (2007).
14. N. Banerji, G. Angulo, I. Barabanov, and E. Vauthey, "Intramolecular Charge-Transfer Dynamics in Covalently Linked Perylene-Dimethylaniline and Cyanoperylene-Dimethylaniline," *Journal of Physical Chemistry A* **112**, 9665-9674 (2008).
15. Y. Nagasawa and H. Miyasaka, "Ultrafast solvation dynamics and charge transfer reactions in room temperature ionic liquids," *Phys. Chem. Chem. Phys.* **16**, 13008-13026 (2014). 10.1039/c3cp55465a
16. K. Sahu, S. J. Kern, and M. A. Berg, "Heterogeneous Reaction Rates in an Ionic Liquid: Quantitative Results from Two-Dimensional Multiple Population-Period Transient

- Spectroscopy," *Journal of Physical Chemistry A* **115**, 7984-7993 (2011). 10.1021/jp2046068
17. H. Y. Lee, J. B. Issa, S. S. Isied, E. W. Castner, Jr., Y. Pan, C. L. Hussey, K. S. Lee, and J. F. Wishart, "A Comparison of Electron-Transfer Dynamics in Ionic Liquids and Neutral Solvents," *J. Phys. Chem. C* **116**, 5197-5208 (2012). 10.1021/jp208852r
 18. J. A. DeVine, M. Labib, M. E. Harries, R. A. M. Rached, J. Issa, J. F. Wishart, and E. W. Castner, "Electron-Transfer Dynamics for a Donor-Bridge-Acceptor Complex in Ionic Liquids," *J. Phys. Chem. B* **119**, 11336-11345 (2015). 10.1021/acs.jpcc.5b03320
 19. X. Li, M. Liang, A. Chakraborty, M. Kondo, and M. Maroncelli, "Solvent-Controlled Intramolecular Electron Transfer in Ionic Liquids," *Journal of Physical Chemistry B* **115**, 6592-6607 (2011). 10.1021/jp200339e
 20. C. A. Rumble and M. Maroncelli, "Solvent controlled intramolecular electron transfer in mixtures of 1-butyl-3-methylimidazolium tetrafluoroborate and acetonitrile," *J. Chem. Phys.*, Ahead of Print (2018). 10.1063/1.5000727
 21. M. Saladin, C. A. Rumble, D. V. Wagle, G. A. Baker, and M. Maroncelli, "Characterization of a New Electron Donor-Acceptor Dyad in Conventional Solvents and Ionic Liquids," *J Phys Chem B* **123**, 9395-9407 (2019). 10.1021/acs.jpcc.9b07077
 22. Y. Nagasawa, A. P. Yartsev, K. Tominaga, P. B. Bisht, A. E. Johnson, and K. Yoshihara, "Dynamical Aspects of Ultrafast Intermolecular Electron Transfer Faster Than Solvation Process: Substituent Effects and Energy Gap Dependence," *J. Phys. Chem.* **99**, 653-662 (1995).
 23. K. Yoshihara, K. Tominaga, and Y. Nagasawa, "Effects of the solvent dynamics and vibrational motions in electron transfer," *Bull. Chem. Soc. Jpn.* **68**, 696-712 (1995). 10.1246/bcsj.68.696
 24. H. Pal, Y. Nagasawa, K. Tominaga, and K. Yoshihara, "Deuterium Isotope Effect on Ultrafast Intermolecular Electron Transfer," *J. Phys. Chem.* **100**, 11964-11974 (1996).
 25. H. Shirota, H. Pal, K. Tominaga, and K. Yoshihara, "Substituent Effect and Deuterium Isotope Effect of Ultrafast Intermolecular Electron Transfer: Coumarin in Electron-Donating Solvent," *J. Phys. Chem. A* **102**, 3089-3102 (1998). 10.1021/JP973376G
 26. H. Shirota, H. Pal, K. Tominaga, and K. Yoshihara, "Ultrafast intermolecular electron transfer in coumarin-hydrazine system," *Chem. Phys.* **236**, 355-364 (1998). 10.1016/S0301-0104(98)00218-3
 27. E. W. J. Castner, D. Kennedy, and R. J. Cave, "Solvent as Electron Donor: Donor/Acceptor Electronic Coupling Is a Dynamical Variable," *Journal of Physical Chemistry A* **104**, 2869-2885 (2000).
 28. H. N. Ghosh, S. Verma, and E. T. J. Nibbering, "Ultrafast Forward and Backward Electron Transfer Dynamics of Coumarin 337 in Hydrogen-Bonded Anilines As Studied with Femtosecond UV-Pump/IR-Probe Spectroscopy," *J. Phys. Chem. A* **115**, 664-670 (2011). 10.1021/jp108090b
 29. T. Kobayashi, Y. Takagi, H. Kandori, K. Kemnitz, and K. Yoshihara, "Femtosecond intermolecular electron transfer in diffusionless, weakly polar systems: Nile blue in aniline and N,N-dimethylaniline," *Chem. Phys. Lett.* **180**, 416-422 (1991). 10.1016/0009-2614(91)85142-J
 30. K. Yoshihara, Y. Nagasawa, A. Yartsev, S. Kumazaki, H. Kandori, A. E. Johnson, and K. Tominaga, "Femtosecond intermolecular electron transfer in condensed systems," *J. Photochem. Photobiol., A* **80**, 169-175 (1994). 10.1016/1010-6030(94)01038-2
 31. S. Engleitner, M. Seel, and W. Zinth, "Nonexponentialities in the Ultrafast Electron-Transfer Dynamics in the System Oxazine 1 in N,N-Dimethylaniline," *J. Phys. Chem. A* **103**, 3013-3019 (1999). 10.1021/JP9843712

32. Q.-H. Xu, G. D. Scholes, M. Yang, and G. R. Fleming, "Probing Solvation and Reaction Coordinates of Ultrafast Photoinduced Electron-Transfer Reactions Using Nonlinear Spectroscopies: Rhodamine 6G in Electron-Donating Solvents," *J. Phys. Chem. A* **103**, 10348-10358 (1999). 10.1021/jp991852s
33. S. Iwai, S. Murata, R. Katoh, M. Tachiya, K. Kikuchi, and Y. Takahashi, "Ultrafast charge separation and exciplex formation induced by strong interaction between electron donor and acceptor at short distances," *J. Chem. Phys.* **112**, 7111-7117 (2000). 10.1063/1.481326
34. V. O. Saik, A. A. Goun, and M. D. Fayer, "Photoinduced electron transfer and geminate recombination for photoexcited acceptors in a pure donor solvent," *J. Chem. Phys.* **120**, 9601-9611 (2004). 10.1063/1.1712826
35. L.-l. Jiang, W.-l. Liu, Y.-f. Song, X. He, Y. Wang, C. Wang, H.-l. Wu, F. Yang, and Y.-q. Yang, "Photoinduced intermolecular electron transfer and off-resonance Raman characteristics of Rhodamine 101/N,N-diethylaniline," *Chem. Phys.* **429**, 12-19 (2014). 10.1016/j.chemphys.2013.11.011
36. G. C. Walker, E. Aakesson, A. E. Johnson, N. E. Levinger, and P. F. Barbara, "Interplay of solvent motion and vibrational excitation in electron-transfer kinetics: experiment and theory," *J. Phys. Chem.* **96**, 3728-3736 (1992). 10.1021/j100188a032
37. P. O. J. Scherer, "Microscopic Models for Ultrafast Photoinduced Solvent to Dye Electron Transfer in DMA/Oxazine Solution," *J. Phys. Chem. A* **104**, 6301-6307 (2000). 10.1021/jp0006983
38. P. O. J. Scherer and M. Tachiya, "Computer simulation studies of electron transfer parameters for cyanoanthracene/N,N-dimethylaniline solutions," *J. Chem. Phys.* **118**, 4149-4156 (2003). 10.1063/1.1541617
39. G. Angulo, A. Cuetos, A. Rosspeintner, and E. Vauthey, "Experimental Evidence of the Relevance of Orientational Correlations in Photoinduced Bimolecular Reactions in Solution," *J. Phys. Chem. A* **117**, 8814-8825 (2013). 10.1021/jp407203r
40. B. Wu, M. Maroncelli, and E. W. Castner, Jr., "Photoinduced Bimolecular Electron Transfer in Ionic Liquids," *J Am Chem Soc* **139**, 14568-14585 (2017). 10.1021/jacs.7b07611
41. M. Porel, C. H. Chuang, C. Burda, and V. Ramamurthy, "Ultrafast photoinduced electron transfer between an incarcerated donor and a free acceptor in aqueous solution," *J Am Chem Soc* **134**, 14718-14721 (2012). 10.1021/ja3067594
42. S. Pandey, L. E. Roy, W. E. Acree, Jr., and J. C. Fetzer, "Examination of dodecylpyridinium chloride as a potentially selective fluorescence quenching agent for discriminating between alternant versus nonalternant polycyclic aromatic hydrocarbons," *Talanta* **48**, 1103-1110 (1999). 10.1016/s0039-9140(98)00332-4
43. A. Yadav, S. Trivedi, V. Haridas, J. B. Essner, G. A. Baker, and S. Pandey, "Effect of ionic liquid on the fluorescence of an intramolecular exciplex forming probe," *Photochem Photobiol Sci* **19**, 251-260 (2020). 10.1039/c9pp00458k
44. S. Nad and H. Pal, "Electron Transfer from Aromatic Amines to Excited Coumarin Dyes: Phosphorescence Quenching and Picosecond Transient Absorption Studies," *J. Phys. Chem. A* **104**, 673-680 (2000).
45. S. Nad and H. Pal, "Electron transfer from diphenyl and triphenyl amines to excited coumarin dyes," *Journal of Photochemistry and Photobiology A: Chemistry* **134**, 9-15 (2000). 10.1016/s1010-6030(00)00240-9
46. J. A. Gardecki and M. Maroncelli, "Set of secondary emission standards for calibration of the spectral responsivity in emission spectroscopy," *Appl Spectrosc* **52**, 1179-1189 (1998). Doi 10.1366/0003702981945192

47. J. Breffke, B. W. Williams, and M. Maroncelli, "The Photophysics of Three Naphthylmethylene Malononitriles," *Journal of Physical Chemistry B* **119**, 9254-9267 (2015). 10.1021/jp509882q
48. S. Arzhantsev and M. Maroncelli, "Design and characterization of a femtosecond fluorescence spectrometer based on optical Kerr gating," *Appl Spectrosc* **59**, 206-220 (2005). Doi 10.1366/0003702053085007
49. C. A. Rumble, J. Breffke, and M. Maroncelli, "Solvation Dynamics and Proton Transfer in Diethylaminohydroxyflavone," *Journal of Physical Chemistry B* **121**, 630-637 (2017). 10.1021/acs.jpcc.6b12146
50. D. T. Sawyer, A. Sobkowiak, and J. L. Roberts, *Electrochemistry for Chemists*, 2nd ed. (Wiley, United Kingdom, 1995).
51. Y. Marcus, *The Properties of Solvents* (Wiley, New York, 1998).
52. M. Tariq, P. A. S. Forte, M. F. C. Gomes, J. N. C. Lopes, and L. P. N. Rebelo, "Densities and refractive indices of imidazolium- and phosphonium-based ionic liquids: Effect of temperature, alkyl chain length, and anion," *J. Chem. Thermodyn.* **41**, 790-798 (2009).
53. A. Nazet, S. Sokolov, T. Sonnleitner, S. Friesen, and R. Buchner, "Densities, Refractive Indices, Viscosities, and Conductivities of Non-Imidazolium Ionic Liquids [Et3S][TFSI], [Et2MeS][TFSI], [BuPy][TFSI], [N8881][TFA], and [P14][DCA]," *J. Chem. Eng. Data* **62**, 2549-2561 (2017). 10.1021/acs.jced.7b00060
54. G. Jones, S. F. Griffin, C. Y. Choi, and W. R. Bergmark, "Electron Donor-Acceptor Quenching and Photoinduced Electron-Transfer for Coumarin Dyes," *J Org Chem* **49**, 2705-2708 (1984). DOI 10.1021/jo00189a010
55. C. A. M. Seidel, A. Schulz, and M. H. M. Sauer, "Nucleobase-specific quenching of fluorescent dyes .1. Nucleobase one-electron redox potentials and their correlation with static and dynamic quenching efficiencies," *J Phys Chem-Us* **100**, 5541-5553 (1996). DOI 10.1021/jp951507c
56. D. Zuniga-Nunez, P. Barrias, G. Cardenas-Jiron, M. S. Ureta-Zanartu, C. Lopez-Alarcon, F. E. Moran Vieyra, C. D. Borsarelli, E. I. Alarcon, and A. Aspee, "Atypical antioxidant activity of non-phenolic amino-coumarins," *RSC Adv.* **8**, 1927-1933 (2018). 10.1039/C7RA12000A
57. H. G. Roth, N. A. Romero, and D. A. Nicewicz, "Experimental and Calculated Electrochemical Potentials of Common Organic Molecules for Applications to Single-Electron Redox Chemistry," *Synlett* **27**, 714-723 (2016). 10.1055/s-0035-1561297
58. R. Raghavan and R. T. Iwamoto, "Characterization of the dimeric one-electron electrolytic reduction products of 1-alkylpyridinium ions in acetonitrile," *J. Electroanal. Chem. Interfacial Electrochem.* **92**, 101-114 (1978). 10.1016/S0022-0728(78)80120-X
59. D. S. McDaniel and H. C. Brown, "Extended table of Hammett substituent constants based on the ionization of substituted benzoic acids," *J. Org. Chem.* **23**, 420-427 (1958). 10.1021/jo01097a026
60. M. Tariq, P. J. Carvalho, J. A. P. Coutinho, I. M. Marrucho, J. N. C. Lopes, and L. P. N. Rebelo, "Viscosity of (C2-C14) 1-alkyl-3-methylimidazolium bis(trifluoromethylsulfonyl)amide ionic liquids in an extended temperature range," *Fluid Phase Equilib.* **301**, 22-32 (2011). 10.1016/j.fluid.2010.10.018
61. P. Dahiya, M. Kumbhakar, T. Mukherjee, and H. Pal, "Effect of protic solvents on twisted intramolecular charge transfer state formation in coumarin-152 and coumarin-481 dyes," *Chemical Physics Letters* **414**, 148-154 (2005).
62. G. Jones, W. R. Jackson, C.-y. Choi, and W. R. Bergmark, "Solvent effects on emission yield and lifetime for coumarin laser dyes. Requirements for a rotary decay mechanism," *J. Phys. Chem* **89**, 294-300 (1985).

63. Y. Nagasawa, A. P. Yartsev, K. Tominaga, P. B. Bisht, A. E. Johnson, and K. Yoshihara, "Dynamical Aspects of Ultrafast Intermolecular Electron Transfer Faster than Solvation Process: Substituent Effects and Energy Gap Dependence," *J. Phys. Chem* **99**, 653-662 (1995).
64. A. Pedone, "Role of solvent on charge transfer in 7-aminocoumarin dyes: New hints from TD-CAM-B3LYP and state specific PCM calculations," *Journal of Chemical Theory and Computation* **9**, 4087-4096 (2013).
65. P. K. Singh, S. Nath, M. Kumbhakar, A. C. Bhasikuttan, and H. Pal, "Quantitative distinction between competing intramolecular bond twisting and solvent relaxation dynamics: An ultrafast study," *J. Phys. Chem. A* **112**, 5598-5603 (2008).
66. D. Rehm and A. Weller, "Kinetics of fluorescence quenching by electron and hydrogen-atom transfer," *Isr. J. Chem.* **8**, 259-271 (1970).
67. S. S. Jayanthi and P. Ramamurthy, "Excited Singlet State Reactions of Triphenylpyrylium Ion with Electron Donors: Evidence for Electron Transfer and the Observation of Marcus Inverted Region for the Charge Shift in the Radical Pair," *J. Phys. Chem. A* **101**, 2016-2022 (1997). 10.1021/JP9639408
68. S. Fukuzumi, K. Ohkubo, T. Suenobu, K. Kato, M. Fujitsuka, and O. Ito, "Photoalkylation of 10-Alkylacridinium Ion via a Charge-Shift Type of Photoinduced Electron Transfer Controlled by Solvent Polarity," *J. Am. Chem. Soc.* **123**, 8459-8467 (2001). 10.1021/ja004311l
69. S. Nad and H. Pal, "Photoinduced electron transfer from aliphatic amines to coumarin dyes," *The Journal of Chemical Physics* **116**, 1658-1670 (2002). 10.1063/1.1415451
70. S. Farid, J. P. Dinnocenzo, P. B. Merkel, R. H. Young, D. Shukla, and G. Guirado, "Reexamination of the Rehm-Weller Data Set Reveals Electron Transfer Quenching That Follows a Sandros-Boltzmann Dependence on Free Energy," *J. Am. Chem. Soc.* **133**, 11580-11587 (2011). 10.1021/ja2024367
71. S. Farid, J. P. Dinnocenzo, P. B. Merkel, R. H. Young, and D. Shukla, "Bimolecular Electron Transfers That Follow a Sandros-Boltzmann Dependence on Free Energy," *J. Am. Chem. Soc.* **133**, 4791-4801 (2011). 10.1021/ja104536j
72. X.-X. Zhang, M. Liang, N. P. Ernsting, and M. Maroncelli, "Complete Solvation Response of Coumarin 153 in Ionic Liquids," *The Journal of Physical Chemistry B* **117**, 4291-4304 (2013). 10.1021/jp305430a
73. M. R. Wasielewski, M. P. Niemczyk, W. A. Svec, and E. B. Pewitt, "Dependence of rate constants for photoinduced charge separation and dark charge recombination on the free energy of reaction in restricted-distance porphyrin-quinone molecules," *J. Am. Chem. Soc.* **107**, 1080-1082 (1985). 10.1021/ja00290a066
74. N. Mataga, H. Chosrowjan, Y. Shibata, N. Yoshida, A. Osuka, T. Kikuzawa, and T. Okada, "First Unequivocal Observation of the Whole Bell-Shaped Energy Gap Law in Intramolecular Charge Separation from S2 Excited State of Directly Linked Porphyrin-Imide Dyads and Its Solvent-Polarity Dependencies," *J. Am. Chem. Soc.* **123**, 12422-12423 (2001). 10.1021/ja010865s
75. I. R. Gould, D. Ege, S. L. Mattes, and S. Farid, "Return electron transfer within geminate radical ion pairs. Observation of the Marcus inverted region," *J. Am. Chem. Soc.* **109**, 3794-3796 (1987). 10.1021/ja00246a055
76. N. Mataga, T. Asahi, Y. Kanda, T. Okada, and T. Kakitani, "The bell-shaped energy gap dependence of the charge recombination reaction of geminate radical ion pairs produced by fluorescence quenching reaction in acetonitrile solution," *Chem. Phys.* **127**, 249-261 (1988). 10.1016/0301-0104(88)87122-2

77. E. Vauthey, P. Suppan, and E. Haselbach, "Free-energy dependence of the ion yield of photo-induced electron-transfer reactions in solution," *Helv. Chim. Acta* **71**, 93-99 (1988). 10.1002/hlca.19880710111
78. J. Jortner and M. Bixon, "Intramolecular vibrational excitations accompanying solvent-controlled electron transfer reactions," *J. Chem. Phys.* **88**, 167-170 (1988). 10.1063/1.454632
79. H. Sumi and R. A. Marcus, "Dynamical effects in electron transfer reactions," *J. Chem. Phys.* **84**, 4894-4914 (1986). 10.1063/1.449978
80. A. Morandeira, A. Fuerstenberg, J.-C. Gummy, and E. Vauthey, "Fluorescence Quenching in Electron-Donating Solvents. 1. Influence of the Solute-Solvent Interactions on the Dynamics," *J. Phys. Chem. A* **107**, 5375-5383 (2003). 10.1021/jp0343133
81. A. Morandeira, A. Fürstenberg, and E. Vauthey, "Fluorescence Quenching in Electron-Donating Solvents. 2. Solvent Dependence and Product Dynamics," *J. Phys. Chem. C* **108**, 8190-8200 (2004).
82. M. G. Kuzmin, I. V. Soboleva, and E. V. Dolotova, "Evolution of the reaction mechanism during ultrafast photoinduced electron transfer," *J. Phys. Chem. A* **112**, 5131-5137 (2008). 10.1021/jp8004794
83. B. T. Conway, "Molecular Dynamics Simulations of Ionic Liquids and Ionic liquid - Conventional Solvent Mixtures," The Pennsylvania State University, 2019.
84. G. Zhu, L. Zhang, Y. Wang, X. Xu, and X. Peng, "Interactions between pyrene and pyridinium ionic liquids studied by ultraviolet-visible spectroscopy," *J. Mol. Liq.* **213**, 289-293 (2016). 10.1016/j.molliq.2015.11.026
85. M. Liang, X.-X. Zhang, A. Kaintz, N. P. Ernsting, and M. Maroncelli, "Solvation Dynamics in a Prototypical Ionic Liquid + Dipolar Aprotic Liquid Mixture: 1-Butyl-3-methylimidazolium Tetrafluoroborate + Acetonitrile," *J. Phys. Chem. B* **118**, 1340-1352 (2014). 10.1021/jp412086t
86. E. W. Castner, Jr., C. J. Margulis, M. Maroncelli, and J. F. Wishart, "Ionic liquids: structure and photochemical reactions," *Annu Rev Phys Chem* **62**, 85-105 (2011). 10.1146/annurev-physchem-032210-103421

Chapter 5

Summary and Future Work

Ionic liquids provide a relatively new liquid medium, one composed entirely of ions, in which to do chemistry. For over a decade, the Maroncelli group has studied the physical properties of ionic liquids, seeking to understand how chemical reactions might differ in ionic liquids compared to conventional solvents. Motivation for this work is partly curiosity and partly because such an understanding should help guide and expand the use of ionic liquids in a variety of applications. Of most interest to the present work, ionic liquids have a number of advantages as potential electrolytes in a number of energy technologies. Before a broad implementation in these technologies, a better understanding of the effects of a purely ionic environment on electron transfer is needed.

Early studies of bimolecular electron transfer between dilute donors and acceptors in ionic liquids provided some insights on the distinctions between electron transfer in ionic and conventional dipolar liquids. However, due to the difficulty of accurately modeling reactant diffusion in ionic liquids, complex analyses are required to separate out the diffusive and actual electron transfer components of the overall reaction.^{1,2} This dissertation describes two methods of studying electron transfer between an electron donor and acceptor without the need to consider the diffusional component to bimolecular reaction: (1) electron transfer in a new donor-acceptor intramolecular dyad and (2) in a neat ionic liquid that acts as an electron acceptor to photo-excited reactants.

In the first project, a new donor-acceptor dyad was characterized in both conventional solvents and ionic liquids. The dyad was composed of coumarin 152 and dimethylaniline components, a commonly used bimolecular pairing, linked by a methylene bridge. While the conformational flexibility of the dyad was an initial concern, it was found that this flexibility only caused the kinetics to be distributed over a small range, unlike several other dyads previously created for such studies.^{3,4} Electron transfer rates measured in the dyad were similar to those estimated from contact pairs of coumarin 152 and dimethylaniline in the corresponding bimolecular reaction. Reaction rates of the dyad in over twenty different solvents were measured, including dipolar and quadrupolar liquids, solvent mixtures, and ionic liquids, and found to be strongly correlated with solvent polarity. The three ionic liquids studied and ethylene glycol deviated from this trend, presumably due to their much higher viscosities. The dependence on viscosity was confirmed based on temperature-dependent measurements, primarily in a single ionic liquid. This dependence was hypothesized to result either from the effect of viscosity on intramolecular motions required for reaction or from reaction being controlled by solvation, which slows roughly in proportion to viscosity. More experiments are needed to confirm dependence on viscosity/solvation time and to try to distinguish between these two factors.

One proposed set of experiments are measurements in a series of mixtures of acetonitrile and propylene carbonate.^{5,6} These two solvents have similar polarities, but very different viscosities ($\eta = 0.341$ and 2.53 mPa·s respectively). Using Kerr-gated emission spectroscopy, the quenching rate of the probe in these mixtures could be measured and the effect of viscosity studied in the absence of changes to reaction

energetics. Additionally, more ionic liquids should be tested for suitability with this probe, such as popular imidazoliums and pyrrolidiniums with different alkyl chain lengths or anion pairings to systematically vary physical properties. However, the ionic liquids will need to be carefully purified in order to avoid acidic impurities, which cause dissociation of the dyad.

In the second study, a pyridinium ionic liquid, $[\text{Py}_4][\text{Tf}_2\text{N}]$, was used as a neat electron-accepting solvent for reactions with twelve coumarin dyes. Characterization of these coumarins in studied in $[\text{Py}_4][\text{Tf}_2\text{N}]$, as well as acetonitrile and a nonreactive imidazolium ionic liquid showed that despite the differences in viscosity and ionicity, the electronic states of the coumarins were quite similar among the three solvents. This similarity allowed for accurate estimation of the reaction free energy of the electron transfer in the neat ionic liquid using measurements in acetonitrile. In this manner, reaction energies were found to vary over a 0.7 eV range. Electron transfer rates $[\text{Py}_4][\text{Tf}_2\text{N}]$ were measured using both TCSPC and KGE spectroscopy. The emission decays observed were broadly distributed in time, with overall rates that showed a strong dependence on the driving force for reaction. Further study is needed in order to distinguish between two alternative explanations for the quenching behavior observed: (i) reaction control via solvent fluctuations altering the reactant and product energies or (ii) control by small-amplitude relative reactant motions that affect the electronic coupling. Both of these factors should be slower in ionic liquids compared to conventional solvents and a combination of experimental and computational work will be needed to try to distinguish between these possibilities.

Future experimental work for this project should include measurements of the temperature dependence of the rates to examine how they relate to the viscosity of the ionic liquid. Additionally, a few more ionic liquids should be used as quenchers to understand the effects of properties such as viscosity and ion size. The most easily accessible liquids would be similar pyridinium ionic liquids with different alkyl chain lengths and paired with different anions. Especially valuable would be studies of liquids that form glasses, where quenching could be studied under conditions where reactants are immobilized. These ionic liquids need to be selected and/or carefully purified to ensure a sufficiently low level of fluorescing impurities for these studies. Finally, additional measurements of mixtures of reactive and nonreactive ionic liquids should be helpful in better defining how the electron transfer rate varies with the number of nearest neighbors reacting partners.

References

1. M. Liang, A. Kaintz, G. A. Baker, and M. Maroncelli, "Bimolecular Electron Transfer in Ionic Liquids: Are Reaction Rates Anomalously High?," *J. Phys. Chem. B* **116**, 1370-1384 (2012). 10.1021/jp210892c
2. B. Wu, M. Maroncelli, and E. W. Castner, Jr., "Photoinduced Bimolecular Electron Transfer in Ionic Liquids," *J Am Chem Soc* **139**, 14568-14585 (2017). 10.1021/jacs.7b07611
3. J. A. DeVine, M. Labib, M. E. Harries, R. A. M. Rached, J. Issa, J. F. Wishart, and E. W. Castner, "Electron-Transfer Dynamics for a Donor-Bridge-Acceptor Complex in Ionic Liquids," *J. Phys. Chem. B* **119**, 11336-11345 (2015). 10.1021/acs.jpcb.5b03320
4. H. Y. Lee, J. B. Issa, S. S. Isied, E. W. Castner, Jr., Y. Pan, C. L. Hussey, K. S. Lee, and J. F. Wishart, "A Comparison of Electron-Transfer Dynamics in Ionic Liquids and Neutral Solvents," *J. Phys. Chem. C* **116**, 5197-5208 (2012). 10.1021/jp208852r
5. J. A. Gardecki and M. Maroncelli, "Solvation and rotational dynamics in acetonitrile/propylene carbonate mixtures: a binary system for use in dynamical solvent effect studies," *Chem. Phys. Lett.* **301**, 571-578 (1999).
6. C. A. Rumble, J. Breffke, and M. Maroncelli, "Solvation Dynamics and Proton Transfer in Diethylaminohydroxyflavone," *J. Phys. Chem. B* **121**, 630-637 (2017). 10.1021/acs.jpcb.6b12146

Appendix A

Supporting Information for Chapter 3

A.1 Acid-Catalyzed Decomposition of the Dyad and Impurity Emission

In the presence of traces of acid (e.g., HCl, acidic silica gel), the C152-DMA dyad undergoes decomposition via protonation at the 7-amino position of the coumarin ring. This protonation results in cleavage of the C–N bond between the benzylic carbon and nitrogen. Upon cleavage, the C–N bond electron pair migrates to the amine nitrogen, resulting in the formation of the highly fluorescent coumarin H152 molecule (Figure A.1) and an *N,N*-dimethyl-*p*-toluidine benzylic carbocation, which reacts with the conjugate base (e.g., Cl[−]) of the acid to form a stable byproduct.

As discussed in the text, emission decays of the dyad often contained a clearly separated slow component of small amplitude whose time constant was close to that of H152.

Figure A.2 shows the longest component of the dyad emission (τ_4) obtained from unconstrained multi-exponential fits plotted versus the lifetime of H152 (τ_{H152}) in various solvents. Only solvents for which the amplitude of τ_4 was $\leq 6\%$ are included. The values of τ_4 are systematically smaller than the τ_{H152} , with the average difference being 0.65 ns or -14%. This deviation is likely due to other components of the fits, all of which have shorter lifetimes, mixing in with these very small amplitude components. When this longest component is constrained to equal τ_{H152} the quality of the fit was not degraded and the changes to the other components were minor and had little impact on quantities

such as $\langle \tau \rangle_{\text{dyad}}$. Thus, treating this component as H152 impurity in the dyad samples seems safe and well justified.

Quantification the amount of impurity in various samples was attempted using HPLC. Use of a reversed-phase C18 column with a mobile phase of 25/75 vol% acetonitrile/water enabled clear separation of a peak due to H152 in select dyad samples at levels of less than a few percent. Unfortunately, neither electronic absorption nor emission detection provided reproducible concentrations.

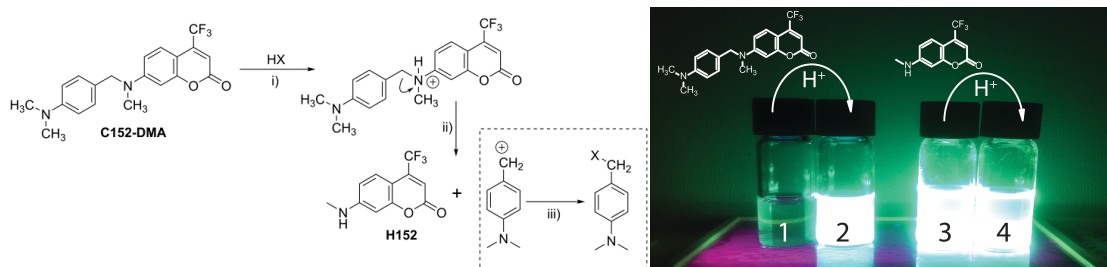


Figure A.1: *Left*: Mechanism of the acid-catalyzed decomposition of C152-DMA: (i) protonation; (ii) cleavage with concomitant formation of the highly fluorescent by product H152; and (iii) carbocation scavenging. *Right*: Vials 1 and 2 show C152-DMA dissolved in ethanol containing one drop of water (vial 1) or one drop of 0.1 N HCl (vial 2). The dye cleavage is essentially instantaneous upon acid addition leading to the fluorescent product H152. Vials 3 and 4 show the aminocoumarin H152 in ethanol, in the absence and presence of a drop of HCl, respectively. Under UV lamp excitation, no visual difference was discernable for these two samples.

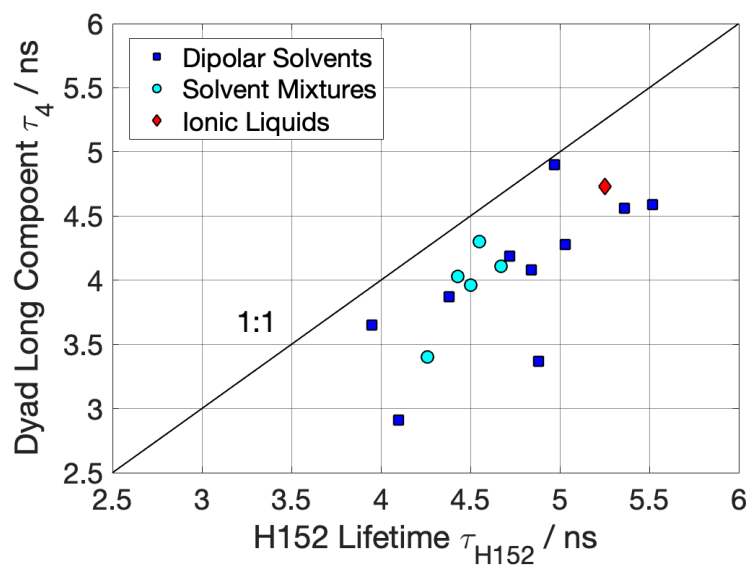


Figure A.2: Comparison of the longest lifetime component (τ_4) of the dyad with the lifetime of H152. Dyad decays were fit to 4 exponential components without any constraints on the time constants. Only solvents in which the longest lifetime dyad component accounted for $\leq 6\%$ of the amplitude are included.

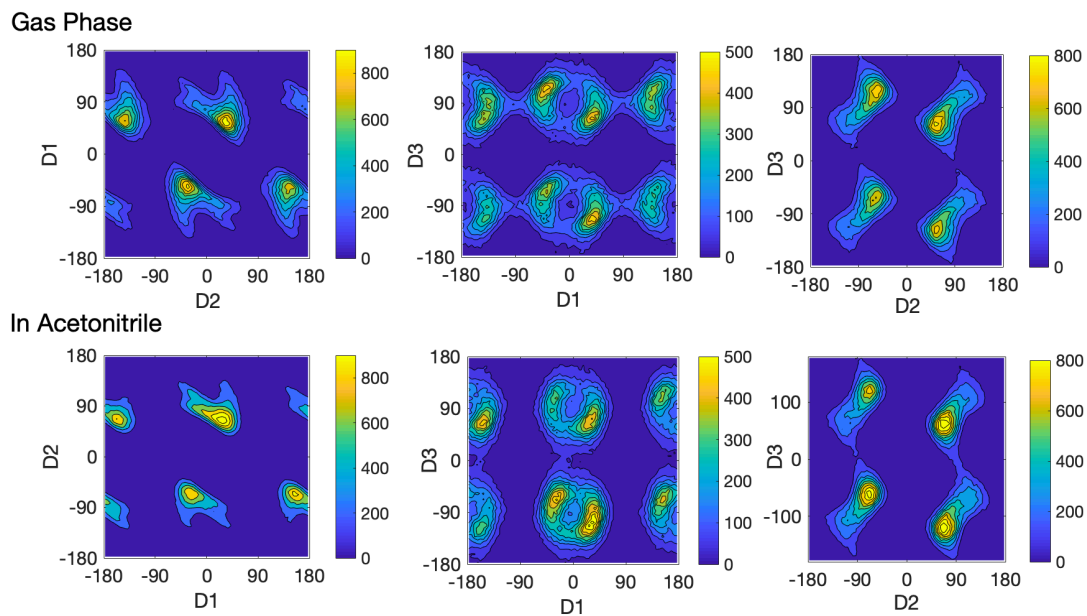


Figure A.3: 2d representations of dyad conformational distributions in the gas-phase and in acetonitrile solution. The values indicated here are the numbers of occurrences out of 5×10^5 samples. Angles are measured in degrees.

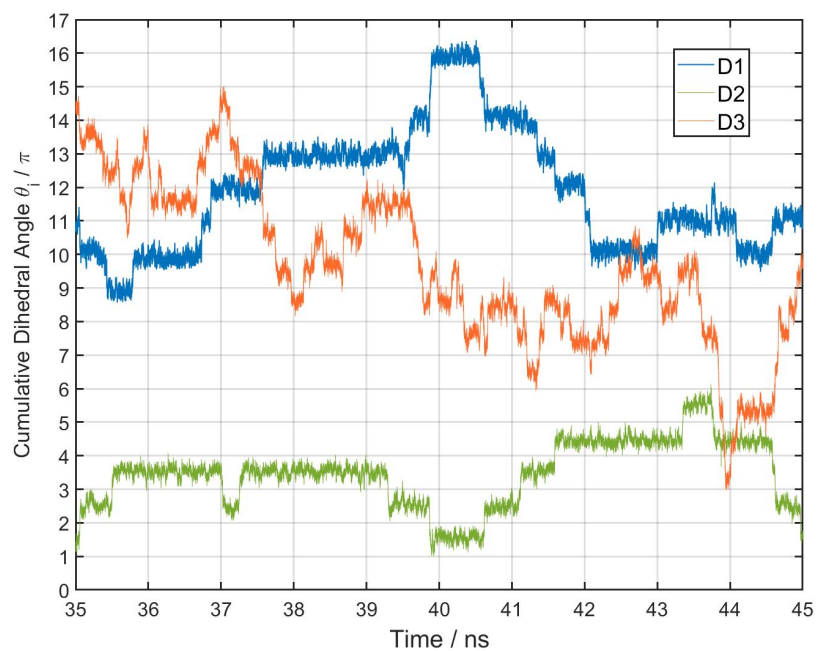


Figure A.4: Time dependence of the dyad dihedral angles D1-D3 during a 10 ns portion of the acetonitrile simulations.

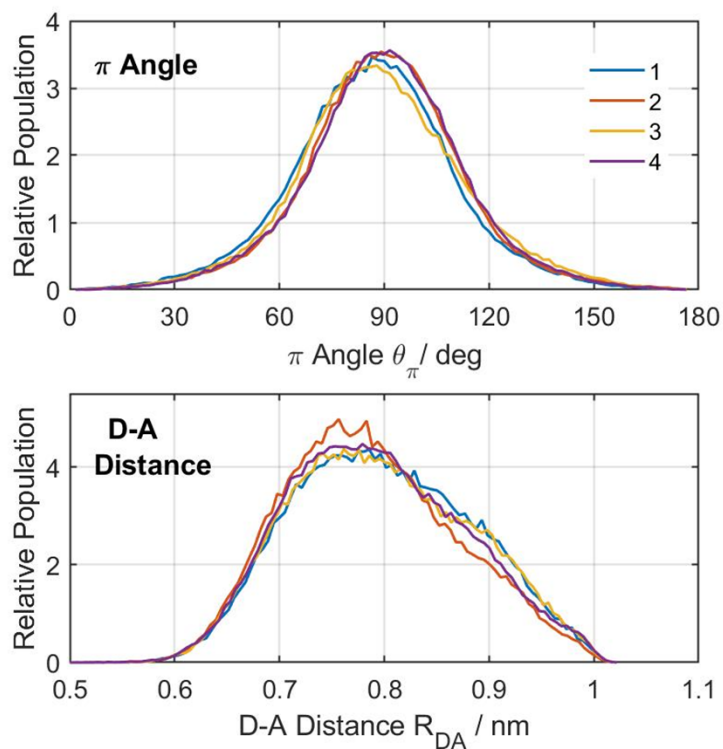


Figure A.5: Distributions of (a) the angle between the aromatic planes and (b) the center-of-mass distance between the donor and acceptor groups of the dyad in acetonitrile. The distributions are separated into contributions from the four conformational regions defined by the quadrants D2 and D3 = 0 (as shown in Fig. 3.2).

Table A.1: Solvent Properties and Characteristics of the Steady-State Spectra of C152, H152, and the C152-DMA Dyad^(a)

Solvent	Abbr.	ϵ_r	n_D	Δf	η (20 °C) / mPa s	$\langle \nu_{abs} \rangle$ C152 / 10^3 cm^{-1}	$\langle \nu_{abs} \rangle$ H152 / 10^3 cm^{-1}	$\langle \nu_{abs} \rangle$ Dyad / 10^3 cm^{-1}	$\langle \nu_{em} \rangle$ C152 / 10^3 cm^{-1}	$\langle \nu_{em} \rangle$ H152 / 10^3 cm^{-1}	$\langle \nu_{em} \rangle$ Dyad / 10^3 cm^{-1}
Ethylene Glycol	EG	37.7	1.4306	0.399	16.1	25.21	25.63	25.28	18.04	18.73	19.19
Methanol	MEOH	32.66	1.3265	0.710	0.551	25.70	26.09	25.51	18.41	19.08	19.30
Acetonitrile	ACN	35.94	1.341	0.709	0.341	25.84	26.68	25.74	19.08	19.91	19.34
Dimethyl Sulfoxide	DMSO	46.45	1.477	0.655	1.991	25.27	25.63	25.14	18.44	19.07	19.49
Propylene Carbonate	PC	64.92	1.419	0.703	2.53	25.57	26.32	25.47	18.86	19.69	19.70
Methyl Acetate	MEAC	6.68	1.3589	0.433	0.364	26.19	26.73	25.95	19.82	20.56	20.11
Tetrahydrofuran	THF	7.58	1.4050	0.441	0.462	26.08	26.52	25.81	20.02	20.59	20.15
Dibutyl Ether	DBE	3.08	1.3968	0.170	0.645	26.67	27.02	26.37	21.35	21.69	21.16
Toluene	TOL	2.38	1.4941	0.024	0.553	26.20	27.15	25.96	21.10	21.67	20.71
Dioxane	DIOX	2.21	1.4203	0.031	1.194	26.48	27.13	26.18	20.50	21.11	20.28
Cyclohexane	CHEX	2.02	1.4235	0	0.898	27.13	28.12	26.63	22.72	23.03	22.20
[Pr ₄₁][Tf ₂ N]	PR41	11.9	1.4243 ^e	--	98 ^e	25.72	26.48	25.72	19.05	19.79	19.97
[N ₈₈₈₁][Tf ₂ N]	N8881	7.6 ^b	1.4388 ^c	0.424	680 ^c	25.86	26.00	25.87	20.04	20.26	20.60
[P _{14,666}][Tf ₂ N]	P14,666	--	1.4516 ^d	0.418	470	25.43	25.88	25.43	20.05	20.61	20.60

(a) ϵ_r , n_D , Δf , and η are the relative permittivity, refractive index, nuclear polarizability (Eq. 2) and viscosity of the solvent. Most values are for 25 °C unless otherwise noted. Values from Ref. ¹. $\langle \nu_{abs} \rangle$ and $\langle \nu_{em} \rangle$ are the first moment wavenumbers of the S₁ absorption and emission spectra (20 ± 1°C).

(b) Ref. ²

(c) Ref. ³

(d) Ref. ⁴

(e) Ref. ⁵

(f) Ref. ⁶

(g) Ref. ⁷

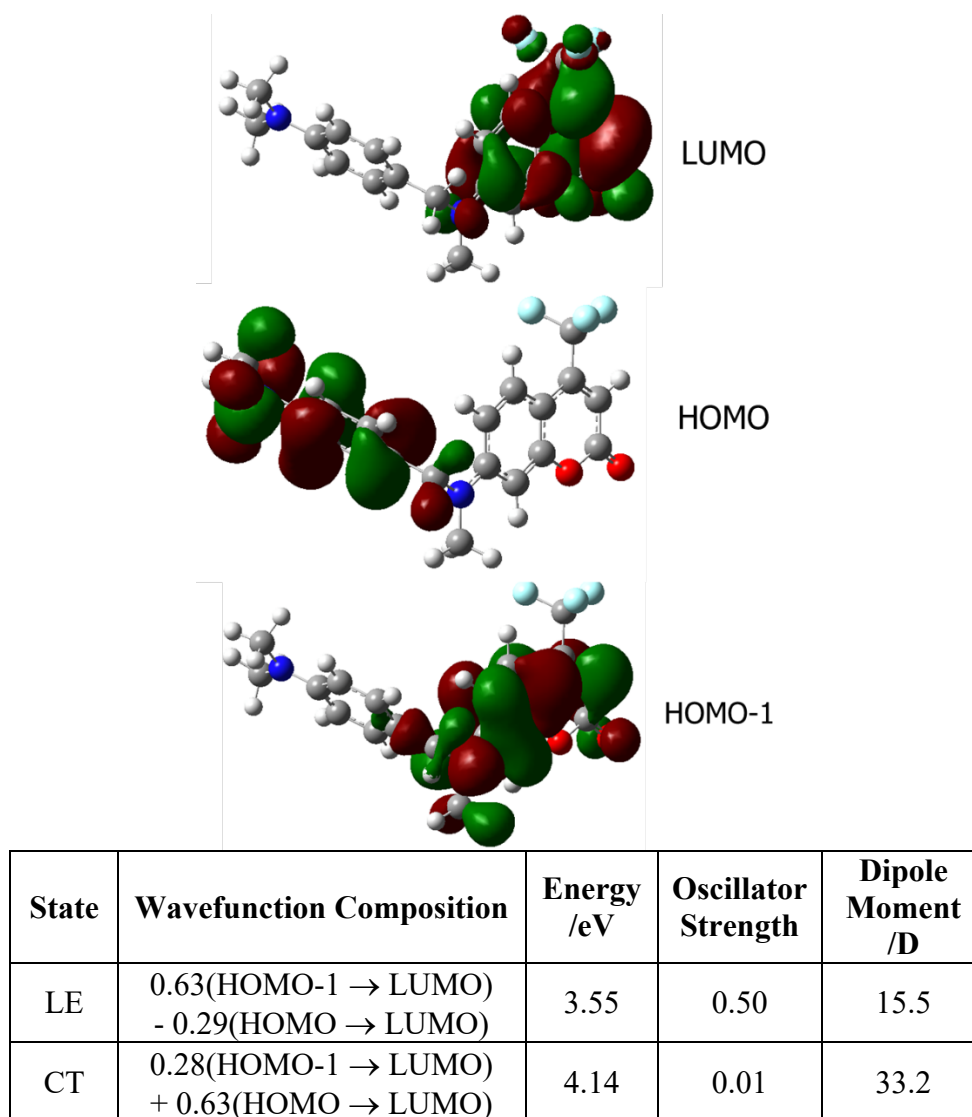


Figure A.6: The frontier molecular orbitals and select properties of the LE and CT states of C152-DMA based on gas-phase TD-DFT calculations at a typical ground state geometry using the CAM-B3LYP/6-311++G(d,p) model chemistry.

A.2 The TICT Reaction of C152 and its use as a Lifetime Reference

Coumarin 152 is known to undergo an excited-state twisted intermolecular charge transfer (TICT) reaction in high-polarity solvents.⁸⁻¹² This reaction leads to internal conversion, which is signaled by a reduction in the quantum yield and fluorescence lifetime. In light of this reaction, the aptness of C152 for estimating the lifetime of the C152-DMA dyad in the absence of electron transfer should be considered, as should the question of whether such a TICT reaction might also occur in the dyad.

Figure A.7 compares the lifetimes of C152 with those of H152 and the dyad, all plotted versus the dyad emission frequency. The drop in C152 lifetime when $\langle \nu \rangle_{em} < 20 \times 10^3 \text{ cm}^{-1}$, equivalent to an effective dielectric constant $\epsilon > 10$, is taken as evidence for the TICT process becoming accessible. No such change in lifetime is apparent in the case of H152. A similar lack of TICT formation was previously reported in C500, the variant of H152 in which the NHCH_3 group is replaced by NHC_2H_5 .⁹ Apparently, removal of one of the alkyl groups increases the amino oxidation potential sufficiently that this reaction turns off.

The dyad data included in Figure A.7 make it clear that the TICT reaction in C152 should have a negligible effect on its use as a lifetime reference for the dyad. The TICT reaction only alters the lifetime of C152 in the more polar solvents studied and, in such solvents, the dyad fluorescence rate $1/\langle \tau \rangle_{dyad}$ is over 50 times greater than the C152 decay rate.

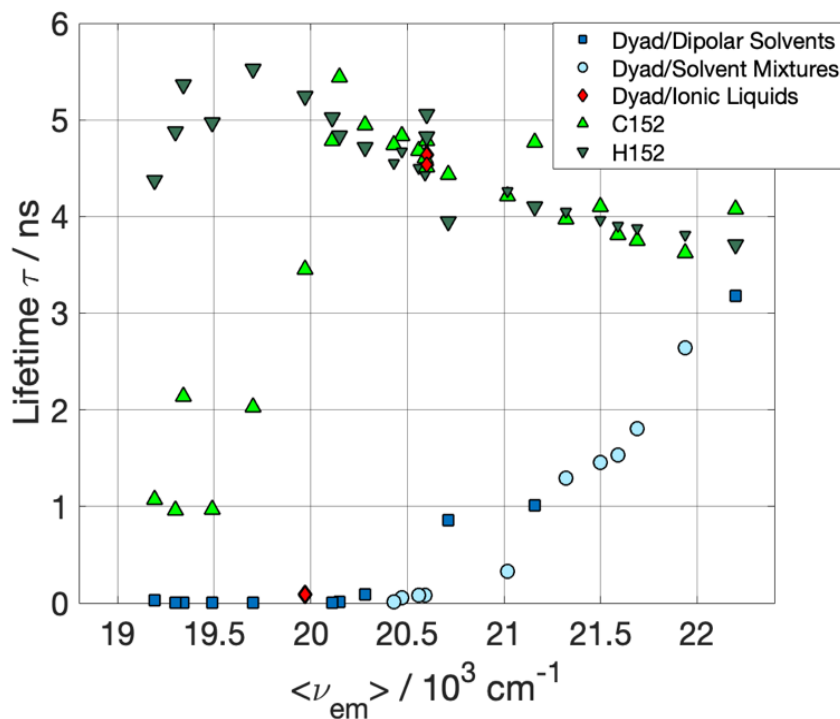


Figure A.7: Lifetimes of C152, H152, and the C152-DMA dyad plotted versus average emission frequency of the dyad. For the dyad lifetime $\langle \tau \rangle_{dyad}$ is used, which omits the small decay component attributed to H152 impurity.

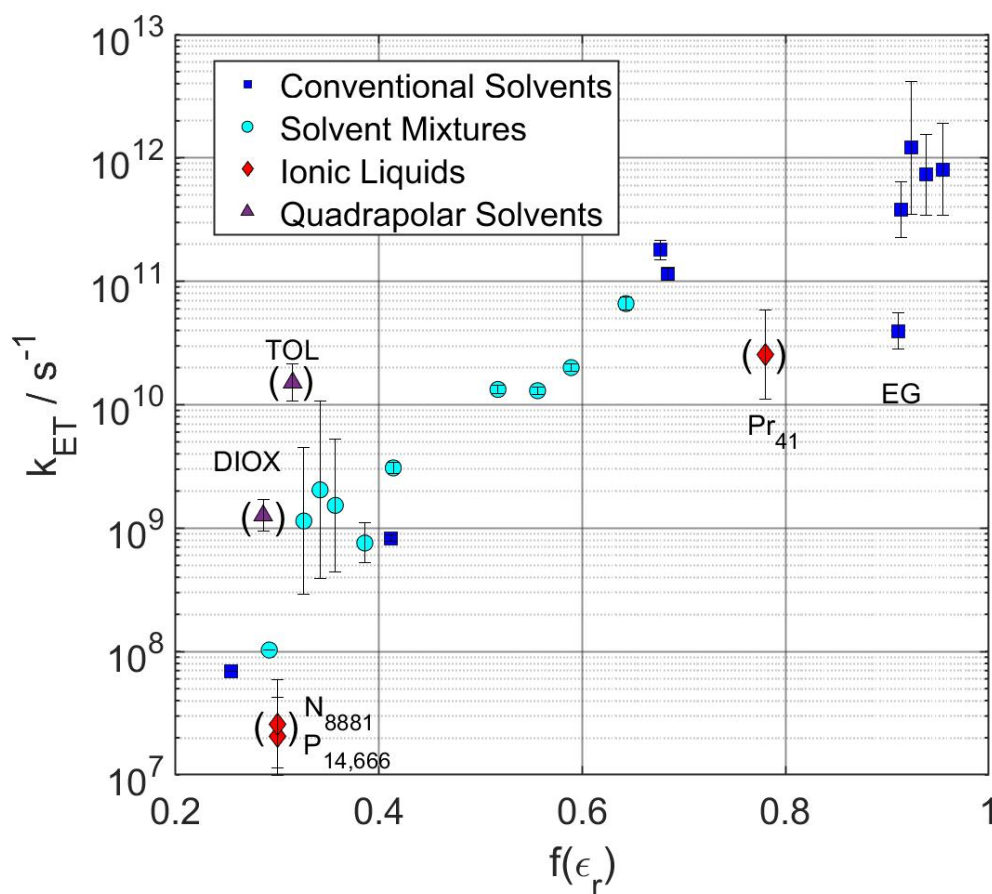


Figure A.8: Electron transfer rate constants of the dyad plotted versus the total electric polarizability of the solvent. Symbols denote the logarithmic average of $k_{ET}^{(1)}$ and $k_{ET}^{(2)}$, and the ends of the error bars their individual values. Note that the polarities of the quadrapolar solvents toluene and dioxane and the ionic liquids are not properly represented by $f(\epsilon_r)$ and are therefore shown in parenthesis.

A.3 Temperature Dependence in [N₈₈₈₁][Tf₂N] and [P_{14,666}][Tf₂N]

The two high-viscosity ionic liquids [N₈₈₈₁][Tf₂N] and [P_{14,666}][Tf₂N] were studied over a wide temperature range to determine whether electron transfer occurs at higher temperatures and to compare relative solvation times in the two liquids.

Figure A.9 shows the steady-state emission of C152 and the dyad in [P_{14,666}][Tf₂N]. The spectra of both solutes shift to the red with increasing temperature, with little change in spectral shape. Average emission frequencies from these and equivalent spectra in [N₈₈₈₁][Tf₂N] are shown in Figure A.10.

Also shown in Fig. A.10(a) are viscosities of all three of the ionic liquids studied. These viscosities are from fits of literature data to the equation $\ln(\eta / \text{mPa} \cdot \text{s}) = A + B/(T - T_0)$. Fit parameters are summarized in Table A.2. Over the temperature range studied, the viscosities of the high-viscosity liquids range from $>10^6$ mPa*s at temperatures below 230 K to ~ 30 mPa s at the high temperature, 353 K. As discussed shortly, there is no indication that the electron transfer reaction takes place at a detectable rate ($k_{ET} > 10^7$) in either [N₈₈₈₁][Tf₂N] or [P_{14,666}][Tf₂N] even up to 353 K, where the viscosity is less than that of [Pr₄₁][Tf₂N] at room temperature. This lack of reaction is presumably due to the lower polarity and thus smaller driving force for electron transfer in the former ionic liquids.

The dependence of $\langle \nu \rangle_{em}$ on temperature displayed in Figure SI-10 may be ascribed to the change in solvation time, which tracks that of viscosity. At low temperatures solvent is essentially immobilized on the fluorescence time scale, whereas at the highest temperatures it is sufficiently fluid to achieve equilibrium within the S₁

lifetime. As shown here, $\langle \nu \rangle_{em}(T)$ of C152 and the dyad are very similar in each solvent, with the main difference being a ~ 120 larger frequency shift of C152, reflecting its greater solvatochromic response (Fig. 3.9). The magnitude of the shifts observed in these two ionic liquids are also quite similar, $1420|1300 \text{ cm}^{-1}$ in $[\text{N}_{8881}][\text{Tf}_2\text{N}]$ and $1420|1300 \text{ cm}^{-1}$ in $[\text{P}_{14,666}][\text{Tf}_2\text{N}]$ for C152|the dyad. These similarities underscore the nearly identical effective polarities of these two solvents. The dynamics are also rather similar, as indicated by their comparable viscosities at 293 K (Table A.2). Solvation times have been measured in $[\text{P}_{14,666}][\text{Tf}_2\text{N}]$ at three temperatures over the range 298-343 K.¹³ Extrapolating these data, the (integral) solvation time of $[\text{P}_{14,666}][\text{Tf}_2\text{N}]$ is predicted to be $\langle \tau \rangle_{solv} \sim 15 \text{ ns}$ at 293 K. Based on the difference in viscosities, the solvation time in $[\text{N}_{8881}][\text{Tf}_2\text{N}]$ is expected to be about twice as long. These values may be compared to $\langle \tau \rangle_{solv} \sim 0.37 \text{ ns}$ in $[\text{Pr}_{41}][\text{Tf}_2\text{N}]$.¹⁴

Figure A.11 compares the temperature dependence of the lifetimes of C152 and the dyad in the two high-viscosity ionic liquids. At lower temperatures, decays of both solutes showed some nonexponentiality; in these cases, the average time $\langle \tau \rangle$ is plotted. Two important conclusions can be drawn from the data plotted. First, the decay times $\langle \tau \rangle$ of the two solutes are the same to within the 5% uncertainties in the data up to 313 K in $[\text{N}_{8881}][\text{Tf}_2\text{N}]$ and 303 K in $[\text{P}_{14,666}][\text{Tf}_2\text{N}]$. Thus, below these temperatures, there is no indication of that electron transfer occurs in the dyad. The fact that the dyad lifetimes either increase or remain constant at higher temperatures also rules out electron transfer occurring at higher temperatures, at least with rates much larger than 10^7 s^{-1} . Finally, it is clear that some process that quenches C152 emission becomes operative at above 313/303 K, where both solvents have viscosities of $\sim 220 \text{ mPa s}$. It is likely that this

process is the TICT reaction discussed in Section B. While it is clear that this process renders C152 a poor lifetime reference above these temperatures, it still appears to be valid at room temperature, as assumed here.

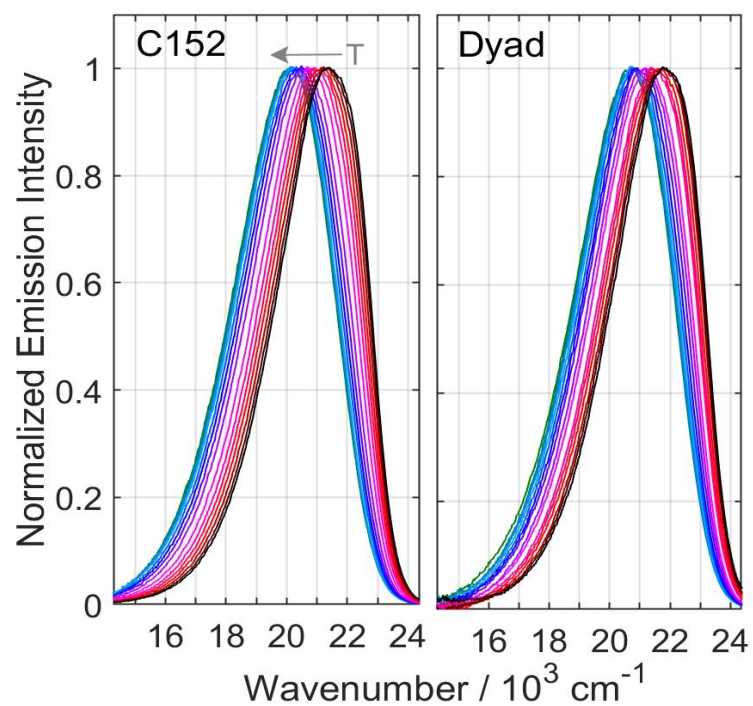


Figure A.9: Emission spectra of C152 and the dyad in $[P_{14,666}][Tf_2N]$ between 213-353 K.

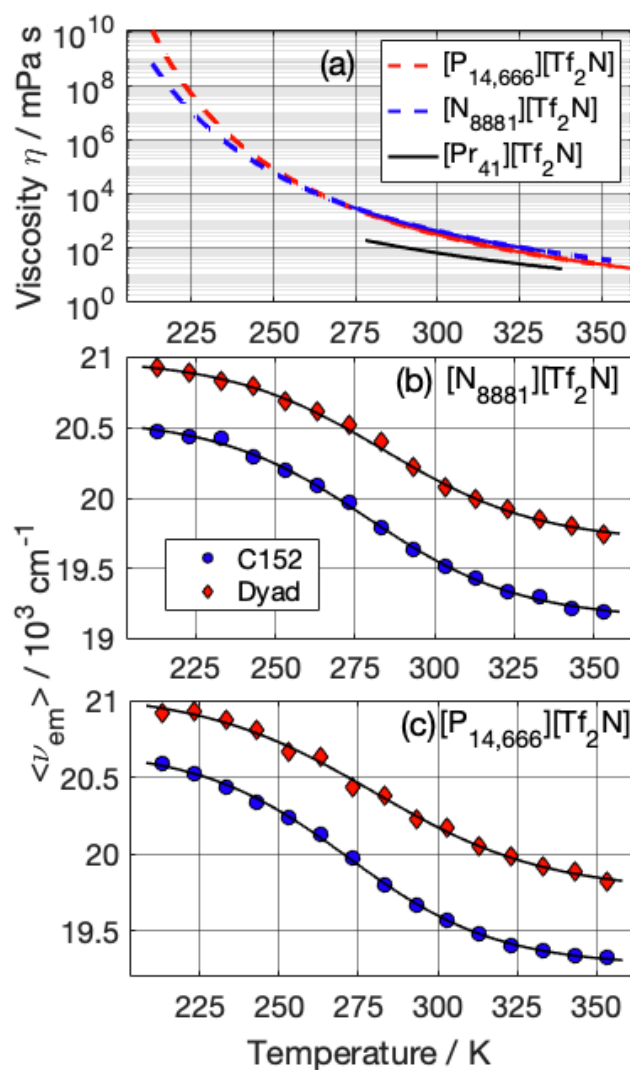


Figure A.10: (a) Parameterized viscosities of the ionic liquids studied. The solid portions of the curves indicate the temperature range over which experimental data are available. (b, c) Average emission frequencies of C152 (blue) and the dyad (red) in $[N_{8881}][Tf_2N]$ and $[P_{14,666}][Tf_2N]$.

Table A.2: Fits to Reported Viscosity Data of the Ionic Liquids^(a)

Ionic Liquid	T_g /K	T Range /K	A	B /K	T_0 /K	\square (293 K)	η Refs.	$T_{1/2}^{(b)}$ /K
[Pr ₄₁][Tf ₂ N]	186 ¹⁵	278- 338	-3.14	1266	128	92	⁷	—
[N ₈₈₈₁][Tf ₂ N]	192 ^{16,17}	273- 333	-3.16	1325	157	715	³	282±3
[P _{14,666}][Tf ₂ N]	200 ^{18,19}	278- 368	-3.58 (-2.59)	1257 (1200)	166 (154)	548 (417)	^{7,18-21}	276±4

- (a) Parameters A , B , and T_0 are based on fits of compiled literature data to the VFT function $\ln(\eta / \text{mPa} \cdot \text{s}) = A + B / (T - T_0)$. The fit for [Pr₄₁][Tf₂N] was taken directly from Ref.⁷. The other fits include several data sets from the cited papers plus a point at the assumed value $\eta(T_g) = 10^{15}$ mPa s, used to constrain the low temperature behavior. [P_{14,666}][Tf₂N] was not well fit when this T_g constraint was included. The parameter values in parenthesis are those obtained without this added point.
- (b) $T_{1/2}$ is the temperature at which sigmoidal fits to the emission frequencies of C152 and the dyad are halfway between their low and high temperature limits (averaged over the C152 and dyad data).

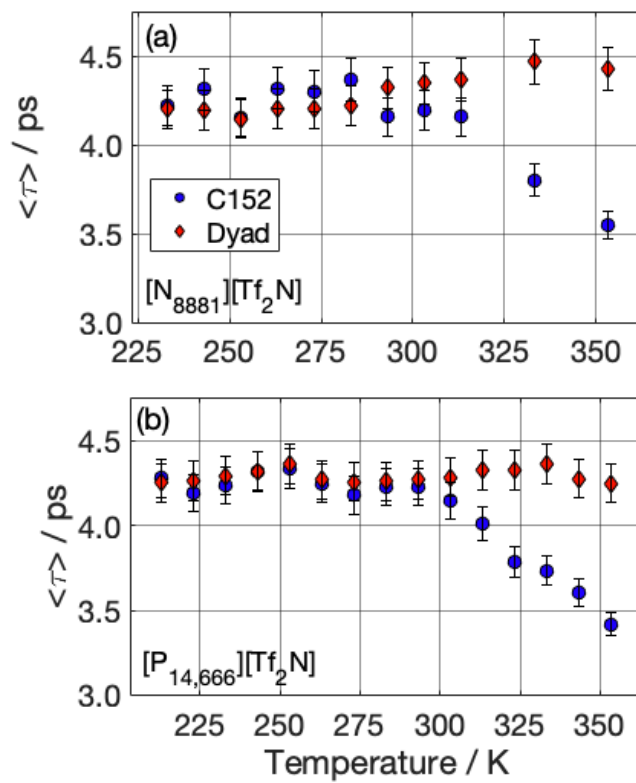


Figure A.11: Average lifetimes of the dyad and C152 at different temperatures in [N₈₈₈₁][Tf₂N] and [P_{14,666}][Tf₂N].

References:

1. Y. Marcus, *The Properties of Solvents* (Wiley, New York, 1998).
2. P. J. Griffin, A. P. Holt, Y. Wang, V. N. Novikov, J. R. Sangoro, F. Kremer, and A. P. Sokolov, "Interplay Between Hydrophobic Aggregation and Charge Transport in the Ionic Liquid Methyltrioctylammonium Bis(trifluoromethylsulfonyl)imide," *J. Phys. Chem. B* **118**, 783-790 (2014). 10.1021/jp412365n
3. A. P. Froeba, H. Kremer, and A. Leipertz, "Density, Refractive Index, Interfacial Tension, and Viscosity of Ionic Liquids [EMIM][EtSO₄], [EMIM][NTf₂], [EMIM][N(CN)₂], and [OMA][NTf₂] in Dependence on Temperature at Atmospheric Pressure," *J. Phys. Chem. B* **112**, 12420-12430 (2008). 10.1021/jp804319a
4. M. Tariq, P. A. S. Forte, M. F. C. Gomes, J. N. C. Lopes, and L. P. N. Rebelo, "Densities and refractive indices of imidazolium- and phosphonium-based ionic liquids: Effect of temperature, alkyl chain length, and anion," *J. Chem. Thermodyn.* **41**, 790-798 (2009). 10.1016/j.jct.2009.01.012
5. A. B. Pereiro, H. I. M. Veiga, J. M. S. S. Esperanca, and A. Rodriguez, "Effect of temperature on the physical properties of two ionic liquids," *J. Chem. Thermodyn.* **41**, 1419-1423 (2009). 10.1016/j.jct.2009.06.020
6. M.-M. Huang, Y. Jiang, P. Sasisanker, G. W. Driver, and H. Weingartner, "Static Relative Dielectric Permittivities of Ionic Liquids at 25°," *J. Chem. Eng. Data* **56**, 1494-1499 (2011). 10.1021/je101184s
7. M. Liang, A. Kaintz, G. A. Baker, and M. Maroncelli, "Bimolecular Electron Transfer in Ionic Liquids: Are Reaction Rates Anomalously High?," *J. Phys. Chem. B* **116**, 1370-1384 (2012). 10.1021/jp210892c
8. G. Jones, II, W. R. Jackson, C. Y. Choi, and W. R. Bergmark, "Solvent effects on emission yield and lifetime for coumarin laser dyes. Requirements for a rotatory decay mechanism," *J. Phys. Chem.* **89**, 294-300 (1985). 10.1021/j100248a024
9. C. Guo and Y. Feng, "Solvent and substituent effects on intramolecular charge transfer of selected derivatives of 4-trifluoromethyl-7-aminocoumarin," *J. Chem. Soc., Faraday Trans. 1* **83**, 2533-2539 (1987).
10. K. Rechthaler and G. Koehler, "Excited state properties and deactivation pathways of 7-aminocoumarins," *Chem. Phys.* **189**, 99-116 (1994). 10.1016/0301-0104(94)80010-3
11. S. Nad, M. Kumbhakar, and H. Pal, "Photophysical properties of Coumarin-152 and Coumarin-481 dyes: unusual behavior in nonpolar and in higher polarity solvents," *J. Phys. Chem. A* **107**, 4808-4816 (2003). 10.1021/jp021543t
12. P. Dahiya, M. Kumbhakar, T. Mukherjee, and H. Pal, "Effect of protic solvents on twisted intramolecular charge transfer state formation in coumarin-152 and coumarin-481 dyes," *Chem. Phys. Lett.* **414**, 148-154 (2005). 10.1016/j.cplett.2005.08.051
13. N. Ito, S. Arzhantsev, M. Heitz, and M. Maroncelli, "Solvation Dynamics and Rotation of Coumarin 153 in Alkylphosphonium Ionic Liquids," *J. Phys. Chem. B* **108**, 5771-5777 (2004). 10.1021/jp0499575

14. X.-X. Zhang, M. Liang, N. P. Ernsting, and M. Maroncelli, "Complete Solvation Response of Coumarin 153 in Ionic Liquids," *J. Phys. Chem. B* **117**, 4291-4304 (2013). 10.1021/jp305430a
15. H. Jin, B. O'Hare, J. Dong, S. Arzhantsev, G. A. Baker, J. F. Wishart, A. Benesi, and M. Maroncelli, "Physical Properties of Ionic Liquids Consisting of the 1-Butyl-3-Methylimidazolium Cation with Various Anions and the Bis(trifluoromethylsulfonyl)imide Anion with Various Cations," *J. Phys. Chem. B* **112**, 81-92 (2008).
16. G. V. S. M. Carrera, R. F. M. Frade, J. Aires-de-Sousa, C. A. M. Afonso, and L. C. Branco, "Synthesis and properties of new functionalized guanidinium based ionic liquids as non-toxic versatile organic materials," *Tetrahedron* **66**, 8785-8794 (2010). 10.1016/j.tet.2010.08.040
17. P. S. Kulkarni, L. C. Branco, J. G. Crespo, M. C. Nunes, A. Raymundo, and C. A. M. Afonso, "Comparison of physicochemical properties of new ionic liquids based on imidazolium, quaternary ammonium, and guanidinium cations," *Chem. - Eur. J.* **13**, 8478-8488 (2007). 10.1002/chem.200700965
18. R. E. Del Sesto, C. Corley, A. Robertson, and J. S. Wilkes, "Tetraalkylphosphonium-based ionic liquids," *J. Organomet. Chem.* **690**, 2536-2542 (2005). 10.1016/j.jorganchem.2004.09.060
19. F. Wishart James, unpublished results (2011).
20. R. G. Evans, A. J. Wain, C. Hardacre, and R. G. Compton, "An electrochemical and ESR spectroscopic study on the molecular dynamics of TEMPO in room temperature ionic liquid solvents," *ChemPhysChem* **6**, 1035-1039 (2005). 10.1002/cphc.200500157
21. L. Ferguson and P. Scovazzo, "Solubility, Diffusivity, and Permeability of Gases in Phosphonium-Based Room Temperature Ionic Liquids: Data and Correlations," *Ind. Eng. Chem. Res.* **46**, 1369-1374 (2007). 10.1021/ie0610905

Appendix B

Supporting Information for Chapter 4

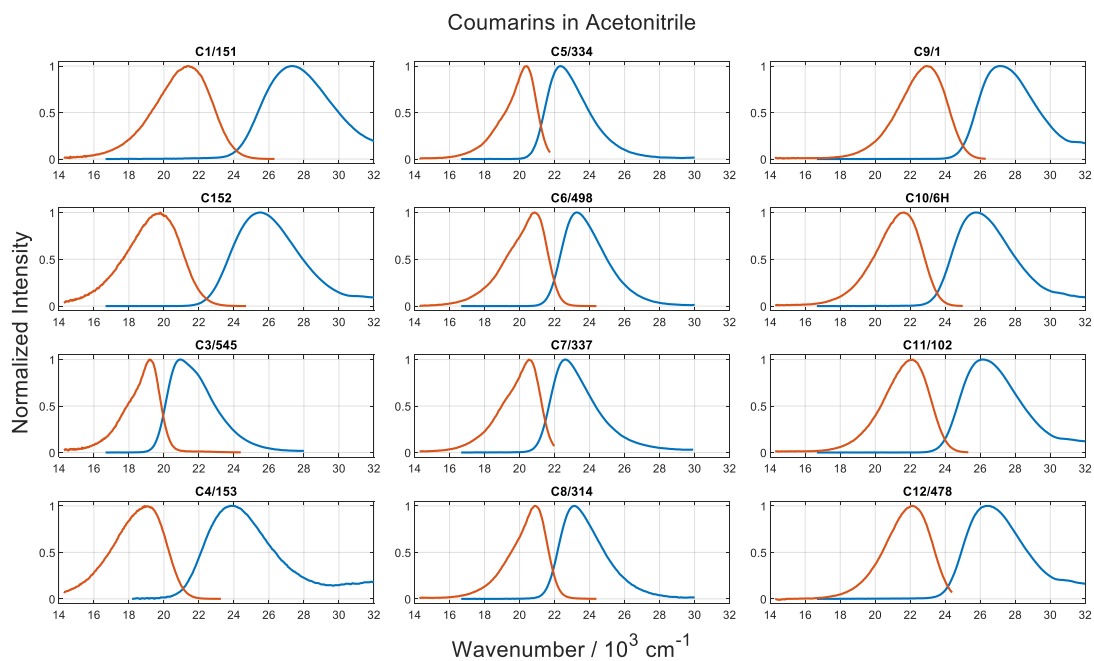


Figure B.1: Steady state absorption and emission spectra of coumarins in acetonitrile

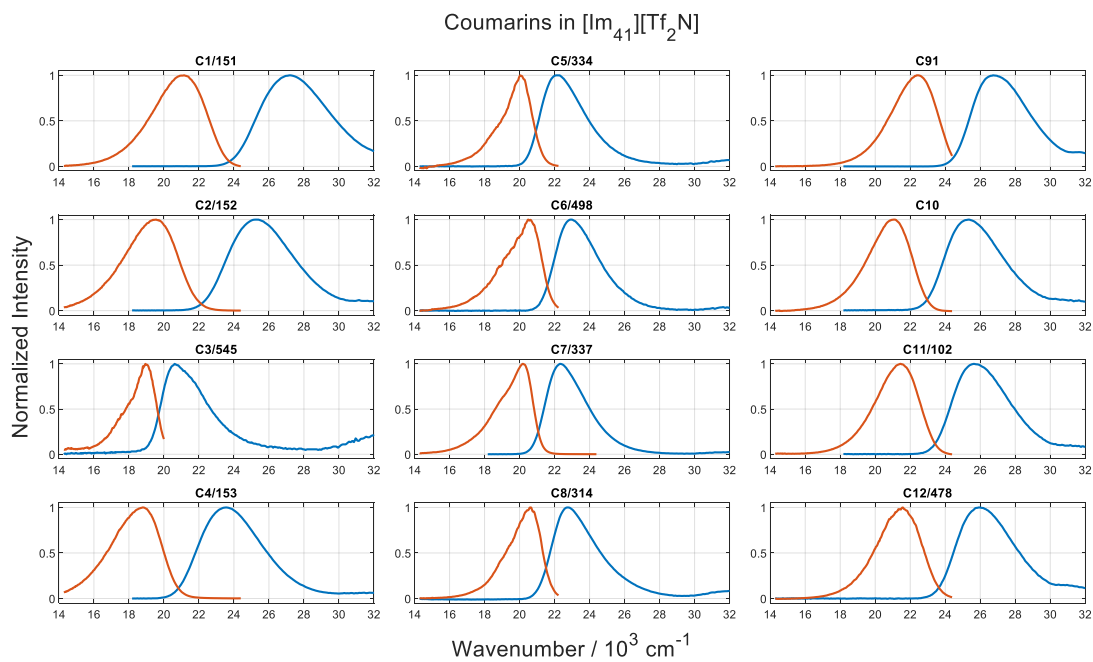


Figure B.2: Steady state absorption and emission spectra of coumarins in $[\text{Im}_{41}][\text{Tf}_2\text{N}]$

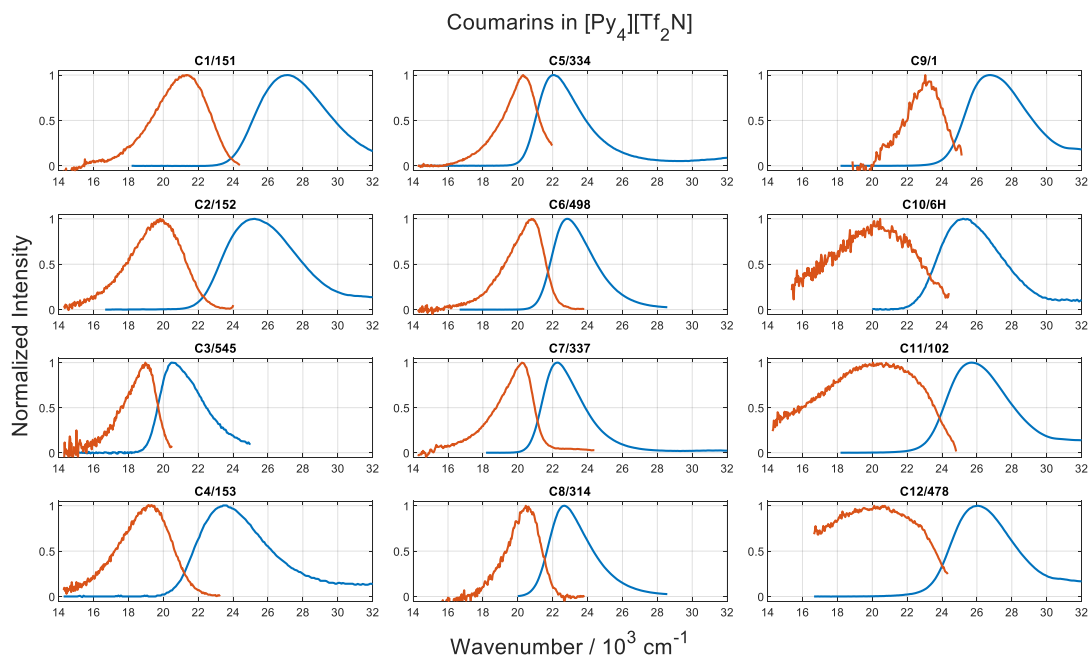


Figure B.3: Steady state absorption and emission spectra of coumarins in $[\text{Py}_4][\text{Tf}_2\text{N}]$.

B.1 [Py₄][Tf₂N] Impurity Absorption and Emission and its Effect on Coumarin Spectra

Figure B.4 compares the absorbance (1 cm⁻¹ pathlength) and emission spectra and emission decays of [Py₄][Tf₂N] with those of **C2** (152) and **C9** (1) under typical conditions employed here. The emission spectra and decays were collected for the same excitation conditions and collection times for the neat solvent and for the coumarin-containing solutions. Figure B.4(a) shows the optical quality of the [Py₄][Tf₂N] used here to be quite good, with an OD < 0.1 down to 300 nm and much less where the coumarins were excited (~25,000 cm⁻¹). Emission of neat [Py₄][Tf₂N] is negligible compared to the emission of typical coumarin solutions. In the example shown here, emission of **C2** in [Py₄][Tf₂N] is about 20 times more intense than the solvent background, even though **C2** has a quantum yield of <0.05 in this solvent. The background emission becomes more problematic for coumarins **C9** - **C12**, which have quantum yields of <10⁻³ in [Py₄][Tf₂N]. For **C9**, illustrated here, the solute and background emission are of comparable intensity, which increases the uncertainty in the reported emission characteristics.

In **C10** - **C12**, the least fluorescent of the coumarins in [Py₄][Tf₂N], it was not possible to adequately remove solvent emission by subtraction. For these three dyes, the early-time spectra obtained from the KGE measurements were used to establish approximate solute emission frequencies. This approach is illustrated in **Figure B.5** for the case of **C10** (102). Prior to quenching (< 1 ps here) the spectra consist primarily of that **C10** emission, whose emission peaks near 23,000 cm⁻¹. Once this solute emission is quenched, emission from the solvent begins to dominate, as shown by the peak

normalized spectra in panel (b). At intermediate times two emission bands are evident in the KGE spectra enabling fits to two lognormal lineshape functions (Fig. B.5 (c)). The width and asymmetry of the coumarin emission are constrained to be the same as observed in acetonitrile, and only the peak height and frequency are allowed to vary. Using the same approach provides reasonable estimates of the frequencies of **C10 - C12** under steady-state illumination, where the spectra are less clearly bimodal (panel (d)).

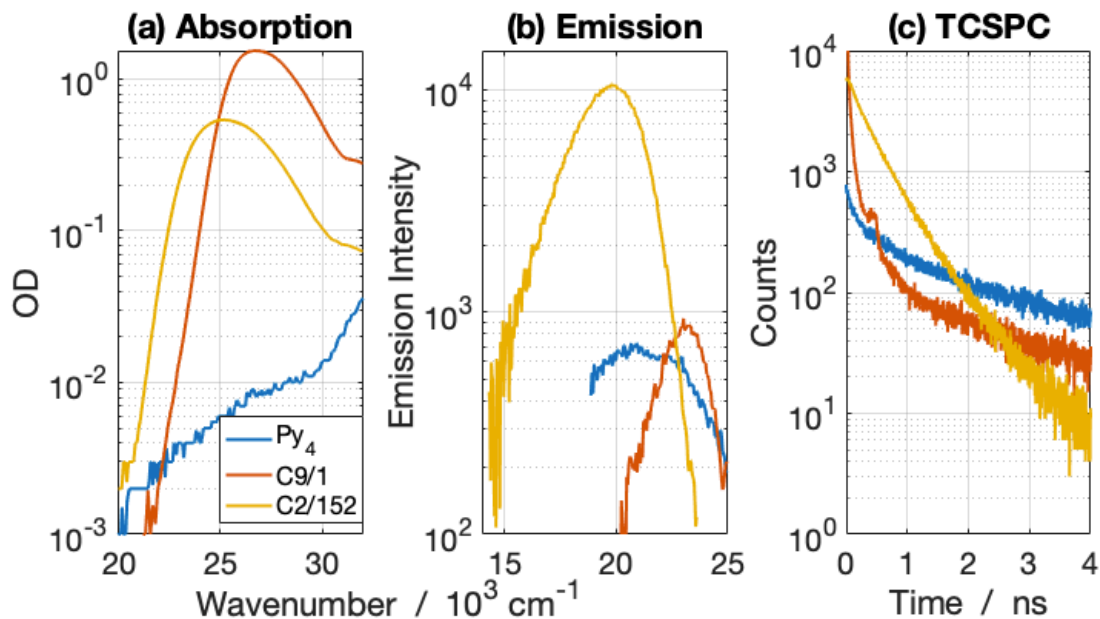


Figure B.4: Comparison of the (a) absorption and (b) emission spectra and (c) emission decays of neat $[\text{Py}_4][\text{Tf}_2\text{N}]$ to two coumarin dye solutions. In (b) and (c) the same excitation and emission collection parameters were used for the neat solvent and the dye solutions.

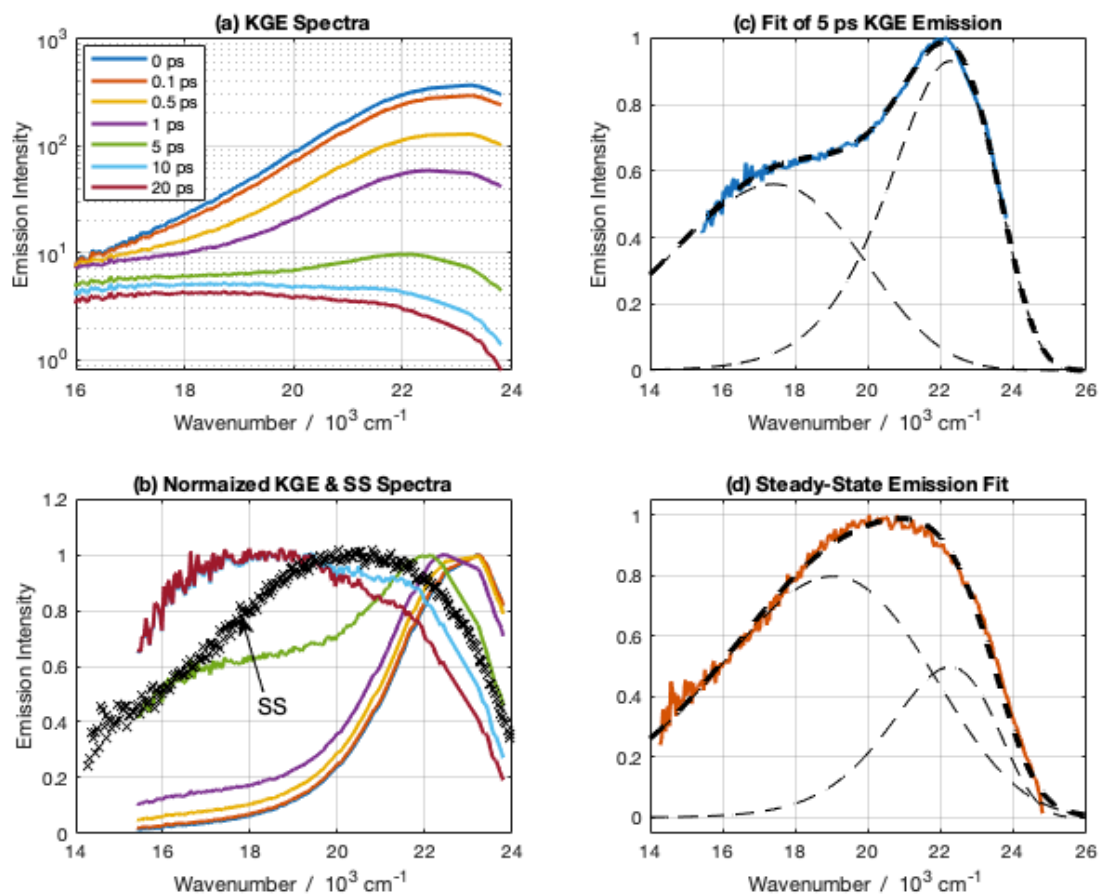


Figure B.5: Spectra of C10/102 in [Py₄][Tf₂N] illustrating the method of extracting C10 spectral information from the steady-state spectrum: (a) time-resolved emission at the times indicated; (b) peak-normalized spectra at the same times as panel (a) (solid curves) and the steady-state spectrum (“SS”, points); (c) fit of the 5 ps.

B.2 Oxidation Potentials from Cyclic Voltammetry and Quantum Chemical Calculations

Representative cyclic voltammetry data are shown in **Figure B.6** for the coumarins **C3/337** and **C11/102**. Shown are three oxidation cycles scanned at a rate of 100 mV/s. **C3** provides an example of a chemically reversible measurement. The oxidation and reduction half cycles are of approximately equal area and change little upon repeated scanning. For such cases the value of the oxidation potential was taken as $E_{1/2}$, the average of the potentials of the positive and negative current peaks. The difference between the positive and negative (100 mV for C3) ranged between 100-250 mV in these measurements, all larger than the Nernstian ideal of 57 mV.¹ **C11** is an example of an irreversible reaction. Only a small fraction of the C11 oxidized in the forward cycle is reduced back to neutral form in the reverse cycle, and successive sweeps continue to decrease in current amplitude. Of the coumarins studied, irreversible behavior was observed for **C9/1**, **C10/6H** and **C11/102** and largely reversible behavior for the remainder.

To estimate the oxidation potentials for the two coumarins (**C1/151** and **C4/545**) not directly measured, we explored the use of two previously reported computational methods. The first was an early approach developed by Crespo-Hernández *et. al*³ for predicting the redox properties of DNA nucleosides, nucleobases, and related molecules. They showed that simple calculations of gas-phase vertical ionization energies (VIEs) and electron affinities (VEAs) calculated at the B3LYP/6-31++G(d,p) level sufficed to correlate high-quality redox data on 20 organic molecules having features similar to the target DNA species.⁵ Relevant to the present work, Crespo-Hernandez *et al.* showed that

these correlations provided good predictions for the solution-phase oxidation and reduction potentials of six 7-amino and 7-methoxy dyes. They proposed the following equations for estimating oxidation (E_{ox}^o) and reduction (E_{red}^o) potentials in acetonitrile relative to the normal hydrogen electrode (NHE)

$$E_{ox}^o = (-2.59 \pm 0.26) + (0.56 \pm 0.03) \times VIE \quad (B.1)$$

$$E_{red}^o = (-2.09 \pm 0.03) \pm (0.81 \pm 0.05) \times VEA \quad (B.2)$$

with potentials in units of V. (For prediction of potentials relative to SCE requires subtraction of 0.241 V from these equations.)

The second, more recent method, developed by Roth *et. al.*⁶ employs an implicit solvent representation rather than gas-phase calculations. This process was developed for applicability to a much wider range of molecules, and it was calibrated against to data on 180 organic molecules. For this method, of the optimized structures and frequencies of the neutral and charged species were calculated at the with B3LYP/6-31+G(d,p) level in the presence of a conductor-like polarizable continuum model (CPCM) to account for solvation in acetonitrile. The difference in free energies between the neutral and oxidized states,

$$\Delta G_{1/2}^{o,calc} = G_{298}(neutral) - G_{298}(oxidized) \quad (B.3)$$

is used to calculate the oxidation potential $E_{1/2}^{o,calc}$ via

$$E_{1/2}^{o,calc} = -\frac{\Delta G_{1/2}^{o,calc}}{n_e \mathcal{F}} - E_{1/2}^{o,ref}, \quad (B.4)$$

where the n_e is number of electrons involved (1 here) and \mathcal{F} is Faraday's constant. $E_{1/2}^{o,ref}$ here is subtracted to adjust the value to a reference electrode. For this paper, we report all

values as saturated calomel electrode (SCE), so $E_{1/2}^{o,ref} = 4.037$ eV. This value is a combination of the initial adjustment to a standard hydrogen electrode (SHE) of 4.281 eV and the adjustment from SHE to SCE of 0.244 eV.⁷

$$E_{1/2}^{o,calc} = -\frac{\Delta G_{1/2}^{o,calc}}{n_e \mathcal{F}} - E_{1/2}^{o,ref} \quad (\text{B.5})$$

The table compiling the results from the experimental measurements and calculations from both methods is shown below in Table B.1. The vertical ionization potential from the CH method and the ΔG_{ox} from the Roth method were plotted against the experimentally observed oxidation potentials for the coumarins studied shown in Figure B.7. The trendline from these plots were used to estimate the optimized experimental values for both methods.

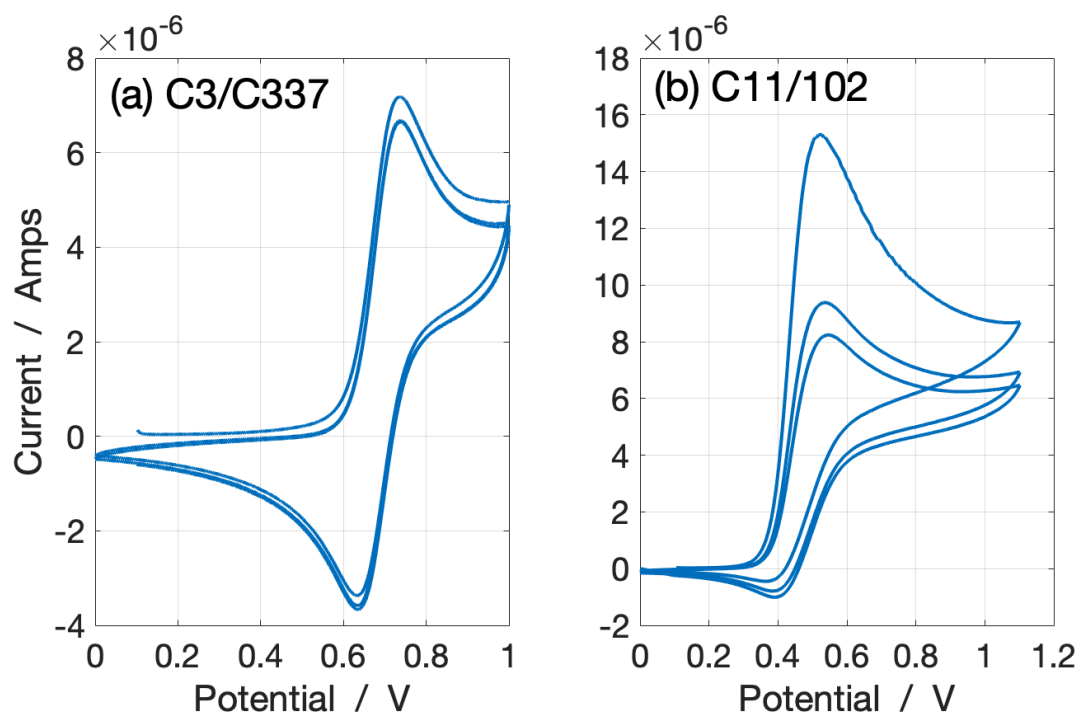


Figure B.6: Cyclic voltammetry measurements of (a) **C3/337** and (b) **C11/102** in acetonitrile.

Table B.1: Compilation of data from calculations estimating oxidation potentials using methods of Crespo-Hernández et. al. and Roth et. al.

Paper Label	Kodak Label	Observed E_{ox} / V vs. SCE	C-H Calc Vertial IP /V	C-H Calc E_{ox} / V ^(a)	C-H Calc E_{ox} Opt / V ^(b)	Roth Calc ΔG_{ox} / V	Roth Calc E_{ox} / V ^(a)	Roth Calc E_{ox} Opt / V ^(b)
C2	152	0.91(2)	7.57	1.404	0.96	5.64	1.12	0.99
C3	337	0.73(4)	7.32	1.267	0.86	5.45	0.93	0.84
C5	334	0.67(2)	7.14	1.167	0.79	5.38	0.85	0.78
C6	498	0.75(2)	6.93	1.049	0.71	5.44	0.92	0.83
C7	153	0.67(2)	7.21	1.203	0.82	5.33	0.81	0.75
C8	314	0.67(2)	6.92	1.042	0.7	5.35	0.82	0.76
C9	1	0.73(3)	7.14	1.163	0.79	5.4	0.88	0.80
C10	6H	0.45(2)	6.96	1.064	0.72	5.16	0.64	0.61
C11	102	0.50(2)	6.91	1.036	0.7	5.14	0.62	0.59
C12	478	0.45(2)	6.59	0.854	0.57	5.05	0.53	0.52
			Std Err: ^(c)	0.1	0.07			
			Mean Rel. Abs. Err: ^(d)	0.5	0.09			
C1	151	--	8.09	1.696	1.16	5.92	1.4	1.22
C4	545	--	6.6	0.863	0.58	5.21	0.69	0.65

(a) Calculated values using the correlation provided by original work

(b) Calculated values using the best fit of observed to calculated values (i.e. Vert IP for C-H and dG_{ox} for Roth)

(c) Standard error of fit (using regression toll of Excel)

(d) Mean Absolute Relative Error (average of $|Calc-Exp|/Exp$)

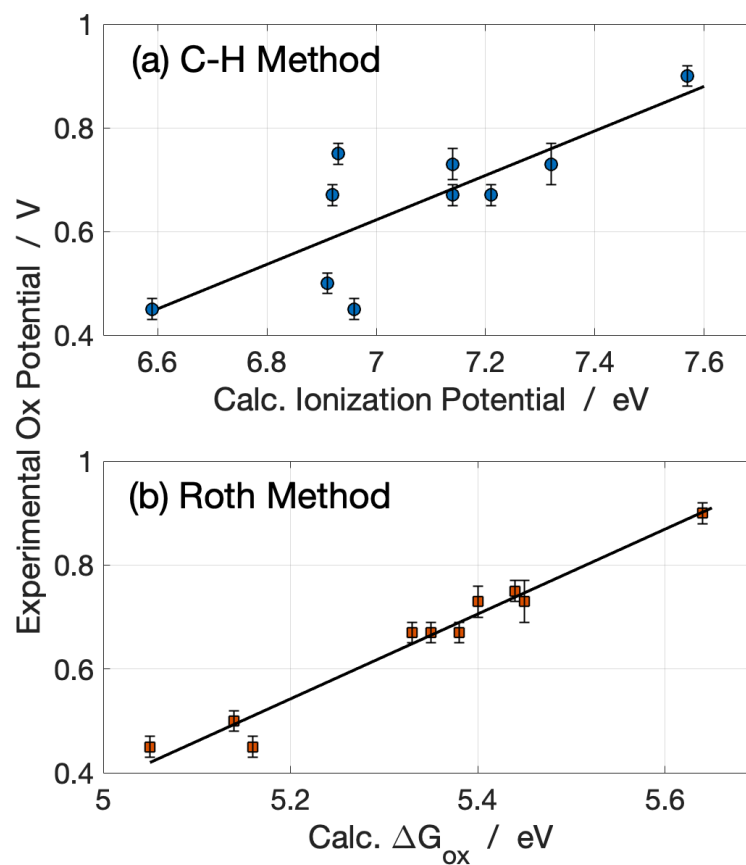


Figure B.7: Results of computational estimations of calculated oxidation potential vs. experimental results for coumarins with reversible oxidation peaks using methods by Roth et. al.⁶ and Crespo-Hernández et. al.³ using Gaussian 09 calculations.

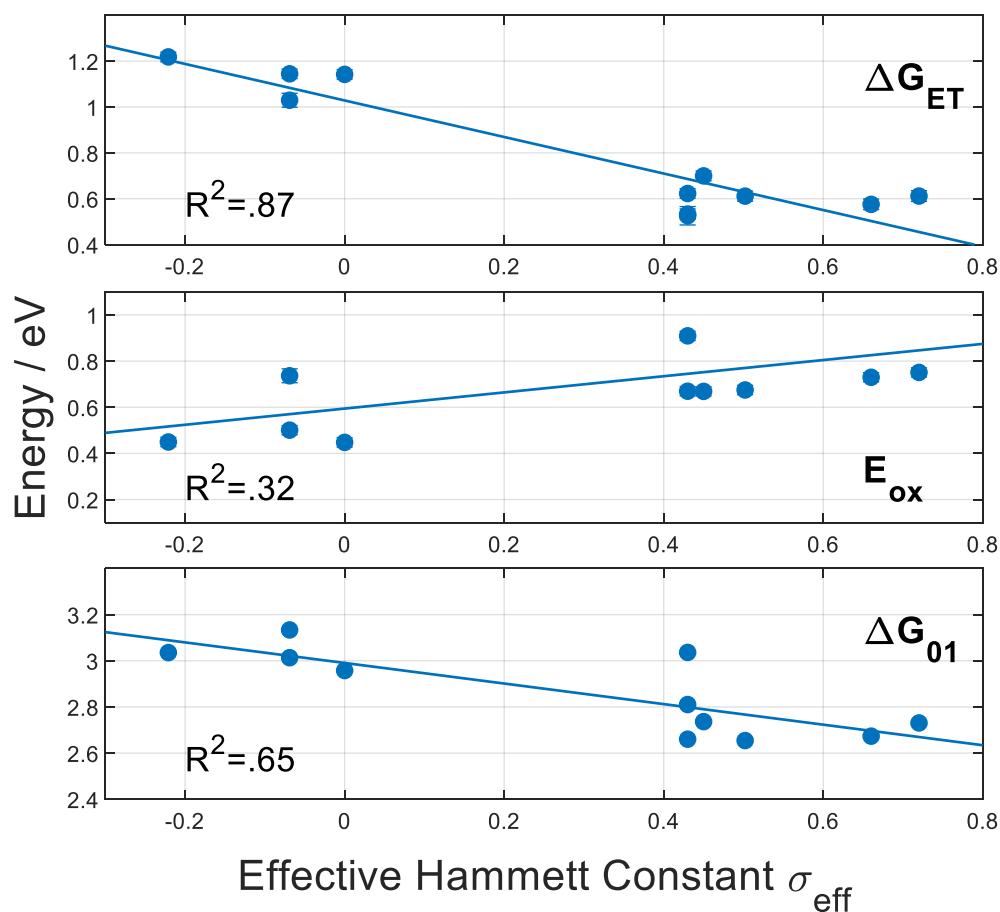


Figure B.8: Correlation between the net Hammett σ values of substituents at the 3 and 4 coumarin ring positions and ΔG_{ET} , E_{ox} , and ΔG_{01} . Effective values of σ were obtained from the tabulation in Ref. 8 assuming $\sigma_{\text{eff}} \cong \sigma_p^{(3)} + \sigma_m^{(4)}$ where para and meta refer to the location relative to the 7-amino ring position. Values of σ_{eff} calculated in this manner for C1-C12 are: 0.43, 0.43, 0.66, n.a., 0.50, 0.72, 0.43, 0.45, -0.069, 0, -0.069, -0.221.

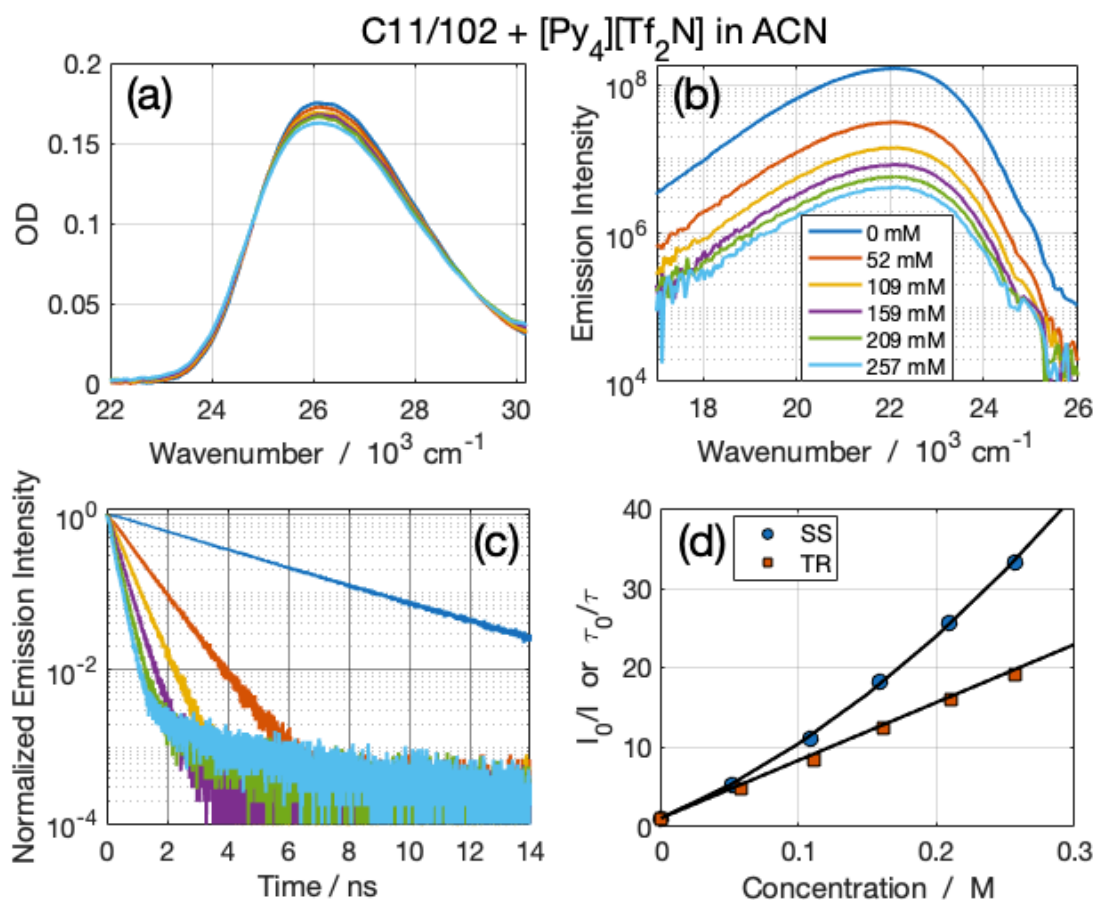


Figure B.9: Representative data for Stern-Volmer experiment in acetonitrile with [Py₄][Tf₂N] as addition quencher to C11/102. (a) Steady state absorption spectra. (b) Steady state emission spectra. (c) TCSPC emission decays. (d) Resulting Stern-Volmer analysis from both steady-state and time-resolved results.

B.3 Photodegradation of Coumarins by Py_4^+ and its Effects

As briefly discussed in Chapter 4, all of the coumarin dyes studied here showed some signs of photodegradation in the presence of Py_4^+ . Samples of coumarins, either in the presence of dilute $[\text{Py}_4][\text{Tf}_2\text{N}]$ in acetonitrile or in neat $[\text{Py}_4][\text{Tf}_2\text{N}]$ were stable in the dark. There was also little change in moderate exposure to room light or under normal conditions used for steady-state spectroscopy. Substantial degradation was only observed upon laser irradiation in TCSPC measurements. The situation in dilute acetonitrile solutions is illustrated by the **C3** (337) data in **Figure B.10**. **C3** exhibited some of the largest effects of photodegradation of all of the solutes examined. Figure MM-C1 shows a pair of experiments in which two identical samples of **C3** in acetonitrile were subjected to 1 hour of laser irradiation (400 nm) in the presence of either 100 mM $[\text{Im}_{41}][\text{Tf}_2\text{N}]$ (top panels) or 100 mM $[\text{Py}_4][\text{Tf}_2\text{N}]$. Emission decays were collected during irradiation, which was interrupted every 10 minutes to quickly record absorption and emission spectra. In the case of dilute $[\text{Im}_{41}][\text{Tf}_2\text{N}]$ the spectra show little systematic variation with time and the emission decays (490 nm) are single exponential with time constant 3.71 ± 0.02 ns over the 7 samples. In contrast, in the 100 mM $[\text{Py}_4][\text{Tf}_2\text{N}]$ case, more than half of the absorbance and emission intensity is lost during irradiation. There is also an approximate isosbestic point near $26,000\text{ cm}^{-1}$ suggesting potentially a direct conversion of **C3** to some UV-absorbing product. The emission decay profile (Figure B.10 (f)) shows a marked change after only 10 minutes after which the time-zero amplitude continues to decrease and the slowly decaying tail increases in relative importance. These comparisons indicate that electron transfer to the Py_4^+ cation is

responsible for initiating the irreversible degradation observed for **C3** and the other coumarins.

Figure B.11 shows emission decays of four coumarins in neat [Py₄][Tf₂N]. These decays were recorded under continuous laser irradiation without removing the sample to record absorption or emission spectra. The behavior displayed here is representative of the behavior observed in the other coumarins. **C3** (337) again shows the most rapid change with irradiation. In all cases, leads to a decreasing $t=0$ amplitude, and in most cases, this decrease is accompanied by a growth in nanosecond components of the decays. In some cases, such as **C12** here, the characteristics of the decay change little and any slow component buildup is too small to interfere with measurement of the faster components of interest. No signs of such photodegradation were observed for coumarins in neat [Im₄₁][Tf₂N]. Based on measurements of this sort, the coumarins can be categorized as being minimally (**C5**, **C6**, **C7**, **C9**, **C10**), moderately (**C1**, **C2**, **C4**, **C12**), and most (**C3**, **C11**) affected by photodegradation as it may interfere with proper measurement of the electron transfer quenching kinetics. No relationship between these groupings and any of the properties of these fluorophores examined here were found.

It should be noted that the aforementioned samples were not stirred because of the difficulty of doing so with high-viscosity liquids like [Py₄][Tf₂N] and [Im₄₁][Tf₂N]. In these samples, it is likely that photoreaction was largely confined to the neighborhood of the ~ 1 mm zone of the sample being irradiated. This supposition was confirmed with the more fluid acetonitrile samples by inverting the cuvette several times during a measurement series. Doing so returned the absorption and emission characteristics closer to those prior to irradiation but did not reverse the changes completely. In order to

minimize the effect of laser degradation in the dilute fluorescence quenching experiments and the TCSPC measurements in neat [Py₄][Tf₂N] we exposure of the sample to laser irradiation was limited to less than 4 minutes. In addition, when analyzing the dilute quenching kinetics, k_q values were those extrapolated to time zero, in order to help minimize effects of cumulative degradation of the higher concentration samples.

In the KGE experiments ~10 mL of sample was flowed throughout data collection. In these experiments, no evidence of photodegradation was observed over the course of three successive measurements, which typically required a time of about three hours.

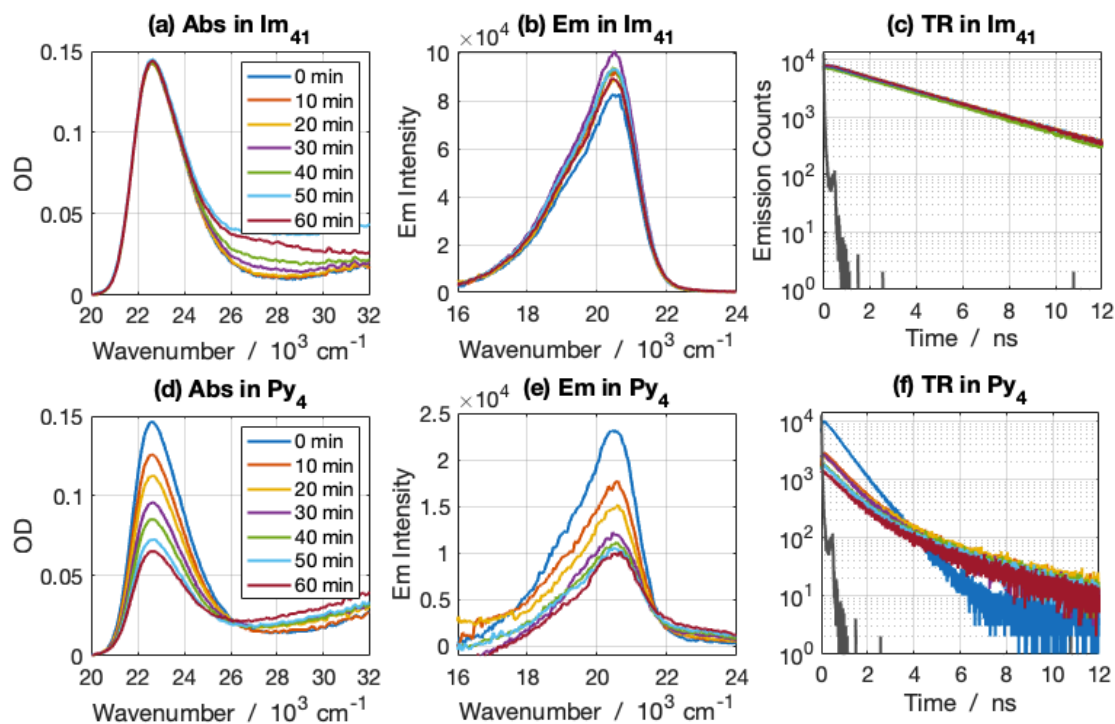


Figure B.10: Set of absorption, emission, and TCSPC measurements of C3/337 in acetonitrile in neat (a-c) [Im₄₁][Tf₂N] and (d-f) [Py₄][Tf₂N] over time. Excitation wavelength for both sets is 400 nm and emission decays were collected at 470 nm for TCSPC measurements.

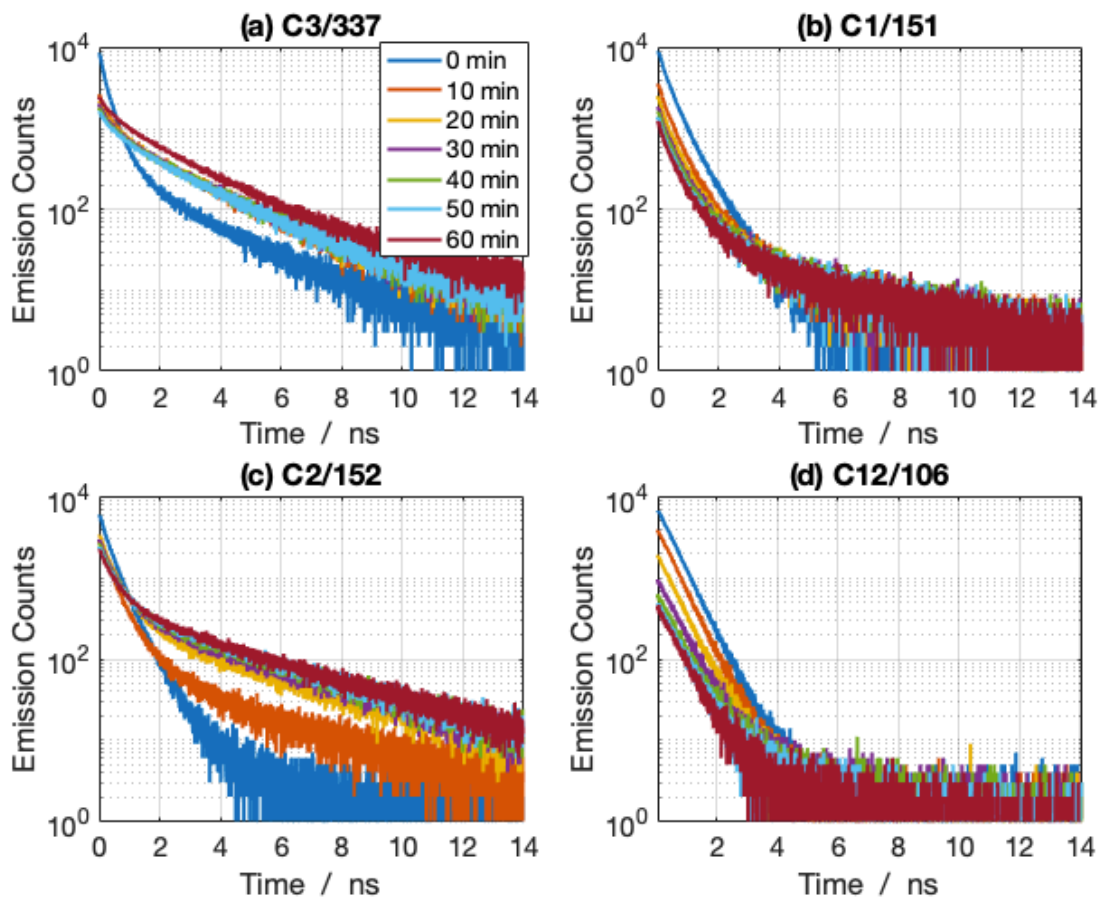


Figure B.11 TCSPC emission decays in neat $[\text{Py}_4][\text{Tf}_2\text{N}]$, measured over time to demonstrate the photodegradation of the coumarins.

Table B.2: Results of Stern-Volmer measurements of coumarins in acetonitrile with Py4⁺ added as quencher

Probe		τ_0 / ns	a / M ⁻¹	b / M ⁻²	SS $k_q^{(a)}$ / 10 ¹⁰ s ⁻¹	a	TR $k_q^{(b)}$ / 10 ¹⁰ s ⁻¹	$f_{obs}^{(c)}$
C1	151	5.15	54	-	10(1)	43	9(1)	0.94
C2	152	2.08	17	-	8(1)	16	8(1)	0.95
C3	337	3.76	36	-	10(1)	31	9(1)	0.95
C4	545	2.77	44	-	16(2)	30	11(1)	0.88
C5	334	3.40	43	-	12(1)	34	10(1)	1.00
C6	498	3.89	44	-	12(1)	38	9(1)	0.92
C7	153	5.68	67	-	11(2)	54	9(1)	0.97
C8	314	3.32	32	67	10(1)	37	11(1)	0.95
C9	1	5.15	54	122	11(1)	56	11(1)	0.96
C10	6H	3.96	77	202	17(6)	72	18(2)	0.96
C11	102	3.75	65	248	18(2)	73	20(2)	0.97
C12	106	3.35	77	320	23(2)	75	23(2)	0.95

(a) SS $k_q = a/\tau_0$, where a is the fitted slope of the plot I_0/I vs. $[Py_4][Tf_2N]$ ($y = a[Q] + 1$).

(b) TR $k_q = a/\tau_0$, where a is the fitted linear slope of the plot I_0/I vs. $[Py_4][Tf_2N]$ ($y = b[Q]^2 + a[Q] + 1$).

(c) f_{obs} is the fraction of the reaction observed from the time-resolved experiments, where

$$f_{obs} = 1 + \frac{I}{I_0} + \frac{\langle \tau \rangle}{\tau_0}.$$

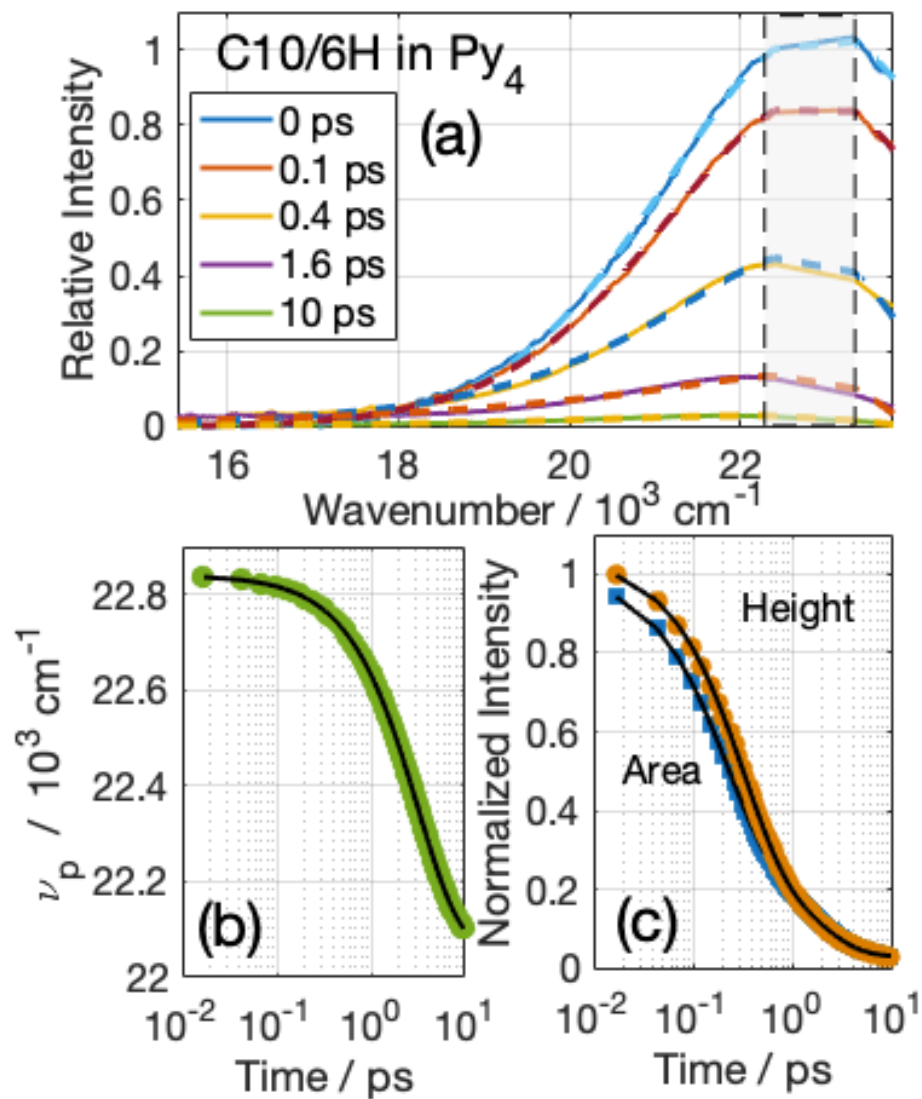


Figure B.12: A representative KGE data set of **C10/6H** in neat [Py₄][Tf₂N]. (a) Time-resolved spectra (solid curves) and lognormal fits (dashed). (b) The peak frequency and (c) the normalized peak height and integrated area. Symbols in panels (b) and (c) are the KGE data and the curves are multi-exponential fits.

B.4 Combining of TCSPC and KGE Data Sets

To obtain more complete representations of the S_1 population decay kinetics, $S(t)$, data from the TCSPC and KGE experiments were combined in the following manner. First, KGE and TCSPC data were and were individually fit to multi-exponential functions of time to partially remove instrumental broadening. The KGE data consisted of complete time-resolved spectra, and the time-dependence of both the peak and integral intensities of the fitted lognormal spectra were used to represent the population decays. These decays required between 2-3 exponential components for proper fit. Because three replicate sets of time-resolved spectra were collected, a total of six intensity decays were available for each system. After normalizing at $t=0$, the mean and the standard deviation of the mean of the 6 decays at each time were used as the best representation of the data and its uncertainty. An example data set (C7, coumarin 153) is shown in Fig. **B.13 (a)**, and the mean decay and its uncertainty of this set are shown in Fig. **B.13 (b)**.

The TCSPC data consisted of single-wavelengths decays (4 nm bandpass) collected near the peak of the steady-state emission. It is clear from Fig. B.13(b) that much of the decay faster than the ~ 25 ps response of the TCSPC experiment are missed by this technique. To combine the short-time KGE data and the long-time TCSPC data, it is assumed that the long-time decay measured by TCSPC experiments is correct apart from an overall scaling factor. A composited decay is therefore determined by scaling the TCSPC data to best match the average KGE data over the range 50-200 ps, shaded region in Fig. B.13 (b), where both experiments are expected to provide reliable results. The result is the red curve in Fig. **B.13(c)**. The scale factor required in the case of C7 shown here is 0.56.

This value is typical of slower fluorophores. For the faster-reacting solutes **C9 - C12**, values are much smaller, and the TCSPC data contributes little to the composite decays.

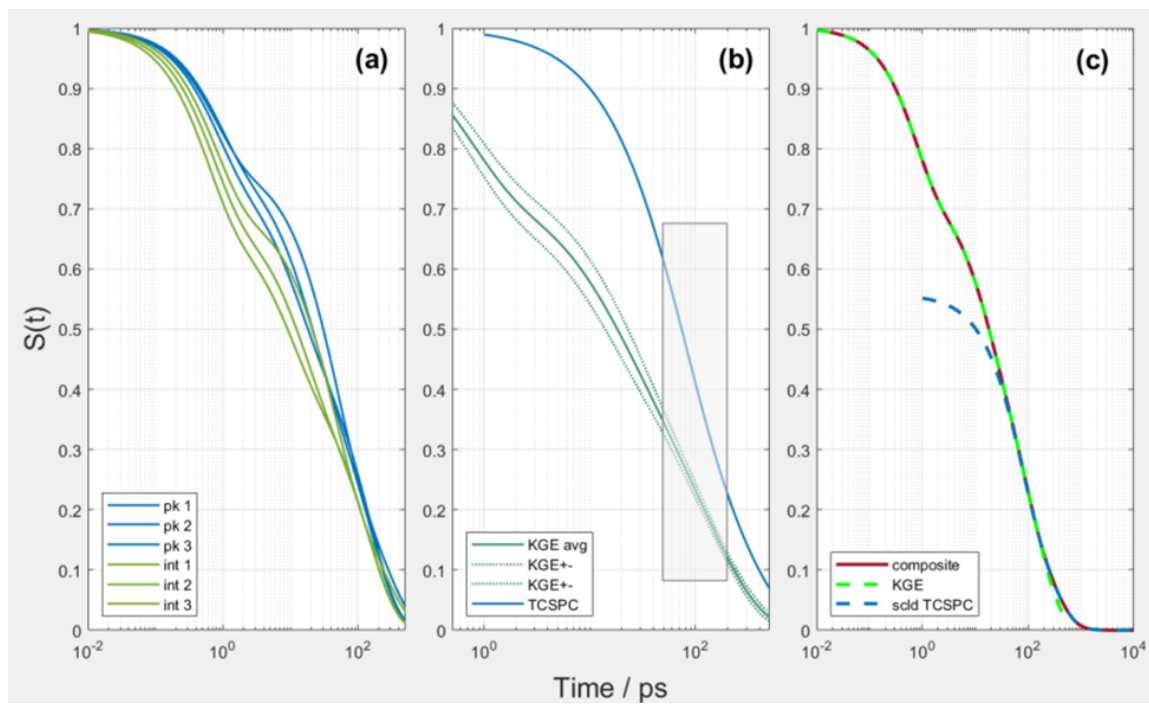


Figure B.13: **C7/153** data illustrating the method of combining KGE and TCSPC data. (a) Normalized peak (pk, blue) and integral (int, green) intensities from three KGE data sets. (b) Average (solid green curve) and uncertainties (dotted green) from the data in panel (a) as well as the normalized TCSPC decay collected at the steady-state emission peak. (c) The composite data set (solid red) and its components – the KGE data in lime green and the scaled TCSPC decay (blue). The combined set is an interpolation of the KGE data for $t \leq 50$ ps, the scaled TCSPC data for $t \geq 200$ ps, and a weighted average of the two between $50 < t < 200$ ps, the gray shaded region in panel (b).

B.5 Maximum Entropy Estimation of Lifetime Distributions:⁹⁻¹²

Lifetime distributions $A(\tau)$ were obtained from the normalized composite decays

$I_n(t) = I(t) / I(0)$ by fitting them with the model

$$I_n^{fit}(t) = \sum_{j=1}^M A(\tau_j) \exp(-t / \tau_j) , \quad (\text{B.6})$$

where the τ_j are $M = 40$ logarithmically space time constants between $10^{-2} - 10^4$ ps. The amplitudes were those that maximized the Shannon-Jaynes entropy of the discretized distribution,

$$S = - \sum_{j=1}^M A_j \ln A_j , \quad (\text{B.7})$$

subject to the least-squares constraint

$$C = \frac{1}{N} \sum_{i=1}^N [I_n^{obs}(t_i) - I_n^{fit}(t_i)]^2 / \sigma^2(t_i) = 1 \quad (\text{B.8})$$

The composite decays $I_n(t)$ were represented at 200 logarithmically spaced times t_i between $10^{-3} - 10^4$ ps. Rather than directly using individual uncertainties $\sigma(t_i)$ in Eq. B.8,

we instead used the mean value $\overline{\sigma^2} = \sum_{i=1}^N \sigma^2(t_i) / N$ for all t_i in order to smooth the

resulting lifetime distributions. These calculations were carried out in Matlab using the optimization routine *fmincon*. Representative fits to $I_n(t)$ and the resulting $A(\tau)$ distributions obtained from them are shown in **Figure B.14**.

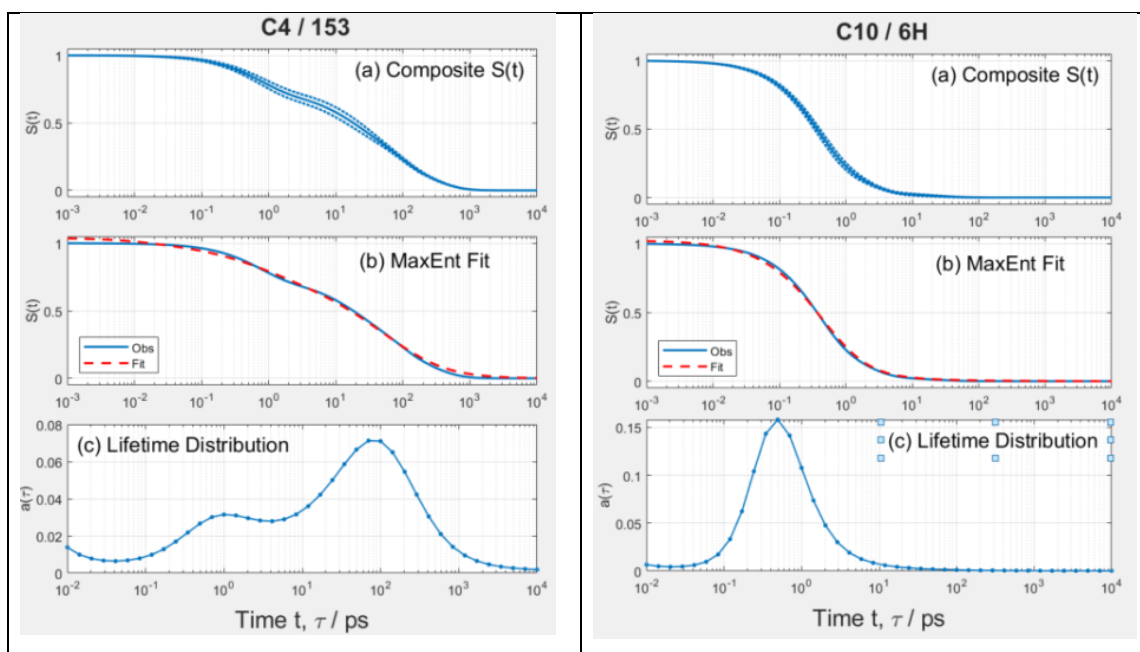


Figure B.14: Two example fits to composite $I_n(t)$ decays for **C4/153** and **C10/6H**. Panels (a) show average composite $S(t)$ curves (solid) and the uncertainties used in fitting (dashed limiting curves). Panels (b) reproduce the average $I_n(t)$ data (solid blue curve) and their fits (red dashed curve). Panels (c) are the lifetime distributions that provide the fits shown in panels (b). The points in these distributions show the 40 discrete $\{\tau_j\}$ used to represent them.

References

1. N. Elgrishi, K. J. Rountree, B. D. McCarthy, E. S. Rountree, T. T. Eisenhart, and J. L. Dempsey, "A Practical Beginner's Guide to Cyclic Voltammetry," *J. Chem. Educ.* **95**, 197-206 (2018). 10.1021/acs.jchemed.7b00361
2. G. Jones, S. F. Griffin, C. Y. Choi, and W. R. Bergmark, "Electron Donor-Acceptor Quenching and Photoinduced Electron-Transfer for Coumarin Dyes," *J Org Chem* **49**, 2705-2708 (1984). DOI 10.1021/jo00189a010
3. C. E. Crespo-Hernandez, D. M. Close, L. Gorb, and J. Leszczynski, "Determination of Redox Potentials for the Watson-Crick Base Pairs, DNA Nucleosides, and Relevant Nucleoside Analogs," *J. Phys. Chem. B* **111**, 5386-5395 (2007). 10.1021/jp0684224
4. D. Zuniga-Nunez, P. Barrias, G. Cardenas-Jiron, M. S. Ureta-Zanartu, C. Lopez-Alarcon, F. E. Moran Vieyra, C. D. Borsarelli, E. I. Alarcon, and A. Aspee, "Atypical antioxidant activity of non-phenolic amino-coumarins," *RSC Adv.* **8**, 1927-1933 (2018). 10.1039/C7RA12000A
5. C. A. M. Seidel, A. Schulz, and M. H. M. Sauer, "Nucleobase-specific quenching of fluorescent dyes .1. Nucleobase one-electron redox potentials and their correlation with static and dynamic quenching efficiencies," *J Phys Chem-Us* **100**, 5541-5553 (1996). DOI 10.1021/jp951507c
6. H. G. Roth, N. A. Romero, and D. A. Nicewicz, "Experimental and Calculated Electrochemical Potentials of Common Organic Molecules for Applications to Single-Electron Redox Chemistry," *Synlett* **27**, 714-723 (2016). 10.1055/s-0035-1561297
7. D. T. Sawyer, A. Sobkowiak, and J. L. Roberts, *Electrochemistry for Chemists*, 2nd ed. (Wiley, United Kingdom, 1995).
8. D. S. McDaniel and H. C. Brown, "Extended table of Hammett substituent constants based on the ionization of substituted benzoic acids," *J. Org. Chem.* **23**, 420-427 (1958). 10.1021/jo01097a026
9. J. R. Banavar, A. Maritan, and I. Volkov, "Applications of the principle of maximum entropy: from physics to ecology," *J. Phys.: Condens. Matter* **22**, 063101/063101-063101/063113 (2010). 10.1088/0953-8984/22/6/063101
10. A. K. Livesey and J. C. Brochon, "Analyzing the distribution of decay constants in pulse-fluorometry using the maximum entropy method," *Biophys. J.* **52**, 693-706 (1987). 10.1016/S0006-3495(87)83264-2
11. J.-C. Brochon, "Maximum entropy method of data analysis in time-resolved spectroscopy," *Methods Enzymol.* **240**, 262-311 (1994).
12. P. J. Steinbach, R. Ionescu, and C. R. Matthews, "Analysis of kinetics using a hybrid maximum-entropy/nonlinear-least-squares method: application to protein folding," *Biophys. J.* **82**, 2244-2255 (2002). 10.1016/S0006-3495(02)75570-7

CURRICULUM VITAE

Marissa Saladin

EDUCATION

Ph. D. Pennsylvania State University, University Park, PA	December 2020
B.S. Aquinas College, Grand Rapids, MI	May 2014

TEACHING EXPERIENCE

Teaching Assistant: General Chemistry	2018-2020
Teaching Assistant: Problem Solving in Chemistry	2018-2020
Cottrell Scholars Collaborative: National Teaching Assistant Workshop	2019
Graduate Student Online Teaching Certification, Pennsylvania State University	2019
Graduate Student Teaching Certification, Pennsylvania State University	2019
Course in College Teaching, Schreyer Institute for Teaching Excellence	2019
Teaching Assistant: Experimental Physical Chemistry	2015-16, 2017-2018

PUBLICATIONS AND PRESENTATIONS

Saladin, M.; Maroncelli, M. Electron Transfer Kinetics in Neat Quenching Ionic Liquid. *Manuscript in Preparation.*

Saladin, M.; Rumble, C. A.; Wagle, D V.; Baker, G. A.; Maroncelli, M. Characterization of a New Donor-Acceptor Dyad in Conventional Solvents and Ionic Liquids. *J. Phys. Chem. B*, **2019**, *123* (44), 9395-9407. DOI: 10.1021/acs.jpcc.9b07077.

Saladin, M.; Maroncelli, M.; Yennawar, H. *n*-Decyltrimethylammonium bromide. *IUCrData* **2019**, *4*, x190933. DOI: 10.1107/S2414314619009337.

Saladin, M.; Rumble, C.; Wu, B.; Castner, E.; Maroncelli, M. Intermolecular Electron Transfer in Neat Pyridinium Ionic Liquids. Poster presented at American Chemical Society Middle Atlantic Regional Meeting; June 4-6, 2017; Hershey, PA.

Jensen, E.; **Saladin, M.** Determination of Physical Property Trends of Alkylammonium Metal Bromide Liquid Crystals. *J. Undergrad. Chem. Res.* **2014**, *13*, 26-28.

HONORS

Dan. H. Waugh Teaching Award	2019
Continuing Graduate Student Teaching Assistant Award	2018
Bunton-Waller Assistantship	2014-2016